Deterministic and Stochastic Modelling of Fines Attachment and Detachment during Colloidal Flows

Thomas Russell, B.Eng. (Hons)

A thesis submitted for the degree of Doctor of Philosophy (Ph.D.)

Australian School of Petroleum and Energy Resources
Faculty of Engineering, Computer & Mathematical Sciences
The University of Adelaide

February 2021

To

my family

who have been an unending and unwavering source of support in all my endeavours

Table of Contents

Abstract

Hereby I present a PhD thesis by publication. This thesis includes seven journal publications, four of which have been published, two have been accepted for publication, and one which has been submitted for publication.

This thesis is focussed on using mathematical techniques alongside laboratory tests to improve the modelling of microscale processes in porous media. Both deterministic and stochastic processes are used in order to most accurately model these processes.

The laboratory tests are largely centred around investigating particle detachment. By developing a methodology to produce artificial sand-kaolinite cores with uniform and reproducible properties including clay content, the impact of clay content on low-salinity water induced permeability decline is investigated. It is found that above a certain clay threshold, between 1-3% total mass content, particle detachment and straining manifest in similar ways, evidenced by the measured drop in permeability. It also shown that only a fraction of clay particle can be potentially detached.

Additional laboratory tests investigate in more detail the process by which changing the fluid salinity results in particle detachment. In both a single-phase environment and in the presence of residual oil, it is shown that when using calcium ions in the injected water, reduction of the fluid salinity does not detach particles. The opposite is found to be true for sodium ions. Investigations around these laboratory tests are presented, and a tentative conclusion is drawn that calcium ions adsorb on the clay surface with significant hysteresis during the loading and unloading stages.

Novel analytical solutions are presented for fines migration accounting for the delay in particle detachment observed in experimental studies in the literature. Both the linear case and axi-symmetric flow cases are presented, and analytical solutions are given for the suspended and strained particle concentrations and the pressure drop. The solutions highlight the impact of the delay, which significantly affects the stabilisation time, but does not affect the stabilised strained particle profile or the final pressure profile.

The thesis also presents three models derived using Boltzmann's kinetic equation applied to colloidal flows in porous media. The model allows for coupling of a distribution of particle velocities and a particle velocity dependent capture. The models are upscaled using Fourier transforms and Hilbert space projection operators. First, the base model is presented, compared with laboratory data, and investigated, revealing inherent relationships between the model coefficients. The upscaled model exhibits delayed advective velocity for the particles compared with the fluid.

Two generalisations of this model are presented, in the form of an arbitrary dependence of the capture on velocity, and the general 3-Dimensional anisotropic case. The former allows for investigation of emergent macroscale behaviour using various microscale models for capture, and the latter is capable of modelling the effects of transverse flow on capture, which is shown to be significant even in quasi-1-Dimensional flows.

The models presented in this work are relevant and applicable to many industries, including water management, environmental and chemical engineering, and energy-generation technologies. The use of more accurate models provides better predictions and allow operators to make more informed decisions. The key findings include a greater understanding of particle detachment, and new models for fines migration with delayed particle detachment, and particle flow in porous media with simultaneous capture and dispersion.

Declaration

I certify that this work contains no material which has been accepted for the award of any other degree or diploma in my name, in any university or other tertiary institution and, to the best of my knowledge and belief, contains no material previously published or written by another person, except where due reference has been made in the text. In addition, I certify that no part of this work will, in the future, be used in a submission in my name, for any other degree or diploma in any university or other tertiary institution without the prior approval of the University of Adelaide and where applicable, any partner institution responsible for the joint-award of this degree.

I acknowledge that copyright of published works contained within this thesis resides with the copyright holder(s) of those works.

I also give permission for the digital version of my thesis to be made available on the web, via the University's digital research repository, the Library Search and also through web search engines, unless permission has been granted by the University to restrict access for a period of time.

I acknowledge the support I have received for my research through the provision of an Australian Government Research Training Program Scholarship.

Thomas Russell **25/02/2021**

Acknowledgement

The completion of this thesis would not have been possible without the love and support I received from those around me.

I would like to extend my thanks to my supervisor Prof. Pavel Bedrikovetsky, who provided me with support and technical guidance, but who above all demonstrated a passion for his work that allowed me to maintain my passion in mine. I consider his devotion to his work an inspiration and I can only hope to replicate a fraction of it in my lifetime.

A sincere thank you to all of the people whom I have had the pleasure of collaborating with in my research. My co-supervisor Dr. Abbas Zeinijahromi deserves thanks for his guidance and support. I extend my gratitude to Duy Pham, Dr. Sara Borazjani, Dr. Larissa Chequer, Dr. Zhenjiang You, Kiet Wong, Dr. Abdullah Al-Sarihi, Dr. Themis Carageorgos, and Dr. Osipov Dinariev among many others for their support, patience, and rigour in their research. A special thank you is reserved for Dr. Alexander Badalyan, whose tireless efforts and unrelenting kindness has provided me with an example I will not soon forget.

I must also extend gratitude to my fellow PhD students. I consider frank technical discussions not an advantage, but an absolute necessity in performing my research. Your contributions to my research are largely uncredited, but please know that they are greatly appreciated. In addition, your support, guidance, and above all humour, have made this journey not only possible but enjoyable.

Lastly, I must thank my friends and family.

To Cameron, you have never failed in being a great friend. Our friendship means more to me than you could know and despite our distance from each other, I know I can always rely on you. To my mother and father, Karen and Robin, I thank you for your love, your support, your patience, and your care. I have received no greater blessing than being born to you both. A big thank you is also owed to my brother and sister-in-law, James and Kate. Lastly, a thank you to my grandparents, whose love and support will remain eternally as the standard for unconditional.

Thesis by Publication

Published Peer-Reviewed Journal Papers

Russell, T., Pham, D., Neishaboor, M. D., Badalyan, A., Behr, A., Genolet, L., Kowollik, P., Zeinijahromi, A., Bedrikovetsky, P., Effects of kaolinite in rocks on fines migration, Journal of Natural Gas Science and Engineering,Volume 45,2017,Pages 243-255

Russell, T., Bedrikovetsky, P., Colloidal-suspension flows with delayed fines detachment: Analytical model & laboratory study, Chemical Engineering Science, Volume 190, 2018, Pages 98-109

Russell, T., Wong, K., Zeinijahromi, A., Bedrikovetsky, P., Effects of delayed particle detachment on injectivity decline due to fines migration, Journal of Hydrology, Volume 564, 2018, Pages 1099-1109

Al-Sarihi, A., **Russell, T.**, Bedrikovetsky, P., Zeinijahromi, A., Fines Stabilization by Ca Ions and Its Effect on LSW Injection, Energy & Fuels 2019 33 (11), 10775-10786

Journal Papers Accepted for Publication

Russell, T., Dinariev, O. Yu., Pessoa Rego, L. A., Bedrikovetsky, P., Averaged Boltzmann's kinetics for colloidal transport in porous media, Water Resources Research, Accepted for publication

Russell, T., Bedrikovetsky, P., Boltzmann's colloidal transport in porous media with velocity-dependent capture probability, Physics of Fluids, Accepted for publication, e2020WR029557

Submitted Journal Papers

Russell, T., Bedrikovetsky, P., Colloidal transport in anisotropic porous media: kinetic equation and its upscaling, Physics of Fluids, Submitted

Published Book Chapter

Russell, T., Chequer, L., Borazjani, S., You, Z., Zeinijahromi, A., Bedrikovetsky, P., Chapter Three - Formation Damage by Fines Migration: Mathematical and Laboratory Modeling, Field Cases, Editor(s): Bin Yuan, David A. Wood, Formation Damage During Improved Oil Recovery, Gulf Professional Publishing, 2018, Pages 69-175

International Conference Papers and Presentations

Russell, T., Pham, D., Petho, G., Neishaboor, M.D., Badalyan, A., Behr, A., Genolet, L., Kowollik, P., Zeinijahromi, A., Bedrikovetsky, P., Kaolinite Mobilisation in Unconsolidated Porous Media: Effect of Brine Salinity and Salt Type Na- and Ca Salts. Paper presented at the SPE Asia Pacific Oil and Gas Conference and Exhibition, Brisbane, Australia, October 2018

Russell, T., Chequer, L., Badalyan, A., Behr, A., Genolet, L., Kowollik, P., Zeinijahromi, A., Bedrikovetsky, P., Systematic Laboratory and Modelling Study of Kaolinite in Rocks on Formation-Damage-Fines-Migration Non-Equilibrium Effects, Analytical Model, SPE International Conference and Exhibition on Formation Damage Control. Society of Petroleum Engineers, Lafayette, Louisiana, USA, 2018, https://doi.org/10.2118/189533-MS

Borazjani, S., Chequer, L., **Russell, T.**, Bedrikovetsky, P., Injectivity Decline During Waterflooding and PWRI due to Fines Migration, SPE International Conference and Exhibition on Formation Damage Control. Society of Petroleum Engineers, Lafayette, Louisiana, USA, 2018, https://doi.org/10.2118/189521-MS

Russell, T., Chequer, L., Badalyan, A., Zeinijahromi, A., Bedrikovetsky, P., Effect of kaolinite content on formation damage due to fines migration: Systematic laboratory and modelling study. The APPEA Journal, 58: 743-747, 2018, https://doi.org/10.1071/AJ17189

1. Contextual Statement

Significance of the project The significance and impact of this PhD project lie in the novel formulations of colloidal processes, outlining a stronger adherence to microscale physics. These formulations are supported by experimental works designed to both investigate phenomena and confirm the accuracy of modelling efforts. Modelling efforts are combined with mathematical techniques to produce analytical solutions to enhance the usability of the models. The combination of these efforts underpins a strong academic contribution, as well as novel techniques for industrial application.

Colloidal formation damage is present both due to injection of foreign particles, and due to detachment of natural fines. Both processes are present in injection and production operations in the petroleum industry. Fines detachment and the associated formation damage is vital to low-salinity waterflooding projects, due to the propensity of the low-salinity water to detach fine particles.

The underlying processes particle attachment, detachment, and colloidal flow are often available for observation only through indirect measurements of particle concentrations and pressure gradients. Accurate mathematical models provide not only the ability to better differentiate and understand the underlying processes, but also more accurate means to characterise the interaction between particles and the porous media. The development of these models and existence of analytical solutions allows researchers to develop a deep understanding of processes that are too often out of reach.

Accurate and consistent models are also central to decision making in industrial processes. Whether it is through making predictive analysis of formation damage, uncertainty analysis of colloidal/contaminant transport, or assessing the viability of damage mitigation and prevention techniques, the ability of practitioners to model colloidal processes is crucial. In addition, the existence of analytical solutions improves the ease and speed with which these calculations can be made.

State of the art Modelling of colloidal processes has long garnered attention in industrial and theoretical areas. Strong modelling efforts have been driven by interest in environmental, agricultural, chemical, and petroleum applications (Civan, 2014; Hunt & Sahimi, 2017; Khilar & Fogler, 1998). Petroleum applications in particular has been concerned with injectivity decline in injection wells(Barkman, Abrams, Darley, & Hill, 1975; Pang & Sharma, 1997) and the potential for fines migration to improve sweep efficiency (Zeinijahromi, Nguyen, & Bedrikovetsky, 2013) and reduce residual oil saturation (Al-Sarihi et al., 2018), thus increasing oil production. Central to these modelling efforts is a mass continuity equation of the suspended particle population:

$$\frac{\partial}{\partial t}\left(\phi c + \sigma_a + \sigma_s\right) + U\frac{\partial c}{\partial x} = D\frac{\partial^2 c}{\partial x^2} \tag{1.1}$$

where t is time, ϕ is the porosity, c is the suspended particle concentration, σ_a is the attached particle concentration, σ_s is the strained, or captured particle concentration, U is the mean particle velocity, x is the spatial coordinate, and D is the diffusion coefficient.

Two important questions in modelling flow and capture of suspended particles is the form of the detachment and attachment (capture) equations. Detachment is governed by the rate of decrease of attached particles, $\frac{\partial \sigma_a}{\partial t}$, while detachment is determined by $\frac{\partial \sigma_s}{\partial t}$.

Particle detachment is governed by the balance of forces acting on attached particles(Bedrikovetsky, Siqueira, Furtado, & Souza, 2011; You, Yang, Badalyan, Bedrikovetsky, & Hand, 2016). Early approaches relied on an empirical detachment rate coefficient(Herzig, Leclerc, & Goff, 1970), which left the detachment rate without any physical intuition or more fundamental physical justification. More recent approaches have used explicit formulae for acting forces and formulated the so-called critical retention function, σ_{cr}. Using the equations, the critical retention function can be related to system parameters such as the fluid velocity or salinity. This approach however limits the kinetics of detachment to be equal to the rate with which these system parameters change.

A less studied issue surrounding Equation (1.1) is the relationship between particle capture and dispersion. Individually, each process has been modelled successfully; particle capture is proportional

to the particle velocity and suspended particle concentration (Civan, 2014), while particle dispersion in the form presented in Equation (1.1) follows from a distribution of particle velocities on the pore scale, and any number of upscaling techniques (Einstein, 1905). What remains unclear is how to accurately model the co-existence of both processes. When particles move with varying velocities, the question arises, to which velocity is their capture proportional to?

Careful examination of existing microscale models of capture reveals that many of them capture a non-linear dependence on the fluid velocity (Andrade, Araújo, Vasconcelos, & Herrmann, 2008; Tien & Payatakes, 1979; Tufenkji & Elimelech, 2004). These more complex velocity capture models also need to be combined with particle diffusion/dispersion to analyse any emerging macroscale phenomena.

Scope of the work In light of the above presentation of the state of the art, the main achievements of this thesis are

- Development of a reproducible and reliable experimental technique which produces artificial sand-kaolinite cores with uniform attached particle profile with known concentration
- A series of experimental tests which demonstrate the impact of total clay content on detached concentration, illustrating for the first time the small fraction of attached particle that are subject to detachment
- Development and analytical solution of a 1-Dimensional model which accounts for delay in particle detachment while still utilising the critical retention function and which explicitly models the fluid salinity
- Development and analytical solution of a 1-Dimensional axi-symmetric model which accounts for delay in particle detachment while still utilising the critical retention function in order to model injectivity decline in low-salinity water injection wells
- Formulation and upscaling of Boltzmann's kinetic equation for colloidal flow and capture as well as comparison with laboratory data and development of relationships between coefficients

- Formulation and upscaling of Boltzmann's kinetic equation for arbitrary capture function
- Formulation and upscaling of Boltzmann's kinetic equation for 3-Dimensional flow and capture of particles in general anisotropic case

1.1 Thesis Structure

This is a PhD thesis by publication. Seven publications are presented in this thesis, of which four have been published in journals, two have been accepted for publication, and one has been submitted for publication.

The thesis body is formed by five Chapters. The first Chapter includes an introduction to the problems addressed in the thesis and outlines their importance. The second Chapter presents a discussion of the contemporary literature surrounding the works of this thesis, including discussions of modelling efforts for particle attachment, detachment, and flow. A detailed literature review is included in this chapter. Chapters three, four, and five present the novel research performed as part of this thesis.

Paper	Chapter	Title	Status
1	Chapter 3	Effects of kaolinite in rocks on fines migration	Published
2		Fines Stabilization by Ca Ions and Its Effect on LSW Injection	Published
3	Chapter 4	Colloidal-suspension flows with delayed fines detachment: Analytical model & laboratory study	Published
4		Effects of delayed particle detachment on injectivity decline due to fines migration	Published
5	Chapter 5	Averaged Boltzmann's kinetics for colloidal transport in porous media	Accepted for Publication
6		Boltzmann's colloidal transport in porous media with velocity-dependent capture probability	Accepted for Publication
7		Colloidal transport in anisotropic porous media: kinetic equation and its upscaling	Submitted for Publication

Accurate modelling of colloidal flows in porous media is of great importance to many industries, including petroleum engineering. However current models are not accurately modelling the underlying microscale processes that define the observed behaviour in laboratory and field studies. Particle detachment in particular has a large history of empirical modelling, with more recent attempts at accurate microscale models falling short due to a lack of laboratory works to support their

assumptions. As a result, two experimental studies are presented in Chapter three which allow for a better physical understanding of the detachment process. The results demonstrate that previous studies vastly overestimated the proportion of particles that can detach under any conditions, and that the influence of selective cation exchange can cause significant inconsistencies between experiments and current modelling efforts. In order to study the effect of total clay content on particle detachment, a novel laboratory methodology is developed which allows for reproducible production of artificial cores with uniform properties. Such cores allow for comparison across multiple tests, which carries significant uncertainty when using real cores due to unseen heterogeneity.

In Chapter four, more rigorous mathematical models of particle detachment are formulated and consequently solved analytically. This model is first discussed in the linear case, as is appropriate for laboratory corefloods and fracture-linear flows in industrial applications. In this Chapter, the influence of a delay in particle detachment is emphasized. It has long been observed that changing the salinity of injected water will result in particle detachment, but over time scales substantially larger than expected. Previous works relied on the assumption that particles travel slower than the injected fluid. While this has backing in physical intuition, an incredibly slow particle velocity is typically required to explain experimental results. Thus, we investigate the long experimental times under the assumption that particles detach with delay. The combination of delayed detachment with the use of the critical retention function brings the model more in line with experimental evidence that changes to fluid salinity will impact particles only after some time. The delay is justified by the time-limiting cation exchange on the particle surface. During incompressible axi-symmetric flow, such as during water injection in an oilfield, particle detachment will occur in two stages, first by the induced velocity field, causing some particles to detach instantaneously within the formation fluid, and secondly by the injected fluid, which moves through the porous media causing detachment with some delay. This ‘dual-delay’ situation is also modelled in Chapter three, with an analytical solution presented alongside the formulation.

Lastly, Chapter five addresses the co-existence of both significant particle capture and dispersion/diffusion. While each process has a strong microscale understanding and consequent

models, the existence of both processes results in complex interactions that have until now only been addressed intuitively. The models presented in this Chapter rely on Boltzmann's kinetic equation, which is formulated to describe colloidal flow and capture. Upscaling of this equation results in an advection-diffusion equation with capture and delayed advective velocity. Each of the upscaled coefficients are presented as explicit functions of the microscale parameters directly associated with the underlying processes. Three major developments are presented in this Chapter. First the model is presented, compared with laboratory data, and analysed in detail with respect to the model coefficients. Analysis of the coefficients reveals that the interaction between processes on the microscale leads to an explicit relationship linking the macroscale parameters. Secondly the model is generalised to account for any velocity-dependent capture function, which is shown to be present in many existing models for particle capture. Lastly the model is generalised to three dimensions, where anisotropy is allowed. Reduction of the 3-Dimensional solution to a single spatial dimension produces a 1-D advection diffusion equation which accounts for capture in the two directions perpendicular to flow, a previously unaddressed phenomenon.

1.2 How the Publications are related to the Thesis

The paper "Effects of kaolinite in rocks on fines migration" presents the novel experimental technique to produce reproducible cores with controlled and uniform properties. The study utilised a number of coreflooding tests to analyse the impact of total clay content on the extent of formation damage and the total detached concentration. DLVO (Derjaguin, Landau, Verwey, and Overbeek) theory, which describes the electrostatic interaction between two substrates, is used to analyse the effect of salinity, which is varied across different corefloods. The study shows that above a certain clay content threshold, here between 1 and 3% total mass, sufficient clay is available for detachment that the cores exhibit qualitatively similar behaviour. The results provide greater insight into the nature of particle detachment in porous media.

While many studies are dedicated to investigating low-salinity waterflooding, recent works have paid more attention not only to the total salinity of the injected fluid, but also to the specific ionic content. Given their role in mitigating the charge of clay materials, cations are of more importance than their

negatively charged counterparts. In the paper "Fines Stabilization by Ca Ions and Its Effect on LSW Injection" the typical NaCl fluid composition is compared with the less common $CaCl_2$. The tests are performed by decreasing the total salinity of each particular fluid stepwise, down to deionised water, which contains negligible amounts of each ion. The tests were performed in both single-phase, and in the presence of residual oil. All observed indicators of fines detachment being a spike in outlet suspended concentration, a sharp increase in pressure drop across the core, and a decrease in the residual oil saturation, all indicate that when saturated with $CaCl_2$, no change in salinity, even down to deionised water, can release fines. On the contrary, when, in the same core, NaCl is injected, followed by deionised water, all measurements indicate significant fines detachment. Thus this experimental work reveals an important and novel result: that the cation exchange on the particle surface, which dictates its detachment, can exhibit hysteresis. Hysteresis in cation adsorption is exhibited by Ca^{2+} ions, which remain even during deionised water injection, maintaining the strong electrostatic force which holds particles to the surface. The inherent hysteresis may be a kinetic effect, not one of equilibrium, but its impact remains: accurate modelling of particle detachment in the presence of multiple cations must account for potential hysteresis. This effect is not evident in the traditional modelling using the critical retention function.

The same cation exchange that detaches particles, has been shown in other works to occur with significant delay. This delay is accounted for quantitatively in the paper "Colloidal-suspension flows with delayed fines detachment: Analytical model & laboratory study". The objective of the paper is not only to include the delay in detachment, but to do so in such a way as to include the critical retention function, a widely used formulation that allows for explicitly linking system parameters (velocity, salinity, etc.) to detached particle concentrations. This formulation requires explicitly modelling the salinity front as it progresses through the porous media. Neglecting both particle and ion diffusion/dispersion, an analytical solution is presented using the method of characteristics, allowing for explicit expressions for the suspended and strained concentrations as well as the pressure drop. Laboratory experiments are presented in this study and compared with the model in order to assess its accuracy. Good agreement is found.

A natural extension of such a model is an axi-symmetric coordinate system. This is the formulation most commonly used to model fluid flow in production and injection wells in the petroleum industry. In the paper "Effects of delayed particle detachment on injectivity decline due to fines migration" precisely this model is presented. The nuance of this model lies not only in the dependence of the velocity on the radial coordinate, but again in how particle detachment is formulated. Here we cannot rely solely on the first-order delay term used in the linear model, because the initiation of flow will cause particle detachment variably across the reservoir due to the induced flow field. These particles will detach instantly, according to the critical retention function. Once injection commences, the new injection fluid will travel through the reservoir, resulting in the same delayed detachment discussed earlier. Thus detachment occurs for two reasons, first due to increased drag on the attached particles, and secondly, due to a weaker electrostatic force holding them to the porous matrix. A physical understanding of these processes necessitates using two delays, one infinitesimally small, and one finite. Again, an analytical solution is presented using the method of characteristics, which in this case results in implicit equations for the suspended concentration. A by-product of this formulation is a requirement for a more thorough characterisation of the porous media. Whereas in previous studies the critical retention function would have to be defined at initial and injected salinities, velocities, etc., in this case, it is required that σ_{cr} is defined for all velocities encountered, and across the entire salinity range, even if the absence of diffusion means that only two salinity values are encountered.

While the focus remains on more accurate modelling of the underlying physical processes, the above-mentioned modelling efforts are deterministic. In the paper "Averaged Boltzmann's kinetics for colloidal transport in porous media" a stochastic approach is used, not to introduce new phenomena, but to reconcile two existing microscale processes. Both particle attachment and transport and formulated in Boltzmann's kinetic equation, with a linear BGK type relaxation term governing diffusion/dispersion. The equation is upscaled using Hilbert space projections and the Fourier transform, resulting in an advection-diffusion equation with delayed advective velocity. This new effect results exactly from the coupling of capture and transport, and vanishes in the absence of either capture, or varying microscale particle velocity variation. The upscaled coefficients are related explicitly to the microscale coefficients and much attention is paid to understanding their nature.

Comparison with laboratory results demonstrates the effectiveness of the model but also highlights potential shortcomings.

The final two papers present generalisations to this theory. The first, "Boltzmann's colloidal transport in porous media with velocity-dependent capture probability" presents the same derivations while allowing for the particle capture to depend on the velocity in any way. Careful inspection of existing models reveals that a number of velocity dependent capture processes have already been investigated and quantified. What is discussed in this paper is how these velocity dependent capture processes interact with a particle population with different velocities. While each model produces the same advection-diffusion equation with capture, the different microscale descriptions lead to widely varying macroscale behaviour in the form of the coefficients. We show that when the capture preferentially captures slower particles, as is the case for Tufenkji and Elimelech's attachment model, then the mean advective velocity of the particles can be faster than that of the carrier fluid. The chosen models are compared with several laboratory tests, and significant deviation is found in their ability to match the breakthrough curves. The inherent correlations found between the coefficients provide a fingerprint for each microscale capture model, and consequently, laboratory tests studying different phenomena to those described in the models will produce datasets incompatible with the models. Thus the derived model provides a means to derive from laboratory data not just the system parameters, but also information on the potential underlying microscale phenomena.

Lastly, the paper "Colloidal transport in anisotropic porous media: kinetic equation and its upscaling" generalises the model to three dimensions. The formulation allows for general anisotropy in capture, equilibrium flow properties, and relaxation, the effect which leads to diffusion/dispersion. The upscaling procedure results in a 3-Dimensional advective diffusion equation with capture, with cross diffusion terms and delayed velocity in each of the three advective terms. Each coefficient now accounts for the impact of particle capture in all three directions. It is shown that in certain simplified cases, the upscaled capture coefficient is equal to the scalar product of the three microscale capture coefficients and the three average velocities. The three-dimensional equation can be reduced to a one-dimensional equation of the same form as the two previous papers, with the key difference that the

coefficients now account explicitly for the motion and capture of the particles in the two directions perpendicular to flow. This inclusion is shown to be significant to the emergent macroscale behaviour.

The above-mentioned seven papers represent an effort to more accurately model particle capture and flow in porous media. The papers provide insight into microscale phenomena, and present formulations and subsequent analytical solutions for models that account for these phenomena to provide more accurate predictions of formation damage and fines transport in waterflooding and oil production processes.

1.3 References

Al-Sarihi, A., Zeinijahromi, A., Genolet, L., Behr, A., Kowollik, P., Bedrikovetsky, P. J. E., & Fuels. (2018). Effects of fines migration on residual oil during low-salinity waterflooding. *32*(8), 8296-8309.

Andrade, J. S., Araújo, A. D., Vasconcelos, T. F., & Herrmann, H. J. (2008). Inertial capture in flow through porous media. *The European Physical Journal B, 64*(3), 433-436. doi:10.1140/epjb/e2008-00079-y

Barkman, J., Abrams, A., Darley, H., & Hill, H. (1975). An Oil-Coating Process To Stabilize Clays in Fresh Waterflooding Operations (includes associated paper 6405). *Journal of Petroleum Technology, 27*(09), 1,053-051,059.

Bedrikovetsky, P., Siqueira, F. D., Furtado, C. A., & Souza, A. L. S. (2011). Modified Particle Detachment Model for Colloidal Transport in Porous Media. *Transport in Porous Media, 86*(2), 383-413. doi:10.1007/s11242-010-9626-4

Civan, F. (2014). *Reservoir Formation Damage* (3rd ed. ed.). Burlington, MA, USA: Gulf Professional Publishing.

Einstein, A. (1905). On the motion of small particles suspended in liquids at rest required by the molecular-kinetic theory of heat. *J Annalen der physik, 17*(549-560), 208.

Herzig, J., Leclerc, D., & Goff, P. L. (1970). Flow of suspensions through porous media—application to deep filtration. *Industrial & Engineering Chemistry, 62*(5), 8-35.

Hunt, A. G., & Sahimi, M. (2017). Flow, Transport, and Reaction in Porous Media: Percolation Scaling, Critical-Path Analysis, and Effective Medium Approximation. *55*(4), 993-1078. doi:https://doi.org/10.1002/2017RG000558

Khilar, K. C., & Fogler, H. S. (1998). *Migrations of fines in porous media*. Dordrecht: Kluwer Academic Publishers.

Pang, S., & Sharma, M. (1997). A model for predicting injectivity decline in water-injection wells. *SPE Formation Evaluation, 12*(03), 194-201.

Tien, C., & Payatakes, A. C. (1979). Advances in deep bed filtration. *25*(5), 737-759. doi:https://doi.org/10.1002/aic.690250502

Tufenkji, N., & Elimelech, M. (2004). Correlation equation for predicting single-collector efficiency in physicochemical filtration in saturated porous media. *Environ Sci Technol, 38*(2), 529-536.

You, Z. J., Yang, Y. L., Badalyan, A., Bedrikovetsky, P., & Hand, M. (2016). Mathematical modelling of fines migration in geothermal reservoirs. *Geothermics, 59*, 123-133. doi:10.1016/j.geothermics.2015.05.008

Zeinijahromi, A., Nguyen, T. K. P., & Bedrikovetsky, P. (2013). Mathematical model for fines-migration-assisted waterflooding with induced formation damage. *Spe Journal, 18*(03), 518-533.

2 Literature Review

2.1 Introduction

Particle detachment, transport, and capture occurs during a number of industrial processes. Particles are introduced into systems either through the injection particle-laden fluids (referred to as deep bed filtration), or through the detachment of natural fine particles that are attached to the inner surface of the porous matrix (referred to as fines migration). Once suspension flows are established within the porous media, particles can become captured through interaction with the porous matrix. Particle capture has long been reported to reduce the capability of the porous media to permit flow, quantitatively measured as a decline in permeability.

Both the transport of fine particles, and their capture have drawn substantial attention due to their prevalence in industry. There are a number of studies that have shown fines detachment and subsequent injectivity decline during low-salinity water injection in oilfields (Akhmetgareev & Khisamov, 2015; Barkman, Abrams, Darley, & Hill, 1975). Fines migration can occur even before injection, as a result of the leak-off of drilling fluid, lifting fines and causing often undetected formation damage (Salimi & Ghalambor, 2011). Fines migration can also occur during underground water management and has been reported during fresh water storage in shallow aquifers (Prommer et al., 2013), during the encroachment of seawater into coastal aquifers (Goldenberg, Magaritz, & Mandel, 1983), and during contamination of fresh water aquifers (Kretzschmar, Borkovec, Grolimund, & Elimelech, 1999).

Fines migration is not always a negative process and has been shown in several studies to potentially increase the volumetric sweep efficiency of waterflooding operations (Lemon, Zeinijahromi, Bedrikovetsky, & Shahin, 2011; Zeinijahromi, Al-Jassasi, Begg, & Bedrikovetski, 2015), or decrease the residual oil saturation. Both of these effects result in higher oil productivity and overall recovery (Al-Sarihi et al., 2018).

Due to the presence of suspended particles in both seawater and produced water, oilfield injection wells are commonly prone to formation damage due to deep bed filtration (Ogletree & Overly, 1977;

Mukul M. Sharma, Pang, Wennberg, & Morgenthaler, 2000). Operators often turn to costly filtration methods to avoid or mitigate injectivity decline (Guan, Du, Wang, & Xu, 2006).

Common to all colloidal flow problems is the need for accurate and reliable modelling supported by laboratory studies. Inverse modelling performed on laboratory data provides a means to characterise the porous medium, particles, and their interactions. With a proper and accurate characterisation, mathematical models can then be used to make predictions for field operations allowing for uncertainty quantification, assessment of treatment/mitigation strategies, and ultimately a quantifiable indication of the effectiveness and profitability of the operation.

In the following subsections I provide more background on the physical understanding and mathematical modelling of colloidal processes that preceded this thesis. Section 2.2 presents the physics and existing efforts for particle detachment. Section 2.3 presents modelling of fines migration and Section 2.4 presents modelling and considerations for the co-occurrence of particle capture and diffusion/dispersion.

2.2 Particle detachment

2.2.1 Physics of particle detachment

The detachment of particles is central to the process of fines migration as it provides a source for suspended particles. Figure 1b presents a schematic representation of an attached particle and the acting forces.

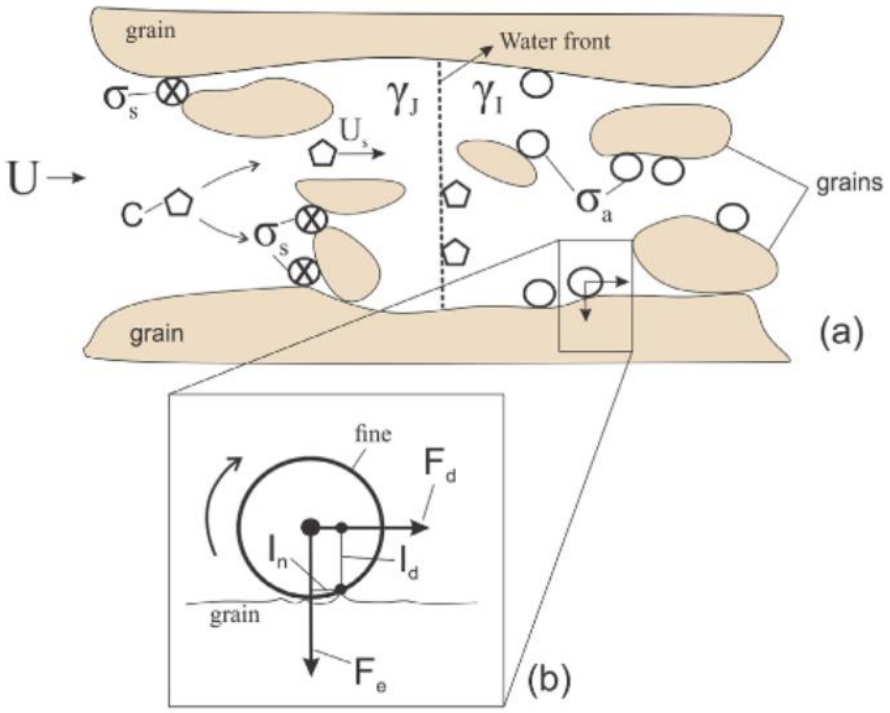

Figure 1: Schematic representation of particle detachment, transport, and capture: a) Schematic of suspended particles, attached, and strained particles (with concentrations c, σ_a, and σ_s respectively) within the porous space, b) schematic of an attached particle with acting forces and lever arm (Chequer, Vaz, & Bedrikovetsky, 2018)

This figure shows two forces, the drag force, which results from the interaction between the moving fluid and the attached particle, and the electrostatic force between the particle and the rock matrix. The drag force acts to detach particles while the electrostatic force acts to detach particles. In addition, there exists a lifting force, being the vertical counterpart to the drag force, and a gravitational force. In most applications, the lifting and gravitational force are negligibly small compared to the drag and electrostatic (P. Bedrikovetsky, Zeinijahromi, Siqueira, Furtado, & de Souza, 2012; Kalantariasl & Bedrikovetsky, 2013), and thus they are neglected.

The detachment of particles is determined by three balances: the balance of vertical and horizontal forces acting on the particle, and the balance of torques acting on the particle. These three balances represent the possibility for the particle lifting from the surface, moving across the surface, and rotating along the porous matrix respectively. Of particular interest is the conditions under which

particle will begin to detach, so the point at which the forces/torques are balanced exactly is considered, i.e. where their sum is zero. Analysis of these three equilibria has shown that in almost all cases, the torque balance is violated first (Mukul M Sharma, Chamoun, Sarma, & Schechter, 1992), meaning that analysis of particle detachment can be simplified to the single equation:

$$F_d\left(U, r_s\right) l_d\left(r_s\right) = \left[F_e\left(r_s, \gamma, pH, T\right) - F_L\left(U, r_s\right) + F_g\left(r_s\right)\right] l_n \tag{2.1}$$

where F_d is the drag force, U is the fluid velocity, r_s is the particle size, l_d is the drag force lever arm, F_e is the electrostatic force, γ is the fluid salinity, $pH=\log_{10}(H^+)$ is a measure of the acidity of the fluid, T is the fluid temperature, F_L is the lifting force, F_g is the gravitational force, and l_n is the normal lever arm.

The normal level arm can be calculated based on two different assumptions. First, as in Figure 1b, it can be assumed that the particle will rotate around some asperity. The second assumption is that the particle deforms due to the normal force which acts perpendicular to the rock surface. In this case, using Hertz's theory of deformation, the normal lever arm can be calculated as (Boris V Derjaguin, Muller, & Toporov, 1975):

$$l_n^3 = \frac{F_e r_s}{4K} \tag{2.2}$$

where the composite Young's modulus is calculated as

$$K = \frac{4}{3\left(\frac{1-\nu_1^2}{E_1} + \frac{1-\nu_2^2}{E_2}\right)} \tag{2.3}$$

where ν is the Poisson's ratio, E is the Young's modulus, and the subscripts 1 and 2 refer to the particle and rock surface respectively.

The drag lever arm can be calculated from the normal lever arm following geometrical considerations, resulting in

$$l_d = \sqrt{r_s^2 - l_n^2} \tag{2.4}$$

In most cases, the normal lever arm has been shown to be significantly smaller than the particle size, due to the negligible deformation of the particle. Thus in this case

$$r_s \gg l_n,\ l_d \simeq r_s \tag{2.5}$$

Assuming that the particle is spherical, the gravitational force can be expressed as

$$F_g = \frac{4}{3}\pi r_s^3 \Delta\rho g \tag{2.6}$$

where $\Delta\rho$ is the density difference between the particle and surrounding fluid, and g is the gravitational acceleration.

The lift and drag forces can be expressed as

$$F_L = \chi r_s^3 \sqrt{\frac{\rho\mu U^3}{r_p^3}} \tag{2.7}$$

$$F_d = \frac{\omega\pi\mu r_s^2 U}{r_p} \tag{2.8}$$

where χ is the lift coefficient, ρ is the particle density, μ is the fluid viscosity, U is the fluid velocity, r_p is the pore radius, and ω is the drag coefficient. The lift and drag coefficients can be calculated from computational flow dynamics simulations.

Equations (2.7) and (2.8) express explicitly the increasing lift and drag forces with increasing fluid velocity. This is the reason that increasing fluid velocity results in particle detachment.

The electrostatic force is calculated using the extended DLVO (Dejaguin, Landau, Verwey, Overbeek) theory. This theory accounts for three contributions to the total electrostatic potential from the interaction between the particle and internal porous surface: the London-Van der Waals, Electrical Double Layer, and Born repulsive potential (B.V. Derjaguin & Landau, 1941; John Gregory, 1975; J. Gregory, 1981; Verwey, Overbeek, & Overbeek, 1999). The total potential energy is the sum of each component:

$$V = V_{LVW} + V_{EDL} + V_{BR}$$

(2.9)

where V is the total energy, V_{LVW} is the London-Van der Waals potential, V_{EDL} is the electrical double layer potential, and V_{BR} is the Born repulsive potential.

The London-Van der Waals potential is a largely attractive force that acts between two closely separated surfaces. It arises due to the spontaneous electrical and magnetic polarizations in the medium between the two surfaces, giving rise a to a fluctuating electromagnetic field. The expression for the retarded London-Van der Waals interaction potential between a sphere and plate is given by

$$V_{LVW} = -\frac{A_{132} r_s}{6h}\left[1 - \frac{5.32h}{\lambda_w}\ln\left(1 + \frac{\lambda_w}{5.32h}\right)\right] \tag{2.10}$$

where A_{132} is the Hamaker constant, λ_w is the characteristic wavelength of the interaction, and h is the separation distance between the two surfaces.

The Hamaker constant is given by the following expression (Israelachvili, 2011):

$$A_{132} = \frac{3}{4}k_B T\left(\frac{\varepsilon_1 - \varepsilon_3}{\varepsilon_1 + \varepsilon_3}\right)\left(\frac{\varepsilon_2 - \varepsilon_3}{\varepsilon_2 + \varepsilon_3}\right) + \frac{3h\nu_e}{8\sqrt{2}}\frac{\left(n_1^2 - n_3^2\right)\left(n_2^2 - n_3^2\right)}{\left(n_1^2 + n_3^2\right)^{0.5}\left(n_2^2 + n_3^2\right)\left[\left(n_1^2 + n_3^2\right)^{0.5} + \left(n_2^2 + n_3^2\right)\right]}$$

(2.11)

where k_B is Boltzmann constant, ε_1, ε_2, and ε_3 are static dielectric constants of the particle, surface, and fluid, respectively, n_1, n_2, and n_3 are the refractive indices of particle, surface, and fluid, respectively, and ν_e is the constant value of absorption frequency.

The next component of the total interaction energy is the Born repulsive force. This is a short-range interaction that results from the repulsion between atoms as their electron shells overlap. The expression for the Born repulsion is given below (Ruckenstein & Prieve, 1976)

$$V_{BR} = \frac{A_{132}}{7560}\left(\frac{\sigma_{LJ}}{r_s}\right)^6 \left(\frac{8+\frac{h}{r_s}}{\left(2+\frac{h}{r_s}\right)^7} + \frac{6-\frac{h}{r_s}}{\left(\frac{h}{r_s}\right)^7} \right) \tag{2.12}$$

where σ_{LJ} is the atomic collision diameter.

The last component of the interaction potential is the electrical double layer. This interaction is perhaps the most important because it is the most sensitive to the ionic composition of the surrounding fluid, which results in the salinity dependence of the electrostatic force.

Both the particle and internal surface of the porous medium will typically exhibit some electrical charge. Most commonly, this charge exists due to the dissociation of charged ions on the external surface of each species, resulting in an excess surface charge. Due to this surface charge, ionic species within the surrounding fluid will accumulate in the region around each species. The notion of the double layer follows from the concept that there exists a layer of fixed ions close to the surface, and a larger layer of diffuse ions, whose concentration differs from that of the bulk fluid. When the two species are close to each other, their double layers will overlap, resulting in a potential energy of interaction. As the two surfaces are brought closer to each other, the interaction potential increases. Given that most species in subterraneous rocks are negatively charged (e.g. clays, silica), the interaction will be repulsive. The concentration of ions within the double layer is determined by an equality of chemical potential between those ions and the free ions within the bulk fluid. This equilibrium results in the salinity dependence of the EDL interaction; as the fluid salinity increases, the chemical potential of the ions in bulk increases, resulting in diffusion more ions into the region between the particle and rock surface.

An expression for the electrical double layer interaction potential for a sphere and plate is given below (John Gregory, 1975)

$$V_{EDL} = \frac{128\pi r_s n_\infty k_B T}{\kappa^2}\psi_s \psi_g e^{-\kappa h} \tag{2.13}$$

$$\kappa = \sqrt{\frac{e^2 \sum_i n_{io} z_i^2}{\varepsilon_0 \varepsilon_3 k_B T}} \tag{2.14}$$

$$\psi_s = \tanh\left(\frac{ze\zeta_s}{4k_B T}\right), \psi_g = \tanh\left(\frac{ze\zeta_g}{4k_B T}\right) \tag{2.15}$$

where κ is the inverse Debye length which is the characteristic length of the potential energy of each surface, n_∞ is the bulk ion density, e is the elementary electric charge, n_{i0} is the concentration of ion species i in the bulk solution, z is the valence of symmetrical electrolyte solution, ε is the dielectric permittivity of vacuum, ε_3 is the dielectric constant of the fluid, ψ_s and ψ_g are the reduced zeta potentials for the particle and grain, and ζ_s and ζ_g are the zeta potentials for the particle and grain. Below in Figure 2 a typical form for the total interaction potential plotted against the separation distance between the particle and surface is presented.

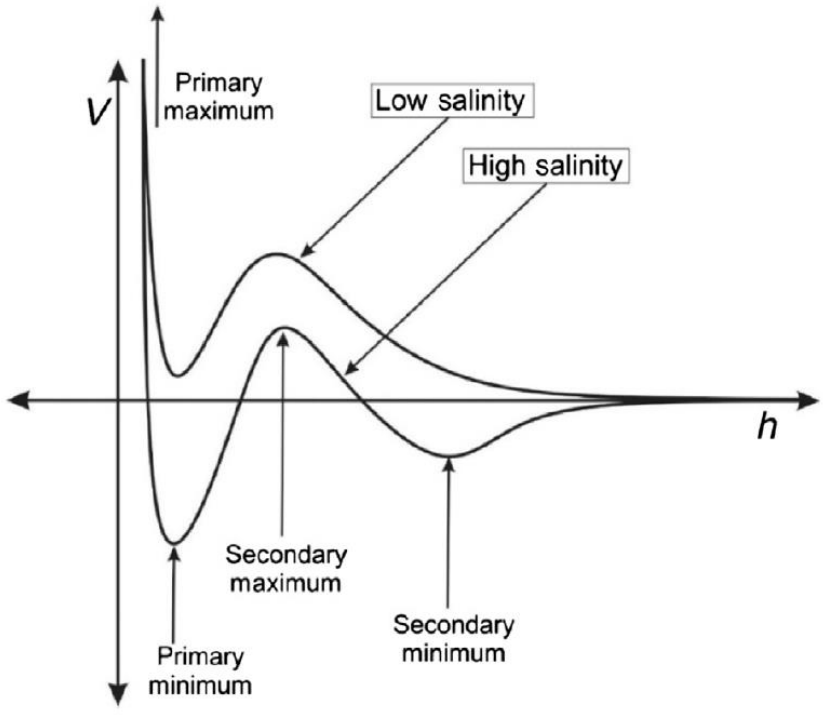

Figure 2: Two plots of the total interaction potential energy, *V*, plotted against the separation distance, *h* (Russell et al., 2018)

The force acting on the particle is equal to the negative of the derivative of V over h. The system will tend towards an equilibrium point, where the force is zero. These points exist at the primary and secondary minima, and at infinite separation distance. When particles reside in either of the two minima, detaching forces will move the particle to the inflection point, where the attractive force is maximum. If the force is sufficient, as determined by the mechanical equilibrium, then particles will detach.

2.2.2 Modelling of particle detachment

Early approaches to modelling particle detachment relied heavily on empirical parameters that could under ideal conditions be determined from laboratory tests. The traditional model for colloidal attachment and detachment is (Herzig, Leclerc, & Goff, 1970)

$$\frac{\partial \sigma_a}{\partial t} = \lambda c U - k_{det} \sigma_a \tag{2.16}$$

where t is time, λ is the filtration coefficient, and k_{det} is the detachment coefficient.

This formulation has several important implications. First, it assumes that particles can simultaneously be detached and attached, and that any detached particle can become re-attached and vice-versa. The attachment takes the typical form, in that it is proportional to the advective flux of the suspended particles, cU (Bradford, Simunek, Bettahar, Van Genuchten, & Yates, 2003; Tufenkji, 2007). The detachment portion of the equation is based simply on the idea that that particle detachment will occur more quickly the higher the number of particles there are to be detached, σ_a. The coefficient of proportionality, k_{det} is empirical and needs to be determined from laboratory data.

A direct consequence of this model is that if attachment is small, then all attached particles will eventually detach. This picture is also inconsistent with the mechanical equilibrium or torque balance on particles that was described above. To remedy these issues, authors have introduced the critical retention function, σ_{cr} (P. Bedrikovetsky, Siqueira, Furtado, & Souza, 2011). This function describes the concentration of attached particles that will remain attached under a given set of system

parameters, such as fluid velocity, salinity, pH, temperature, etc. When the attached concentration is below the critical retention function, detachment does not occur, and in fact in certain systems attachment will take occur instead, and if the attached concentration is below the critical retention function, detachment will occur, resulting in equality between σ_a and σ_{cr}. Thus we arrive at a different model for particle detachment (P. Bedrikovetsky et al., 2011; P. Bedrikovetsky et al., 2012; You, Yang, Badalyan, Bedrikovetsky, & Hand, 2016):

$$\frac{\partial \sigma_a}{\partial t} = \begin{cases} \lambda c U & \sigma_a < \sigma_{cr}\left(U, \gamma, pH, T\right) \\ \sigma_a = \sigma_{cr}\left(U, \gamma, pH, T\right) & \sigma_a > \sigma_{cr}\left(U, \gamma, pH, T\right) \end{cases} \tag{2.17}$$

The dependence of the critical retention function on the fluid velocity comes largely from the drag and lifting force, while the dependence on the salinity, pH, and temperature comes from the electrostatic force.

The advantage of this model for particle detachment is first that it allows for directly relating system parameters to the particle detachment, and secondly it allows for describing the sequential detachment of particles during sequential changes to the system parameters, as has been observed in many laboratory tests (Khilar & Fogler, 1983; Ochi & Vernoux, 1998; Oliveira et al., 2014).

In order for the critical retention function to vary in magnitude across a range of velocities or salinities, etc., the detachment criteria for the population of attached particles must vary. That is, some effect must exist such that conditions that detach some particles will not detach others. Below we discuss two such models, first we proceed by assuming that all particles are the same size, but that they form a multiplayer internal filter cake within each pore, and secondly, we assume a monolayer of particles with varying particle size.

First we consider the case where all particles are equal: they have the same size and electrostatic properties. The pores are modelled as a bundle of square capillaries all of equal size. This model of attached particles is reflected in Figure 3.

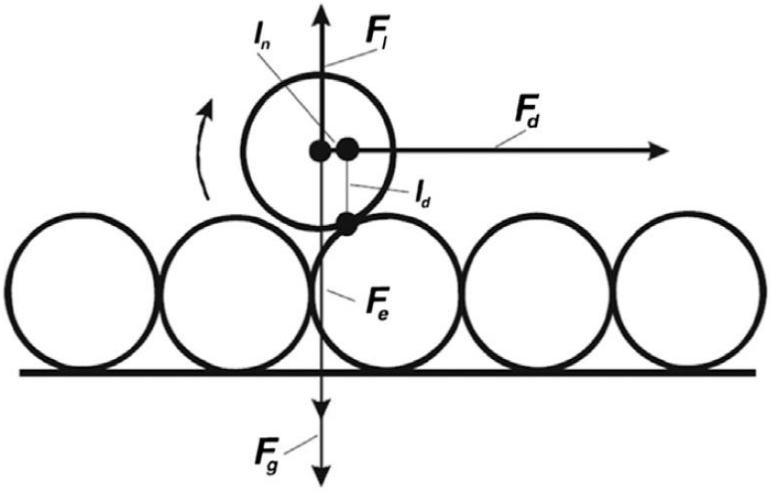

Figure 3: Mechanical equilibrium of particles on the rock surface forming a multilayer filter cake (P. Bedrikovetsky et al., 2011)

The particles attach to the pore walls in a series of discrete layers. As more particles attach, the width of the filter cake increases, consequently decreasing the available space within the pore for fluid flow. This will result in an increase in the pore fluid velocity, which will increase the drag force, shifting the condition of mechanical equilibrium towards detachment. Thus, there exists a balance, as particles accumulate, the next layer will be less stable on the surface.

Assuming that all particles are spherical and are arranged evenly on the inner surface of pores, it is possible to approximate the lever arm ratio, l_d/l_n as $\sqrt{3}$. This allows writing the torque balance as:

$$F_e + \frac{4\pi r_s^3}{3}\Delta\rho g - \chi r_s^3\sqrt{\frac{\rho\mu U^3}{\left(H-2h_c\right)^3}} = \frac{\sqrt{3}\omega\pi\mu r_s^2 U}{H-2h_c} \tag{2.18}$$

where H is the pore width, and h_c is the filter cake width.

For square pores, the critical retention function can be related directly to the pore and filter cake dimensions as per

$$\sigma_{cr} = \left[1-\left(1-\frac{h_c}{H}\right)^2\right]\left(1-\phi_c\right)\phi \tag{2.19}$$

where ϕ_c and ϕ are the filter cake and rock porosity, respectively.

If we assume that the gravitational and lift forces are negligible, then we can combine Equations (2.18) and (2.19) to arrive at an explicit expression for the critical retention function:

$$\sigma_{cr}\left(U,\gamma,pH,T\right)=\left[1-\left(\frac{1}{2}+\frac{\sqrt{3}\omega\pi\mu r_s^2 U}{2F_e\left(\gamma,pH,T\right)H}\right)\right]\left(1-\phi_c\right)\phi \tag{2.20}$$

This expression links the critical retention function to the system parameters, as required. Increasing the fluid velocity will increase the drag force, while decreasing the salinity will decrease the electrostatic force. Both of these actions will result in a monotonic decrease in the critical retention function, consistent with the picture of particle detachment. Figure 4 below shows typical forms for the critical retention function plotted against the fluid velocity and salinity.

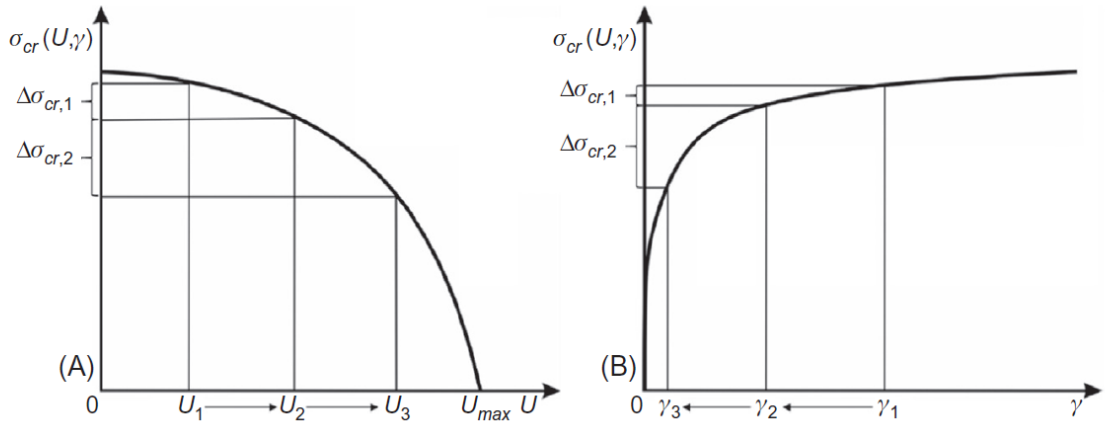

Figure 4: Typical forms for the critical retention function when plotted against the A) fluid velocity, U and B) fluid salinity, γ (Russell et al., 2018)

The assumptions of constant pore and particle size can easily be relaxed. Given a particle size distribution $f_s(r_s)$ and pore width distribution $f_H(H)$, we arrive at the integral expression (Russell et al., 2018):

$$\sigma_{cr}\left(U,\gamma,pH,T\right)=\int_0^\infty\int_0^\infty\left[1-\left(\frac{1}{2}+\frac{\sqrt{3}\omega\pi\mu r_s^2 U}{2F_e\left(\gamma,pH,T\right)H}\right)\right]\left(1-\phi_c\right)\phi\, f_H\left(H\right) f_s\left(r_s\right)dHdr_s \tag{2.21}$$

The second means of deriving the critical retention function is to begin with a distribution of particle sizes, which attach in monolayer. Each of the forces present in the equation for mechanical equilibrium is dependent on the particle size. A larger particle size will result in a higher value for each of the forces, at least for spherical particles. However, when calculations are performed it can be shown that larger particles exhibit a higher likelihood for detachment than smaller particles, true for any two particle sizes (Ochi & Vernoux, 1998). Thus during any gradual change in system parameters, such as increasing the fluid velocity, first larger particles will detach, followed by smaller and smaller particles. This leads naturally to the notion of the critical particle size:

$$r_{scr} = r_s\left(U, \gamma, pH, T\right) \tag{2.22}$$

For given conditions, particles larger than the critical particle size will detach, and those smaller will not. Thus we can express the critical retention function as (Russell et al., 2018)

$$\sigma_{cr}\left(U, \gamma, pH, T\right) = \sigma_{aI} \int_{0}^{r_{scr}\left(U, \gamma, pH, T\right)} f_s\left(r_s\right) dr_s \tag{2.23}$$

where σ_{aI} is the initial attached particle concentration. We visualise this representation of the critical retention function in Figure 5 below.

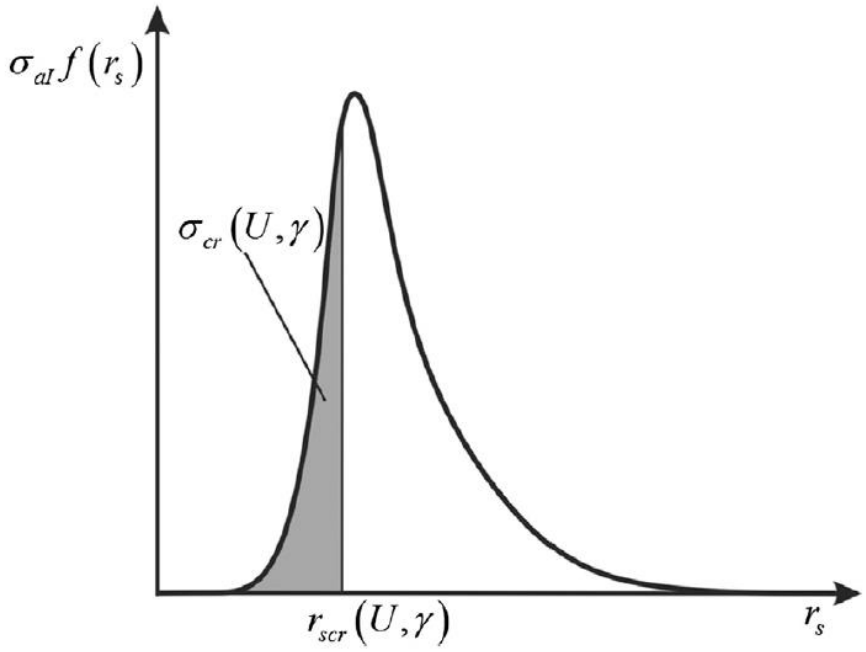

Figure 5: Calculation of the critical retention function from the critical particle size for a population of particles with size distribution $f(r_s)$ forming a monolayer on the internal surface of a porous medium (Russell et al., 2018)

While the critical retention function can, in multiple ways, be expressed in terms of the system parameters, it loses the capability of previous modelling approaches to capture a finite rate of detachment. As it stands, the critical retention function predicts particle detachment at the same rate with which the system parameters change; an abrupt increase in the fluid velocity will result in an abrupt detachment of particles. While this may be true for some changes, some researchers have shown that particle detachment by salinity changes may occur with significant delay (Joekar-Niasar & Mahani, 2016; Mahani, Berg, Ilic, Bartels, & Joekar-Niasar, 2015). These works show that when the bulk fluid salinity is changed, the salinity between an oil droplet and flat surface changes gradually, with magnitudes up to days. This delay is a result of diffusion of the ionic species from the bulk solution to the region between the particle and surface. Diffusion rates alone are not enough to explain the significant delay, but accounting for the effect of electric charge on diffusion, through the Nernst-Planck equation, these authors can explain the observed delay. The combination of a delay in particle detachment and adherence to an accurate physical description of particle detachment as with the critical retention function, is not available in the literature.

2.3 Modelling colloid transport and capture

In this section the basic model for particle capture and transport in porous media is presented. The primary equation used is a mass balance on the suspended particle concentration. The form of this equation is

Rate of accumulation = Divergence of advective flux – Rate of detachment – Rate of straining

Note here that it is assumed that particle diffusion/dispersion is negligible. This follows from the relatively large size of most colloids found in petroleum reservoirs. In the following section, the case where diffusion/dispersion is significant is discussed. The continuity equation in 1-Dimension can be written as

$$\frac{\partial \phi c}{\partial t} = -\frac{\partial cU}{\partial x} - \frac{\partial \sigma_a}{\partial t} - \frac{\partial \sigma_s}{\partial t} \tag{2.24}$$

where ϕ is the porosity, t is the time, x is the spatial coordinate, U is the fluid velocity, and c, σ_a, and σ_s are the suspended, attached, and strained particle concentrations respectively. The inclusion of porosity follows from the definition of the suspended particle concentration as the volume of suspended particles per unit pore volume, while the attached and strained concentrations are volumetric concentrations relative to the bulk rock volume. This difference is due to the means with which each variable is typically measured in laboratory studies. The distinction between attached and strained concentration follows from the notion that if particles are being captured by size exclusion or other irreversible processes, then attached and captured particles are qualitatively different, in that one population can become suspended, and the other cannot.

It is assumed that the volume of particles and fluid are additive (Amagat's law). The concentrations of each species is also assumed to negligibly small when compared with the mass of the carrier fluid.

The detachment rate was discussed in the previous section, with most modern approaches using the assumption that the attached concentration is equal to the critical retention function

$$\sigma_a\left(x,t\right) = \sigma_{cr}\left(U,\gamma,pH,T\right) \tag{2.25}$$

The straining rate is taken to be proportional to the particle advective flux, cU (Herzig et al., 1970)

$$\frac{\partial \sigma_s}{\partial t} = \lambda\left(\sigma_s\right) cU \tag{2.26}$$

The coefficient of proportionality, λ, is referred to as the filtration coefficient. Its dependence on the strained concentration follows from the consideration that the number of available straining sites may be finite. Thus, as these sites are filled due to straining, straining becomes less and less likely as suspended particles encounter these sites less frequently. One common approach to model this dependence is by analogy to Langmuir adsorption, which similarly quantifies the finite number of adsorption sites for molecules in suspension. The resulting expression is

$$\lambda(\sigma_s) = \lambda_0\left(1 - \frac{\sigma_s}{\sigma_m}\right) \tag{2.27}$$

where λ_0 is the filtration coefficient in the absence of strained particles, and σ_m is the maximum strained concentration, determined from the quantity of straining sites. Commonly it is assumed that the strained particle concentration always remains low enough as to be negligible compared with the number of straining sites. In this case, it can be assumed that the filtration coefficient is constant.

As was discussed earlier, one of the main industrial interests in colloidal transport follows from the induced permeability decline. Thus in addition to the continuity equation, an equation linking the attached and strained particle concentrations to the rock permeability is desired. This equation is most commonly derived using a Taylor series expansion (P. G. Bedrikovetsky, Vaz Jr, Machado, Zeinijahromi, & Borazjani, 2011; Pang & Sharma, 1997)

$$\frac{k_0}{k(\sigma_a, \sigma_s)} = 1 + \beta_a\sigma_a + \beta_s\sigma_s + O(\sigma^2) \tag{2.28}$$

Higher order terms are typically neglected. Combining this expression with Darcy's law results in

$$U = -\frac{k_0}{\mu(c)(1 + \beta_a\sigma_a + \beta_s\sigma_s)}\frac{\partial p}{\partial x} \tag{2.29}$$

where p is the fluid pressure. For the sake of generality, the viscosity has been expressed as a function of the suspended concentration. In most cases, the suspended concentration is too low to affect the fluid viscosity, and so this dependence is neglected. In addition, the effect of attached particles, which line pores, on permeability is often significantly less than the effect of strained particles, who can plug pores. In this case, β_a is assumed to be negligibly small and thus this term is neglected.

Laboratory tests on fines migration have demonstrated long stabilisation times, beyond what can be explained from the above model (Oliveira et al., 2014; Yang, Siqueira, Vaz, You, & Bedrikovetsky, 2016). This has led researchers to suggest that following detachment, suspended particles travel through the porous space at a velocity much lower than the fluid velocity. Thus their ratio is introduced as an unknown dimensionless parameter referred to as the drift delay factor

$$\alpha = \frac{U_s}{U} \tag{2.30}$$

where U_s is the particle velocity.

This leads to the following system of equations

$$\frac{\partial}{\partial t}\left(\phi c + \sigma_a + \sigma_s\right) + \alpha U \frac{\partial c}{\partial x} = 0 \tag{2.31}$$

$$\frac{\partial \sigma_s}{\partial t} = \lambda c \alpha U \tag{2.32}$$

$$\sigma_a = \sigma_{cr}\left(U, \gamma, pH, T\right) \tag{2.33}$$

$$U = -\frac{k_0}{\mu(c)\left(1+\beta_s \sigma_s\right)} \frac{\partial p}{\partial x} \tag{2.34}$$

The initial conditions correspond to a clean core:

$$c(x,0) = \Delta\sigma, \sigma_s(x,0) = 0 \tag{2.35}$$

where $\Delta\sigma$ is the concentration of particles that detach when flow is initiated.

The boundary condition posed at the inlet corresponds to the injection of particle-free water

$$c(0,t) = 0 \tag{2.36}$$

Introduce dimensionless variables

$$X = \frac{x}{L}, T = \frac{Ut}{\phi L}, S_a = \frac{\sigma_a}{\phi}, S_s = \frac{\sigma_s}{\phi}, \Lambda = \lambda L \tag{2.37}$$

where L is the system length.

An analytical solution of this system can be obtained by using the method of characteristics. This method relies on comparing the continuity equation with the following equation, which follows from the definition of partial and total derivatives:

$$dc = \frac{\partial c}{\partial x} dx + \frac{\partial c}{\partial t} dt \tag{2.38}$$

Comparison with Equation (2.31) in the new dimensionless coordinates results in

$$\frac{dc}{dT} = 0, \frac{dX}{dT} = \alpha \tag{2.39}$$

or

$$\frac{dc}{dX} = 0, \frac{dT}{dX} = \frac{1}{\alpha} \tag{2.40}$$

Integrating these two equations gives the analytical solution for the suspended concentration:

$$c = \Delta\sigma e^{-\alpha\Lambda T} \tag{2.41}$$

This equation is valid behind the particle front, $X=\alpha T$. Ahead of this front, the suspended particle concentration is zero. The strained concentration and pressure can be determined by subsequent integration of Equations (2.32) and (2.34). The full solution for each variable is provided in Table 1 as presented in Russell et al. (2018).

Table 1: Analytical solution for fines migration with instantaneous detachment (velocity alteration)

Line	Term	Zone	Solution
1	$C(X,T)$	$X > \alpha T$	$e^{-\alpha\Lambda T}$
2		$X < \alpha T$	0
3	$S_s(X,T)$	$X > \alpha T$	$1 - e^{-\alpha\Lambda T}$
4		$X < \alpha T$	$1 - e^{-\Lambda X}$
5	$J(T)$	$T < \frac{1}{\alpha}$	$1 + \beta\phi\Delta\sigma_{cr}\left[1 - \frac{1}{\Lambda} - \left(1 - \frac{1}{\Lambda} - \alpha T\right)e^{-\alpha\Lambda T}\right]$

6		$T > \frac{1}{\alpha}$	$1+\beta\phi\Delta\sigma_{cr}\left[1-\frac{1}{\Lambda}-\frac{e^{-\Lambda}}{\Lambda}\right]$

This model for fines migration assumes that particles detach throughout the core instantaneously when flow is initiated. This is consistent with the physical understanding of fines detachment by alteration of flow velocity. When particle detachment is induced by the injection of fluid with different properties such as salinity of pH, then the detachment will occur only once the injected fluid front reaches the core. This case has been studied by Chequer et al. (2018), who modelled this phenomenon by explicitly modelling the fluid salinity via another continuity equation

$$\phi\frac{\partial\gamma}{\partial t}+U\frac{\partial\gamma}{\partial x}=0 \tag{2.42}$$

Again, diffusion and dispersion have been neglected. Under these conditions the fluid salinity behind and ahead of the fluid front $X=T$ is simply the injected and initial salinities respectively. In this case, rather than particles detaching instantaneously throughout the core, they do so along the salinity front, when the new salinity reaches that area of the system. The full solution is presented in Table 2, following the full derivation presented in Chequer et al. (2018).

Table 2: Analytical solution for fines migration with instantaneous detachment (salinity alteration)

Line	Term	Zones	Solution
1	$\Gamma(X,T)$	$X>T$	1
2		$X<T$	0
3	$S_a(X,T)$	$X>T$	$S_{cr}(\gamma_I)$
4		$X<T$	$S_{cr}(\gamma_J)$
5	$C(X,T)$	$X>T$	0

6		$\alpha T < X < T$	$\frac{1}{(1-\alpha)\phi}\exp\left(-\alpha\Lambda\left(\frac{T-X}{1-\alpha}\right)\right)$
7		$X < \alpha T$	0
8	$S_s(X,T)$	$X > T$	0
9		$\alpha T < X < T$	$\frac{1}{\phi}\left[1-\exp\left(-\alpha\Lambda\left(\frac{T-X}{1-\alpha}\right)\right)\right]$
10		$X < \alpha T$	$\frac{1}{\phi}\left[1-\exp(-\Lambda X)\right]$
	$J(T)$	$T < 1$	$1+\frac{\beta\Delta\sigma}{(1-\alpha)}\left[T+\frac{1}{\Lambda(1-\alpha)}\left(\exp\left(-\alpha\Lambda(1-\Lambda)T\right)-1\right)-\frac{1}{\alpha\Lambda}\exp(-\alpha\Lambda T)\left(\exp(\alpha\Lambda T)-\exp\left(\alpha^2\Lambda T\right)\right)\right]$
		$1 < T < \frac{1}{\alpha}$	$1+\frac{\beta\Delta\sigma}{(1-\alpha)}\left[1+\frac{1}{\Lambda(1-\alpha)}\left(\exp\left(-\alpha\Lambda(1-\alpha)T\right)-1\right)-\frac{1}{\alpha\Lambda}\exp(-\alpha\Lambda T)\left(\exp(\alpha\Lambda)-\exp\left(\alpha^2\Lambda T\right)\right)\right]$
		$T > \frac{1}{\alpha}$	$1+\frac{\beta\Delta\sigma}{(1-\alpha)}\left[1+\frac{1}{\Lambda(1-\alpha)}\left(\exp\left(-\Lambda(1-\alpha)\right)-1\right)\right]$

Both solutions here are presented for linear flow, where the fluid velocity is independent on the spatial dimension. During injection in a well, whether for waterflooding, freshwater storage, or aquifer recharge, the flow profile around the well is such that the fluid velocity is larger the closer to the surface of the wellbore. Assuming axi-symmetric flow, then the fluid velocity becomes

$$U = \frac{q}{2\pi r} \tag{2.43}$$

Where q is the volumetric injection rate per unit formation height, and r, used in place of x, is the radial distance from the wellbore. Using clever non-dimensionalisation (see Equation (2.44) below), the non-dimensionless system remains largely unchanged, with the exception that the equation for the straining rate.

$$T = \frac{qt}{\pi r_e^2 \phi}, X = \left(\frac{r}{r_e}\right)^2, S_s = \frac{\sigma_s}{\phi}, S_a = \frac{\sigma_a}{\phi}, S_{cr} = \frac{\sigma_{cr}}{\phi}, \Lambda = \lambda r_w, P = \frac{\pi kp}{q\mu}, \Gamma = \frac{\gamma - \gamma_J}{\gamma_I - \gamma_J} \tag{2.44}$$

where r_e is the reservoir boundary, and r_w is the wellbore radius. With these new variables, the straining rate becomes

$$\frac{\partial S_s}{\partial T} = \frac{\alpha \Lambda c}{2\sqrt{X}\sqrt{X_w}} \tag{2.45}$$

where $X_w=(r_w/r_e)^2$. This equation reflects the higher velocity nearer to the wellbore, which results in a higher capture rate.

For a full derivation and list of all analytical equations, see Russell et al. (2018).

While these analytical solutions provide a useful tool for practitioners, there still remains a clear disjoint between the assumptions of the model and the observed behaviour of the underlying processes. As discussed earlier, changes to salinity ought to result in detachment with significant delay. While the above equations explicitly model the salinity front, correctly accounting for the detachment occurring only once the new salinity has arrived, they do not account for this delay. The extension of the above models both in linear and axi-symmetric forms to account for this delay is required to describe fines detachment more accurately.

2.4 Particle capture and dispersion

In the previous sections, particle diffusion and dispersion have been neglected. While diffusion is often neglected due to the large size of particles, dispersion, which arises due to the complex nature of the flow field within porous media, can be significant for colloidal flows. Dispersion and diffusion at their essence are quantifications of the macroscale behaviour arising from particles' exhibiting different velocities on the pore scale. This distribution of velocities has been studied extensively, and can be upscaled in many ways to produce the diffusion/dispersion term in the continuity equation for suspended particles (Einstein, 1905)

$$\frac{\partial c}{\partial t} = D\frac{\partial^2 c}{\partial x^2} \tag{2.46}$$

where D is the diffusion coefficient, and in this case advection has been neglected.

An issue arises when one imagines this distribution of velocities alongside particle capture, which, as reasoned in the previous section, depends on the particle velocity. In this case, how is one to resolve the fact that particles ought to experience capture at different rates?

Some authors have attempted to tackle this problem intuitively, by arguing that if in the absence of dispersion particles are captured according the advective flux, then in the presence of dispersion, particle capture should remain proportional to the total flux, which now includes a dispersive component (P Bedrikovetsky, Siqueira, de Souza, & Shecaira, 2006)

$$\frac{\partial \sigma_s}{\partial t} = \lambda \left| cU - D\frac{\partial c}{\partial x} \right| \tag{2.47}$$

where the absolute value is taken to reflect that capture is always positive, regardless of the direction of the total flux.

This approach leads to a continuity equation of the form

$$\phi \frac{\partial c}{\partial t} + \left(U - \lambda D\right)\frac{\partial c}{\partial X} = D\frac{\partial^2 c}{\partial x^2} - \lambda cU \tag{2.48}$$

Thus the presence of dispersion leads not only to the addition of the second order derivative of c in x, but also to a delay in the advective velocity proportional to the filtration and diffusion coefficients.

This model presents several problems. First, it is derived intuitively, and thus has little physical justification, despite the reasoning behind the formulation. Secondly, when the quantity λD exceeds the fluid velocity U, then despite the fluid velocity moving in one direction, the mean movement of the suspended particles will be in the opposite direction. This is a paradox, and without a more thorough derivation, it is unclear from where it arises. Thirdly, if we imagine a population of particles that move with zero mean velocity, and whose initial profile is uniform in X, then the above equation predicts a total capture rate of zero. However these particles are still moving back and forth due to the

effects of diffusion/dispersion and so should experience capture during this movement. This is another shortcoming of this model.

2.5 References

Akhmetgareev, V., & Khisamov, R. (2015). *40 Years of Low-Salinity Waterflooding in Pervomaiskoye Field, Russia: Incremental Oil.* Paper presented at the SPE European Formation Damage Conference and Exhibition.

Al-Sarihi, A., Zeinijahromi, A., Genolet, L., Behr, A., Kowollik, P., Bedrikovetsky, P. J. E., & Fuels. (2018). Effects of fines migration on residual oil during low-salinity waterflooding. *32*(8), 8296-8309.

Barkman, J., Abrams, A., Darley, H., & Hill, H. (1975). An Oil-Coating Process To Stabilize Clays in Fresh Waterflooding Operations (includes associated paper 6405). *Journal of Petroleum Technology, 27*(09), 1,053-051,059.

Bedrikovetsky, P., Siqueira, A., de Souza, A., & Shecaira, F. (2006). Correction of basic equations for deep bed filtration with dispersion. *Journal of Petroleum Science Engineering, 51*(1-2), 68-84.

Bedrikovetsky, P., Siqueira, F. D., Furtado, C. A., & Souza, A. L. S. (2011). Modified Particle Detachment Model for Colloidal Transport in Porous Media. *Transport in Porous Media, 86*(2), 383-413. doi:10.1007/s11242-010-9626-4

Bedrikovetsky, P., Zeinijahromi, A., Siqueira, F. D., Furtado, C. A., & de Souza, A. L. S. (2012). Particle Detachment Under Velocity Alternation During Suspension Transport in Porous Media. *Transport in Porous Media, 91*(1), 173-197. doi:10.1007/s11242-011-9839-1

Bedrikovetsky, P. G., Vaz Jr, A., Machado, F. A., Zeinijahromi, A., & Borazjani, S. (2011). *Well productivity decline due to fines migration and production:(Analytical model for the regime of strained particles accumulation).* Paper presented at the SPE European Formation Damage Conference.

Bradford, S. A., Simunek, J., Bettahar, M., Van Genuchten, M. T., & Yates, S. R. (2003). Modeling colloid attachment, straining, and exclusion in saturated porous media. *Environ Sci Technol, 37*(10), 2242-2250.

Chequer, L., Vaz, A., & Bedrikovetsky, P. (2018). Injectivity decline during low-salinity waterflooding due to fines migration. *Journal of Petroleum Science and Engineering, 165*, 1054-1072. doi:https://doi.org/10.1016/j.petrol.2018.01.012

Derjaguin, B. V., & Landau, L. D. (1941). Theory of the stability of strongly charged lyophobic sols and of the adhesion of strongly charged particles in solutions of electrolytes. *Acta Physiochimica URSS, 14*(6), 633-662.

Derjaguin, B. V., Muller, V. M., & Toporov, Y. P. (1975). Effect of contact deformations on the adhesion of particles. *Journal of Colloid and Interface Science, 53*(2), 314-326.

Einstein, A. (1905). On the motion of small particles suspended in liquids at rest required by the molecular-kinetic theory of heat. *J Annalen der physik, 17*(549-560), 208.

Goldenberg, L. C., Magaritz, M., & Mandel, S. (1983). Experimental Investigation on Irreversible Changes of Hydraulic Conductivity on the Seawater-Freshwater Interface in Coastal Aquifers. *Water Resources Research, 19*(1), 77-85. doi:Doi 10.1029/Wr019i001p00077

Gregory, J. (1975). Interaction of unequal double layers at constant charge. *Journal of Colloid and Interface Science, 51*(1), 44-51.

Gregory, J. (1981). Approximate expressions for retarded van der Waals interactions. *Colloid and Interface Science, 83*(1), 138-145.

Guan, L., Du, Y., Wang, Z., & Xu, W. (2006). Water Injectivity-What We Have Learned in the Past 30 Years. *Journal of Canadian Petroleum Technology, 45*(05). doi:10.2118/06-05-TB %J Journal of Canadian Petroleum Technology

Herzig, J., Leclerc, D., & Goff, P. L. (1970). Flow of suspensions through porous media—application to deep filtration. *Industrial & Engineering Chemistry, 62*(5), 8-35.

Israelachvili, J. N. (2011). *Intermolecular and surface forces: revised third edition*: Academic press.

Joekar-Niasar, V., & Mahani, H. (2016). Nonmonotonic Pressure Field Induced by Ionic Diffusion in Charged Thin Films. *Industrial & Engineering Chemistry Research, 55*(21), 6227-6235.
Kalantariasl, A., & Bedrikovetsky, P. (2013). Stabilization of external filter cake by colloidal forces in a "well–reservoir" system. *Industrial & Engineering Chemistry Research, 53*(2), 930-944.
Khilar, K. C., & Fogler, H. S. (1983). Water sensitivity of sandstones. *Society of Petroleum Engineers Journal, 23*(01), 55-64.
Kretzschmar, R., Borkovec, M., Grolimund, D., & Elimelech, M. (1999). Mobile subsurface colloids and their role in contaminant transport. *Advances in Agronomy, Vol 66, 66*, 121-193. doi:Doi 10.1016/S0065-2113(08)60427-7
Lemon, P., Zeinijahromi, A., Bedrikovetsky, P., & Shahin, I. (2011). Effects of injected-water salinity on waterflood sweep efficiency through induced fines migration. *Journal of Canadian Petroleum Technology, 50*(9/10), 82-94.
Mahani, H., Berg, S., Ilic, D., Bartels, W. B., & Joekar-Niasar, V. (2015). Kinetics of Low-Salinity-Flooding Effect. *Spe Journal, 20*(1).
Ochi, J., & Vernoux, J.-F. (1998). Permeability decrease in sandstone reservoirs by fluid injection: hydrodynamic and chemical effects. *Journal of Hydrology, 208*(3), 237-248.
Ogletree, J., & Overly, R. (1977). Sea-water and subsurface-water injection in West Delta Block 73 waterflood operations. *Journal of Petroleum Technology, 29*(06), 623-628.
Oliveira, M. A., Vaz, A. S., Siqueira, F. D., Yang, Y., You, Z., & Bedrikovetsky, P. (2014). Slow migration of mobilised fines during flow in reservoir rocks: Laboratory study. *Journal of Petroleum Science and Engineering, 122*, 534-541.
Pang, S., & Sharma, M. (1997). A model for predicting injectivity decline in water-injection wells. *SPE Formation Evaluation, 12*(03), 194-201.
Prommer, H., Descourvieres, C. D., Handyside, M., Johnston, K., Harris, B., Li, Q., . . . Martin, M. (2013). *Final Report - Aquifer storage and recovery of potable water in the Leederville Aquifer*. Retrieved from Australia:
Ruckenstein, E., & Prieve, D. C. (1976). Adsorption and desorption of particles and their chromatographic separation. *AIChE Journal, 22*(2), 276-283.
Russell, T., Chequer, L., Borazjani, S., You, Z., Zeinijahromi, A., & Bedrikovetsky, P. (2018). Chapter Three - Formation Damage by Fines Migration: Mathematical and Laboratory Modeling, Field Cases. In B. Yuan & D. A. Wood (Eds.), *Formation Damage During Improved Oil Recovery* (pp. 69-175): Gulf Professional Publishing.
Salimi, S., & Ghalambor, A. (2011). Experimental Study of Formation Damage during Underbalanced-Drilling in Naturally Fractured Formations. *Energies, 4*(10), 1728-1747. doi:10.3390/en4101728
Sharma, M. M., Chamoun, H., Sarma, D. S. R., & Schechter, R. S. (1992). Factors controlling the hydrodynamic detachment of particles from surfaces. *Journal of Colloid and Interface Science, 149*(1), 121-134.
Sharma, M. M., Pang, S., Wennberg, K. E., & Morgenthaler, L. N. (2000). Injectivity Decline in Water-Injection Wells: An Offshore Gulf of Mexico Case Study. *SPE Production & Facilities, 15*(01), 6-13. doi:10.2118/60901-PA %J SPE Production & Facilities
Tufenkji, N. (2007). Colloid and Microbe Migration in Granular Experiments: A Discussion of Modelling Methods. In F. H. Frimmel, F. von der Kammer, & F. C. Flemming (Eds.), *Colloidal Transport in Porous Media*. Berlin: Springer-Verlag.
Verwey, E. J. W., Overbeek, J. T. G., & Overbeek, J. T. G. (1999). *Theory of the stability of lyophobic colloids*: Courier Corporation.
Yang, Y., Siqueira, F. D., Vaz, A. S., You, Z., & Bedrikovetsky, P. (2016). Slow migration of detached fine particles over rock surface in porous media. *Journal of Natural Gas Science and Engineering, 34*, 1159-1173.
You, Z., Yang, Y., Badalyan, A., Bedrikovetsky, P., & Hand, M. (2016). Mathematical modelling of fines migration in geothermal reservoirs. *Geothermics, 59*, 123-133.
Zeinijahromi, A., Al-Jassasi, H., Begg, S., & Bedrikovetski, P. (2015). Improving sweep efficiency of edge-water drive reservoirs using induced formation damage. *Journal of Petroleum Science and Engineering, 130*, 123-129.

3 Experimental studies on fines detachment

3.1 Effects of kaolinite in rocks on fines migration

Russell, T., Pham, D., Neishaboor, M. D., Badalyan, A., Behr, A., Genolet, L., Kowollik, P., Zeinijahromi, A., Bedrikovetsky, P.

Journal of Natural Gas Science and Engineering,Volume 45,2017,Pages 243-255

Statement of Authorship

Title of Paper	Effects of kaolinite in rocks on fines migration
Publication Status	☑ Published ☐ Accepted for Publication ☐ Submitted for Publication ☐ Unpublished and Unsubmitted w ork w ritten in manuscript style
Publication Details	Thomas Russell, Duy Pham, Mahdi Tavakkoli Neishaboor, Alexander Badalyan, Aron Behr, Luis Genolet, Patrick Kowollik, Abbas Zeinijahromi, Pavel Bedrikovetsky, Effects of kaolinite in rocks on fines migration, Journal of Natural Gas Science and Engineering,Volume 45,2017,Pages 243-255

Principal Author

Name of Principal Author (Candidate)	Thomas Russell		
Contribution to the Paper	Performed laboratory experiments, performed analysis of laboratory data, contributed to writing		
Overall percentage (%)	60%		
Certification:	This paper reports on original research I conducted during the period of my Higher Degree by Research candidature and is not subject to any obligations or contractual agreements with a third party that would constrain its inclusion in this thesis. I am the primary author of this paper.		
Signature		Date	16/02/2021

Co-Author Contributions

By signing the Statement of Authorship, each author certifies that:

i. the candidate's stated contribution to the publication is accurate (as detailed above);

ii. permission is granted for the candidate in include the publication in the thesis; and

iii. the sum of all co-author contributions is equal to 100% less the candidate's stated contribution.

Name of Co-Author	Duy Pham		
Contribution to the Paper	Performed laboratory experiments, contributed to writing		
Signature		Date	2/15/2021

Name of Co-Author	Mahdi Tavakkoli Neishaboor		
Contribution to the Paper	Performed laboratory experiments		
Signature		Date	17/02/2021

Please cut and paste additional co-author panels here as required.

Name of Co-Author	Alexander Badalyan
Contribution to the Paper	Design of laboratory experiments, performed laboratory experiments
Signature	Date: 16/02/2021

Name of Co-Author	Aron Behr
Contribution to the Paper	Design of laboratory experiments
Signature	Date: 23/02/2021

Name of Co-Author	Luis Genolet
Contribution to the Paper	Design of laboratory experiments
Signature	Date: 23/02/2021

Name of Co-Author	Patrick Kowollik
Contribution to the Paper	Design of laboratory experiments
Signature	Date: 23/02/2021

Name of Co-Author	Abbas Zeinijahromi
Contribution to the Paper	Design of laboratory experiments
Signature	Abbas Zeinijahromi Digitally signed by Abbas Zeinijahromi DN: cn=Abbas Zeinijahromi, o=The University Adelaide, ou=Australian School Petroleum, email=abbas.zeinijahromi@adelaide.ed Date: 2021.02.16 14:18:33 +10'30' Date:

Name of Co-Author	Pavel Bedrikovetsky
Contribution to the Paper	Design of laboratory experiments, contributed to writing
Signature	Date: 23/02/2021

Journal of Natural Gas Science and Engineering 45 (2017) 243–255

Contents lists available at ScienceDirect

Journal of Natural Gas Science and Engineering

journal homepage: www.elsevier.com/locate/jngse

Effects of kaolinite in rocks on fines migration

Thomas Russell [a], Duy Pham [a], Mahdi Tavakkoli Neishaboor [a], Alexander Badalyan [a], Aron Behr [b], Luis Genolet [b], Patrick Kowollik [b], Abbas Zeinijahromi [a], Pavel Bedrikovetsky [a, *]

[a] Australian School of Petroleum, The University of Adelaide, Adelaide, 5000, SA, Australia
[b] Wintershall Holding GmbH, EOT/R, Friedrich-Ebert Straße 160, 34119 Kassel, Germany

ARTICLE INFO

Article history:
Received 4 February 2017
Received in revised form
6 April 2017
Accepted 8 May 2017
Available online 27 May 2017

Keywords:
Fines migration
Formation damage
Permeability
Laboratory study
Particle detachment
Porous media

ABSTRACT

A laboratory study has been undertaken on the effect of permeability variation during low-salinity water injection as a function of kaolinite content in the rock. A novel methodology of preparing artificial sand-packs with a given kaolinite fraction has been established. Sequential injections of aqueous solutions in order of decreasing salinity were performed in six sand-packs with different kaolinite fractions varying from 0 to 10 wt percents. The permeability declined by a factor of 9–54 during salinity alteration from typical seawater conditions to deionized water. A new phenomenon of permeability increase during injection of high salinity water into low kaolinite content rocks has been observed. The phenomenon is explained by re-attachment of the mobilised fines at high salinities. As a result of the low-salinity water floods, only 0.2–1.6% of the initial kaolinite fraction was recovered.

1. Introduction

Fines migration and consequent permeability damage is one of the most wide spread physical mechanisms of formation damage in gas and oilfields (Khilar and Fogler, 1998; Civan, 2007; Byrne and Waggoner, 2009). Lifting of natural reservoir fines at high injection/production rates or in the presence of low-salinity water with resulting migration and straining usually yields a significant increase in the flow trajectory tortuosity and resulting drastic permeability decline (Zeinijahromi et al., 2016; Farajzadeh et al., 2016). Numerous measures that fix the reservoir fines (against fines mobilization) include injection of different salts or nano-fluids (Habibi et al., 2013; Assef et al., 2014; Yuan et al., 2015, 2016).

Fig. 1 shows the sequential processes of fines detachment from the pore surface, migration and straining in a thin pore throat. Fines-sensitive technologies of oil and gas recovery are primarily focused on enhancing or inhibiting the particle detachment process (Zeinijahromi et al., 2015; Yuan et al., 2016). Understanding the mechanics of particle detachment and under which conditions this process occurs involves computing the forces acting on the attached particles. Fig. 2 shows an idealized case of an attached particle and the four primary forces acting on it: the lifting force, F_L, the hydrodynamic drag force, F_d, the electrostatic force, F_e and the gravitational force, F_g. The principle of the torque balance approach is that particle detachment will occur if the torque generated by forces acting to detach the particle, being the lifting and drag forces, exceeds the torque generated by the forces acting to retain the particle, being the electrostatic and gravitational forces. It should be noted that the gravitational force can act to detach the particle depending on the orientation of the particle in the pore space.

Numerous laboratory studies exhibit fines migration accompanied by permeability decline at high flow rates, where the large drag force is sufficient to mobilize the attached fines (Gruesbeck and Collins, 1982; Khilar and Fogler, 1998). This explains observed productivity and injectivity impairment in high-rate wells.

Another reason for particle release is a decrease in the injected fluid salinity. This results in a reduction of the electrostatic attraction between the fine particles and the pore surface (Kia et al., 1987; Mohan and Fogler, 1997). Permeability decline during injection of low-salinity water has been observed in several experimental coreflooding projects (Lever and Dawe, 1984; Valdya and Fogler, 1990; Civan, 2007). Several field cases have exhibited

* Corresponding author.
E-mail address: pavel.russia@gmail.com (P. Bedrikovetsky).

http://dx.doi.org/10.1016/j.jngse.2017.05.020
1875-5100/

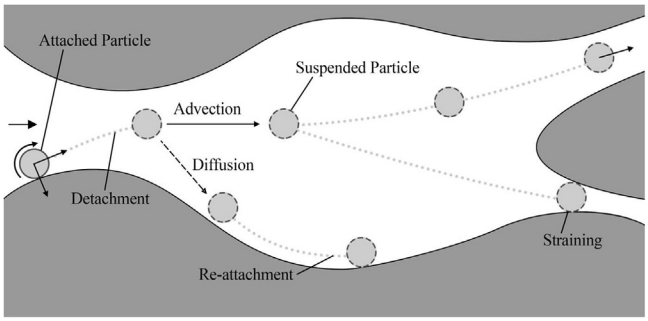

Fig. 1. Particle mobilisation, migration, diffusion in stagnant areas and straining in thin pore throats.

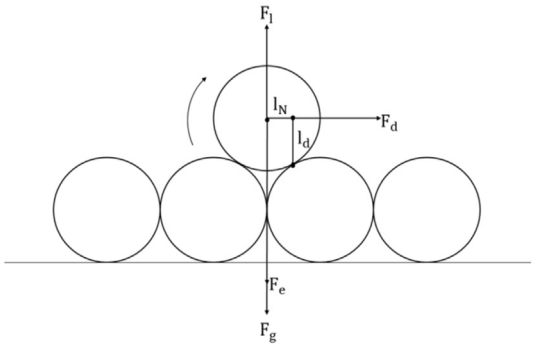

Fig. 2. Torques of drag, electrostatic, lift and gravity forces exerting particle on the grain surface.

well productivity decline after the low-salinity water breakthrough (Galal et al., 2016).

Increasing the temperature also reduces the electrostatic attractive force between particles and pore grains (Rosenbrand et al., 2013). This explains why geothermal reservoirs are highly susceptible to formation damage resulting from fines migration (Rosenbrand et al., 2014). Fines release has also been reported as a result of rock stress during methane production from coal beds (Guo et al., 2015, 2016). Fines migration is thus inextricably linked to many scenarios of fluid flow in the subsurface and should therefore be a critical component of commercial investigations into these areas.

Low-salinity waterflooding is one of the most prospective, cost-effective methods of improved waterflooding. Under the current low-oil-price environment, low-salinity waterflooding provides a cost effecting alternative to increasing the oil recovery in petroleum reservoirs. Migration of natural reservoir fines during low-salinity waterflooding yields a decline of well injectivity and productivity (Bedrikovetsky et al., 2011). However, it also results in a deceleration of the injected water and a consequent increase in the volumetric sweep efficiency (Zeinijahromi et al., 2015). As such, the prediction of the extent of permeability decline is critical in evaluating and designing low-salinity waterflooding projects. Prediction of permeability decline also helps to characterize productivity decline and to design stimulation programs during production.

The main fine mineral associated with fines migration related formation damage is kaolinite (Kia et al., 1987; Khilar and Fogler, 1998; Civan, 2007). As such, one might expect that the extent of permeability decline in kaolinite-bearing rocks would be significantly impacted by the fraction of kaolinite present in the rock. Planning and design of smart waterflooding with changing injected water composition may be improved by incorporating knowledge of the effect of kaolinite content on permeability decline However, the current authors are not aware of any systematic studies of the effect of kaolinite fraction on the permeability decline during fines migration.

In the present work, laboratory analysis was performed to investigate fines migration and the consequent permeability decline in artificial rocks with different kaolinite fractions. The methodology of preparing a consolidated sand-pack with a given clay composition was established. A new phenomenon of non-monotonic permeability variation during salinity decrease of the injected water has been observed. The permeability increase has been observed at high salinities in low kaolinite content cores. This is explained by re-attachment of mobilised fines due to strong electrostatic attraction under high salinity.

The structure of the text is as follows. Section 2 briefly presents the physics of fines detachment in natural rocks. Section 3 presents the methodology of the laboratory study, including preparation of artificial rocks with given kaolinite content and sequence of water injections with decreasing piece-wise constant salinity. Section 4 describes and analyses the obtained results which are discussed in Section 5. Section 6 concludes the paper.

2. Physics of fines detachment in natural rocks

In this Section, the main physical phenomena for fines detachment with further migration and straining in natural reservoir rocks will be described.

Fig. 2 shows the simplified model used to investigate particle detachment. Under the conditions of flow in porous media, the lift and gravity forces are negligibly small when compared with the drag and electrostatic forces. As such particle detachment is balanced primarily by the torques generated by the hydrodynamic drag force, which acts to detach particles, and the electrostatic force, which acts to keep particles immobile on the pore wall.

The drag force is mostly velocity-, viscosity- and particle-size dependent and has been quantified as (Goldman et al., 1967):

$$F_d = 6\pi\mu r(r+h)\dot{\gamma}\tilde{F} \tag{1}$$

where μ is the fluid viscosity, r is the particle radius, h is the particle-surface separation distance, $\dot{\gamma}$ is the shear rate, and $\tilde{F}$ is the dimensionless shear force, for which values have been tabulated by Goldman et al.

The electrostatic force is typically calculated by first quantifying the potential energy of the interaction between the particle and the pore grain. The electrostatic interaction energy is a total of Van der Waals, electric-double-layer and Born repulsion energy potentials (Derjaguin and Landau, 1941; Ruckenstein and Prieve, 1976; Gregory, 1981; Elimelech et al., 1995):

$$V_{total} = V_{VdW} + V_{EDL} + V_{BRN} \tag{2}$$

$$V_{VdW} = -\frac{A_{132}}{6h}\left[1 - \frac{5.32h}{\lambda_w} ln\left(1 + \frac{\lambda_w}{5.32h}\right)\right] \tag{3}$$

$$V_{EDL} = \frac{128\pi r_s r_g n_\infty k_B T}{(r_s + r_g)\kappa^2}\psi_1\psi_2 e^{-\kappa h} \tag{4}$$

$$V_{BRN} = \frac{A_{132}\sigma_c^6}{7560}\left[\frac{8r_s + h}{(2r_s + h)^7} + \frac{6r_s - h}{h^7}\right] \tag{5}$$

where V is the potential energy, A_{132} is the Hamaker constant, h is the particle-surface separation distance, λ_w is the characteristic

wavelength of interaction, r_s is the grain size, n_∞ is the bulk number density of ions, k_B is the Boltzmann constant (4.116×10^{-21} J), T is the absolute temperature of the system in degrees Kelvin, κ is the Debye-Hückel parameter, ψ_1 and ψ_2 are the surface potentials of particles and grains respectively, and σ_c is the atomic collision diameter.

Surface potentials (ψ_1, ψ_2) are estimated from the zeta potentials using the following formulae (Elimelech et al., 1995):

$$\psi_1 = tanh\left(\frac{ze\zeta_{clay}}{4k_BT}\right) \tag{6}$$

$$\psi_2 = tanh\left(\frac{ze\zeta_{sand}}{4k_BT}\right) \tag{7}$$

where z is the valence of the cation in solution, e is the elementary charge (1.602×10^{-19} C), T is the temperature in degrees Kelvin and ζ_{clay} and ζ_{sand} are the zeta potentials of the clay and sand particles respectively in volts. Fig. 5 shows measured values of zeta-potential for kaolinite and silica sand for different salinities.

The electrostatic force is quantified as the negative of the electrical potential energy gradient:

$$F_e = -\frac{\partial V}{\partial h} \tag{8}$$

Fig. 3 shows, schematically, the electrostatic interaction between two spherical particles. While these interactions are generally attractive due to the van der Waals force, the repulsion resulting from the similar sign of the surface charges reduces the net attractive force experienced by the fine particle. When in electrolyte solutions, counter-ions (cations in this case) adsorb to the surfaces of the particles and in essence 'mask' the negative surface charge. The interactions between the surface charges and the influence of aqueous ions are quantified as the Electrostatic Double Layer force as above. The presence of adsorbed counter-ions results in a contraction of the electrostatic double layer, reducing its contribution to the interaction, but has a negligible effect on the attractive vdW component (Schembre and Kovscek, 2005). Hence the presence of an electrolyte increases the total electrostatic attractive force. The higher the salinity, the more ions are present to adsorb to the charged surfaces and hence the stronger is the net attractive force. This explains why the electrostatic force is highly dependent on the water composition.

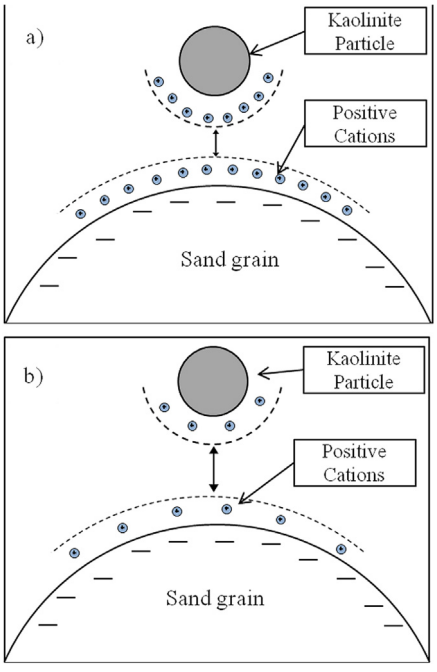

Fig. 3. Schematic for particle-grain electrostatic attraction at high (a) and low (b) salinity.

Quantitative predictions of particle detachment often assume that the detached particle rotates around its neighbour at the moment of mobilisation. Thus, the mechanical equilibrium condition for the particle on the grain/rock surface is the equation of torque equality (Bergendahl and Grasso, 2000)

$$F_d l_d = F_e l_N \tag{9}$$

where l_d is the drag lever arm ratio and l_N is the normal lever arm ratio. A similar approach has been utilized to evaluate particle immobilization in the form of a filter cake (Kalantariasl and Bedrikovetsky, 2014; Kalantariasl et al., 2015).

Fig. 2 shows attaching and detaching forces, as well as the lever arms for drag and electrostatic forces. Considering the SEM photograph of kaolinite platelets in Fig. 4, it is clear that the assumption that kaolinite particle is a sphere in the torque balance can yield a significant overestimation of the drag force. Thus, it is necessary to introduce a shape factor into expression for drag force in torque balance equation (9).

The dependency of the total electrostatic interaction energy on the particle-surface separation distance is presented in Fig. 6.

For a given particle size, salinity and fluid velocity, the torque balance Eq. (9) defines whether particle detachment will occur. So, Eq. (9) defines the volumetric concentration of particles which remain attached for a given particle size, salinity, and velocity. Averaging the attached concentration over particle size using the particle size distribution results in the total volumetric concentration of attached particles as a function of salinity and velocity. This function expresses the maximum attached concentration and is referred to as the maximum retention function. The calculation of the maximum retention function requires the expressions for the velocity-dependency of drag force and the salinity-dependency of electrostatic force, which can be seen in Eqs. (2)–(7). Fig. 7 presents the typical form of the maximum retention function.

3. Laboratory study

In this section, a detailed description of the methodology for preparing an artificial sand-pack with fixed kaolinite fraction,

Fig. 4. SEM photograph of kaolinite leaflets attached to the grain surface.

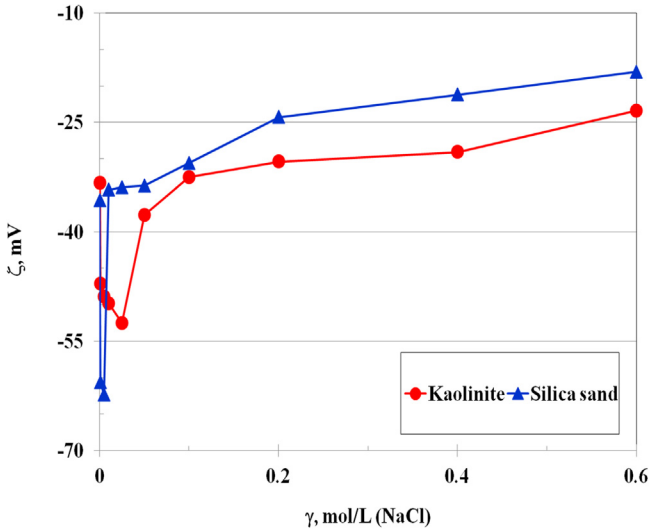

Fig. 5. Zeta-potentials for kaolinite particles and sand grains at different salinities.

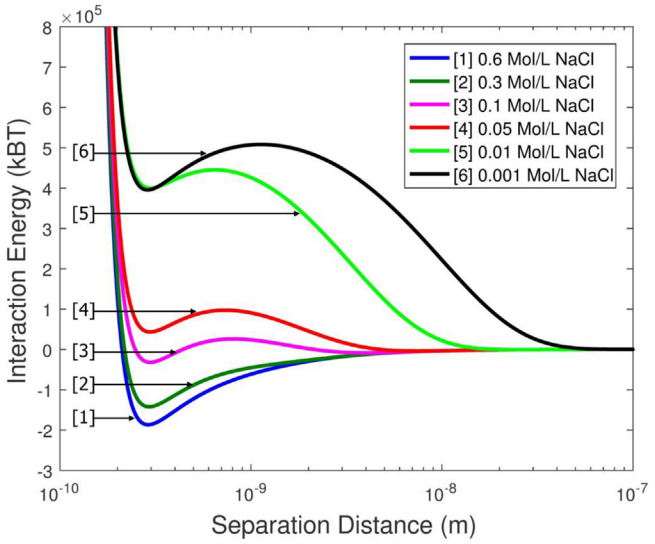

Fig. 6. Electrostatic interaction between kaolinite fines and sand grain for different salinities.

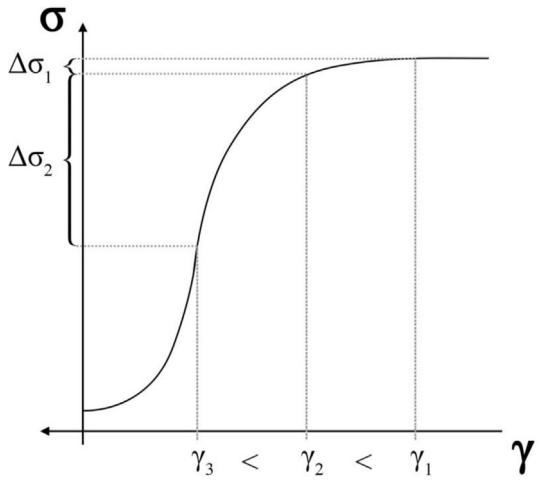

Fig. 7. Maximum retention curve for a function $\sigma_{cr}(\gamma)$ versus salinity.

properties of artificial cores and fluids used, laboratory set-up and methodology of experimental study of fines mobilisation and migration are presented.

3.1. Rock properties

Unconsolidated cores, made of a mixture of silica sand and kaolinite, were used in all experiments.

The sand used in the present study is silica sand with >99% of silica (brand 50N, SIBELCO, AUSTRALIA). The sand was first sieved to constrain the particle size. This assisted reproducibility of the core properties. Prior to chemical washing, a magnet was passed over the sand to remove the visible ferromagnetic impurities.

This sand underwent several cleaning procedures to ensure its purity. Initially, sand was washed with hexane to remove organic impurities, followed by acetone to remove hexane, and consequently with deionised water to remove the acetone. The sand was then dried in an atmospheric oven at 60 °C for 24 h. Hydrochloric acid was added to the dried sand to remove inorganic impurities, followed by rinsing the sand in deionised water to remove the HCl. This rinsing procedure continued until the pH of the rinsed water was equal to that of fresh deionised water, ensuring that all acid had been removed. Shani et al. (1998) demonstrated the significance of removing impurities from sand samples but stressed that vigorous processes such as boiling sand in acid would significantly alter the surface roughness properties of the sand. As surface roughness has been shown to significantly affect particle detachment kinetics (Torkzaban and Bradford, 2016), these rigorous washing methods were avoided here.

The kaolinite powder used in the present study was purchased from Sigma-Aldrich, AUSTRALIA. The authors found that the mass of kaolinite samples decreased by about 0.1% when dried in the atmospheric oven at 60 °C for 24 h. As such, to maintain accuracy of quoted clay concentrations, kaolinite was dried at 60 °C for 24 h prior to its use.

For each experiment, set masses of kaolinite and silica sand were weighed and mixed dry. Several studies have emphasized the benefits of wet compaction (Haug and Wong, 1992; Chiu and Shackelford, 1998) and so a high salinity (0.6 Mol/L NaCl) solution was added to the mixture until the grains were just coated in fluid. Adding too much fluid could create a layer of water which would induce the separation of kaolinite and sand, which would significantly alter the flow properties of the core.

3.2. Fluids

Injection fluids were created by adding ChemSupply 99.7% purity NaCl salt to MilliQ analytical grade deionised water. The fluids were deaerated for a minimum of an hour to prevent dissolved air from evolving within the core and damaging the core permeability. Seven different sodium chloride solutions were injected sequentially during the experiment: 0.6 M, 0.3 M, 0.1 M, 0.05 M, 0.01 M, 0.001 M and deionised water. Ionic concentrations given by M refer to molar concentrations (mol/L) of sodium chloride.

3.3. Methodology for preparation of artificial rocks

A schematic of the core holder used in this study is shown in Fig. 8. The main consideration to assist reproducibility was the manner in which the core was compacted. For this setup, axial compaction was provided by steel distributors with an incised pattern designed to evenly distribute flow into the cross-sectional area of the core. Tightening of 'end caps' into the core holder body forces the distributors further into the core holder, compacting the core. This process also allows direct

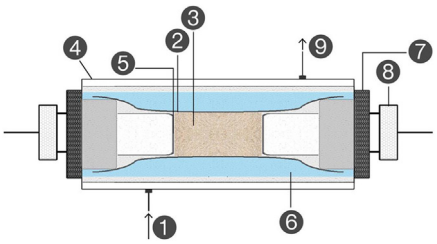

Fig. 8. Core holder with unconsolidated core: 1 – overburden inlet line; 2 – Viton sleeve; 3 – core sample; 4 - coreholder; 5 – distributor and mesh; 6 – overburden fluid; 7 – brass screw cap; 8 – end cap; 9 – overburden outlet line.

measurement of core length, which is necessary to calculate permeability.

A radial component of compression was provided by fresh water, kept at high pressure (1000 psi) between the steel core body and the Viton sleeve holding the core. This overburden pressure assisted with compaction in a manner that could be controlled across each experiment. The high pressure also caused grains to embed slightly into the Viton sleeve, minimising the potential for annular flow between grains and the core holder.

A 20 μm aperture size stainless steel mesh was adhered to the distributors using a silica-based glue. The mesh size prevented sand (mean diameter = 123 μm) but would allow kaolinite (mean diameter = 2.064 μm) to enter the effluent stream. This would allow fines migration to be studied without dealing with complete or partial breakdown of the core itself.

To prevent radial expansion of the Viton sleeve during compression of the core, three layers of paper-based, non-expandable tape were applied to the sleeve.

The sequencing of the core compaction is as follows. One of the stainless-steel distributors was fastened into the steel core holder using the end cap. A measured sample of 85 g of the sand-kaolinite mixture was prepared and placed into the core holder. The mixture was placed carefully, in small portions, with occasional compression using a plastic cylindrical rod to prevent cavity formation. The other stainless steel distributor was tightened into the core holder using the other end cap, which consequently compressed the sample. After both distributors were placed within the core holder, the inlet and outlet lines were blocked and the core holder was placed into position for coreflooding. At this point, the end caps were tightened consecutively in small increments until the core was at the desired length. The mass of the sample (85 g) was held constant for all experiments in this study to enhance reproducibility.

3.4. Laboratory set-up

Experimental studies on fines mobilization in artificial non-consolidated sand-kaolinite cores were carried out using a real-time permeability apparatus. A schematic of this setup is shown in Fig. 9 and a photograph is shown in Fig. 9b References to components on the schematic in the following section will be in parentheses.

A core *(1)* is placed inside a 1.5″ diameter Viton sleeve *(2)*. Two

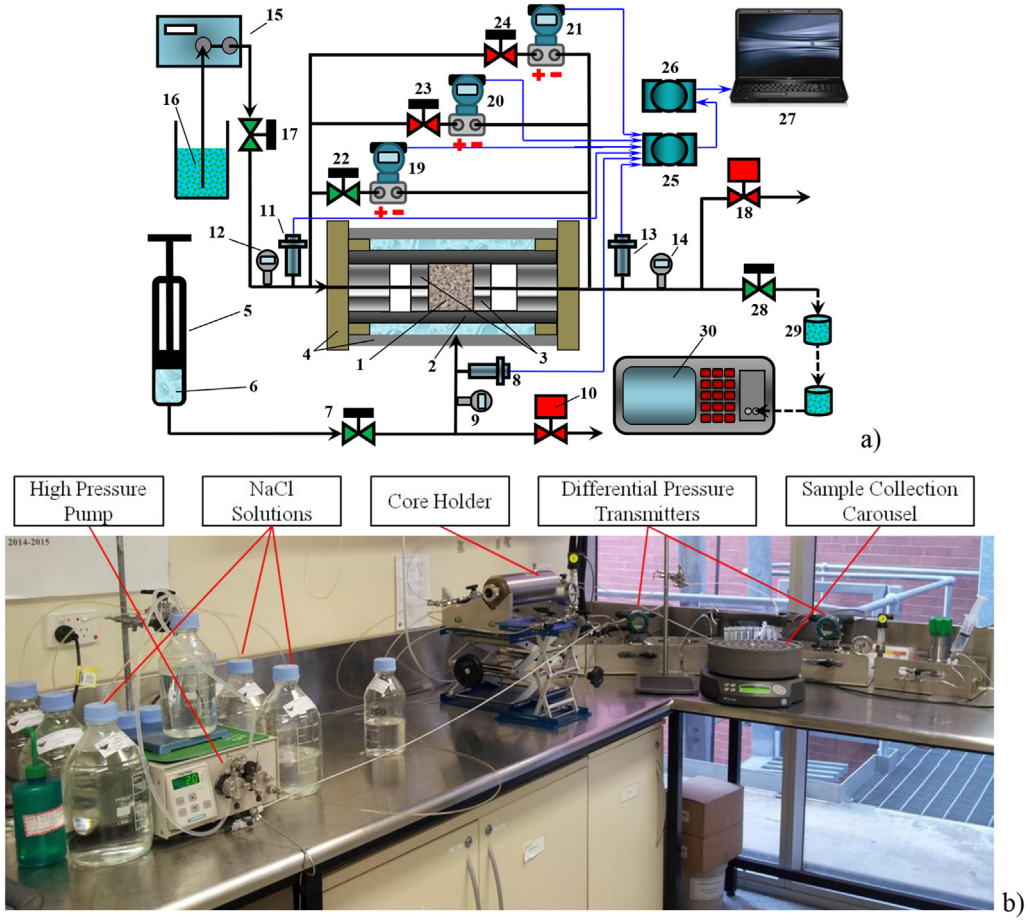

Fig. 9. Laboratory set-up: a) schematic for all elements; b) photo for pressure and rate measurements and sample collection.

stainless steel fluid distributors *(3)* fix the core in place by compression. A Hassler-type coreholder *(4)* (model RCH, CoreLab, USA) accommodates the sleeve and core. This arrangement is rated to 5000 psi maximum pressure. A manual HiP piston pressure generator *(5)* rated to 5000 psi maximum pressure (model 87-6-5, High Pressure Equipment Company, USA) develops an overburden pressure by compressing deionised water *(6)*. An overburden pressure is fixed by a manual valve *(7)* and measured by an absolute pressure transmitter *(8)* (model PA-33X, KELLER AG fur Druckmesstechnik, SWITZERLAND) and Bourdon-type pressure indicator *(9)*. A pressure relief valve *(10)* is used for safety purposes. Inlet and outlet pressures in the coreholder are measured and indicated by pressure transmitters *(11)* and *(13)* (model PA-33X, KELLER AG fur Druckmesstechnik, SWITZERLAND) and by Bourdon-type pressure indicators *(12)* and *(14)*. A high-pressure pump *(15)* (model Prep-36, Scientific Systems, Inc., USA) pumps saline solutions *(16)* through the unconsolidated core via a manual valve *(17)*. A back-pressure regulator *(18)* (model BP-series, CoreLab, USA) maintains pressure inside the core at 300 psi. The pressure drop across the unconsolidated core is measured by three differential pressure transmitters *(19–21)* (model EJX110A, Yokogawa Electric Corporation, JAPAN) with measuring ranges 0–1, 0–10 and 0–100 psi. Switching between differential pressure transmitters is carried out via manual valves *(22–24)*. An ADAM-4019 + inlet data acquisition module *(25)* (ADVANTECH™, TAIWAN) and an RS-232/RS/485 signal conditioner ADAM-5060 *(26)* (ADVANTECH™) receive electrical signals from all transmitters in real-time and feed them into a PC-based data acquisition system *(27)*. A custom-built data acquisition software (Advantech ADAMView Ver. 4.25 application builder) recording of all experimental parameters in real-time mode and performs all necessary calculations. Effluent suspensions via a manual valve *(28)* are collected in plastic sampling tubes *(29)* (15 and 50 mL) located in the sampling carousel. Concentration of kaolinite particles in collected effluent samples are measured by a POLA-2000 particle counter/sizer *(30)* (Particle and Surface Sciences, Australia).

3.5. Methodology of fines migration study

Cores were initially saturated by flowing high salinity (0.6 M NaCl) solution at a low flow rate of 0.2 mL/min (superficial velocity 2.93×10^{-6} m/s) to ensure complete saturation and attachment of fine particles to sand grains. This flowrate is a magnitude smaller than that used in the test, and was chosen to minimize particle detachment prior to commencing the test. Corefloods were carried out at constant superficial velocity of 2.9×10^{-5} m/s (volumetric flowrate $Q = 2$ mL/min). The tests were carried out at the following fluid ionic strengths (NaCl solutions): 0.6M, 0.1M, 0.05M, 0.01M, 0.001M and deionised (DI) water. The following effluent volumes were sampled: 10 samples taken at 0.2 PVI, 5 samples taken at 0.6 PVI, 10 samples taken at 2.5 PVI; a bulk overnight sample until permeability stabilization was achieved within experimental uncertainty (3.2%), and 5 samples taken at 0.2 PVI after permeability stabilization to detect the presence of kaolinite particles in the effluent. Here we use pore volume injected (PVI) as a unit for dimensionless time. For each collected sample, the fluid mass, electrolytic conductivity, and particle concentration were measured. The fluid mass provided estimates of fluid volumes for each sample and the electrolytic conductivity was converted to fluid ionic strength. The particle concentrations were either converted to total particle volumes using fluid volumes or were used directly as particle concentration. Pressure transducers measured the differential pressure across the core and along with the flow rate, core dimensions and viscosity, allowed for calculation of permeability at intervals throughout the experiment. Fluid viscosity was corrected in real-time for changes in NaCl concentration, temperature and pressure according to established correlations (Kestin et al., 1981; Aleksandrov et al., 2012).

4. Analysis of results

In the following section, the results of the six corefloods with piecewise-constant decreasing salinity will be presented.

4.1. Validation of experimental procedure

While other experimental procedures for creating artificial sand-packs have been presented in the literature, none so far have proven the reproducibility and stability of permeability to the degree required to investigate the phenomena presented in this text. Some authors used vibration to assist compaction (Al Sayari, 2009) which is likely to be inappropriate for kaolinite-sand mixtures due to separation of the two minerals as a result of the difference in particle size. Other authors failed to purify sand samples (Mullins and Panayiotopoulos, 1984) which, while more representative, induces significant chemical heterogeneity on the sand samples (Shani et al., 1998) which could alter particle detachment properties across several tests. While some authors have increased the reproducibility of core permeability through standardized compaction curves (Chiu and Shackelford, 1998), this process significantly reduces the cores' ability to represent subsurface sedimentary formations. While appropriate in other contexts, the above described procedures do not provide the necessary qualities to investigate the effect of kaolinite content on the degree of fines migration within petroleum reservoirs.

The proposed methodology incorporates aspects of previous methodologies to provide a means of investigating the phenomenon described in this text. What remains is to validate that the experimental method described in Section 3 provides reproducible and stable permeability to allow comparison of separate experimental results. To test reproducibility and stability, two pure sand-packs were prepared and run using two separate sets of core-flooding apparatus. The mean permeabilities of the results from the two setups are 1477 mD for the first setup and 1517 mD for the second. The two mean values coincide within the experimental uncertainty of 3.2% (see Badalyan et al., 2014) and thus demonstrate the reproducibility of the results. The permeability results, normalized by respective mean values, presented in Fig. 10 demonstrate the stability of the results. The standard deviation of permeability was 0.49% for the first setup and 0.2% for the second.

The reproducibility of the compaction procedure was also tested for cores with 5% kaolinite contents. Following the 0.6 M injection, the stabilised permeabilities of the two tests were 499 and 484 mD, which suggests that the methodology produces reproducible results even when the cores contain kaolinite.

To validate the underlying assumption that the kaolinite is initially distributed evenly throughout the core, the coreflooding of one of the two above cores with 5% kaolinite was stopped following permeability stabilisation after 0.6 M NaCl injection. The core was then cut into five pieces whose clay content was determined through sedimentation and filtration. The concentrations were, from inlet to outlet, 4.86%, 5.05%, 5.06%, 5.16%, and 4.97%. These results validate the above-mentioned assumption.

4.2. Pore and particle size distributions

The sieved sand particle size (radius) distribution was measured by a POLA 2000 particle counter/sizer (Particle & Surface Sciences, AUSTRALIA). The distribution is shown in Fig. 11a. It allows

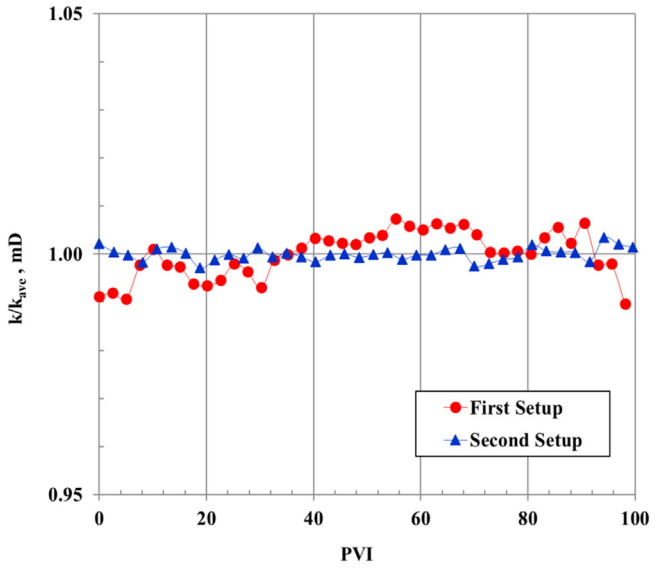

Fig. 10. The normalised sand-pack permeability as obtained by independent measurements at two different set-ups.

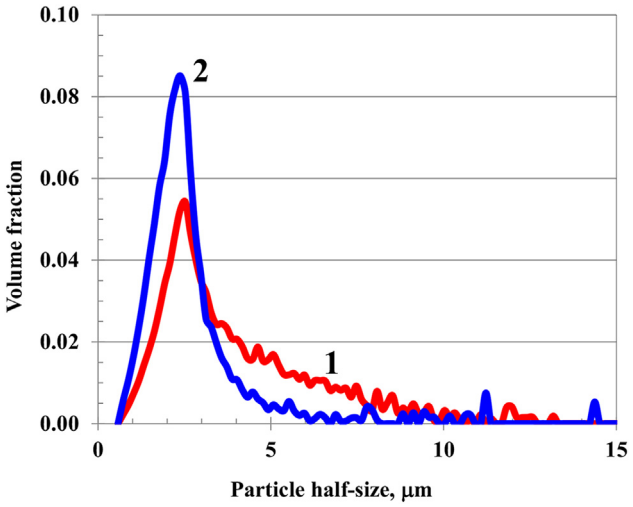

Fig. 12. Size distribution of kaolinite particles: 1 - placed in the core; 2 - collected in effluent suspension.

calculation of the pore size distribution. For any three sphere-form grains, touching each other, the pore size is determined as a minimum size sphere that can pass between the grains. It is equal to a radius of inscribed circle in the plane crossing the sphere centres (Descarte's theorem). Grain triples are randomly chosen from the above-mentioned distribution, and the pore radii are calculated. A more detailed algorithm is presented by Chalk et al. (2012). The pore size distribution (Fig. 11b) is obtained from the grain size distribution (Fig. 11a) by 100,00 iterations of the Monte-Carlo method. The mean pore size is $r_p = 11.1$ μm.

The measured rock porosity (0.395) and stabilised permeability (1497 md) of the sand-only porous medium also allow for estimating the mean pore radius (Barenblatt et al., 1989):

$$r_p = 5\sqrt{\frac{k}{\phi}} \tag{10}$$

which yields a mean pore size of 9.7 μm. Both estimates are close. As such, formula (10) is used further in the text for estimation of the mean pore size.

Size distribution for kaolinite particles was also measured by POLA-2000 particle counter/sizer. The size distribution of kaolinite placed in the core and of produced kaolinite particles are shown in Fig. 12a and b respectively. The calculated kaolinite particle volume-mean radius prior to placement in the core is equal to 2.064 μm.

The sieving of sand was done to ensure that particle migration and straining could occur simultaneously in the core. The jamming ratio, defined as the ratio between kaolinite particle volume-mean radius and mean pore throat, radius is equal to $j = \frac{2.064\ \mu m}{11.1\ \mu m} = 0.19$. Deep bed filtration, wherein particle both migrate and strain, occurs when $\frac{1}{7} < j < \frac{1}{3}$ (or $0.14 < j < 0.33$) (van Oort et al., 1993). Therefore, for the kaolinite and sand used in the current experimental study, deep bed filtration is expected. Fig. 12 shows that the percentage of large particles in the effluent is lower than that in the core. This can be explained by the presence of particle straining within the core. The larger is the particle the larger is the probability of it straining in a thin pore throat. As such, smaller particles

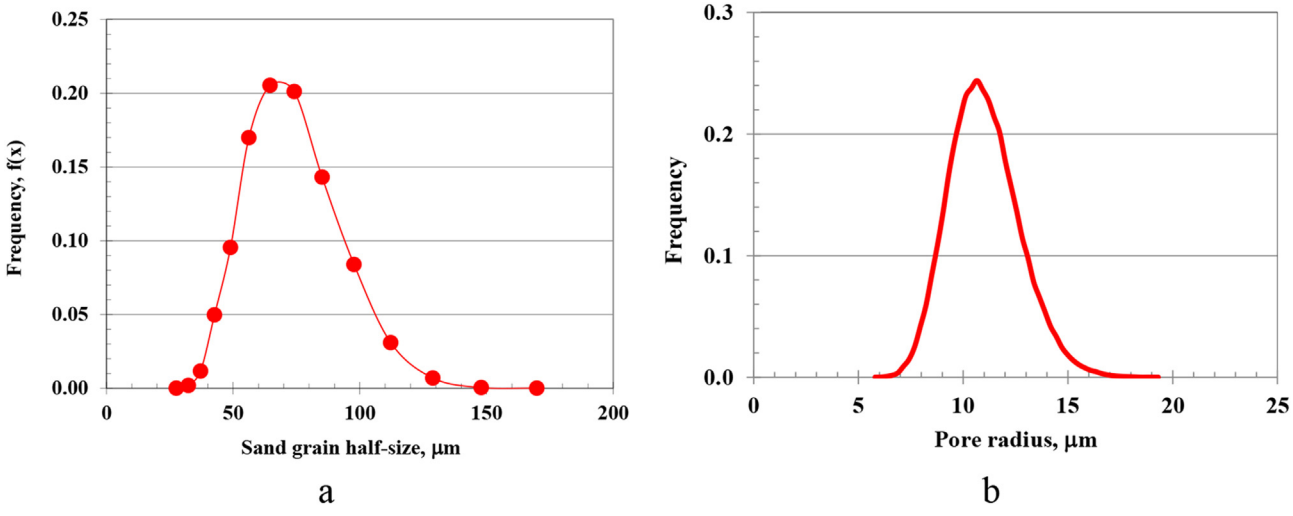

Fig. 11. Half-size (radius) distribution for sand grains (a) and for sand-formed pore radius (b).

are more likely to be collected at the effluent. This explains why the proportions of large and small particles are different at the outlet.

Eqs. (1)–(7) show the dependence of both the drag and electrostatic forces on the particle size. For given conditions of flow rate, U and fluid salinity, γ, Eq. (9) can be used to identify the particle size, r_s which satisfies the torque balance and hence lies on the boundary of imminent particle detachment. As the detaching force increases monotonically with particle size, all particles larger than this calculated particle size will be detached, and all those smaller will remain attached. This process of calculating the critical particle size can be repeated for several values of injected fluid salinity to investigate trends in the detached particle size with changes in fluid composition. The resulting function, describing the dependence of detached particle size on the fluid salinity is called the critical particle size curve. Given a constant injection rate, the lower is the injected salinity, the smaller are the mobilized particles, i.e. the fine particles are released in the order of their size decrease during the salinity decrease.

4.3. Core permeability variation

Variation of initial/undamaged rock permeability for artificial cores as a function of kaolinite content is shown in Fig. 13 (red line, circles). The cores with higher kaolinite fractions have lower initial permeability. The final permeabilities for the 6 cores after fresh water injection are presented in Fig. 13 (blue line, triangles). The transition from initial to final permeability appears to be highly variable and will be discussed in the next section.

Porosity values of the 6 cores calculated based on bulk-core and solid volumes are presented in Fig. 14. These values allow calculating the mean pore radius of each core as per Eq. (10). The calculated mean pore radii for the 6 cores are shown in Fig. 14b. The higher is the kaolinite concentration in the rock, the lower is the porosity. This effect is attributed to filling of the pore space by attached kaolinite particles. A schematic representation of multilayer pore filling by kaolinite is presented in Fig. 15.

The permeability results of the corefloods by water with piecewise constant decreasing salinity are presented in Fig. 16. Around 100–150 PVI of constant-salinity water was injected sequentially to allow for permeability stabilization within the experimental uncertainty. The salinity varied from 0.6 M to DI

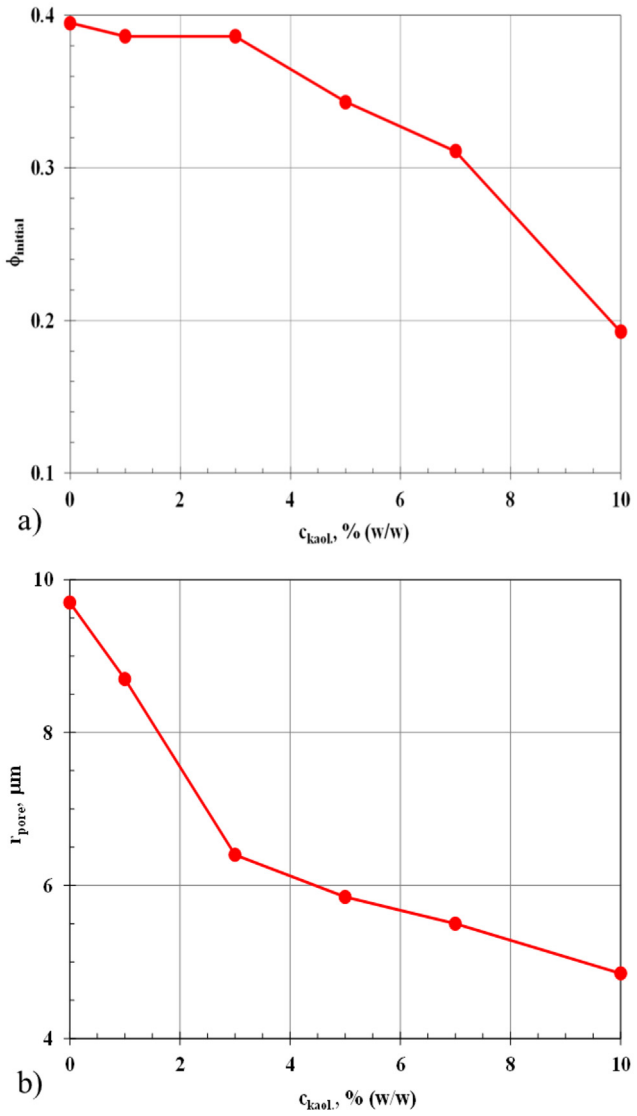

Fig. 14. Initial porosities (a) and mean pore radii (b) for six cores as a function of initial volumetric kaolinite concentration in the core.

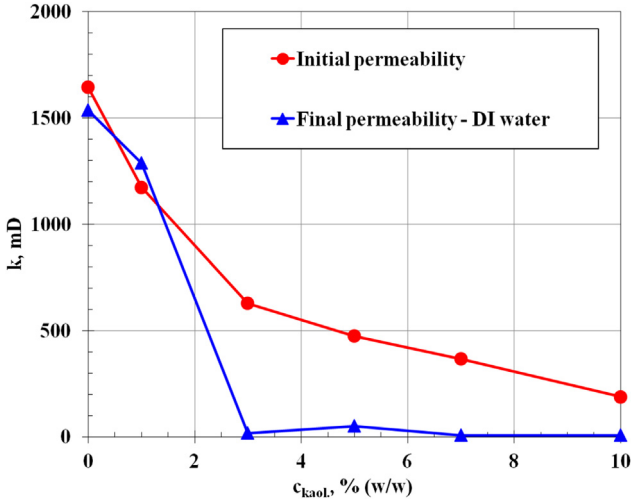

Fig. 13. Initial (following 0.6 Mol/L injection) and final (after de-ionised water injection) core permeabilities as functions of kaolinite concentration.

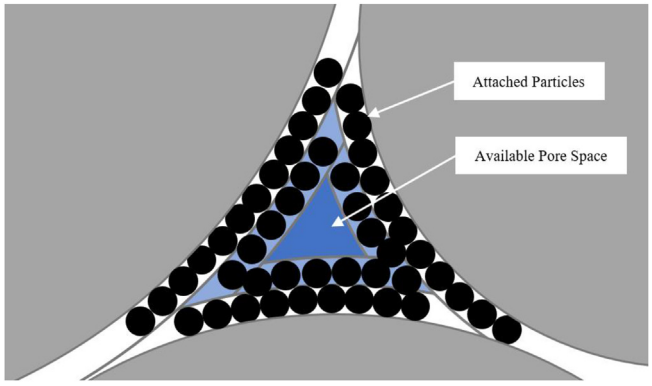

Fig. 15. Schematic of sand grains and kaolinite fines, attached to pore throats in sandpacks.

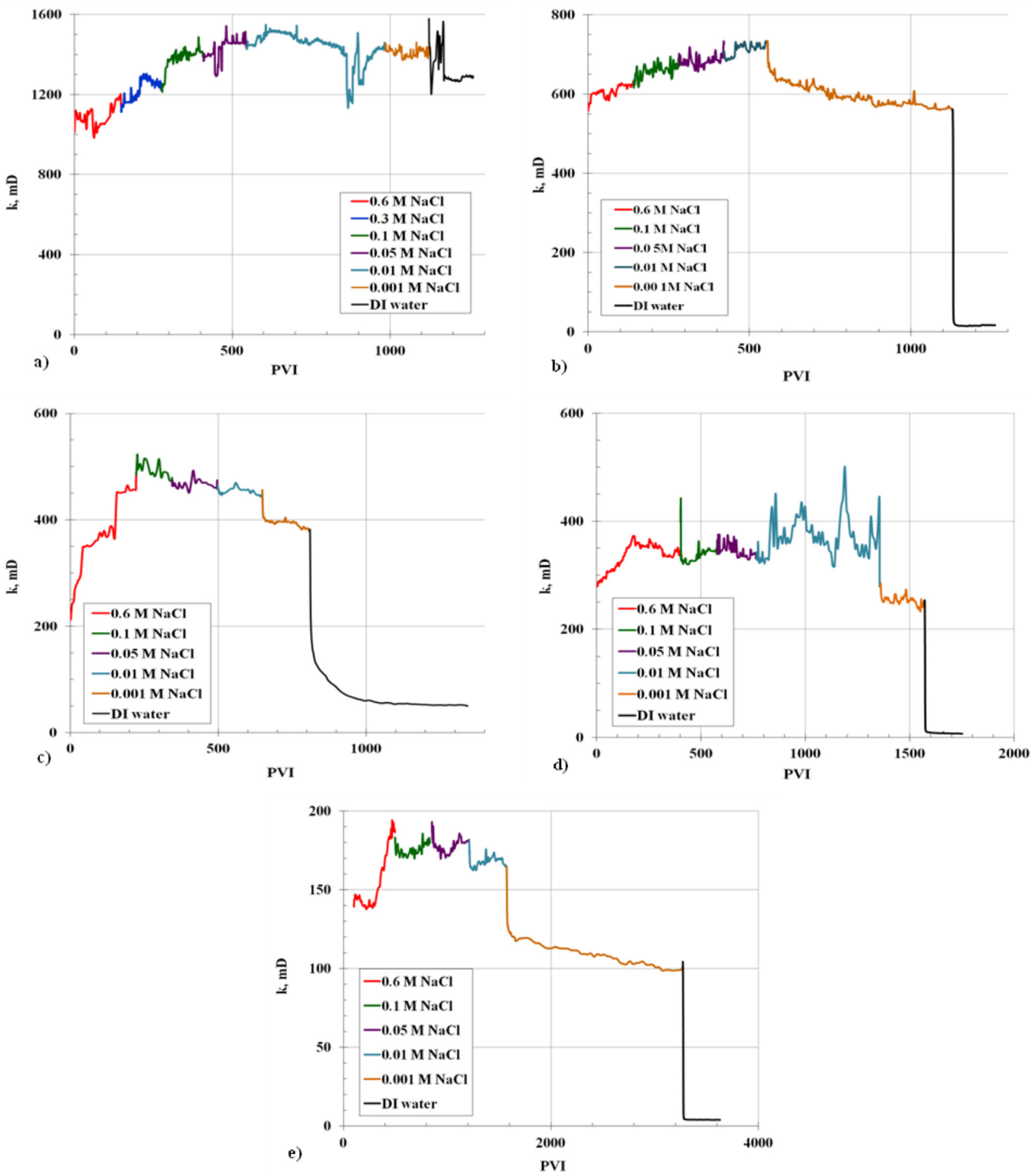

Fig. 16. Core permeability variation during step-wise constant decrease in injected salinity as a function of PVI for various kaolinite contents: a) 1%; b) 3%; c) 5%; d) 7% and e) 10% of kaolinite.

water. While it appears that stabilisation has not been achieved for some injection cycles, this is primarily due to the large time scales in Fig. 16. The final permeability data for all tests at 0.6 M is shown in Fig. 17 to demonstrate stabilisation of these measurements. Comparison of each test can be done readily using the stabilized permeability after each constant-salinity injection period. The stabilised permeability versus salinity is shown in Fig. 18 for all cores.

The accumulated breakthrough concentrations of produced particles (Fig. 19) allow calculating the produced fraction of initial

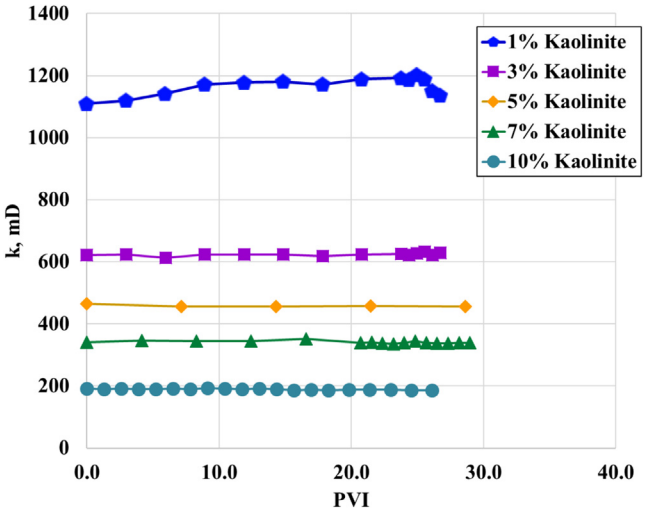

Fig. 17. Permeabilities at the end of the 0.6 Mol/L NaCl injection period demonstrating the stabilisation of permeabilities prior to alternating the injected salinity.

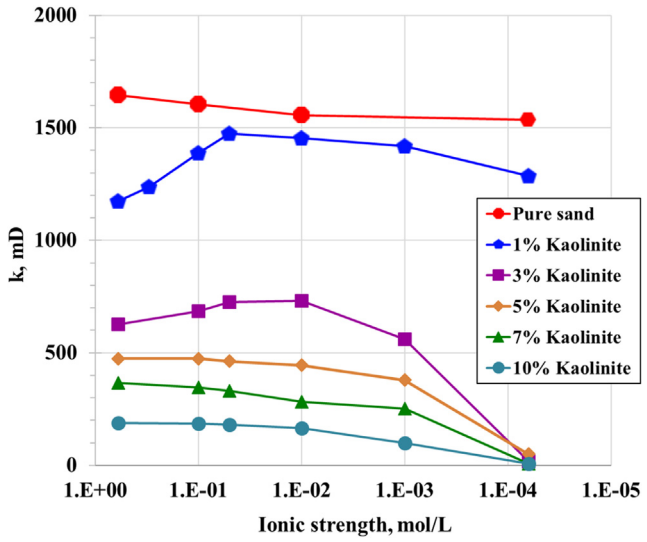

Fig. 18. Stabilised core permeabilities as a function of fluid ionic strength for different kaolinite concentrations in cores.

kaolinite. The percentage of kaolinite recovered during low-salinity corefloods is given in Fig. 20.

5. Discussions

5.1. Initial permeability variation

Differences in the initial permeability for the 5 cores can be explained by interpreting the differences in the calculated mean pore radii. The electrostatic potential curves for the kaolinite-silica interaction, presented in Fig. 6, show that in 0.6 M NaCl solutions (curve [1]) kaolinite particles will experience a solely attractive force upon approach to sand grains until deposition in the primary potential energy minimum. This implies that under the saturation conditions, the kaolinite particles will form a multi-layer coat on each of the sand grains. The higher is the kaolinite fraction in the core, the thicker these layers will be and hence, the smaller will be the pore spaces available for fluid flow. The smaller pore spaces explain the initial permeability variation observed as a function of clay content.

5.2. Non-monotonic permeability variation

Fig. 16 demonstrates a degree of permeability increase at high salinities for cores with low kaolinite fraction, which is present also in the stabilised values presented in Fig. 18. Significantly, this implies that the effect of fines migration on permeability can no longer be thought of as monotonic. For cores with 1% and 3% of kaolinite, the permeability increases for salinities 0.6 M, 0.3 M, 0.1 M and 0.05 M. For low salinities, the permeability of these cores decreases. For cores with 5%, 7% and 10% of kaolinite permeability increase is observed for only 0.6 M salinity, then, the permeability monotonically declines with further decreases in injected fluid salinity.

The above phenomena can be explained by the competitive effects of particle detachment, re-attachment and straining mechanisms. Particle detachment will cause a minor permeability increase due to the increase in the pore volume available for fluid flow. While this process is typically taken to be negligible, particle detachment from relatively small pore throats could produce noticeable variations in the flow properties of the rock. Once mobilized, a particle will migrate through the rock until it meets a pore with diameter less than its own, wherein it will strain. This results in the termination of the flow path and a consequent decrease in the permeability. The permeability decline due to straining is thought to significantly outweigh the permeability increase due to particle detachment, and so the process of detachment, migration and straining will result in a net permeability decrease.

There is however a possibility of a secondary particle capture mechanism, being particle re-attachment. In high salinity solutions, the electrostatic attraction has no apparent energy barrier (see Fig. 6, 0.6 M and 0.3 M). The consequence of this, alluded to previously, is that kaolinite particles require no energy to move from any separation distance to the primary minimum, where it is considered attached to the sand grain. In fact, the particle will be encouraged to deposit in this minimum due to the attractive electrostatic forces. As a consequence of this, at high salinities, mobilized particles may re-attach to the sand surface prior to straining.

Considering again the acting torques on the particle (see Fig. 2), and recalling the velocity dependence of the drag force (Eq. (1)), particle re-attachment is most likely to occur in low-velocity regions of the pore space. The detachment and consequent re-attachment of kaolinite particles is hence most likely to result in the particle being transported from regions of higher velocity to those in the pore space with lower fluid velocities. This will result in a decrease in the pressure drop created by the kaolinite and hence increase the core permeability.

Given that the permeability increase is dictated by particle detachment, it may be possible that the observed permeability increase could be the result of the detachment of small particles, which pass freely through the core, without straining. Such an explanation would not rely on the presence of particle re-attachment, but rather on a significantly small probability of straining. The primary issue with this hypothesis is that permeability increase was observed only during the injection of high salinity NaCl solutions. This could be a result of a change in the straining probability, but as was explained earlier, particles should detach in order of decreasing size, and so straining probabilities should be at their highest during high salinity injections. Thus, explaining the non-monotonicity of the permeability requires a physical mechanism of particle capture which is dependent on the fluid salinity. The proposed mechanism of

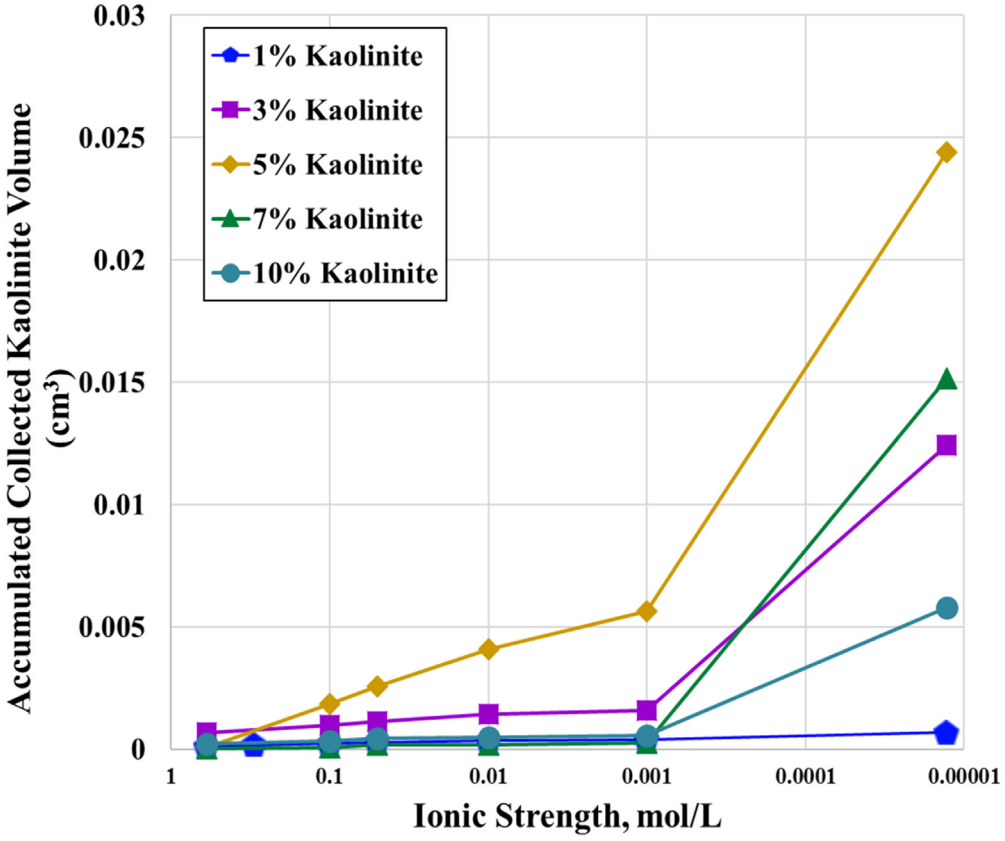

Fig. 19. Accumulated volume of produced particles versus salinity collected during injection of piece-wise constant decreasing salinity.

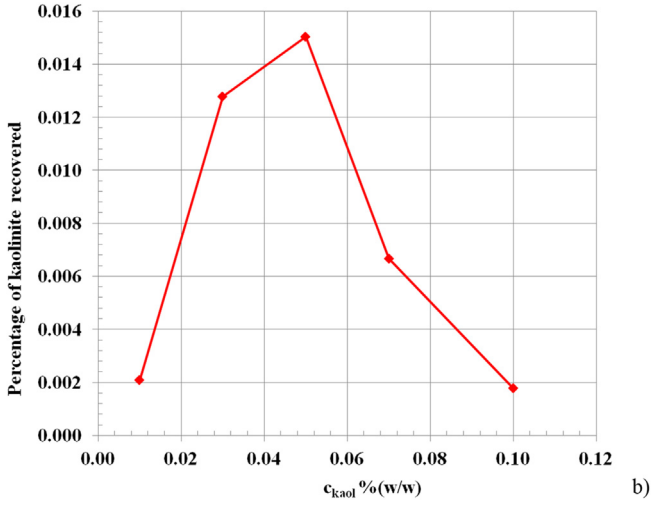

Fig. 20. Percentage of initial kaolinite recovered during corefloods of piece-wise constant decreasing salinity injection fluids.

particle re-attachment satisfies this condition.

A physical mechanism has been proposed to explain the observed permeability increase. This explanation suggests that particle capture occurs not only by particle straining, but also by particle re-attachment. These two processes will inevitably compete for the populations of mobilized particles. This provides a convenient explanation as to why the permeability increase appears to be a function of the clay fraction of the core. As discussed earlier, for high-kaolinite-fraction cores, pore throats are smaller than those for cores with lower kaolinite fraction. As such, straining rates will be substantial, and therefore particle re-attachment rates are likely to be negligible in comparison. This could explain why cores with higher fractions of clay exhibited mostly monotonic permeability decline with decreasing injected fluid salinity.

5.3. Extent of permeability decline

For all cases of permeability decline, the decline is greater for injection of lower salinities. This is explained by the typical form of the maximum retention function versus salinity (see Fig. 7). For a given change in salinity, the volume of detached particles will be greater at lower salinities. Therefore, the majority of fines are mobilised at low salinities, as is demonstrated in Fig. 19. A larger volume of mobilized particles is expected to result in a larger decrease in the core permeability. In order to validate this hypothesis, it would be necessary to model the permeability decline and effluent particle capture to calculate the detached particle volumes for each injection, which is a subject of a separate work.

Initial permeability increase in the 1% Kaolinite core at high salinities is compensated by further permeability decrease at low salinities, resulting in an insignificant difference between initial and final permeabilities. For the four other cores, despite high variation of initial permeability (k varies from 627 mD for the 3%-kaolinite core to 188 mD for the core with 10% kaolinite) the final permeability after fresh-water injection is very similar (k varies from 6.6 mD for 10% kaolinite up to 50 mD for 5% of initial kaolinite).

While changing salinity from 0.6 M to fresh water, if compared with initial permeability, the permeability declines 38, 9.5, 55, and

47 times for the cores with kaolinite contents 3, 7, 5, and 10%, respectively.

The percentage of kaolinite recovered after the first flush with DI water, presented in Fig. 20, varies from 0.2% to 1.6%. To place these results into context, a similar test was done on a Berea sandstone core. XRD analysis on this core demonstrated that 6.91% of the core by weight was comprised of clay, with 4.49% being kaolinite, 0.65% being chlorite and 1.76% being muscovite. After flushing with 0.01M NaCl a total of 0.0039 g of clay was retrieved. This corresponds to 0.0026% of the total core mass and 0.0382% of the total mass of clay. In the 7% kaolinite core prepared in this study, after flushing with 0.01M NaCl, 0.0179 g of clay was retrieved. This amounts to 0.021% of the total core mass and 0.302% of the mass of clay initially in the core. The percentage of clay collected at the outlet was almost 8 times higher for the artificial core when compared with the Berea sandstone core. This is most likely a result of clay cementation induced via diagenetic processes in the Berea core which would not be present in the artificial core. The differences in initial permeabilities (34.19 mD for the Berea core and 338.4 for the artificial core) also suggest that the pore sizes may be larger in the artificial core, which would result in smaller straining probabilities and higher suspended concentrations at the outlet.

The kaolinite recovery is ultimately determined by the form of the maximum retention function and the relationship between the attachment and straining probabilities. The form of the kaolinite recovery factor versus initial kaolinite fraction cannot be explained without rigorous mathematical modelling. The model must include mass balance equation for suspended, attached, strained and re-attached particles along with the kinetics equations for mass exchange between the rock and fluid (Bedrikovetsky, 1993, 2011). Yet, this fines migration modelling is a subject of a separate work.

The effects of illite, chlorite and other clays causing fines migration on reservoir formation damage, could be different than those of kaolinite. The results depend on particle shape, zeta-potential between the particle and brine, clay placing on the rock surface among other factors. However, studies on these minerals can be performed using the methodology developed in the present work.

Very similar permeability damage processes occur in other areas of gas and oil production. Behaviour of gas bubbles in water and oil is also dominated by bubbles straining in pores and consequent permeability reduction. CO2 bubble-plugging of thin pore throats yields significant permeability damage (Farajzadeh et al., 2008, 2009). Gas bubbles decrease well productivity in foamy-oil fields.

6. Conclusions

Laboratory study of fines migration in rocks with different kaolinite-contents allows drawing the following conclusions:

1. Stable and reproducible permeability during long-term flows in the unconsolidated sand-packs validates the proposed methodology of artificial rock preparation.
2. The higher the kaolinite fraction in the core, the lower is the undamaged (initial) permeability. This effect is explained by coating of the pore throats by attached kaolinite particles under high kaolinite concentration in the rock.
3. Permeability decrease after fresh water injection (the difference between the initial and final permeabilities) in rocks with high kaolinite concentration is higher than that under small kaolinite concentration. This is explained by larger pore radii associated with lower kaolinite concentrations, yielding lower straining intensity and, consequently, lower permeability damage.
4. During the sequential decrease in injected salinity, the permeability varies non-monotonically in low-kaolinite cores, while it only decreases in cores with high kaolinite content. This is explained by re-attachment of already mobilized fines, yielding a reduced concentration of suspended fines which consequently decreases straining rates. Monotonic permeability decline in high-kaolinite cores is a consequence of thinner pore throats which results in intensive straining.

   The permeability increase occurs under stronger electrostatic attraction at high salinities, where the re-attachment is more intensive. At low salinities, the reattachment probability is low and so permeability increase from particle detachment is dominated by permeability decline due to straining.
5. The percentage of kaolinite recovered during a decrease of injected fluid salinity from 0.6 Mol/L to deionised water, varies from 0.2% to 1.6%.

Acknowledgements

We thank Genna Petho, Robin Pronk and Suparit Tangparitkul (Uni of Adelaide) for contribution to the laboratory work. Yulong Yang and Larissa Chequer (Uni of Adelaide) are gratefully acknowledged for theoretical discussions and physics insights.

References

Aleksandrov, A.A., Dzhuraeva, E.V., Utenkov, V.F., 2012. Viscosity of aqueous solutions of sodium chloride. High Temp. 50 (3), 354–358.
Al Sayari, S.S., 2009. The Influence of Wettability and Carbon Dioxide Injection on Hydrocarbon Recovery. Department of Earth Science and Engineering, Imperial College London.
Assef, Y., Arab, D., Pourafshary, P., 2014. Application of nanofluid to control fines migration to improve the performance of low salinity water flooding and alkaline flooding. J. Petrol. Sci. Eng. 124, 331–340.
Badalyan, A., You, Z., Aji, K., Bedrikovetsky, P., Carageorgos, T., Zeinijahromi, A., 2014. Size exclusion deep bed filtration: experimental and modelling uncertainties. Rev. Sci. Instrum. 85 (015111), 1–13.
Barenblatt, G.I., Entov, V.M., Ryzhik, V.M., 1989. Theory of Fluid Flows through Natural Rocks. Kluwer, Dordrecht.
Bedrikovetsky, P.G., 1993. Mathematical Theory of Oil & Gas Recovery. Kluwer Academic Publishers, London-Boston-Dordrecht, 600 pp.
Bedrikovetsky, P., Siqueira, F.D., Furtado, C., de Souza, A.L.S., 2011. Modified particle detachment model for colloidal transport in porous media. J. Transp. Porous Media 86, 353–383.
Bergendahl, J., Grasso, D., 2000. Prediction of colloid detachment in a model porous media: hydrodynamics. Chem. Eng. Sci. 55, 1523–1532.
Byrne, M.T., Waggoner, S.M., 2009. Fines migration in a high temperature gas reservoir - laboratory simulation and implications for completion design. In: SPE-121897. SPE European Formation Damage Conference Held in Scheveningen, the Netherland, 27e29 May.
Chalk, P., Gooding, N., Hutten, S., You, Z., Bedrikovetsky, P., 2012. Pore size distribution from challenge coreflood testing by colloidal flow. J. Chem. Eng. Res. Des. V. 90 (1), 63–77.
Chiu, T.F., Shackelford, C.D., 1998. Unsaturated hydraulic conductivity of compacted sand-kaolin mixtures. J. Geotech. Geoenviron. Eng. 160–170.
Civan, F., 2007. Reservoir Formation Damage: Fundamentals, Modeling, Assessment, and Mitigation. Gulf Professional Publishing, Elsevier, Burlington, USA.
Derjaguin, B.V., Landau, L.D., 1941. Theory of the stability of strongly charged lyophobic sols and of the adhesion of strongly charged particles in solutions of electrolytes. Acta Physicochim. URSS 14 (6), 633–662.
Elimelech, M., Gregory, J., Jia, X., Williams, R., 1995. Particle Deposition and Aggregartion: Measurement, Modelling, and Simulation. Butterworth-Heinemann, New-York, USA.
Farajzadeh, R., Krastev, R., Zitha, P.L., 2008. Foam film permeability: theory and experiment. Adv. colloid interface Sci. 137 (1), 27–44.
Farajzadeh, R., Zitha, P.L., Bruining, J., 2009. Enhanced mass transfer of CO2 into water: experiment and modeling. Ind. Eng. Chem. Res. 48 (13), 6423–6431.
Farajzadeh, R., Lotfollahi, M., Lake, L.W., 2016. Simultaneous sorption and mechanical entrapment during polymer flow through porous media. Water Resour. Res. 52 (3), 2279–2298.
Galal, S.K., Elgibaly, A.A., Elsayed, S.K., 2016. Formation damage due to fines migration and its remedial methods. Egypt. J. Petrol. 25, 515–524.
Goldman, A.J., Cox, R.G., Brenner, H., 1967. Slow viscous motion of a sphere parallel to a plane wall - II Couette flow. Chem. Eng. Sci. 22, 653–660.
Gregory, J., 1981. Approximate expressions for retarded van der Waals interactions. J. Colloid Interface Sci. 83 (1), 138–145.
Gruesbeck, C., Collins, R.E., 1982. Entrainment and deposition of fine particles in porous media. Soc. Petrol. Eng. J. Dec. 847–856.
Guo, Z., Hussain, F., Cinar, Y., 2015. Permeability variation associated with fines

production from anthracite coal during water injection. Int. J. Coal Geol. 147–148, 46–57.
Guo, Z., Hussain, F., Cinar, Y., 2016. Physical and analytical modelling of permeability damage in bituminous coal caused by fines migration during water production. J. Nat. Gas Sci. Eng. 35, 331–346.
Habibi, A., Ahmadi, M., Pourafshary, P., Ayatollahi, S., Al-Wahaibi, Y., 2013. Reduction of fines migration by nanofluids injection: an experimental study. SPE J. Apr. 309–318.
Haug, M.D., Wong, L.C., 1992. Impact of molding water content on hydraulic conductivity of compacted sand-bentonite. Can. Geotech. J. 29, 253–262.
Kalantariasl, A., Bedrikovetsky, P., 2014. Stabilization of external filter cake by colloidal forces in "Well-Reservoir" system. J. Ind. Eng. Chem. Res. 53, 930–944.
Kalantariasl, A., Farajzadeh, R., You, Z., 2015. Non-uniform external filter cake in long injection wells. J. Ind. Eng. Chem. Res. 54, 3051–3061.
Kestin, J., Khalifa, H.E., Correia, R.J., 1981. Tables of the dynamic and kinematic viscosity of aqueous NaCl solutions in the temperature range 20-150 °C and the pressure range 0.1-35 MPa. J. Phys. Chem. Ref. Data 10 (1), 71–87.
Khilar, K.C., Fogler, H.S., 1998. Migration of Fines in Porous Media. Kluwer Academic Publishers, Dordrecht.
Kia, S.F., Fogler, H.S., Reed, M.G., Vaidya, R.N., 1987. Effect of salt composition on clay release in Berea sandstones. SPE Prod. Eng. 277–283.
Lever, A., Dawe, R.A., 1984. Water-sensitivity and migration of fines in the Hopeman sandstone (Scotland). J. Petrol. Geol. 7, 97–107.
Mohan, K.K., Fogler, H.S., 1997. Colloidally induced smectitic fines migration: existence of microquakes. AIChE J. 43 (3), 565–576.
Mullins, C.E., Panayiotopoulos, K.P., 1984. The strength of unsaturated mixtures of sand and kaolin and the concept of effective stress. School of agriculture, Aristotelian university. J. Soil Sci. 35, 459–468.
Rosenbrand, E., Fabricius, I.L., Yuan, H., 2013. Thermally induced permeability reduction due to particle migration in sandstone: the effect of temperature on kaolinite mobilisation and migration. In: Thirty-Eight Workshop on Geothermal Reservoir Engineering. Stanford University, Stanford, California, USA.
Rosenbrand, E., Haugwitz, C., Jacobsen, P.S.M., Kjoller, C., Fabricius, I.L., 2014. The effect of hot water injection on sandstone permeability. Geothermics 50, 155–166.
Ruckenstein, E., Prieve, D.C., 1976. Adsorption and desorption of particles and their chromatographic separation. Am. Inst. Chem. Eng. J. 22 (2), 276–283.
Schembre, K.M., Kovscek, A.R., 2005. Mechanism of formation damage at elevated temperature. J. Energy Resour. Technol. 127, 171–180.
Shani, C., Weisbrod, N., Yakirevich, A., 1998. Colloid transport through saturated sand columns: influence of physical and chemical surface properties on deposition. Colloids Surf. A Physicochem. Eng. Asp. 316 (1–3), 142–150.
Torkzaban, S., Bradford, S.A., 2016. Critical role of surface roughness on colloid retention and release in porous media. Water Res. 88, 274–284.
Valdya, R.N., Fogler, H.S., 1990. Fines migration and formation damage: influence of pH and ion exchange. SPE Pet. Eng. 7 (4), 325–330.
van Oort, E., van Velzen, J.F.G., Leerlooijer, K., 1993. Impairment by suspended solids invasion: testing and prediction. SPE Prod. Facil. 178–184.
Yuan, B., Moghanloo, R.G., Pattamasingh, P., 2015. Applying method of characteristics to study utilization of nanoparticles to reduce fines migration in deepwater reservoirs. SPE 174192.
Yuan, B., Moghanloo, R., Zheng, D., 2016. Analytical evaluation of Nanoparticle application to mitigate fines migration in porous media. SPE J 21 (6).
Zeinijahromi, A., Al-Jassasi, H., Begg, S., Bedrikovetski, P., 2015. Improving sweep efficiency of edge-water drive reservoirs using induced formation damage. J. Petrol. Sci. Eng. 130, 123–127.
Zeinijahromi, A., Farajzadeh, R., Bruining, J., 2016. Effect of fines migration on oil–water relative permeability during two-phase flow in porous media. Fuel 176, 222–236.

3.2 Fines Stabilization by Ca Ions and Its Effect on LSW Injection

Al-Sarihi, A., **Russell, T.**, Bedrikovetsky, P., Zeinijahromi, A.

Energy & Fuels 2019 33 (11), 10775-10786

Statement of Authorship

Title of Paper	Fines Stabilization by Ca Ions and Its Effect on LSW Injection
Publication Status	☑ Published ☐ Accepted for Publication ☐ Submitted for Publication ☐ Unpublished and Unsubmitted w ork w ritten in manuscript style
Publication Details	A. Al-Sarihi, T. Russell, P. Bedrikovetsky, and A. Zeinijahromi, Fines Stabilization by Ca Ions and Its Effect on LSW Injection, Energy & Fuels 2019 33 (11), 10775-10786

Principal Author

Name of Principal Author (Candidate)	Thomas Russell		
Contribution to the Paper	Performed laboratory tests, analysed data, contributed to writing		
Overall percentage (%)	40%		
Certification:	This paper reports on original research I conducted during the period of my Higher Degree by Research candidature and is not subject to any obligations or contractual agreements with a third party that would constrain its inclusion in this thesis. I am the primary author of this paper.		
Signature		Date	16/02/2021

Co-Author Contributions

By signing the Statement of Authorship, each author certifies that:

i. the candidate's stated contribution to the publication is accurate (as detailed above);

ii. permission is granted for the candidate in include the publication in the thesis; and

iii. the sum of all co-author contributions is equal to 100% less the candidate's stated contribution.

Name of Co-Author	Abdullah Al-Sarihi		
Contribution to the Paper	Performed laboratory tests, analysed data, contributed to writing		
Signature		Date	16/02/2021

Name of Co-Author	Pavel Bedrikovetsky		
Contribution to the Paper	Analysed data, contributed to writing		
Signature		Date	17/02/2021

Please cut and paste additional co-author panels here as required.

Name of Co-Author	Abbas Zeinijahromi		
Contribution to the Paper	Analysed data, contributed to writing		
Signature		Date	

energy&fuels

Article

Cite This: Energy Fuels 2019, 33, 10775−10786

pubs.acs.org/EF

Fines Stabilization by Ca Ions and Its Effect on LSW Injection

A. Al-Sarihi,* T. Russell, P. Bedrikovetsky, and A. Zeinijahromi

Australian School of Petroleum, The University of Adelaide, Adelaide, SA 5005, Australia

ABSTRACT: Fines mobilization during the injection of low-salinity water yields a decrease in well injectivity and productivity but may cause an increase in the reservoir sweep efficiency during oilfield waterflooding. We investigate the stability of clay fines under the combined alteration of Na and Ca concentrations. Consequent injections of Ca and Na solutions in natural and engineered cores intercalated by deionized water (DIW) injections have been performed. Fines migration has not been observed during DIW injection after preflush by $CaCl_2$ solution; further consequent injection of NaCl and DIW yields a significant fines mobilization and permeability decline. The tests demonstrate a strong hysteretic behavior of mutual adsorption−desorption of Ca and Na cations on the reservoir clays and rock. The same phenomena have been observed in the presence of residual oil, where fines migration has been accompanied by incremental oil production.

INTRODUCTION

During fluid flow in subsurface reservoirs, small, naturally occurring particles can detach from the internal surface of the rock and become suspended in the flow.[1−4] The resulting suspension flow forces particles through narrow crevices in the pore space, often resulting in particle capture, referred to here as straining. Straining restricts fluid flow through the pore spaces, causing a decrease in the rock permeability. The process in its entirety is referred to as fines migration and can have both positive and negative impacts on many industrial processes.[1,2,5]

An understanding of fines migration has led to the insight that the permeability decline often originates in the detachment of in situ particles. The enhancement or mitigation of fines migration thus relies on controlling the conditions of particle detachment. Many studies have demonstrated that high fluid velocities,[6] low fluid salinities,[3] and high fluid pH[7] are all effective at detaching particles. These factors are the primary explanation for why fines migration is often discussed in the context of low-salinity (LS) waterflooding projects, as these projects create conditions that favor particle detachment.

Several field studies have demonstrated that the permeability decline resulting from fines migration can have severe detrimental effects on injectivity[8,9] and productivity[10,11] during petroleum operations. Many operators will thus seek to inhibit fines detachment during these projects and often aim to increase salt concentrations in the injected water as a means to achieve this.

The role of fines migration during low-salinity waterflooding is not simply as a detriment to injection and production rates. While a myriad of mechanisms have been proposed to demonstrate why low-salinity water increases oil recovery,[12−26] several studies have shown that fines migration can act as the mechanism for improved oil recovery during low-salinity waterflooding (LSW).[27−29] Initially, the electrostatic forces attach the clay particles on the rock surface due to the abundance of salt ions that lower ζ-potential and the repulsive forces between clay fines and the rock surface, maintaining an equilibrium between the torques of electrostatic and drag (viscous) forces. When low-salinity brine is injected into porous media, this equilibrium is disturbed and, as a result, clay particles are detached and mobilized by the drag forces caused by the displacing phase.[1,12,30−35] Migration of fines leads to the aforementioned fines straining in the rock. As a result, water-permeable channels are plugged and the flow is directed toward unswept zones where residual oil is trapped.[27,30,36−43] This microscale flux diversion causes a decline in water relative permeability and an increase in pressure drop, which improves microscopic sweep efficiency by mobility control, resulting in enhanced oil recovery.[5,43−46]

In contrast with this enhancement of microscopic sweep efficiency, some simulation studies have demonstrated that by progressively damaging the fastest swept layers, fines migration can increase the reservoir scale sweep efficiency, thus unlocking additional reserves.[45]

Due to the demonstrated effectiveness of fines migration in increasing both the microscopic and macroscopic sweep efficiencies, many low-salinity waterflooding projects aim to maximize particle detachment. Typically, this is achieved through minimization of the injected fluid salinity or by combining the low-salinity flood with alkaline solutions.

Despite the wealth of research on fines migration and the advent of new technologies designed to enhance or reduce it, several open problems remain regarding the nature of particle detachment. For instance, several studies have demonstrated that when different ions are used during initial core saturation, the cores show variable sensitivity to low-salinity water injection.[47−49] These tests showed that decreasing the salinity of a $CaCl_2$ solution results in negligible changes in the permeability, whereas the same salinity decrease with a NaCl solution results in a significant permeability decline. Thus, the initiation of particle detachment is highly dependent on the cations that the rock has been exposed to previously, not solely on those in the solution during injection. Most injected fluids for low-salinity waterflooding projects are still designed on the basis that particle detachment is governed entirely by the

Received: August 12, 2019
Revised: October 15, 2019
Published: October 28, 2019

DOI: 10.1021/acs.energyfuels.9b02683
Energy Fuels 2019, 33, 10775−10786

injected fluid. Thus, maximizing the benefit of these programmes by carefully controlling the ion composition will require an understanding of the impact of the observed history-dependent particle detachment.

The origin of this phenomenon as well as its dependence on ion valence and type remains unresolved.

In this work, we perform an experimental study to understand the phenomenon of clay fines stability under the environment of Ca and Na cations. Several coreflooding tests with $CaCl_2$ and NaCl solutions, both in single and two phase, are performed to investigate this phenomenon. We combine two of the single-phase tests with ion chromatography measurements to investigate the underlying ion exchange processes governing particle detachment. Such an investigation into the underlying processes during fines migration is not currently available in the literature. Based on the results of the tests, hysteresis in Ca^{2+} sorption is identified as the cause of the history-dependent sensitivity.

Despite the intensive current research on the influence of ion type on wettability alteration,[2,17−23] a comprehensive study of the impact of this phenomenon on oil recovery is currently unavailable. In this study, we perform two-phase tests with nonpolar oil to avoid the impact of wettability changes and study the effect that ion-dependent fines migration can have on oil recovery.

LABORATORY STUDY

Materials. *Natural Core Plugs.* Three outcrop Berea sandstone core plugs were used in this study. One was used for the single-phase test and the rest for the two-phase tests. All cores were cut using a table saw cooled with a 3% KCl brine. Table 1 shows the properties of these cores.

Table 1. Properties of Berea Rock Samples

	Berea 1	Berea 2	Berea 3
permeability (mD)	120	40	21
porosity	0.19	0.19	0.19
length (cm)	5.05	12.10	12.05
diameter (cm)	3.80	3.80	3.80

Synthetic Core Plugs. Unconsolidated, artificial cores were prepared as part of this study to compare the effect of low-salinity water on clay particle (kaolinite) mobilization with natural core plugs. Artificially constructing cores results in a more homogeneous and reproducible rock with both controlled and consistent properties such as clay content and permeability.

The cores comprised silica sand and kaolinite. The sand used in this study has a silica content of >99% (brand 50N, SIBELCO, Australia). The sand was first sieved to constrain particle size, with a resulting mean diameter of 123 μm. Following sieving, the sand was washed sequentially in hexane, acetone, deionized water (DIW), 0.5 M HCl, and then deionized water. Washing of the sand in the last stage was repeated until the pH of the supernatant water returned to the pH of the natural deionized water. The sand was then dried at 60 °C for 24 h before use.

Analytical-grade kaolinite powder (Sigma-Aldrich, Australia) was used as the fines content of the cores. The mean diameter of the kaolinite was 2.064 μm. The kaolinite powder was first dried at 60 °C for 24 h before use.

The sand and kaolinite were first mixed dry and then suspended in 0.6 mol/L $CaCl_2$ solution before being placed into a Viton sleeve, which was then installed into a Hassler-type coreholder. The wet packing was performed under a side overburden pressure of 1000 psi.

A range of kaolinite mass content from 5 to 10% was chosen to emulate the kaolinite content of the Berea cores.

Brine. Aqueous solutions were prepared by dissolving NaCl (ChemSupply, 99.7% purity) or $CaCl_2$ (ChemSupply, 99% purity) into Milli-Q deionized water. All injected solutions were deaerated using a vacuum pump for at least 1 h to prevent dissolved air from entering the cores. All injected solutions had ionic strengths ranging between 0.6 M and that of deionized water. Salt concentrations given by M refer to the ionic strength of the solution in mol/L.

Oil. Mineral nonpolar paraffin oil (Light 15 LR from ChemSupply) with a viscosity of 20 cP at 25 °C was used in the two-phase tests.

Methodology. Figure 1 shows both a schematic and a photograph of the laboratory setup used in the experiment. The fluid was supplied by the pump (7) through the fluid cylinders (8−10) into the coreholder (3). Effluent samples were collected in a carrousel (21), and differential pressure was measured using differential pressure transmitters (14,17). Detailed specifications of the equipment used are provided in the caption of the figure.

Four single-phase and two two-phase tests were performed in this study. Three of the single-phase tests were on unconsolidated cores and one on a Berea outcrop core (Berea 1). Both two-phase tests were done on Berea cores.

Prior to each test, the cores were dried at 60 °C for at least 24 h, deaerated under vacuum for the same period, and then saturated with 0.6 M $CaCl_2$ under vacuum. The cores were then installed in a Hassler-type coreholder, and a confining pressure of 1000 psi was applied to prevent annular flow between the core and the surrounding Viton sleeve. A backpressure of 500 psi was applied to keep a constant pressure at the outlet.

All tests were performed at constant room temperature.

Single-Phase Coreflooding Tests. The single-phase tests were performed to study the influence of solution ionic strength and injected composition on fines detachment and permeability.

Two unconsolidated cores of differing clay mass contents (7 and 10%) were used to test the influence of injected composition on fines detachment. Both pressure drop and outlet fines concentration measurements were used to detect the detachment and straining of particles. Different clay contents were used to provide more generality to the test results. Each test comprised saturating the cores with high-salinity $CaCl_2$ (0.6 M) and then injecting $CaCl_2$ solutions of progressively decreasing salinity to test the ionic strength dependence of particle stability with $CaCl_2$ solutions. This sequence ended with deionized water to identify whether the $CaCl_2$ had an influence on particle detachment even when not present in the injected solution. This was then followed with a 0.6 M high-salinity NaCl injection and then another deionized water injection. These were performed to determine whether the sensitivity of the cores to low-salinity water could be restored after the exposure to $CaCl_2$.

A third test on an unconsolidated 5% clay content core was performed using a similar procedure. One difference is that the sequential decrease in $CaCl_2$ ionic strength was substituted

DOI: 10.1021/acs.energyfuels.9b02683
Energy Fuels 2019, 33, 10775−10786

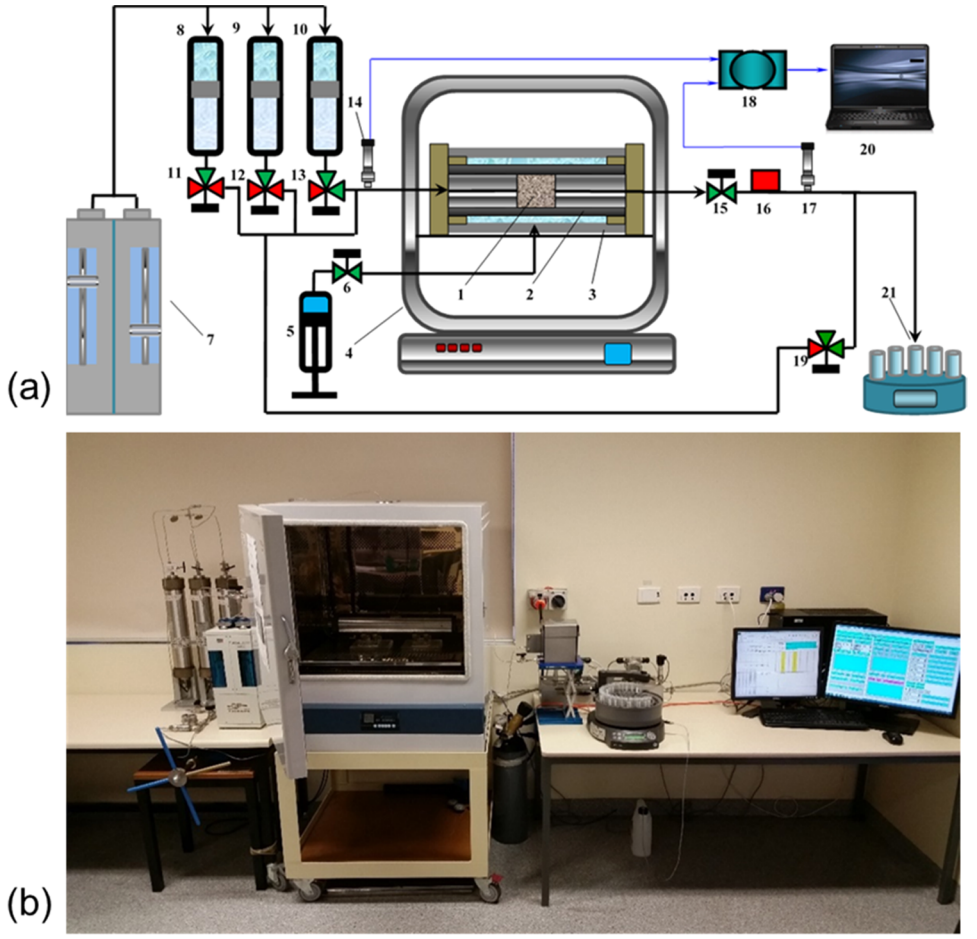

Figure 1. Laboratory setup used for two-phase coreflooding tests: (a) schematic and (b) photograph. (1) Core plug, (2) Viton sleeve, (3) Hassler-type coreholder, (4) oven to keep the temperature constant, (5) manual HiP piston pressure generator, (6) port switching valve, (7) Quizix Q6000 precision pump for two-phase tests (Prep-36, Scientific Systems pump used in the single-phase tests), (8−10) oil transfer vessels, (11−13) port switching valves, (14,17) absolute pressure transmitters, (15) port switching valve, (16) backpressure regulator, (18) ADAM-4019+ inlet data acquisition module, (19) port switching valve, (20) PC-based data acquisition system, and (21) GE Healthcare Frac-920 fractional collector.

with a direct decrease from high-salinity $CaCl_2$ to deionized water. In addition, ion chromatography measurements were performed on outlet samples to determine the Na^+ and Ca^{2+} concentrations separately. This test thus provided additional insight into the ion exchange mechanisms, as well as detecting fines detachment.

The last single-phase test was performed in the same manner as the 5% clay unconsolidated core but on a Berea outcrop core. While potentially less homogeneous, the Berea core is representative of many petroleum sandstone reservoirs and thus allows the results to be readily interpreted in the context of these systems.

During the single-phase tests, the brine solution was injected with a constant flow rate into the cores using a high-accuracy pump (Prep-36, Scientific Systems). The differential pressure across the core was measured using a series of four Yokogawa differential pressure transmitters. Having multiple differential pressure transmitters of varying sensitivities allowed the pressure across the core to be measured accurately over a wide range of differential pressures. Samples were collected at the outlet using a GE Healthcare Frac-920 fractional collector. All samples were processed using a POLA-2000 particle counter to determine the particle concentration and a Metrohm 930 ion chromatograph to determine the concentration of calcium and sodium ions.

The procedure of the single-phase test was as follows:

1. Injection of 0.6 M $CaCl_2$ at a low flow rate of 0.2 mL/min (superficial velocity 2.93×10^{-6} m/s) for a period of 24 h to achieve stable permeability. A lower flow rate is used to avoid particle detachment during permeability stabilization.
2. Sequential injection of 0.6 M $CaCl_2$ (and 0.3, 0.1, 0.05, 0.01, and 0.001 M $CaCl_2$ for the first two tests) and then deionized water at the test flow rate of 2 mL/min (superficial velocity 2.93×10^{-5} m/s). Each injection stage was performed until permeability had stabilized.
3. Injection of 0.6 M NaCl and then deionized water at the test flow rate of 2 mL/min (superficial velocity 2.93×10^{-5} m/s). Each injection stage was performed until permeability had stabilized.

Two-Phase Coreflooding Tests. The two-phase tests were conducted to determine the effect of calcium and sodium ions, both at high and low salinities, on the residual oil saturation (S_{or}).

The two-phase tests were performed on the Berea 2 and 3 cores.

The injected solutions were supplied using a pulse-free syringe pump (Quizix Q6000 precision pump). A dome backpressure regulator, supported by a nitrogen gas cylinder,

DOI: 10.1021/acs.energyfuels.9b02683
Energy Fuels 2019, 33, 10775−10786

was used to maintain a constant outlet pressure of 500 psi. The pressure difference between the inlet and the outlet of the core was measured by Yokogawa (low pressure range) and Keller (high pressure range) pressure transducers. Darcy's law was applied to calculate the permeability of each core at the stabilized pressure drop along the cores. Outlet samples were collected in the same way as in the single-phase tests. Oil and water volumes were determined from the volumetric increments provided on the outlet samples. The particle concentration of the aqueous phase was measured using a POLA-2000 particle counter, with oil being removed from samples where necessary by syringe suction after centrifugation.

The procedure of the two-phase tests was as follows:

1. The core permeability was measured by injecting HS (high-salinity) 0.6 M $CaCl_2$ solution into the core at a constant rate of 0.2 ml/min (superficial velocity 2.93×10^{-6} m/s). This flow rate was used for the remainder of the test.
2. The first drainage displacement was performed by injecting nonpolar oil at the same constant rate until no more water was produced from the cores and the pressure drop stabilized, i.e., until the initial water saturation S_{wi} was obtained.
3. High-salinity waterflooding (HSW) was then performed by displacing oil with HS 0.6 M $CaCl_2$ brine until oil production stopped, indicating that the core was at residual oil saturation, S_{or}.
4. Another drainage stage was then performed to achieve the same initial condition (S_{wi}) before low-salinity waterflooding (LSW) took place by injecting low-salinity (LS) 0.05 M $CaCl_2$ to displace the oil.
5. Low-salinity waterflooding was then performed by injecting 0.05 M ionic strength $CaCl_2$ to displace the oil phase until residual oil was achieved.
6. Tertiary waterflooding with stepwise decreasing salinity of $CaCl_2$ brine was performed using solutions with ionic strengths of 0.025, 0.01 M, and deionized water (DIW). This step is important to provide insights into the impact of low-salinity $CaCl_2$ solutions on fines migration and oil recovery. Each injection continued until the pressure drop stabilized.
7. A 0.05 M NaCl solution was then injected followed by a DIW injection to investigate any effect of Na^+ ions on detaching Ca^{2+} and fines migration. Again, each stage was terminated only after the pressure drop had stabilized.

The oil and water volumes of all of the effluent samples as well as clay particle concentrations were measured immediately after sampling.

Two drainages have been performed to restore the S_{wi} conditions before LSW injection. The aim is to compare HSW and LSW injections for the identical reservoirs. Hysteresis between first and second drainage displacements can be significant. However, usually the difference between S_{wi} and K_{rowi} after first and second drainage displacements is insignificant.[28,29] Table 3 shows very close agreement between the S_{wi} and K_{rowi} values for Berea 3 core and reasonable agreement for the Berea 2.

X-ray Diffraction (XRD) Study. To complement the coreflooding tests done on the Berea cores, an XRD study was performed on a cutting removed from the Berea core used in the single-phase tests. The XRD analysis was conducted qualitatively using a Bruker D8 ADVANCE Powder X-ray diffractometer with a Cu-radiation source. The data was processed using Bruker DIFFRAC.EVA software and Crystallography Open Database reference patterns to identify mineral phases. The quantification of the mineralogy was calculated against an internal standard of zinc oxide at 10% using RockJock software.

EXPERIMENTAL RESULTS

Single-Phase Coreflooding Tests. The results of the tests on the 7 and 10% clay content cores are shown in Figures 2 and 3,

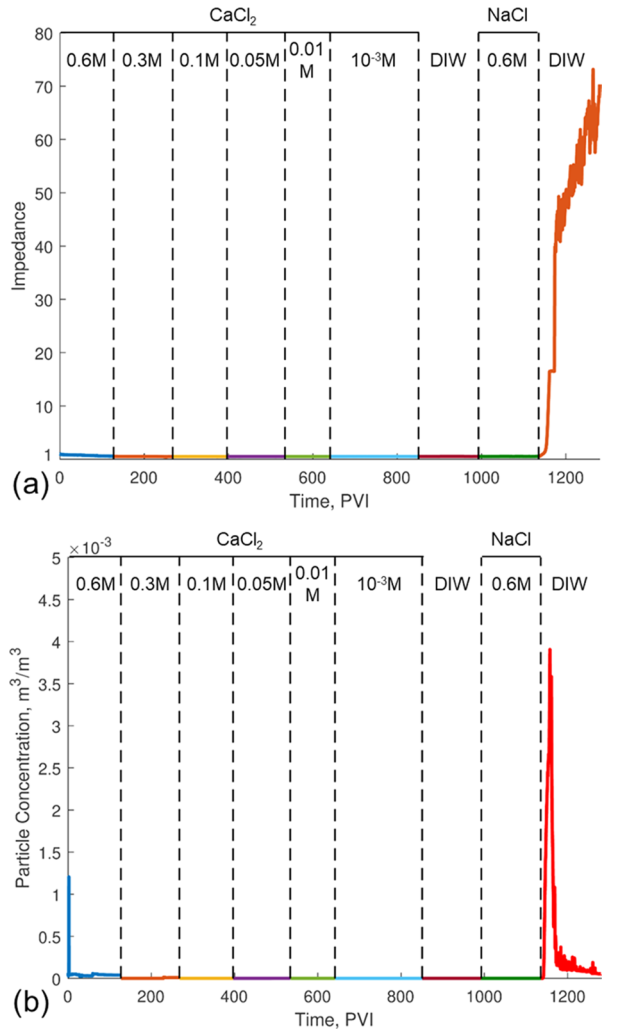

Figure 2. Single-phase test on unconsolidated sand-kaolinite core (7% kaolinite w/w, k = 286 mD): (a) normalized permeability, (b) outlet particle concentration.

respectively. Changes to the pressure drop of the cores are presented in a dimensionless form as the impedance, J

$$J = \frac{\Delta p}{\Delta p_0}$$

where Δp_0 is the stabilized initial pressure drop measured at the start of the test.

Unconsolidated Cores. Figure 2 shows the results from the test on the 7% clay content unconsolidated core. The undamaged permeability of the core was 286 mD, and the porosity was 0.386. Each injection stage lasted for at least 180 PVI. During the injection

DOI: 10.1021/acs.energyfuels.9b02683
Energy Fuels 2019, 33, 10775−10786

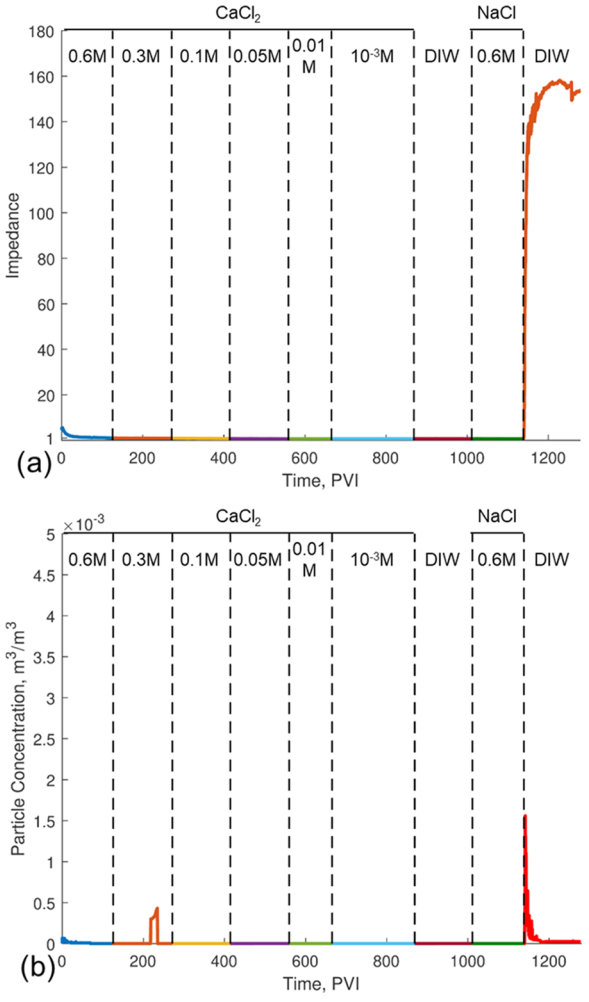

Figure 3. Single-phase test on unconsolidated sand-kaolinite core (10% kaolinite w/w, k = 149 mD): (a) normalized permeability, (b) outlet particle concentration.

of $CaCl_2$ solutions of decreasing salinity, including the first DIW injection stage, the pressure drop remains relatively constant. In addition to the negligible outlet particle concentration, this indicates a lack of fines detachment. A similar response is noted during the injection of 0.6 M NaCl, suggesting a lack of particle detachment. During the second deionized water injection, a significant rise in pressure drop and outlet particle concentration was observed, indicating that a substantial number of particles were detached due to the change in injected solution. The final value of impedance was 65.6, corresponding to a permeability of 4.36 mD.

Figure 3 presents the results from the next single-phase test, performed on the 10% clay unconsolidated core. The undamaged permeability of the core was 149 mD, and the porosity was 0.385. A relatively constant pressure drop and negligible outlet particle concentration during the $CaCl_2$ and the first DIW stages indicate no fines detachment during these injections, similar to the previous test. There is a noticeable exception in the outlet concentration during the 0.3 M $CaCl_2$ injection. This can be attributed to a slight desorption of Ca^{2+} ions, which leads to some attached particles being prone to detachment by the drag force. This persists during the NaCl injection. Fines migration is detected during the second deionized water injection, with a final stabilized impedance of 152, corresponding to a permeability of 0.98 mD.

Figure 4 presents the results of the 5% clay content unconsolidated core, with the additional ion chromatography results shown in Figure 4c. The initial permeability of the core was 537 mD, and the porosity was 0.366. A minor increase in the pressure drop is noted during the first DIW injection, suggesting that some particles were detached. The NaCl injection shows no impact on the pressure drop. The second injection of DIW again shows indications of fines migration, with an increase of impedance to 1.7, with a final permeability of 358 mD.

The ion chromatography results in Figure 4c largely show that the injected solutions are being produced at the outlet. A careful examination of the Ca^{2+} concentration at the beginning of the NaCl injection, shown in Figure 4d, shows a noticeable peak in Ca^{2+} concentration, indicating a release of calcium ions during this injection stage that had not been desorbed during the first deionized water injection.

Berea Core. The results of the XRD study performed on Berea core 1 are presented in Table 2.

The results of the single-phase test on Berea 1 are presented in Figure 5. The initial permeability of the core was 120 mD. Qualitatively similar results are observed for both the pressure drop and outlet fines concentration, with indications of fines migration present only during the DIW injection after the NaCl stage. The final value of impedance was 3968, corresponding to a permeability of 0.03024 mD.

While showing some variation, the ion chromatography results again largely show the production of the injected solutions. The highlight of the NaCl injection stage shown in Figure 5d shows a significant peak in the Ca^{2+} concentration. This is in agreement with the 5% unconsolidated core test, indicating that the NaCl injection results in a desorption of some residual Ca^{2+} ions in the core.

Two-Phase Coreflooding Tests. In the two-phase coreflooding tests, the HSW and LSW effects of $CaCl_2$ brine on fines migration and oil recovery were compared in the secondary waterflooding processes (HSW after the first drainage and LSW after the second drainage) as well as in the tertiary waterflooding mode. To reach similar initial saturation conditions before HSW and LSW, oil was injected into the cores until the pressure drop stabilized at similar magnitudes for the first and second drainage displacements and no more oil was produced.

Berea 2. Figure 6a shows the pressure drop for these two oil displacements for Berea 2. In the first drainage displacement of HS $CaCl_2$ brine by nonpolar oil, the pressure drop increased to ∼56 psi before the breakthrough and then decreased and stabilized at ∼30 psi after injecting 8 pore volumes. In the second drainage displacement, the pressure drop increased to ∼39 psi before the breakthrough and then stabilized at ∼30 psi as well. The initial water saturations were 0.16 and 0.21 for the first and second drainages, respectively. The oil end-point relative permeabilities, K_{rowi}, are 0.97 and 0.90, respectively.

Figure 6b shows the impedance and accumulated oil production for the secondary waterflooding by HS and LS $CaCl_2$ solutions. Each stage involved injecting 8 PV of the solution after the drainage displacement. The injection was stopped when the pressure drop stabilized and when no more oil was produced. At the start of the HSW, the initial pressure drop was ∼28 psi. The impedance increased to ∼2.1 before the breakthrough and then it dropped and stabilized at ∼1.7. In the secondary LSW, the initial pressure drop was ∼27 psi and the impedance increased to ∼2.4 before breakthrough after which it dropped and stabilized at ∼2. There is a slight difference in both impedance and oil recovery between the HSW and the LSW in the secondary mode. Oil production was 0.34 PV for the HSW and 0.38 for the LSW, as shown in Figure 6b, which could be due to the release of some fine particles during the LSW that slightly improved oil recovery. However, residual oil saturation for both displacements is 0.49, as shown in Table 3, which indicates that there is no significant effect of fines migration on oil recovery, unlike in the tertiary injection mode as discussed below.

Tertiary waterflooding was conducted to investigate the effect of $CaCl_2$ and NaCl brine ionic strength on fines migration and incremental oil recovery. The results of sequentially decreasing the injected $CaCl_2$ salinity down to DIW show no change in impedance (stable at ∼1 with an initial pressure drop of ∼27). Cumulative oil recovery also remains unaltered as shown in Figure 7a. The tertiary waterflooding was continued by injecting 0.05 M NaCl followed by DIW. Figure 7a shows that impedance increased significantly after the

DOI: 10.1021/acs.energyfuels.9b02683
Energy Fuels 2019, 33, 10775−10786

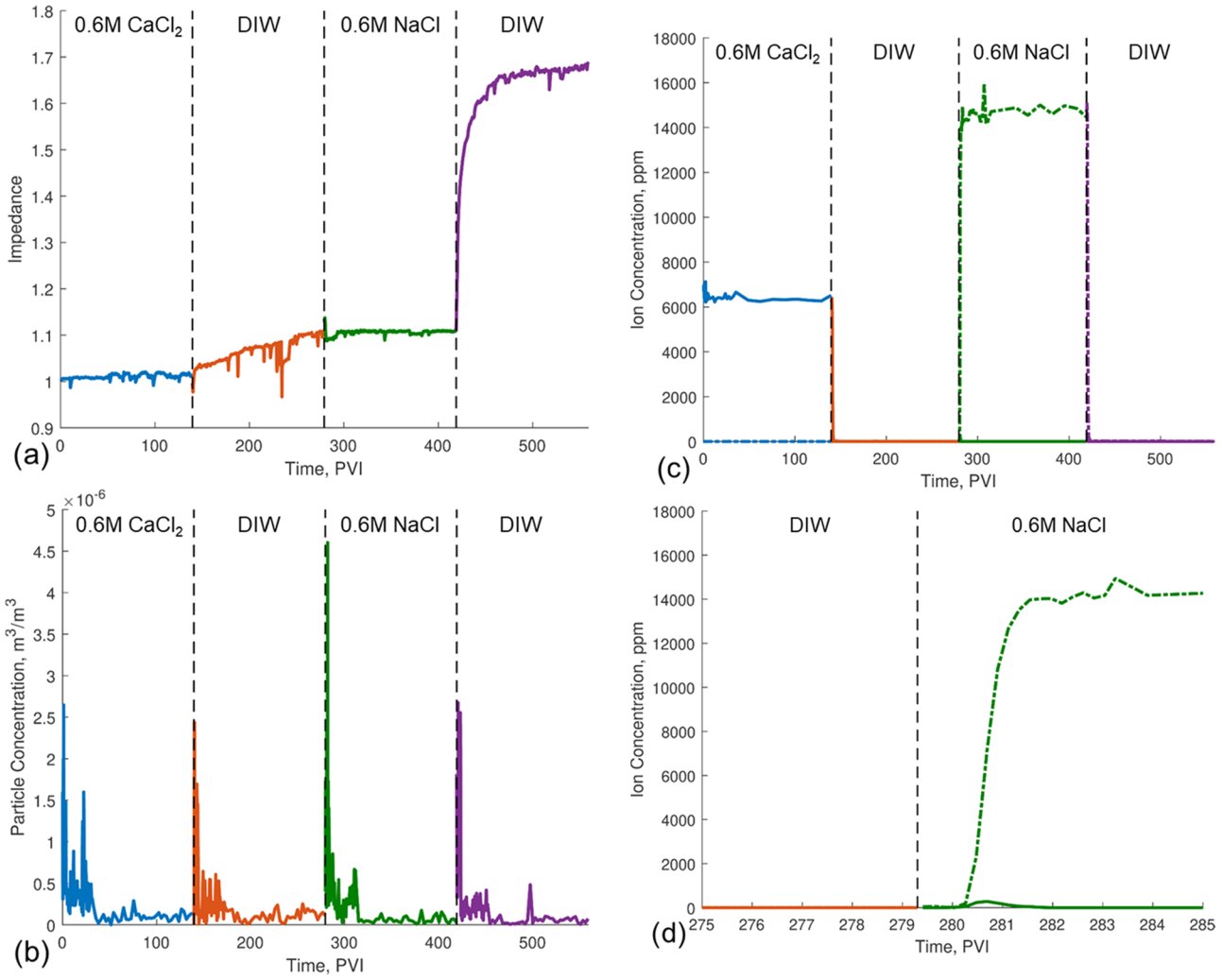

Figure 4. Single-phase test on unconsolidated sand-kaolinite core (5% kaolinite w/w, k = 537 mD): (a) normalized permeability, (b) outlet particle concentration, (c) outlet ion concentrations for sodium and calcium, (d) enlarged graph of outlet ion concentrations during the beginning of the injection of 0.6 M NaCl.

Table 2. Mineralogy of Berea 1 Determined Using XRD

mineral	weight %
quartz	84.6
K-feldspar (ordered microcline)	4.3
plagioclase (albite)	2.6
kaolinite (disordered)	2.3
illite	6.2

second DIW injection, approximately 15 times higher than the stabilized impedance during the $CaCl_2$ injection stages. Figure 7b shows that a substantial amount of clay particles was produced at the core outlet during the second DIW but not in any injection stages before that. This clearly demonstrates that fines migration occurred during the second DIW stage. This coincided with an increase in oil recovery such that the residual oil saturation decreased from 0.49 to 0.34.

Berea 3. Results similar to those of the Berea 2 test were observed in the Berea 3 coreflood. Figure 8a shows the pressure drop of the drainage displacements. In the first drainage, the pressure drop increased to 84 psi before breakthrough and stabilized at 58 psi after 5.5 PVI. In the second drainage, the pressure drop rose to ∼95 psi before the breakthrough and then stabilized at ∼63 psi after 8 PVI. The initial water saturations for the first and second drainage displacements are close, at 0.36 and 0.39, respectively, indicating a reproducibility of the initial conditions. The oil end-point relative permeabilities of these drainages are 0.89 and 0.93, respectively.

Injecting low-salinity $CaCl_2$ in the secondary mode resulted in a slightly higher impedance (stabilized at ∼1.5 after 8 PVI of LS $CaCl_2$ solution injection with an initial pressure drop of ∼71 psi) compared to HSW (stabilized at ∼1.3 after 8 PVI of HS $CaCl_2$ with an initial pressure drop of ∼63 psi) as shown in Figure 8b. The residual oil saturations are 0.32 for the HSW and 0.24 for the LSW, which correspond to 0.32 and 0.38 PV of oil production, respectively, as illustrated in Figure 8b. Tertiary waterflooding of lower $CaCl_2$ salinities had almost no impact on the impedance (stable at ∼2 with an initial pressure drop of ∼71 psi) or oil production, as was seen in the Berea 2 test. However, injecting DIW after 0.05 M NaCl resulted in a significant rise in impedance (∼11 times higher than the stabilized impedance during $CaCl_2$ LSW), fine particle production, and, hence, incremental oil recovery as shown in Figure 9a,b. The residual oil saturation decreased from 0.24 to 0.10.

For low permeability and HSW $CaCl_2$, there is a particle production in two phase, which is permeability dependent. At the time of the 0.05 M $CaCl_2$ injection, the only aqueous solution that the cores had been exposed to was 0.6 M $CaCl_2$. As a result, some Ca^{2+} can desorb during this injection, resulting in some particle detachment. The fact that it is more significant for the lower permeability core could be due to a higher clay content or due to a higher detaching force resulting from particles being situated in smaller pores.

DOI: 10.1021/acs.energyfuels.9b02683
Energy Fuels 2019, 33, 10775−10786

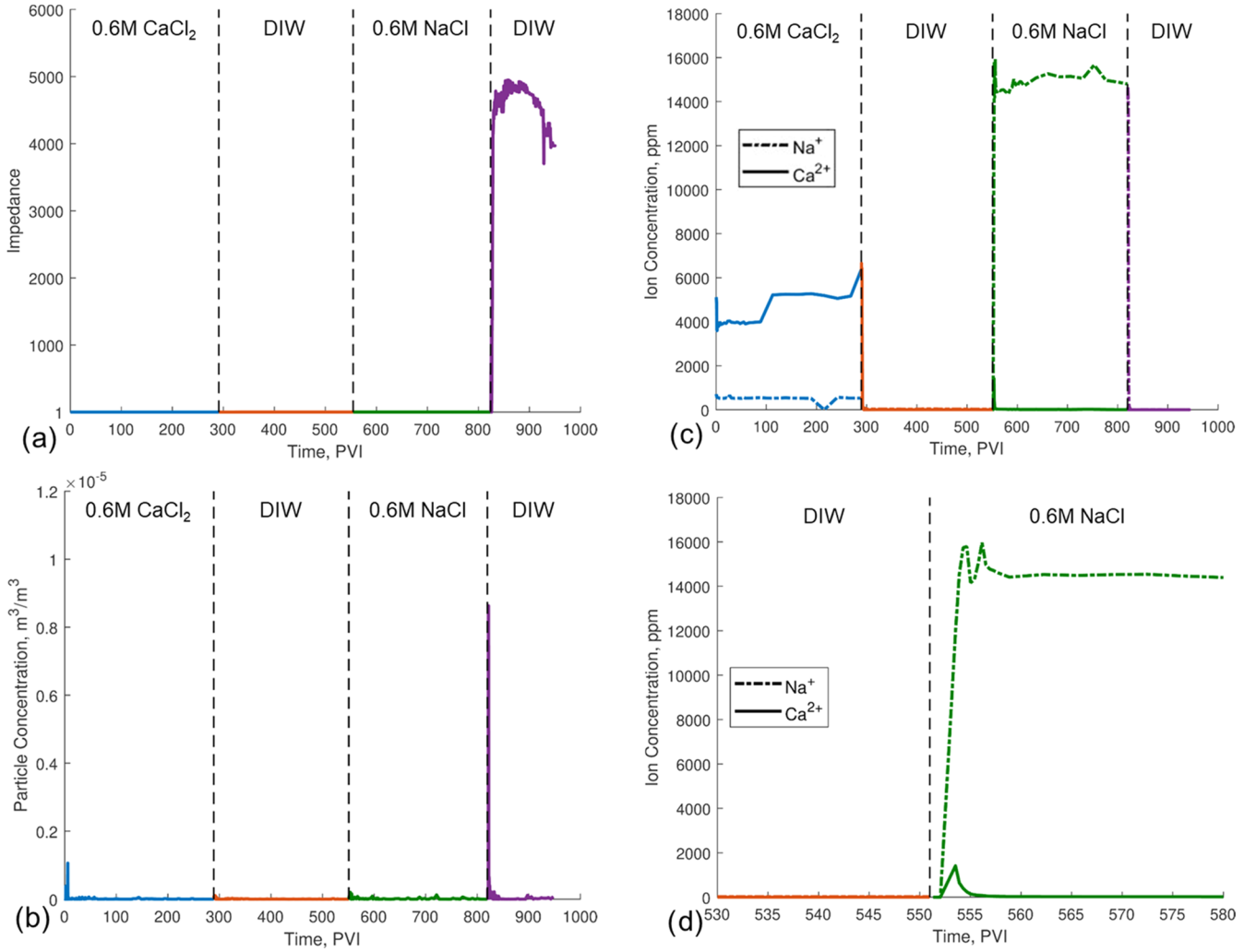

Figure 5. Single-phase test on Berea core 1 with k = 120 mD: (a) normalized permeability, (b) outlet particle concentration, (c) outlet ion concentrations for sodium and calcium, (d) enlarged graph of outlet ion concentrations during the beginning of the injection of 0.6 M NaCl.

DISCUSSION

Ion Sorption and Particle Detachment. The lack of particle detachment during $CaCl_2$ injections can be explained by the strong electrostatic force between the particles and rock surface due to the adsorbed calcium ions. The strong attraction arises from the suppression of the repulsive components of the electrostatic force by the adsorbed cations.[50] Following the injection of deionized water, neither the impedance nor outlet particle concentration showed any indications that particle detachment had occurred. In conjunction with the ion chromatography results, this suggests that the calcium ions were not fully desorbed during this injection cycle. The remaining calcium ions maintain a sufficiently large electrostatic force such that particles remain attached to the rock surface. The desorption of Ca^{2+} ions would in fact be an ion exchange process with the H^+ ions in solution. The experimental results suggest that this exchange has not resulted in the complete desorption of the calcium ions. During the NaCl injection, the high concentration of Na^+ ions present in solution resulted in at least a partial desorption of the remaining Ca^{2+} ions. The resulting adsorbed Na^+ ions can be readily desorbed during deionized water injection, resulting in the observed particle detachment.

This explanation is supported by the data presented on the outlet pH during the two-phase tests in Figures 7c and 9c. These graphs show that the pH is largely constant during all stages except the last, in which DIW is injected after 0.05 M NaCl. Changes to pH indicate that the hydrogen ions in solution are participating in the ion exchange. The lack of change during the first DIW injection supports the argument that very little Ca^{2+} ions are desorbed during this stage, as otherwise hydrogen ions would replace them on the clay surfaces, and a rise in pH would be observed at the outlet. This rise is observed, however, during the second DIW injection, where the Na^+ ions are replaced by the H^+ ions in solution. The lack of a change in pH during the NaCl injection indicates that the ion exchange occurring during this stage is primarily between the previously adsorbed Ca^{2+} ions and the Na^+ ions in solution.

Hysteresis of ionic sorption on clays has been widely reported in ion exchange in aquifers.[51] In particular, Comans[52] showed that the adsorption of cadmium ions onto illite will appear partially irreversible unless given up to 54 days for desorption. Gao et al.[53] showed that the sorption of cadmium and lead on soil samples showed significant hysteresis unless an acidic solution was used to desorb the ions.

DOI: 10.1021/acs.energyfuels.9b02683
Energy Fuels 2019, 33, 10775−10786

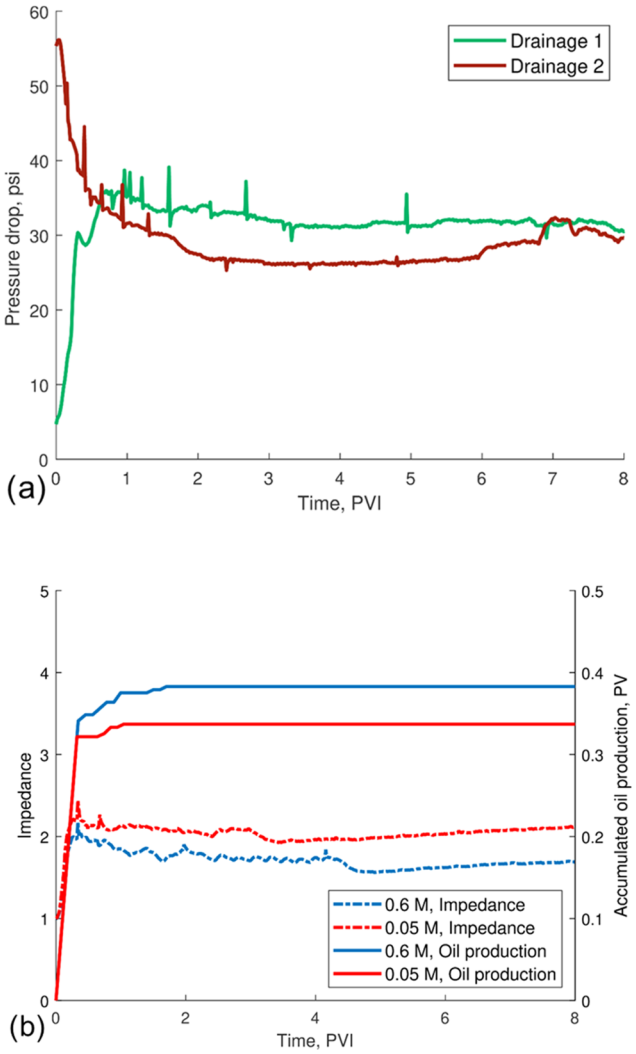

Figure 6. Berea 2 two-phase drainage and secondary displacements: (a) drainage pressure drop, (b) secondary waterflooding pressure drop and oil production.

Table 3. Saturations and End-Point Relative Permeabilities of the Two-phase Displacement Samples

	Berea 2	Berea 3
K_{rowi} (drainage 1)	0.97	0.89
S_{wi} (drainage 1)	0.16	0.36
K_{rwor} (0.6 M $CaCl_2$)	0.02	0.03
S_{or} (0.6 M $CaCl_2$)	0.49	0.32
K_{rowi} (drainage 2)	0.88	0.93
S_{wi} (drainage 2)	0.21	0.39
K_{rwor} (0.05 M $CaCl_2$)	0.02	0.02
S_{or} (0.05 M $CaCl_2$)	0.49	0.24
K_{rwor} (0.025 M $CaCl_2$)	0.02	0.02
S_{or} (0.025 M $CaCl_2$)	0.49	0.24
K_{rwor} (0.01 M $CaCl_2$)	0.02	0.02
S_{or} (0.01 M $CaCl_2$)	0.49	0.24
K_{rwor} (DIW 1)	0.02	0.02
S_{or} (DIW 1)	0.49	0.24
K_{rwor} (0.05 M NaCl)	0.01	0.01
S_{or} (0.05 M NaCl)	0.49	0.24
K_{rwor} (DIW 2)	0.001	0.002
S_{or} (DIW 2)	0.34	0.10

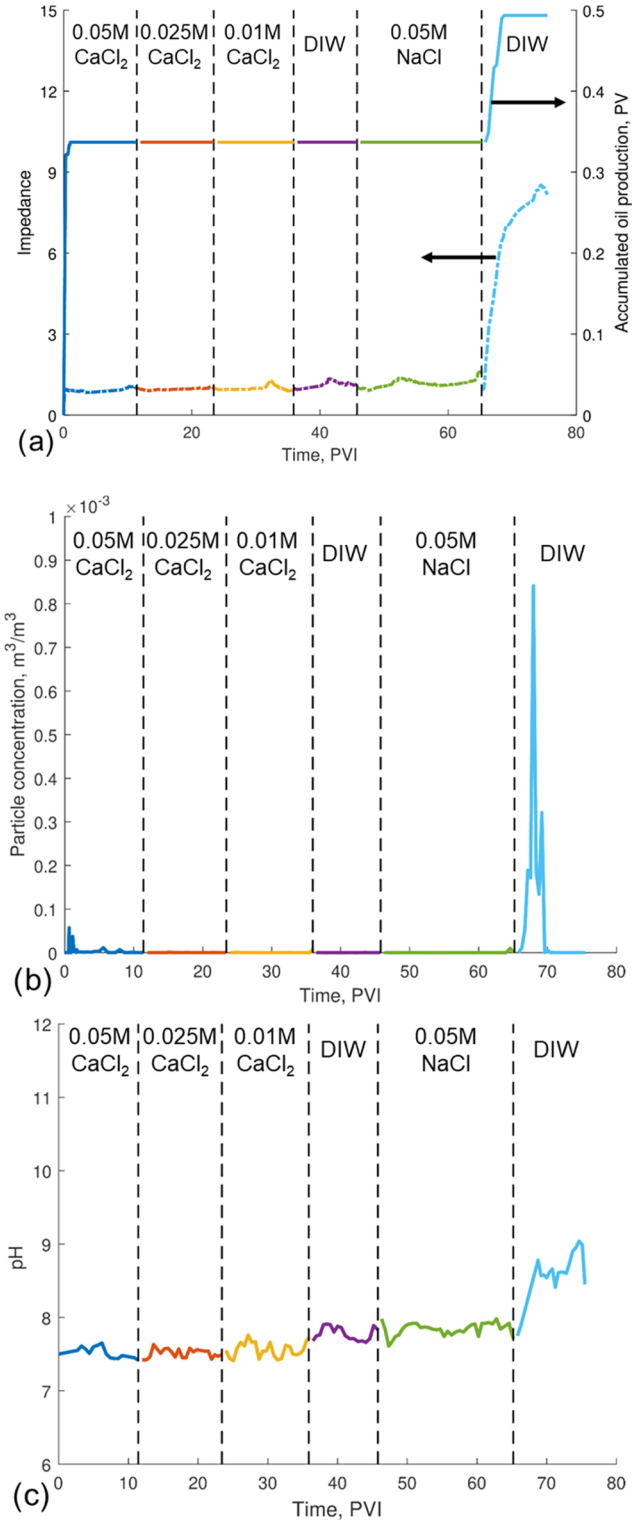

Figure 7. Two-phase tests on Berea core 2 with k = 40 mD: (a) pressure drop and oil production, (b) outlet particle concentration, (c) outlet pH.

This study similarly provides evidence of ion sorption hysteresis but provides little information on the physical basis and nature of the hysteresis. Of particular importance to practical applications is whether the hysteresis is permanent or is a result of ion desorption being substantially slower than adsorption. Strawn and Sparks[54] consider a multitude of existing laboratory tests and support the notion that the

DOI: 10.1021/acs.energyfuels.9b02683
Energy Fuels 2019, 33, 10775−10786

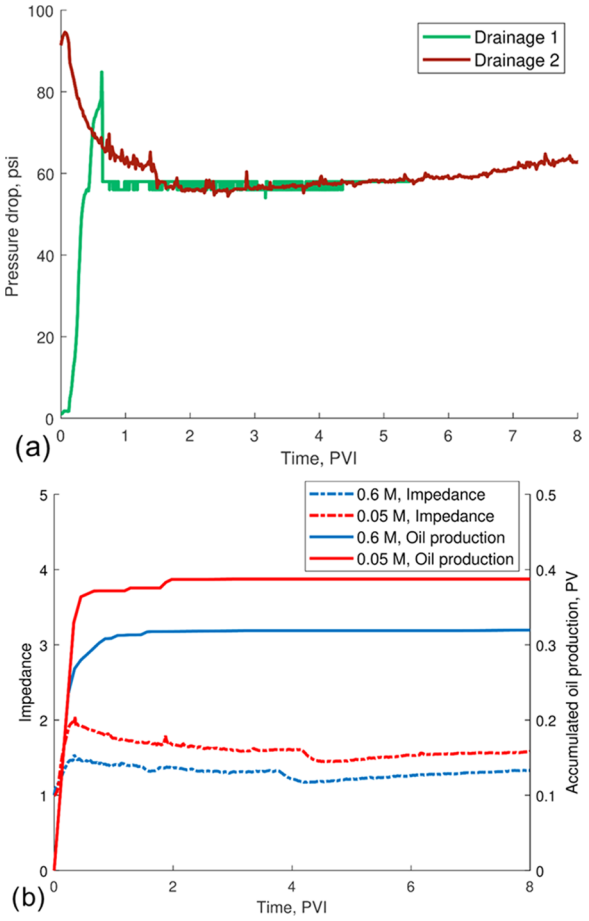

Figure 8. Berea 3 two-phase drainage and secondary displacements: (a) drainage pressure drop, (b) secondary waterflooding pressure drop and oil production.

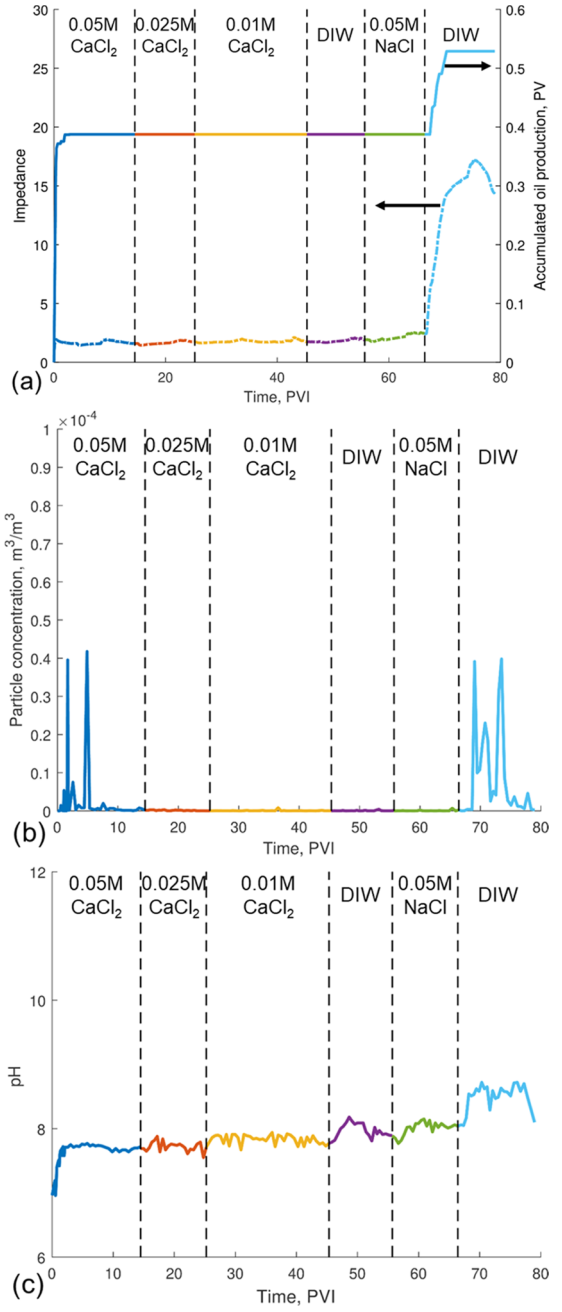

Figure 9. Two-phase tests on Berea core 3 with k = 21 mD: (a) pressure drop and oil production, (b) outlet particle concentration, (c) outlet pH.

apparent hysteresis is a result of slow desorption kinetics. A slow desorption phase could be a result of diffusive mass transfer into micropores followed by adsorption onto interior surfaces as was investigated quantitatively by Joekar-Niasar and Mahani[55] for the desorption of oil droplets from clays. An alternative explanation is that adsorbed ions transition between different adsorption mechanisms while adsorbed to the particle surface.[54] This conceptual model involves a transition from outer-sphere complexes, where adsorption is due to primarily electrostatic bonding, to inner-sphere complexes, where ionic or covalent bonding would provide a more stable ion-surface complex. Several molecular dynamics studies have confirmed the co-existence of multiple adsorption complexes on clays.[56,57] Some authors have shown that while the total adsorbed ion concentration remains constant after some time, the fraction that can be desorbed increases as the clay is left in the saturating solution.[58,59] This supports the notion of a transition between adsorption mechanisms. Given that rock saturation occurs over geological time periods in petroleum reservoirs, the ability to desorb certain ions may be overestimated by relatively short laboratory tests such as those presented in this study.

It should be noted that neither the complete desorption of adsorbed calcium by the NaCl injection nor the complete desorption of sodium during the second deionized water injection can be confirmed from these tests. The only inferences that can be made are that calcium sorption clearly demonstrates hysteretic behavior and that the adsorbed composition during the final deionized water injection favors particle detachment.

Impact on Oil Recovery. The use of nonpolar oil ensures that no wettability alteration takes place during low-salinity injection,[25,26] and any extra oil production can be solely attributed to fines migration. The detachment of fine particles and their capture leads to microscopic flux diversion because the water flow is redirected away from blocked pores and into the thin pores where residual oil is trapped. This leads to the mobilization of oil ganglia and, therefore, a decrease in S_{or}. During redisplacement of the residual oil by the redirected water, the water−oil menisci will pass over a fraction of the rock surface. Attached particles on this surface will be exposed

DOI: 10.1021/acs.energyfuels.9b02683
Energy Fuels 2019, 33, 10775−10786

to a capillary force acting to detach them. Such capillary forces are significantly higher than the electrostatic forces acting to keep the particles attached to the surface.[60,61] Thus, oil mobilization can lead to further fines detachment and capture.

During both two-phase tests, injection of LS $CaCl_2$ brine resulted in almost no change in residual oil saturation compared to HSW. This is explained by a lack of particle detachment, evident from both the impedance and outlet particle concentration measurements (Figures 6b and 8b). This is consistent with the behavior described above, wherein hysteretic calcium sorption leads to a residual adsorbed concentration that is sufficient to inhibit particle detachment. Injection of NaCl results in ion exchange, favoring the adsorption of Na^+ ions. During the deionized water injection, the desorption of these Na^+ ions is sufficient to reduce the electrostatic forces and, hence, detach clay particles. This is reflected in an increase in the impedance and outlet fines concentration, as well as a decrease in the residual oil saturation.

It should be noted that in several tests, notably in the single-phase test of the 5% clay content unconsolidated core and in Berea 3, some evidence of fines migration is observed during the decrease in $CaCl_2$ salinity. This is evidence that while the residual adsorbed calcium ions substantially reduce the sensitivity of the cores to low-salinity water, they do not completely inhibit fines migration. Nonetheless, the increase in impedance is negligible compared to similar tests run with pure NaCl solutions for both single phase[62] and two phase.[43]

An understanding of the hysteretic nature of ion exchange and its relation to fines migration is critical in designing field-scale smart (low-salinity) water injection projects. This study demonstrates that the sensitivity of sandstone rocks to low-salinity water can be controlled by the type of ion in the saturating solution.

Formation damage due to fines migration in the vicinity of injection and production wells remains a major issue in waterflooding projects. Pretreating the near-wellbore region with a solution of high $CaCl_2$ concentration could be used to mitigate injectivity or productivity decline issues during low-salinity waterflooding projects by stabilizing fines. Conversely, far from injection and production wells, increases in macro- and microscale sweep efficiencies can make enhancing fines migration crucial to the success of a waterflood. In these cases, pretreating the rock with NaCl could enhance the sensitivity of the rock to low-salinity water, unlocking further potential for reducing the residual oil saturation.

While calcium and sodium are two of the most abundant cations found in most petroleum reservoirs, many other ions are typically present, and the potential for hysteretic sorption in more complex ionic solutions deserves proper investigation. Furthermore, a quantitative investigation of the hysteresis and potential long-term desorption kinetics would allow for more rigorous modeling of fines migration during low-salinity waterflooding.

Limitations of the Study. This study used both artificial and Berea cores. We use Berea cores as a means to extend the results of this study to petroleum reservoirs. However, the Berea cores are outcrop cores, which are subject to weathering, which might alter the detachment characteristics of the kaolinite particles.[63] This limitation does not prohibit studying the hysteresis of Na−Ca ion exchange and its impact on fines detachment, but it does limit the extension of these results to field-scale applications. A comparison of the results of this study with results from reservoir cores is the subject of further work.

Additional limitations stem from differences between the conditions of the tests in this study and common reservoir conditions. These differences include the chemical composition of crude oil, which commonly includes polar components; high reservoir temperatures; more complex ionic compositions, including trivalent ions in the formation water; the presence of reactive minerals such as feldspars and evaporates; and additional clays not present in the cores used in this study (e.g., montmorillonite). These factors can significantly impact the detachment of fines. For example, the effectiveness of high temperatures in increasing particle detachment has been well studied.[64,65] The application of fines migration coreflooding results to a particular reservoir requires careful replication of these important conditions in the laboratory.

Miscellaneous. Primary and secondary drainages have been performed to create identical oil−water−rock systems before HSW and LSW. Some hysteresis occurs between first and second drainage displacements; however, the values S_{wi} and K_{rowi} were close enough. The method can be improved by HSW injection after the second drainage displacement and then LSW.

CONCLUSIONS

In this study, we performed laboratory corefloods with variation in the sodium and calcium concentrations of the injected brine. Ion chromatography measurements allowed observation of the underlying ion exchange processes. Similar tests in the presence of residual oil were performed to investigate the impact this ion exchange might have on oil recovery. These tests allow concluding the following:

1. During the DIW injection that follows the $CaCl_2$ injection, the impedance remains constant and clay fines do not appear in the effluent. This indicates no fines detachment.
2. Further DIW injection that follows the NaCl injection exhibits a large increase in impedance and significant fines concentration in the effluent, suggesting that the permeability decline can be attributed to fines mobilization and capture.
3. Some Ca^{2+} ions have been released during the NaCl injection, suggesting competitive adsorption of Na^+ and Ca^{2+} ions on the clay and residual adsorbed Ca^{2+} concentration after the DIW injection.
4. Adsorption of Ca ions on kaolinite clay exhibits a hysteretic behavior.
5. The same phenomena have been observed in the presence of residual oil.
6. Induced fines migration results in a decrease in residual oil.

AUTHOR INFORMATION

Corresponding Author

*Email: abdullah.sarihi@adelaide.edu.au.

ORCID

A. Al-Sarihi: 0000-0001-7075-0526

A. Zeinijahromi: 0000-0002-3088-6952

Notes

The authors declare no competing financial interest.

DOI: 10.1021/acs.energyfuels.9b02683
Energy Fuels 2019, 33, 10775−10786

■ ACKNOWLEDGMENTS

The authors would like to thank Drs. Alex Badalyan (Australian School of Petroleum, University of Adelaide), Luis Genolet, Aron Behr, and Patrick Kowollik (Wintershall Holding GmbH) for their fruitful discussions. The authors would also like to thank Dr. Tony Hall for performing the XRD study.

■ NOMENCLATURE

J = impedance
k = permeability
K_{rowi} = oil relative permeability at initial water saturation
K_{rwor} = water relative permeability at residual oil saturation
S_{or} = residual oil saturation
S_{wi} = initial water saturation
Ca = calcium
Ca^{2+} = calcium ions
Na = sodium
Na^{+} = sodium ions

■ GREEK LETTERS

Δp_0 = stabilized initial pressure drop
Δp = stabilized pressure drop

■ ABBREVIATIONS

DIW = deionized water
HS = high salinity (0.6 M ionic strength)
HSW = low-salinity waterflooding
LS = low salinity (0.05 M ionic strength)
LSW = low-salinity waterflooding
M = molar
PVI = pore volume injected

■ REFERENCES

(1) Khilar, K. C.; Fogler, H. S. *Migrations of Fines in Porous Media*; Springer Science & Business Media, 1998; Vol. *12*.
(2) Fogden, A.; Kumar, M.; Morrow, N. R.; Buckley, J. S. Mobilization of Fine Particles during Flooding of Sandstones and Possible Relations to Enhanced Oil Recovery. *Energy Fuels* **2011**, *25*, 1605−1616.
(3) Khilar, K. C.; Fogler, H. S. Water sensitivity of sandstones. *Soc. Pet. Eng. J.* **1983**, *23*, 55−64.
(4) Qajar, J.; Arns, C. H. Characterization of reactive flow-induced evolution of carbonate rocks using digital core analysis-part 2: Calculation of the evolution of percolation and transport properties. *J. Contam. Hydrol.* **2017**, *204*, 11−27.
(5) Yuan, H.; Shapiro, A. A. Induced migration of fines during waterflooding in communicating layer-cake reservoirs. *J. Pet. Sci. Eng.* **2011**, *78*, 618−626.
(6) Zheng, X. L.; Shan, B. B.; Chen, L.; Sun, Y. W.; Zhang, S. H. Attachment-detachment dynamics of suspended particle in porous media: Experiment and modeling. *J. Hydrol.* **2014**, *511*, 199−204.
(7) Kia, S.; Fogler, H. S.; Reed, M. Effect of pH on colloidally induced fines migration. *J. Colloid Interface Sci.* **1986**, *118*, 158−168.
(8) Barkman, J.; Abrams, A.; Darley, H.; Hill, H. An Oil-Coating Process To Stabilize Clays in Fresh Waterflooding Operations (includes associated paper 6405). *J. Pet. Technol.* **1975**, *27*, 1053−1059.
(9) Akhmetgareev, V.; Khisamov, R. In *40 Years of Low-Salinity Waterflooding in Pervomaiskoye Field, Russia: Incremental Oil*, SPE European Formation Damage Conference and Exhibition; Society of Petroleum Engineers, 2015.
(10) Ezeukwu, T.; Thomas, R. L.; Gunneroed, T. In *Fines Migration Control in High-Water-Cut Nigerian Oil Wells: Problems and Solutions*, SPE International Symposium on Formation Damage Control; SPE: Lafayette, Louisiana, 1998.
(11) Reinoso, W.; Torres, F.; Aldana, M.; Campo, P.; Alvarez, E.; Tovar, E. In *Removing Formation Damage from Fines Migration in the Putumayo Basin in Colombia: Challenges, Results, Lessons Learned, and New Opportunities after more than 100 Sandstone Acidizing Treatments*, SPE International Conference & Exhibition on Formation Damage Control; SPE: Lafayette, Louisiana, 2016.
(12) Brady, P. V.; Morrow, N. R.; Fogden, A.; Deniz, V.; Loahardjo, N. Electrostatics and the low salinity effect in sandstone reservoirs. *Energ Fuel* **2015**, *29*, 666−677.
(13) Qiao, C.; Johns, R.; Li, L. Modeling low-salinity waterflooding in chalk and limestone reservoirs. *Energy Fuels* **2016**, *30*, 884−895.
(14) Aksulu, H.; Håmsø, D.; Strand, S.; Puntervold, T.; Austad, T. Evaluation of low-salinity enhanced oil recovery effects in sandstone: Effects of the temperature and pH gradient. *Energy Fuels* **2012**, *26*, 3497−3503.
(15) Mahani, H.; Keya, A. L.; Berg, S.; Bartels, W.-B.; Nasralla, R.; Rossen, W. R. Insights into the mechanism of wettability alteration by low-salinity flooding (LSF) in carbonates. *Energy Fuels* **2015**, *29*, 1352−1367.
(16) Mahani, H.; Menezes, R.; Berg, S.; Fadili, A.; Nasralla, R.; Voskov, D.; Joekar-Niasar, V. Insights into the impact of temperature on the wettability alteration by low salinity in carbonate rocks. *Energy Fuels* **2017**, *31*, 7839−7853.
(17) Zahid, A.; Shapiro, A.; Stenby, E. H.; Yan, W. Managing injected water composition to improve oil recovery: A case study of North Sea chalk reservoirs. *Energy Fuels* **2012**, *26*, 3407−3415.
(18) Bazyari, A.; Soulgani, B. S.; Jamialahmadi, M.; Dehghan Monfared, A.; Zeinijahromi, A. Performance of smart water in clay-rich sandstones: experimental and theoretical analysis. *Energy Fuels* **2018**, *32*, 10354−10366.
(19) Puntervold, T.; Mamonov, A.; Aghaeifar, Z.; Frafjord, G. O.; Moldestad, G. M.; Strand, S.; Austad, T. Role of Kaolinite Clay Minerals in Enhanced Oil Recovery by Low Salinity Water Injection. *Energy Fuels* **2018**, *32*, 7374−7382.
(20) Farajzadeh, R.; Guo, H.; van Winden, J.; Bruining, J. Cation exchange in the presence of oil in porous media. *ACS Earth Space Chem.* **2017**, *1*, 101−112.
(21) RezaeiDoust, A.; Puntervold, T.; Austad, T. Chemical verification of the EOR mechanism by using low saline/smart water in sandstone. *Energ Fuel* **2011**, *25*, 2151−2162.
(22) Torrijos, I. D. P.; Puntervold, T.; Strand, S.; Austad, T.; Abdullah, H. I.; Olsen, K. Experimental Study of the Response Time of the Low-Salinity Enhanced Oil Recovery Effect during Secondary and Tertiary Low-Salinity Waterflooding. *Energy Fuels* **2016**, *30*, 4733−4739.
(23) Bartels, W.-B.; Mahani, H.; Berg, S.; Hassanizadeh, S. Literature review of low salinity waterflooding from a length and time scale perspective. *Fuel* **2019**, *236*, 338−353.
(24) Nasralla, R. A.; Mahani, H.; van der Linde, H. A.; Marcelis, F. H.; Masalmeh, S. K.; Sergienko, E.; Brussee, N. J.; Pieterse, S. G.; Basu, S. Low Salinity Waterflooding for a carbonate reservoir: Experimental evaluation and numerical interpretation. *J. Pet. Sci. Eng.* **2018**, *164*, 640−654.
(25) Hao, J.; Mohammadkhani, S.; Shahverdi, H.; Esfahany, M. N.; Shapiro, A. Mechanisms of smart waterflooding in carbonate oil reservoirs-A review. *J. Pet. Sci. Eng.* **2019**, No. 49.
(26) Mohammadkhani, S.; Shahverdi, H.; Nielsen, S. M.; Esfahany, M. N.; Shapiro, A. Bicarbonate flooding of homogeneous and heterogeneous cores from a carbonaceous petroleum reservoir. *J. Pet. Sci. Eng.* **2019**, *178*, 251−261.
(27) Li, Y. Oil recovery by low salinity water injection into a reservoir: A new study of tertiary oil recovery mechanism. *Trans. Porous Media* **2011**, *90*, 333−362.
(28) Hussain, F.; Zeinijahromi, A.; Bedrikovetsky, P.; Badalyan, A.; Carageorgos, T.; Cinar, Y. An experimental study of improved oil recovery through fines-assisted waterflooding. *J. Pet. Sci. Eng.* **2013**, *109*, 187−197.

DOI: 10.1021/acs.energyfuels.9b02683
Energy Fuels 2019, 33, 10775−10786

(29) Zeinijahromi, A.; Farajzadeh, R.; Bruining, J. H.; Bedrikovetsky, P. Effect of fines migration on oil−water relative permeability during two-phase flow in porous media. *Fuel* **2016**, *176*, 222−236.
(30) Civan, F. Reservoir Formation Damage: Fundamentals. In *Modeling, Assessment, and Mitigation*; Gulf Professional Publishing, 2007; Vol. 2.
(31) Khilar, K. C.; Fogler, H. S.; Ahluwalia, J. Sandstone water sensitivity: existence of a critical rate of salinity decrease for particle capture. *Chem. Eng. Sci.* **1983**, *38*, 789−800.
(32) Bedrikovetsky, P.; Siqueira, F. D.; Furtado, C. A.; Souza, A. L. S. Modified particle detachment model for colloidal transport in porous media. *Trans. Porous Med.* **2011**, *86*, 353−383.
(33) Bedrikovetsky, P.; Zeinijahromi, A.; Siqueira, F. D.; Furtado, C. A.; de Souza, A. L. S. Particle detachment under velocity alternation during suspension transport in porous media. *Trans. Porous Med.* **2012**, *91*, 173−197.
(34) Israelachvili, J. *Intermolecular and Surface Forces*; Academic Press: London, U.K, 1992; p 450.
(35) Mohan, K. K.; Fogler, H. S.; Vaidya, R. N.; Reed, M. G. Water Sensitivity of Sandstones Containing Swelling and Non-swelling Clays. In *Colloids in the Aquatic Environment*; Elsevier, 1993; pp 237−254.
(36) Schembre, J.; Tang, G.-Q.; Kovscek, A. Wettability alteration and oil recovery by water imbibition at elevated temperatures. *J. Petr. Sci. Eng.* **2006**, *52*, 131−148.
(37) Sarkar, A. K.; Sharma, M. M. Fines migration in two-phase flow. *J. Pet. Technol.* **1990**, *42*, 646−652.
(38) Scheuerman, R. F.; Bergersen, B. M. Injection-water salinity, formation pretreatment, and well-operations fluid-selection guidelines. *J. Pet. Technol.* **1990**, *42*, 836−845.
(39) Lever, A.; Dawe, R. A. Water-sensitivity and migration of fines in the hopeman sandstone. *J. Pet. Geol.* **1984**, *7*, 97−107.
(40) Muecke, T. W. Formation fines and factors controlling their movement in porous media. *J. Pet. Technol.* **1979**, *31*, 144−150.
(41) You, Z.; Bedrikovetsky, P.; Badalyan, A.; Hand, M. Particle mobilization in porous media: Temperature effects on competing electrostatic and drag forces. *Geophys. Res. Lett.* **2015**, *42*, 2852−2860.
(42) Yuan, B.; Wang, W. Using nanofluids to control fines migration for oil recovery: Nanofluids co-injection or nanofluids pre-flush?-A comprehensive answer. *Fuel* **2018**, *215*, 474−483.
(43) Al-Sarihi, A.; Zeinijahromi, A.; Genolet, L.; Behr, A.; Kowollik, P.; Bedrikovetsky, P. Effects of fines migration on residual oil during low-salinity waterflooding. *Energy Fuels* **2018**, *32*, 8296−8309.
(44) Zeinijahromi, A.; Nguyen, T. K. P.; Bedrikovetsky, P. Mathematical model for fines-migration-assisted waterflooding with induced formation damage. *SPE J.* **2013**, *18*, 518−533.
(45) Zeinijahromi, A.; Al-Jassasi, H.; Begg, S.; Bedrikovetski, P. Improving sweep efficiency of edge-water drive reservoirs using induced formation damage. *J. Pet. Sci. Eng.* **2015**, *130*, 123−129.
(46) Ahmetgareev, V.; Zeinijahromi, A.; Badalyan, A.; Khisamov, R.; Bedrikovetsky, P. Analysis of low salinity waterflooding in Bastrykskoye field. *Pet. Sci. Technol.* **2015**, *33*, 561−570.
(47) Grolimund, D.; Borkovec, M. Release of colloidal particles in natural porous media by monovalent and divalent cations. *J. Contam. Hydrol.* **2006**, *87*, 155−175.
(48) Bradford, S. A.; Kim, H. Implications of cation exchange on clay release and colloid-facilitated transport in porous media. *J. Environ. Qual.* **2010**, *39*, 2040−2046.
(49) Kia, S.; Fogler, H. S.; Reed, M. *Effect of Salt Composition on Clay Release in Berea Sandstones*, SPE International Symposium on Oilfield Chemistry; Society of Petroleum Engineers, 1987.
(50) Gregory, J. Interaction of unequal double layers at constant charge. *J. Colloid Interface Sci.* **1975**, *51*, 44−51.
(51) Jenne, E. A. *Adsorption of Metals by Geomedia*; Elsevier, 1998.
(52) Comans, R. N. J. Adsorption, Desorption and Isotopic Exchange of Cadmium on Illite - Evidence for Complete Reversibility. *Water Res.* **1987**, *21*, 1573−1576.
(53) Gao, Y.; Kan, A. T.; Tomson, M. B. Critical evaluation of desorption phenomena of heavy metals from natural sediments. *Environ. Sci. Technol.* **2003**, *37*, 5566−5573.
(54) Strawn, D. G.; Sparks, D. L. Sorption Kinetics of Trace Elements in Soils and Soil Materials. In *Fate and Transport of Heavy Metals in the Vadose Zone*; Selim, H. M., Iskandar, I. K., Eds.; CRC Press: Boca Raton, Florida, 1999.
(55) Joekar-Niasar, V.; Mahani, H. Nonmonotonic Pressure Field Induced by Ionic Diffusion in Charged Thin Films. *Ind. Eng. Chem. Res.* **2016**, *55*, 6227−6235.
(56) Vasconcelos, I. F.; Bunker, B. A.; Cygan, R. T. Molecular dynamics modeling of ion adsorption to the basal surfaces of kaolinite. *J. Phys. Chem. C* **2007**, *111*, 6753−6762.
(57) Li, X.; Li, H.; Yang, G. Promoting the Adsorption of Metal Ions on Kaolinite by Defect Sites: A Molecular Dynamics Study. *Sci. Rep.* **2015**, *5*, No. 14377.
(58) Mclaren, R. G.; Lawson, D. M.; Swift, R. S. Sorption and Desorption of Cobalt by Soils and Soil Components. *J. Soil Sci.* **1986**, *37*, 413−426.
(59) Kuo, S.; Mikkelsen, D. S. Kinetics of Zinc Desorption from Soils. *Plant Soil* **1980**, *56*, 355−364.
(60) Lazouskaya, V.; Wang, L.-P.; Or, D.; Wang, G.; Caplan, J. L.; Jin, Y. Colloid mobilization by fluid displacement fronts in channels. *J. Colloid Interface Sci.* **2013**, *406*, 44−50.
(61) Shang, J.; Flury, M.; Chen, G.; Zhuang, J. Impact of flow rate, water content, and capillary forces on in situ colloid mobilization during infiltration in unsaturated sediments. *Water Resour. Res.* **2008**, *44*, No. 516.
(62) Russell, T.; Pham, D.; Neishaboor, M. T.; Badalyan, A.; Behr, A.; Genolet, L.; Kowollik, P.; Zeinijahromi, A.; Bedrikovetsky, P. Effects of kaolinite in rocks on fines migration. *J. Nat. Gas Sci. Eng.* **2017**, *45*, 243−255.
(63) Brady, P. V.; Morrow, N. R.; Fogden, A.; Deniz, V.; Loahardjo, N. Winoto, Electrostatics and the Low Salinity Effect in Sandstone Reservoirs. *Energy Fuels* **2015**, *29*, 666−677.
(64) You, Z. J.; Bedrikovetsky, P.; Badalyan, A.; Hand, M. Particle mobilization in porous media: Temperature effects on competing electrostatic and drag forces. *Geophys. Res. Lett.* **2015**, *42*, 2852−2860.
(65) You, Z.; Badalyan, A.; Yang, Y.; Bedrikovetsky, P.; Hand, M. *Laboratory Study of Fines Migration in Geothermal Reservoirs*, Proceedings World Geothermal Congress, 2014.

DOI: 10.1021/acs.energyfuels.9b02683
Energy Fuels 2019, 33, 10775−10786

4 Analytical modelling of fines migration with delayed particle detachment

4.1 Colloidal-suspension flows with delayed fines detachment: Analytical model & laboratory study

Russell, T., Bedrikovetsky, P.

Chemical Engineering Science, Volume 190, 2018, Pages 98-1

Statement of Authorship

Title of Paper	Colloidal-suspension flows with delayed fines detachment: Analytical model & laboratory study
Publication Status	☑ Published ☐ Accepted for Publication ☐ Submitted for Publication ☐ Unpublished and Unsubmitted w ork w ritten in manuscript style
Publication Details	Thomas Russell, Pavel Bedrikovetsky, Colloidal-suspension flows with delayed fines detachment: Analytical model & laboratory study, Chemical Engineering Science, Volume 190, 2018, Pages 98-109

Principal Author

Name of Principal Author (Candidate)	Thomas Russell		
Contribution to the Paper	Performed laboratory tests, performed calculations, contributed to writing		
Overall percentage (%)	70%		
Certification:	This paper reports on original research I conducted during the period of my Higher Degree by Research candidature and is not subject to any obligations or contractual agreements with a third party that would constrain its inclusion in this thesis. I am the primary author of this paper.		
Signature		Date	16/02/2021

Co-Author Contributions

By signing the Statement of Authorship, each author certifies that:

i. the candidate's stated contribution to the publication is accurate (as detailed above);

ii. permission is granted for the candidate in include the publication in the thesis; and

iii. the sum of all co-author contributions is equal to 100% less the candidate's stated contribution.

Name of Co-Author	Pavel Bedrikovetsky		
Contribution to the Paper	Design of laboratory tests, contributed to writing		
Signature		Date	17/02/2021

Chemical Engineering Science 190 (2018) 98–109

Contents lists available at ScienceDirect

Chemical Engineering Science

journal homepage: www.elsevier.com/locate/ces

Colloidal-suspension flows with delayed fines detachment: Analytical model & laboratory study

Thomas Russell *, Pavel Bedrikovetsky

Australian School of Petroleum, University of Adelaide, Australia

HIGHLIGHTS

- Detachment of fine particles by low-salinity water injection into porous media.
- Corefloods by low-salinity water cause permeability decline and fines production.
- Analytical model for colloidal-suspension transport with delayed particle detachment.
- Concentration shock fronts become smooth after the introduction of delay.
- High agreement between the laboratory and modelling data.

GRAPHICAL ABSTRACT

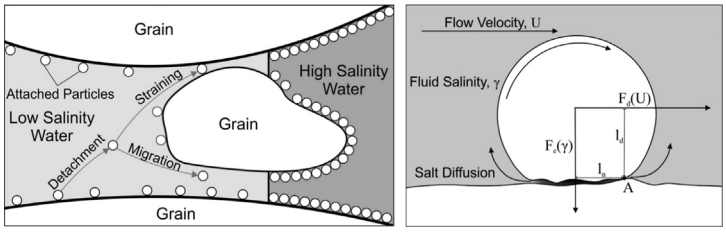

ARTICLE INFO

Article history:
Received 15 April 2018
Received in revised form 25 May 2018
Accepted 31 May 2018
Available online 1 June 2018

Keywords:
Porous media
Colloids
Suspension
Analytical model
Laboratory coreflood
Particle detachment

ABSTRACT

The effects of confinement and electrostatic interactions on the ion diffusion in the particle-rock contact area yields a delay in particle detachment during low-salinity water injection in porous media. The objective of the work is laboratory and mathematical modelling of the effects of delayed particle detachment on colloid-suspension transport in porous media. We present the governing system for single-phase particulate flow accounting for non-equilibrium fines detachment. The exact solution for one-dimensional flow with varying salinity is derived. Laboratory coreflood tests on low-salinity water injection are performed. The measured breakthrough fine particle concentration and pressure drop across the core are matched by the analytical model with high accuracy. Introduction of delay in the model removes the concentration shocks present in the instant fines detachment model as fines detach continuously throughout the injection period.

1. Introduction

It is common during flows in natural porous media for colloidal suspensions to be created by the detachment of fine particles. The suspended particles are transported by the fluid and are subjected to capture in pore throats which results in permeability decline. This phenomenon is referred to as fines migration (Civan, 2014; Khilar and Fogler, 1998).

Field studies have demonstrated that during low-salinity water injection into petroleum reservoirs, fines migration can cause serious injectivity decline (Akhmetgareev and Khisamov, 2015; Barkman et al., 1975). Other applications of fines migration technologies and modelling include formation damage during fluid leak off in drilling operations (Salimi and Ghalambor, 2011), the storage of fresh water in shallow aquifers (Prommer et al., 2013), the contamination of fresh water aquifers by contagions (Kretzschmar et al., 1999; Yu et al., 2012), the encroachment of seawater into coastal aquifers (Goldenberg et al., 1983), among others. Prediction and mitigation of this damage poses a serious engineering problem.

* Corresponding author.
E-mail address: thomas.l.russell@adelaide.edu.au (T. Russell).

https://doi.org/10.1016/j.ces.2018.05.062
0009-2509/

Nomenclature

C	dimensionless suspended particle concentration [–]
c	suspended particle concentration [–]
C_{acc}	accumulated suspended particle concentration [–]
D	slope of characteristic line [–]
F_d	drag force [M][L]$^{-1}$[T]$^{-2}$
F_e	electrostatic force [M][L]$^{-1}$[T]$^{-2}$
J	impedance [–]
k_0	initial core permeability [L]^2
l_d	drag lever arm [L]
l_n	normal lever arm [L]
P	dimensionless fluid pressure [–]
p	fluid pressure [M][T]$^{-2}$[L]
q_0	initial injection rate [L]^3[T]$^{-1}$
R^2	coefficient of determination [–]
S_a	dimensionless attached particle concentration [–]
S_s	dimensionless strained particle concentration [–]
T	dimensionless elapsed time [–]
t	elapsed time [T]
T_0	dimensionless elapsed time (initial condition) [–]
U	fluid velocity [L][T]$^{-1}$
U_p	particle velocity [L][T]$^{-1}$
X	dimensionless distance from the core inlet [–]
x	distance from the core inlet [L]
X_0	dimensionless distance from core inlet (initial condition) [–]
ΔP	dimensionless pressure drop [–]
Δp_0	Initial pressure drop [M][T]$^{-2}$[L]

Greek letters

α	drift delay factor [–]
β	formation damage coefficient [–]
Γ	dimensionless fluid salinity [–]
γ	fluid salinity [N][L]$^{-3}$
γ_i	initial fluid salinity [N][L]$^{-3}$
γ_{inj}	Injected fluid salinity [N][L]$^{-3}$
$\Delta\sigma_{cr}$	total detached particle concentration [–]
ϵ	dimensionless delay factor [–]
Θ	temperature [Θ]
Λ	dimensionless filtration coefficient [–]
λ	filtration coefficient [L]$^{-1}$
μ	fluid viscosity [M][L]$^{-1}$[T]$^{-1}$
σ_a	attached particle concentration [–]
σ_{cr}	critical retention function [–]
σ_s	strained particle concentration [–]
τ	delay factor [T]
ϕ	porosity [–]

The typical approach to quantify and manage the extent of fines migration is mathematical modelling supported by laboratory studies. Laboratory results provide a means to characterise the porous medium, which is necessary to use mathematical models in a predictive capacity.

Mathematical models for fines migration consist of formulations for the processes of particle detachment, transport, and capture. These three processes are shown schematically in Fig. 1. The mechanics of fines detachment is determined by the forces acting on attached particles, which are: the hydrodynamic drag force, F_d, the lifting force, F_l, the gravitational force, F_g, and the electrostatic force, F_e. The drag and lifting force are the tangential and normal components of the force exerted on the particle by the moving fluid and will act to detach the particle. The electrostatic force consists of non-electrostatic London-Van der Waals forces as well as an electrostatic component arising from surface charges on both the particle and the porous surface (Derjaguin and Landau, 1941; Verwey and Overbeek, 1999). Overall the electrostatic force is attractive and will thus act to prevent particle detachment. For the conditions of porous media, the lifting and gravitational forces are of negligible magnitude compared to the drag and electrostatic forces, and so are neglected (Kalantariasl and Bedrikovetsky, 2013). A diagram of the two remaining forces acting on an idealised, spherical particle is given in Fig. 2. Whether conditions are favourable for particle detachment depends on the magnitude of these two forces. The drag force increases with the fluid velocity (Goldman et al., 1967) and so high velocity conditions, such as in the near-wellbore region of injection or production wells, are particularly prone to fines migration. The electrostatic force decreases with decreasing salinity (Bhattacharya et al., 2016; Kia et al., 1987) or increasing pH (Kia et al., 1986), and so low salinity or alkaline solutions will tend to intensify fines detachment. The electrostatic force also weakens at elevated temperatures (You et al., 2015) and consequently geothermal wells are likely to experience formation damage due to fines migration.

A quantification of particle detachment follows from the balance of the abovementioned forces. Investigations into particle mobilisation suggest that particle rotation is more likely than a

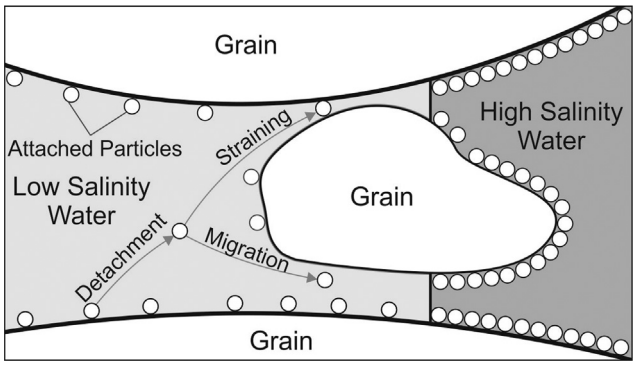

Fig. 1. Schematic of fines detachment, migration, and straining processes in porous media during the injection of low-salinity water.

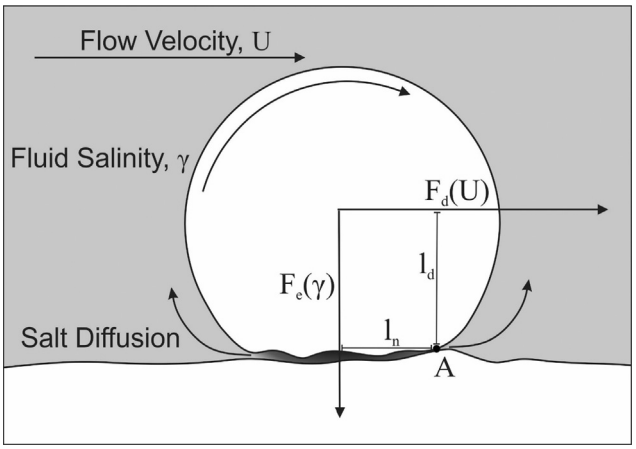

Fig. 2. Attached particle with acting forces and lever arms.

horizontal or vertical translation (Bergendahl and Grasso, 2000). Thus, the condition for detachment becomes the equality of acting torques:

$$F_d(U)l_d = F_e(\gamma, pH, \Theta)l_n. \tag{1}$$

Here l_d and l_n are the lever arms associated with each force, U is the fluid velocity, γ is the fluid salinity, and Θ is the temperature. The expressions for the forces in Eq. (1) can be found in the literature (Goldman et al., 1967; Verwey and Overbeek, 1999; Xie et al., 2017).

Fig. 2 shows the lever arms associated with each force.

When applied to all attached particles within a porous media, condition (1) can quantitatively describe the concentration of attached particles under certain flow conditions. The result is that, under the condition of mechanical equilibrium, the attached concentration is a function of all parameters that affect the electrostatic and drag forces (velocity, salinity, pH, temperature, etc.). This equation is referred to as the critical retention function:

$$\sigma_a = \sigma_{cr}(U, \gamma, pH, \Theta). \tag{2}$$

where σ_a is the attached particle concentration.

Two of the primary methods of upscaling the torque balance to obtain the critical retention function are presented in (Bedrikovetsky et al., 2011; You et al., 2015). The first assumes that mono-sized attached particles form an internal filter cake in cylindrical pores. When the filter cake is thicker, the velocity within the pore increases, shifting the torque balance towards particle detachment. The equilibrium filter cake thickness is calculated by applying the torque balance equation (Eq. (1)). The second method assumes that attached particles adhere only in a single layer on the pore surface but are distributed by size. According to the equations for the forces in Eq. (1), larger particles are more likely to detach than smaller ones. Thus, for any injection conditions there exists a critical particle size above which all particles detach. Using the torque balance equation alongside the particle size distribution results in the critical retention function, Eq. (2).

Several mathematical formulations of fines migration have been presented which make use of the critical retention function (Bedrikovetsky et al., 2011; Chequer et al., 2018; Yuan et al., 2017; Zeinijahromi et al., 2015). The advantage of this formulation over empirical forms presented previously (Kuo and Matijevic, 1979) is the explicit relation between the microscopic conditions for detachment and the macroscopic attached concentration.

The transport of fine particles is described by a mass balance equation:

$$\frac{\partial}{\partial t}(\phi c + \sigma_s + \sigma_a) + U_p \frac{\partial c}{\partial x} = 0, \tag{3}$$

where ϕ is the core porosity, c is the suspended particle concentration, σ_s is the strained particle concentration, U_p is the particle velocity, and x and t are the spatial and time coordinates respectively.

The detachment rate follows from Eq. (2). The straining rate is assumed to be proportional to the advective particle flux, cU_p:

$$\frac{\partial \sigma_s}{\partial t} = \lambda(\sigma_s) c U_p. \tag{4}$$

The coefficient of proportionality, λ, is referred to as the filtration coefficient.

The dependence of the critical retention function on the fluid salinity requires the inclusion of the solute mass balance:

$$\phi \frac{\partial \gamma}{\partial t} + U \frac{\partial \gamma}{\partial x} = 0. \tag{5}$$

Finally, the effect of straining on the permeability is incorporated using a Taylor's series expansion of the permeability damage ratio

$$\frac{k_o}{k(\sigma_s)} \approx 1 + \beta \sigma_s, \tag{6}$$

where k_0 is the undamaged core permeability and β is the formation damage coefficient.

Implementing Eq. (6) into Darcy's law gives

$$U = \frac{k_0}{\mu(c)(1 + \beta\sigma_s)} \frac{\partial p}{\partial x}, \tag{7}$$

where μ is the fluid viscosity, and p is the fluid pressure.

Similar to previous formulations, we recognise that the particle and fluid velocities will not necessarily be equal (Chequer et al., 2018; Oliveira et al., 2014). We introduce their ratio, the drift delay factor, as an additional parameter of the model

$$\alpha = \frac{U_p}{U}. \tag{8}$$

The rolling and sliding of particles along the pore surface would suggest that α is smaller than one.

The system of five Eqs. (2)-(5) and (7) which describes the five unknowns γ, c, σ_a, σ_s, and p, is the traditional model for fines migration. This system has previously been solved analytically for linear flows and has shown good agreement with laboratory results from coreflooding of consolidated sandstone rocks (Chequer et al., 2018).

Eq. (2) assumes mechanical equilibrium of the particles attached on the rock surface. However, various physical mechanisms which influence the forces acting on the particle may prevent the particle from instantly establishing this equilibrium. Fig. 2 shows diffusive flux between the bulk fluid and the contact area between the particle and rock surface, which will yield a delay in establishing equilibrium of the salt concentration between these two regions. Consequently, establishing a new equilibrium critical retention function due to changes to the bulk salinity will occur with some delay.

In the work by Mahani et al. (2015), it was shown that there is a significant delay in the detachment of an oil droplet when low-salinity water is introduced. A reduction in the diffusive flux resulting from electrostatic interactions was highlighted as a potential cause. A similar effect is expected for fines detachment, however a mathematical model for fines migration with delayed detachment is not available.

The present paper derives new basic governing equations for suspension-colloidal transport in porous media accounting for delayed particle detachment. The one-dimensional (1D) problem of coreflooding with varying salinity allows for an exact solution. The solution permits the regularization of a singular problem for the particular case where $\alpha = 1$, where particles move with the velocity of the carrier water. A laboratory coreflooding study with varying salinity was performed and the experimental data exhibits a close match with the analytical model.

The structure of the paper is as follows. Section 2 presents the delayed detachment model for suspension-colloidal flows and derives the exact solution for 1D system of fines transport under varying salinity. Section 3 will discuss the general behaviour of the derived solution and make comparisons with the instant detachment model. Section 4 provides a brief description of a laboratory study of fines migration. The results of the laboratory tests are used to validate the model in Section 5. The discussions in Section 6 and conclusions in Section 7 finalise the paper.

2. Mathematical model for fines migration with delayed particle detachment

2.1. Rate description for delayed particle detachment

Particle detachment due to changes in the bulk fluid salinity occurs due to the weakening of the attractive electrostatic force between particles and the pore surface. This force is governed by the concentration of ions in the region between the particle and pore surface. Changes to the detachment conditions induced by the fluid salinity are thus reliant on the ion transport between the bulk solution and the inter-particle region.

The proximity of the attached particles to the pore surface suggests that the advective flux will be negligible, so ion transport will be diffusion dominated. Both the effect of confinement in the inter-particle region as well as the influence of the surface charge on both solid surfaces will slow the ion transport (Pellicer and Aguilella, 1986; Tada et al., 1987).

An experimental study (Mahani et al., 2015) as well as a numerical investigation (Joekar-Niasar and Mahani, 2016) of the kinetics of wettability alteration by low-salinity water have demonstrated the significance of these transport mechanisms in producing a noticeable delay in changes to the electrostatic force.

In this paper, the delay in particle detachment is described by a non-equilibrium relationship between the attached concentration and the fluid salinity. We propose that Eq. (2) is satisfied only after some delay time, τ:

$$\sigma_a(x, t+\tau) = \sigma_{cr}(\gamma(x,t)). \tag{9}$$

Under the assumption of a constant delay time, we produce the relationship for the detachment kinetics by retaining the linear terms from the Taylor series expansion of Eq. (9):

$$\tau \frac{\partial \sigma_a(x,t)}{\partial t} = \sigma_{cr}(\gamma(x,t)) - \sigma_a(x,t). \tag{10}$$

Eq. (10) is valid for small delay times ($t \gg \tau$). This equation resembles a relaxation kinetics relation commonly used in modelling chemical reactions (Bedrikovetsky, 1993; Bernasconi, 1976).

The reasoning presented for the delay in particle detachment is valid only for chemically induced particle detachment that is reliant on the diffusion of ionic species. Detachment induced by increasing the flow velocity will be instantaneous (Bedrikovetsky et al., 2012; Oliveira et al., 2014) and so the use of Eq. (2) is valid.

2.2. Assumptions of the model

Assumptions of the model include the incompressibility of the bulk fluid and the additivity of particle and fluid volumes during the detachment, transport, and capture processes. Diffusion and dispersion are neglected for both particle and salt transport. In addition, the effect of the suspended particle concentration on the fluid viscosity is assumed to be negligible. The dependency of the filtration coefficient on the strained particle concentration is neglected based on the assumption of a small concentration of strained particles relative to the number of straining sites. Similarly, distributions of filtration coefficients throughout the porous media due to micro-scale heterogeneity (Ding et al., 2018) are ignored. Fines straining and size exclusion in thin pore throats are assumed irreversible for non-deformable particles and rock (Zhou et al., 2017). Finally, the effect of the attached particles on the permeability of the porous medium is ignored.

2.3. Non-Dimensionalisation

We make use of the dimensionless variables

$$T = \frac{Ut}{\phi L},\ X = \frac{x}{L},\ C = \frac{c}{\Delta\sigma_{cr}},\ S_a = \frac{\sigma_a}{\phi\Delta\sigma_{cr}},\ S_s = \frac{\sigma_s}{\phi\Delta\sigma_{cr}},\ \Lambda = \lambda L$$
$$\Gamma = \frac{\gamma - \gamma_{inj}}{\gamma_i - \gamma_{inj}}\ \varepsilon = \frac{U\tau}{\phi L},\ P = \frac{Pk_0}{U\mu L}, \tag{11}$$

where γ_{inj} and γ_i are the injected and initial fluid salinities respectively, and

$$\Delta\sigma_{cr} = \sigma_{cr}(\gamma_i) - \sigma_{cr}(\gamma_{inj}), \tag{12}$$

is the total detached particle concentration.

In dimensionless form, the system (3)–(5), (7) and (10) becomes

$$\frac{\partial}{\partial T}(C + S_a + S_s) + \alpha\frac{\partial C}{\partial X} = 0. \tag{13}$$

$$\frac{\partial \Gamma}{\partial T} + \frac{\partial \Gamma}{\partial X} = 0. \tag{14}$$

$$\varepsilon\frac{\partial S_a}{\partial T} = S_{cr}(\Gamma) - S_a. \tag{15}$$

$$\frac{\partial S_s}{\partial T} = \Lambda C\alpha. \tag{16}$$

$$1 = -\frac{1}{1 + \beta\phi\Delta\sigma_{cr}S_s}\frac{\partial P}{\partial X}. \tag{17}$$

Initial conditions correspond to a constant fluid salinity, γ_i, and an absence of suspended and strained particles. It will be assumed that initially the attached concentration is equal to the critical retention function at the initial salinity.

$$\Gamma(X,0) = 1$$

$$C(X,0) = 0, S_s(X,0) = 0. \tag{18}$$

$$S_a(X,0) = S_{cr}(\Gamma_i)$$

The inlet boundary condition corresponds to the injection of low salinity water ($\gamma = \gamma_{inj}$) with no suspended particles

$$\Gamma(0,T) = 0, C(0,T) = 0. \tag{19}$$

The inlet boundary condition for the strained particle concentration can be obtained by substituting the boundary condition for the suspended particles, Eq. (19), into the straining kinetics Eq. (16) and integrating. This yields

$$S_s(0,T) = 0. \tag{20}$$

2.4. Exact solution

The method of characteristics can be used to solve Eq. (14) for the fluid salinity subject to the initial and boundary conditions (18), (19):

$$\Gamma(X,T) = \begin{cases} 1, & X > T \\ 0, & X < T \end{cases}. \tag{21}$$

The attached concentration is calculated by integrating Eq. (15) using separation of variables accounting for the initial condition (18):

$$S_a = S_{cr}(\Gamma_i)e^{-\frac{T}{\varepsilon}} + e^{-\frac{T}{\varepsilon}}\int_0^T e^{\frac{T}{\varepsilon}}\frac{S_{cr}(\Gamma)}{\varepsilon}dT. \tag{22}$$

Table 1
Exact formulae for suspended, attached and strained concentration, and impedance in zones *0*, *I* and *II*.

Variables	Region	Exact Solution
Attached Concentration, S_a	$X < T$	$S_{cr}(\Gamma_{inj}) + e^{\frac{X-T}{\varepsilon}}$
	$X > T$	$S_{cr}(\Gamma_i)$
Suspended Concentration, C	$X < \alpha T$	$\frac{1}{\alpha\Lambda\varepsilon+\alpha-1}\left(e^{\frac{X-T}{\varepsilon}} - e^{\frac{\frac{X}{\alpha}-T}{\varepsilon}-\Lambda X}\right)$
	$\alpha T < X < T$	$\frac{1}{\alpha\Lambda\varepsilon+\alpha-1}\left(e^{\frac{X-T}{\varepsilon}} - e^{-\alpha\Lambda\left(\frac{X-T}{\alpha-1}\right)}\right)$
	$X > T$	0
Strained Concentration, S_s	$X < \alpha T$	$1 + \frac{\alpha\Lambda}{\alpha\Lambda\varepsilon+\alpha-1}\left(\frac{1-\alpha}{\alpha\Lambda}e^{-\Lambda X} - \varepsilon e^{\frac{X-T}{\varepsilon}} + \varepsilon\left(e^{-\frac{T}{\varepsilon}+X\left(\frac{1}{\alpha\varepsilon}-\Lambda\right)} - e^{-\Lambda X}\right)\right)$
	$\alpha T < X < T$	$1 + \frac{\alpha\Lambda}{\alpha\Lambda\varepsilon+\alpha-1}\left(-\varepsilon e^{\frac{X-T}{\varepsilon}} + \frac{1-\alpha}{\alpha\Lambda}e^{\frac{\alpha\Lambda(X-T)}{1-\alpha}}\right)$
	$X > T$	0
Impedance, J	$T < 1$	$1 + \frac{\beta\phi\Delta\sigma_{cr}\alpha\Lambda}{\alpha\Lambda\varepsilon+\alpha-1}\left(\frac{\alpha-1}{(\alpha\Lambda)^2}e^{-\alpha\Lambda T} + \varepsilon^2 e^{-\frac{T}{\varepsilon}} + \left(\frac{\varepsilon}{\frac{1}{\alpha\varepsilon}-\Lambda}\right)\left(e^{-\alpha\Lambda T} - e^{-\frac{T}{\varepsilon}}\right) + \frac{\varepsilon}{\Lambda}e^{-\alpha\Lambda T} + T\left(\varepsilon - \frac{1-\alpha}{\alpha\Lambda}\right) - \frac{\alpha-1}{(\alpha\Lambda)^2} - \frac{\varepsilon}{\Lambda} - \varepsilon^2\right)$
	$1 < T < \frac{1}{\alpha}$	$1 + \frac{\beta\phi\Delta\sigma_{cr}\alpha\Lambda}{\alpha\Lambda\varepsilon+\alpha-1}\left(\left(\frac{1-\alpha}{\alpha\Lambda}\right)^2 e^{\frac{\alpha\Lambda(1-T)}{1-\alpha}} + \frac{\alpha-1}{(\alpha\Lambda)^2}e^{-\alpha\Lambda T} - \varepsilon^2\left(e^{\frac{1-T}{\varepsilon}} - e^{-\frac{T}{\varepsilon}}\right) + \left(\frac{\varepsilon}{\frac{1}{\alpha\varepsilon}-\Lambda}\right)\left(e^{-\alpha\Lambda T} - e^{-\frac{T}{\varepsilon}}\right) + \frac{\varepsilon}{\Lambda}e^{-\alpha\Lambda T} - \frac{\alpha-1}{\alpha\Lambda^2} - \frac{\varepsilon}{\Lambda} + \varepsilon - \frac{1-\alpha}{\alpha\Lambda}\right)$
	$T > \frac{1}{\alpha}$	$1 + \frac{\beta\phi\Delta\sigma_{cr}\alpha\Lambda}{\alpha\Lambda\varepsilon+\alpha-1}\left(\frac{\alpha-1}{\alpha\Lambda^2}\left(e^{-\alpha\Lambda} - 1\right) - \varepsilon^2\left(e^{\frac{1-T}{\varepsilon}} - e^{-\frac{T}{\varepsilon}}\right) + \left(\frac{\varepsilon}{\frac{1}{\alpha\varepsilon}-\Lambda}\right)\left(e^{-\frac{T}{\varepsilon}+\left(\frac{1}{\alpha\varepsilon}-\Lambda\right)} - e^{-\frac{T}{\varepsilon}}\right) + \frac{\varepsilon}{\Lambda}\left(e^{-\Lambda} - 1\right) + \varepsilon - \frac{1-\alpha}{\alpha\Lambda}\right)$

The integration is performed separately in the two regions separated by the fluid front, $X = T$. The resulting expressions are presented in Table 1.

Substituting the equation for the particle straining rate into the mass balance equation for particles yields

$$\frac{\partial C}{\partial T} + \alpha\frac{\partial C}{\partial X} = -\alpha\Lambda C - \frac{\partial S_a}{\partial T}. \tag{23}$$

With an explicit expression for the detachment rate, Eqs. (13), (15), (16) are reduced to a single hyperbolic equation. This equation can be solved with the method of characteristics (Polyanin and Zaitsev, 2011; Polyanin and Manzhirov, 2007).

The solution space is naturally divided into three regions: ahead of the fluid front, ($X > T$, region *0*), between the fluid front and the suspended particle front, ($T > X > \alpha T$, region *I*), and behind the suspended particle front, ($\alpha T > X$, region *II*). These regions are shown in Fig. 3a. The solution for Eq. (23) will now be presented for all three regions.

In region *0*, evaluated along parametric curves given by,

$$\frac{dX}{dT} = \alpha, \tag{24}$$

the partial differential equation (PDE) (23) reduces to an ordinary differential equation (ODE)

$$\frac{dC}{dT} = -\alpha\Lambda C. \tag{25}$$

Using separation of variables and accounting for initial condition (18) yields the solution

$$C = 0. \tag{26}$$

To solve for the suspended concentration in region *I*, an initial condition is required along the salinity front $X = T$. This condition is determined by applying a mass balance condition on this front (Bedrikovetsky, 1993; Lake, 2010)

$$[C + S_a + S_s]D = \alpha[C]. \tag{27}$$

where square brackets indicate the change in a variable across the parametric curve with slope D. In this case, the parametric curve is the salinity front, and so this slope is equal to one.

Eq. (16) indicates that the strained concentration is continuous wherever the suspended concentration is finite. Thus, along the salinity front

$$[S_s] = 0. \tag{28}$$

Similarly, the attached concentration is continuous by Eq. (15)

$$[S_a] = 0. \tag{29}$$

Then the mass balance condition reduces to

$$[C] = \alpha[C]. \tag{30}$$

The solution of which is

$$[C] = 0. \tag{31}$$

Thus, the suspended concentration is also continuous across the salinity front. This analysis permits the use of the solution in region *0* for the initial condition in region *I*.

In this region, along parametric curves given by Eq. (24), the PDE (23) reduces to

$$\frac{dC}{dT} = -\alpha\Lambda C - \frac{\partial S_a}{\partial T}. \tag{32}$$

Using the expression for the attached concentration behind the salinity front, this equation becomes

$$\frac{dC}{dT} = -\alpha\Lambda C + \frac{1}{\varepsilon}e^{\frac{X(T)-T}{\varepsilon}}. \tag{33}$$

The equation $X(T)$ is derived from Eq. (24)

$$X - X_0 = \alpha(T - T_0), \tag{34}$$

where the initial conditions are provided along some curve $T_0 = f(X_0)$.

As specified above, the initial conditions for this region are given along the salinity front:

$$X = T : C = 0. \tag{35}$$

It then follows that

$$X_0 = T_0, \tag{36}$$

and therefore

$$X(T) = \alpha T + T_0(1 - \alpha). \tag{37}$$

Substituting this equation into Eq. (33) yields an ordinary differential equation in T that can be integrated to obtain an explicit expression for C.

In region *II*, evaluating the PDE (23) along characteristic curves given by

$$\frac{dT}{dX} = \frac{1}{\alpha}, \tag{38}$$

reduces the PDE to an ODE of the form

$$\frac{dC}{dX} = -\Lambda C - \frac{1}{\alpha}\frac{\partial S_a}{\partial T}. \tag{39}$$

Substituting the solution for the attached concentration gives

$$\frac{dC}{dX} = -\Lambda C + \frac{1}{\alpha\varepsilon} e^{\frac{X-T(X)}{\varepsilon}}. \tag{40}$$

Solving Eq. (38) yields the same expression for the characteristic lines as was derived for region *I*. For region *II*, the boundary condition (19) is used, and so $X_0 = 0$. Substituting the resulting expression $T(X)$ and integrating yields the final expression for the suspended concentration in this region.

All expressions for the suspended concentration are explicit and are presented in Table 1.

The solution for the strained concentration is obtained by substituting the expression for the suspended concentration into Eq. (16) and integrating subject to the initial condition (18). This process results in explicit expressions for the strained concentration which can be found in Table 1.

The dimensionless pressure drop is then obtained by integrating Eq. (17). The resulting expression is

$$P(0,T) - P(1,T) = \Delta P = 1 + \phi\Delta\sigma_{cr}\beta \int_0^1 S_s dX. \tag{41}$$

Under the linear flow regime and constant injection rate conditions used in this work, the dimensionless pressure drop is equivalent to the impedance

$$J = \frac{q_0}{\Delta p_0}\frac{\Delta p}{q} = \Delta P. \tag{42}$$

The solution for the Impedance in each zone is presented in Table 1.

3. Qualitative analysis of the solution

3.1. General behaviour of the solution

Fig. 3a presents a schematic of the solution space (X,T) and Fig. 3b–d present general profiles for the attached, suspended, and strained particle concentrations respectively.

The attached concentration takes its initial value $S_{cr}(\gamma_i)$ at time $T = 0$ and begins to decrease upon the arrival of the salinity front. Due to differences in the arrival time of the salinity front, the attached particle concentration will always monotonically increase across the core. The profile of attached particles will tend asymptotically to the final value $S_{cr}(\gamma_{inj})$, corresponding to the injected fluid salinity.

The suspended concentration begins at zero throughout the core and remains zero ahead of the salinity front and at the core inlet. Behind the salinity front, the suspended concentration will increase or decrease based on the balance between the transport, detachment, and straining process. Due to the finite concentration of detached particles, the suspended concentration will eventually tend to zero, as all particles either strain or reach the core outlet.

The strained concentration also begins at zero, and due to the absence of suspended particles, is also zero ahead of the salinity front. As straining is an irreversible process, the strained particle concentration will grow monotonically with time, tending to a finite profile as time tends to infinity. This profile is zero at $X = 0$ and will tend to a constant value some distance from the core inlet. The consequence of a variable strained concentration profile is that the permeability of the porous medium following fines migration will be location-dependent, even after an infinitely long injection period. The non-uniform damage profile supports the necessity of coupling laboratory testing with mathematical models such as the one presented in this work. Simply using the permeability damage ratio as an indication of the extent of fines migration is not indicative of the extent of damage that will occur on larger scales or for different flow regimes.

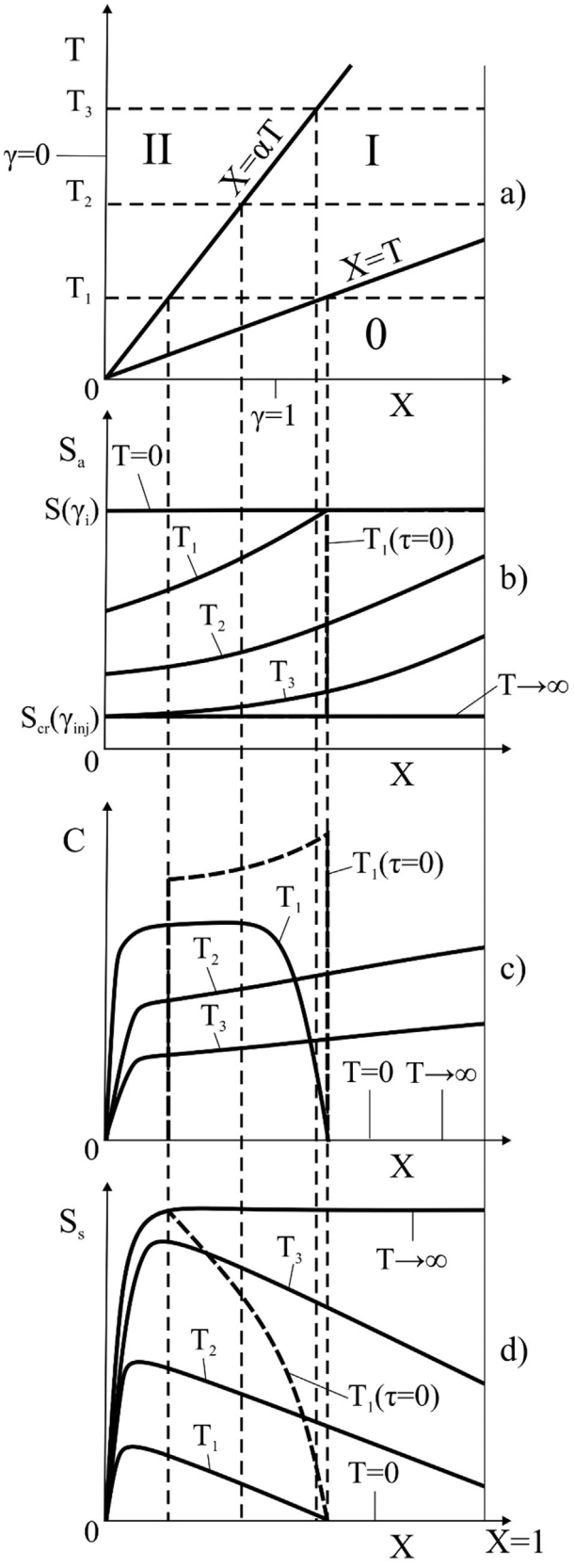

Fig. 3. Exact solution for low-salinity induced fines migration: (a) X(dimensionless distance) – T(dimensionless time) plane demonstrating the fluid ($X = T$) and particle ($X = \alpha T$) fronts, (b) Attached concentration profiles initially $S_a(X,T_j)$ initially ($T_j = 0$), at three intermediate times, $j = 1, 2, 3$ and at infinity ($T_j \to \infty$), (c) Suspended concentration profiles $C(X,T_j)$, d) strained concentration profiles $S_s(X,T_j)$. Dotted lines show the behaviour of the model with no delay at moment T_1.

3.2. Sensitivity analysis

To further elicit the behaviour of the model, sensitivity analysis has been performed on two of the primary parameters of the model. For all calculations, unless otherwise stated, the model parameters are: $\phi = 0.2$, $\alpha = 0.03$, $\varepsilon = 5$, $\Lambda = 100$, $\beta = 1000$, and $\Lambda\sigma_{cr} = 10^{-3}$.

Sensitivity analysis on the dimensionless delay factor, ε, is presented in Fig. 4. Both the impedance and the outlet suspended concentration, $C(1,T)$ are shown for 50 pore volumes injected (PVI). A larger delay time prolongs the time until stabilisation of the impedance, however the final value is independent of the delay time. Trends for the suspended concentration show a sharp increase after 1 PVI followed shortly by an exponential decline to zero. Higher delay times result in smaller peaks but show more pronounced tails. Similar to the impedance, the area under each curve, or the total concentration collected at the outlet, is independent of the delay time.

Fig. 5 shows the sensitivity of the model with varying values of the dimensionless filtration coefficient, Λ. A larger filtration coefficient implies a greater probability of straining. As a result, the total strained concentration in the core is higher, and the resulting impedance is also larger. When a higher proportion of detached particles are strained, the total concentration of particles that reaches the core outlet will be lower. Thus, the outlet concentration is strictly lower when the filtration coefficient is higher.

3.3. Behaviour of the solution with instant detachment

It is interesting to note the behaviour of the solution with the delay factor tending to zero. For comparison, profiles for the attached, suspended, and strained particle concentrations are shown in Fig. 3 at the time T_1. The dashed curves correspond to the case of zero delay, while the delay is non-zero for continuous lines.

The solution for the suspended concentration in Table 1 has an explicit expression for this limit:

$$C(X,T) = \begin{cases} 0 & X < \alpha T \\ \frac{1}{\alpha - 1}\left(1 - e^{-\alpha\Lambda\left(\frac{X-T}{\alpha-1}\right)}\right) & \alpha T < X < T \\ 0 & X > T \end{cases}. \tag{43}$$

The absence of a finite detachment rate results in discontinuities in the suspended concentration at both the fluid and particle front. Due to the absence of suspended particles behind the particle front ($X = \alpha T$), all particle concentrations and consequently the impedance will stabilise after time $T = 1/\alpha$ when particles detached at the inlet reach the core outlet. This property is absent in the solution derived in this paper as particles continue to detach after the arrival of the salinity front.

If we further allow the drift delay factor to be equal to one, the suspended concentration profile will tend to a delta function, with all suspended particles concentrated on the salinity front with an

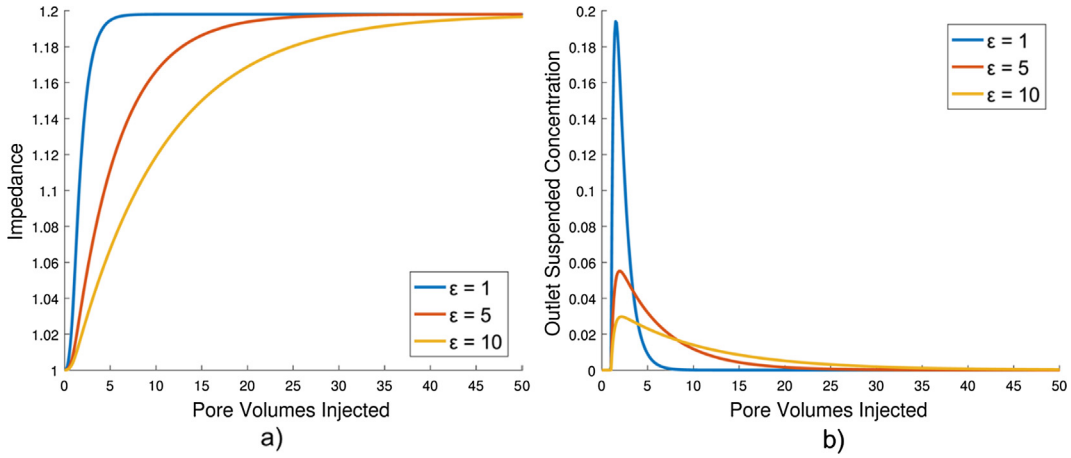

Fig. 4. Sensitivity of the analytical model with the dimensionless delay factor, ε: (a) Impedance, (b) Outlet suspended particle concentration.

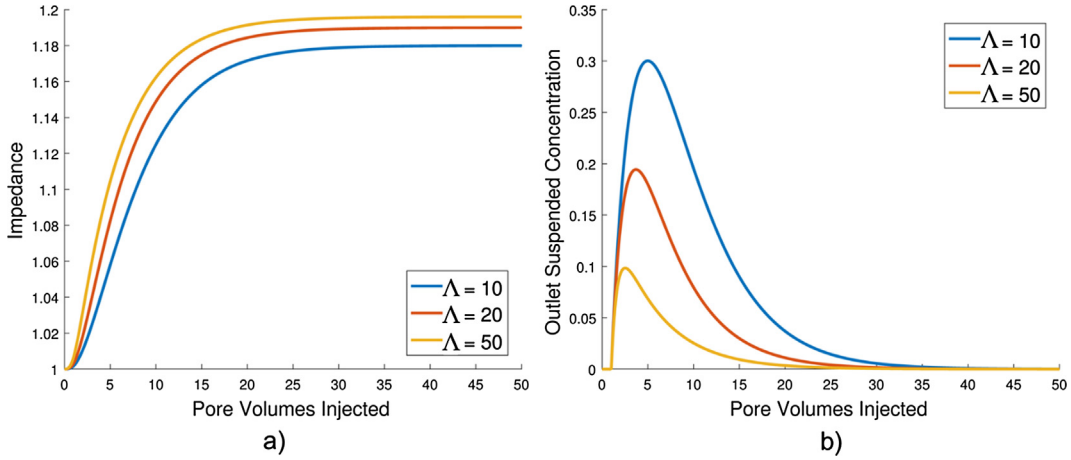

Fig. 5. Sensitivity of the analytical model with the dimensionless filtration coefficient, Λ: (a) Impedance, (b) Outlet suspended particle concentration.

infinite concentration. This special case, where $\alpha = 1$ and $\varepsilon = 0$, is singular. Introduction of diffusion into the governing system will smooth the concentration shock and regularise the solution (Polyanin and Zaitsev, 2011). The solution with diffusion is obtained by using the method of matched asymptotic expansions, which will produce an approximate solution. In this work, we have shown that the introduction of a delay in particle detachment can also regularise the solution, and an exact solution is still obtainable.

If the drift delay factor is set to one in the solution with delayed detachment found in Table 1, the suspended concentration still has a finite distribution. Thus, only the drift delay factor or a delay in detachment is required to produce a finite solution for the suspended particle concentration.

3.4. Comparison between exact and numerical solutions

The system of Eqs. (13)-(17) subject to initial and boundary conditions (18)-(20) has been solved numerically using an implicit first-order finite difference scheme implemented in Matlab. The system of linear equations was solved using a forward substitution solver in Matlab. The parameter values used are $\phi = 0.2$, $\alpha = 0.05$, $\varepsilon = 0.25$, $\Lambda = 10$, $\beta = 2000$, and $\Delta\sigma_{cr} = 10^{-3}$. The (X,T) space was uniformly discretised with $\Delta X = 1 \times 10^{-4}$ and $\Delta T = 5 \times 10^{-3}$. The resulting suspended and strained particle profiles for both the exact and numerical solutions is shown in Fig. 6. The curves coincide well showing that the agreement between the two solutions is high.

4. Laboratory study

A laboratory coreflooding study has been performed on four consolidated sandstone cores. The methodology of these tests will be presented below.

4.1. Rock and fluids

All cores were cut from the same Grey Berea sample. XRD analysis was conducted on a sample from the core using a Bruker D8 ADVANCE Powder X-ray Diffractometer with a Cu-radiation source. The results demonstrated a dominance of quarts (78.2 wt %) with a significant clay fraction primarily composed of kaolinite (3.1%) and illite (2.6%). The cores have varying lengths and were injected with solutions of varying salinity. The core properties and injection conditions are presented in Table 2. The cores were de-aerated using a vacuum pump for 24 h and consequently saturated with a 0.6 mol/L NaCl solution under vacuum for a further 24 h. All solutions prepared for these tests used analytical grade sodium chloride and MilliQ deionised water.

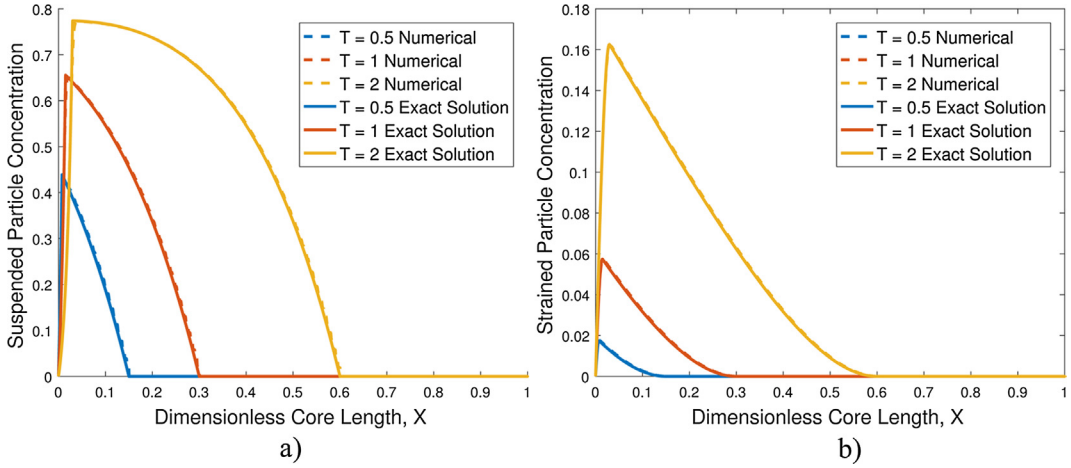

Fig. 6. Comparison between the exact analytical and the numerical solutions: (a) Suspended particle concentration profiles, (b) Strained particle concentration profiles.

Table 2
Core properties and fitted model parameters for the laboratory coreflooding tests.

		Core 1	Core 2	Core 3	Core 4
Core Properties	Core length, cm	1.84	3.899	5.854	10.191
	Initial porosity	0.185	0.185	0.186	0.193
	Initial permeability, mD	74.38	74.08	78.82	100.07
Injection Conditions	Injected Salinity, Mol/L	0.005	0.01	0.03	0.03
	Injection Velocity, cm/s	2.93E−03	2.93E−03	2.93E−03	2.93E−03
Model Parameters	Drift delay factor, α	0.1338	0.4386	0.7396	0.6265
	Delay factor, τ (s)	438.02	359.12	578.91	1045.73
	Dimensionless delay factor, ε	3.78	1.46	1.56	1.56
	Filtration coefficient, λ (1/m)	110.19	19.71	27.86	22.21
	Dimensionless filtration coefficient, Λ	2.03	0.77	1.63	2.26
	Formation damage coefficient, β	1.799E+07	3.131E+07	1.542E+07	2.588E+07
	Detached particle concentration, $\Delta\sigma_{cr}$	2.342E−04	2.427E−04	4.676E−05	3.937E−05
	Coefficient of determination, R^2 (Impedance)	0.9801	0.9966	0.9768	0.9913
	Coefficient of determination, R^2 (Accumulated Concentration)	0.7156	0.7694	0.8487	0.9088

4.2. Equipment and set-up

The laboratory set-up used in these tests is presented schematically in Fig. 7. Aqueous salt solutions are injected into the core at a constant flow rate using a Prep pump. The core is held within a TEMCO HCH-1.5 coreholder, constrained axially by two flow distributors, and radially by a viton sleeve. An overburden pressure of 1000 psi was maintained around the viton sleeve during the tests to minimise annular flow between the core and the sleeve. The pressure difference across the core was measured continuously using a series of Yokogawa EJX 110A differential pressure transmitters. Four differential pressure transducers with capacities of 1, 10, 100, and 1000 psi are used to accurately cover a wide range of pressure drawdowns. Pressure differences above 1000 psi are measured using two Keller PA-33X pressure transmitters at the inlet and outlet. A thermocouple is connected to the inlet fluid line to measure the fluid temperature continuously throughout the test. The fluid viscosity used to calculate the core permeability is corrected for temperature, pressure, and salinity in real-time according to previously established correlations (Aleksandrov et al., 2012; Kestin et al., 1981).

The fluid was collected at the outlet in test-tubes using a GE Frac 920 sample collection carousel. The effluent suspended particle concentration for each sample was measured using a POLA-2000 particle counter.

4.3. Laboratory-study methodology

Following the saturation of the core in 0.6 M NaCl, the core was placed in the coreholder and the overburden pressure was established. The test then began by injecting a 0.6 M NaCl solution into the core at a flow rate of 2 mL/min. The injection of the low salinity solution commenced only after complete stabilisation of the core permeability had been achieved. In each core, a period of 24 h was used to ensure complete stabilisation. Continuous pressure drop measurements were recorded using data collection software.

5. Matching the laboratory data by the analytical model

Two sets of data from the experiment were used to tune the model parameters. These were the dimensionless, normalised pressure drop, or the impedance, and the accumulated outlet concentration

$$C_{acc}(T) = \alpha \int_0^T C(1,T)dT. \tag{44}$$

Both data sets were tuned simultaneously within Matlab (MathWorks Inc, 2016) using a genetic least-squares algorithm. This algorithm was used because it has a greater ability to avoid convergence to local minima. The algorithm minimised the observed difference between the model and experimental data by tuning five model parameters: the drift-delay factor, α, the dimensionless delay factor, ε, the dimensionless filtration coefficient, Λ, the formation damage coefficient, β, and the total detached concentration, $\Delta\sigma_{cr}$.

Figs. 8–11 show the experimental results alongside the fitted model. The fitting parameters and coefficients of determination are presented in Table 2. The results are presented only for the second stage of injection, where the introduction of low-salinity water resulted in significant permeability decline for all cores. During the permeability decline, a significant volume of suspended particles was collected at the outlet for all tests.

The model fitting demonstrates good agreement between the model and the experimental data. This is supported by the high value of R^2 calculated for the two plots. The fitting of the impedance curves is significantly better than for the accumulated concentration. Measurement of the suspended particle concentration required significant dilution of the samples which would have introduced a significant error beyond the measurement error of the apparatus. This error supports the difference in fitting quality of the two data sets. The discrepancy is most prominent in the two shorter cores, suggesting that a portion of this error could be a result of ignoring diffusion.

If compared with tuning of the same experimental data by the model with instant fines release, introduction of the delay factor increases the overall coefficient of determination by 0.02 to 0.1.

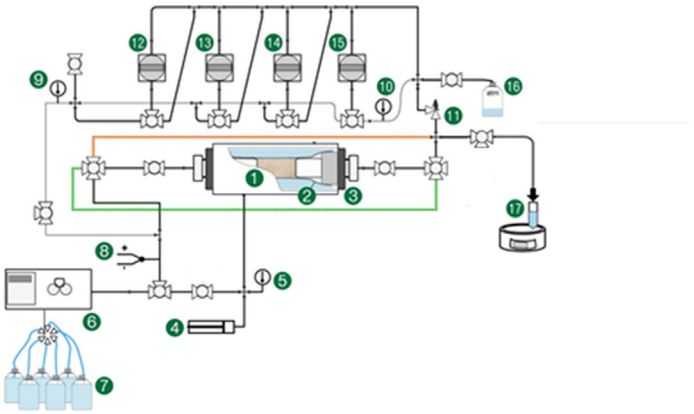

Number	Apparatus	Number	Apparatus
1	Core Holder	7	Injection Solutions
2	Viton Sleeve	8	Thermocouple
3	Flow Distributors	11	Safety Valve
4	Overburden Pressure Piston	12-15	Differential Pressure Transmitters
5, 9, 10	Pressure Transmitter	16	Waste collection beaker (For flushing)
6	Injection Pump	17	Sample Collection Carousel

Fig. 7. Schematic of experimental set-up with labels for primary components.

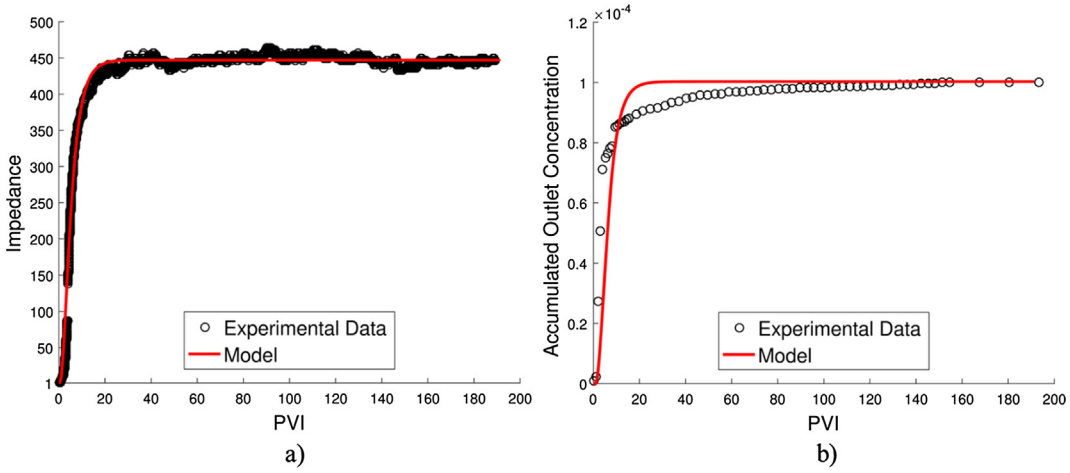

Fig. 8. Experimental data and tuned theoretical model for core 1: (a) Impedance, and (b) Accumulated outlet concentration.

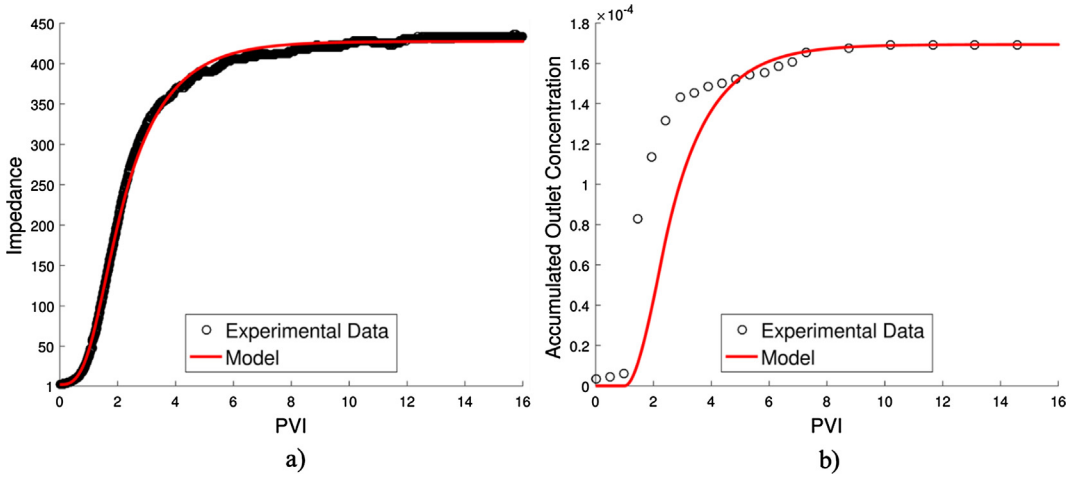

Fig. 9. Experimental data and tuned theoretical model for core 2: (a) Impedance, and (b) Accumulated outlet concentration.

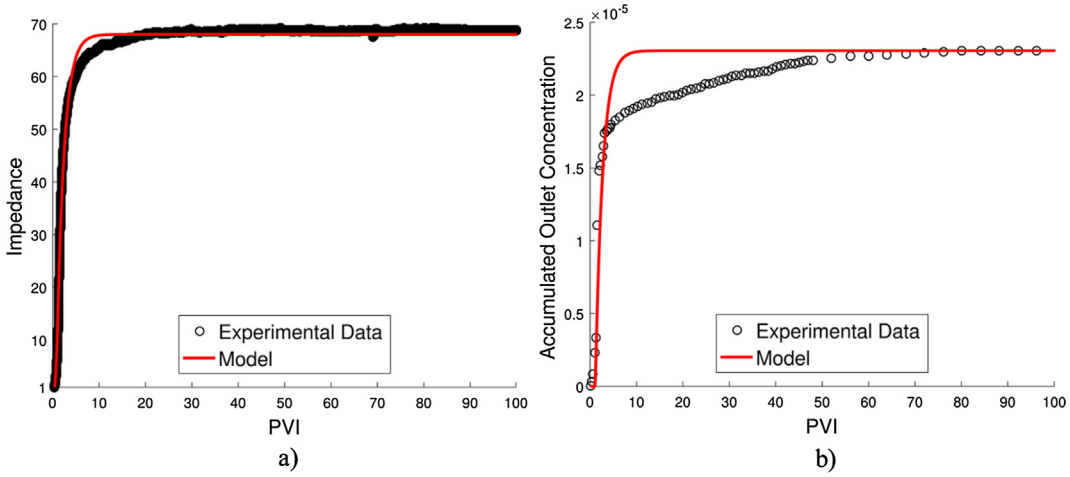

Fig. 10. Experimental data and tuned theoretical model for core 3: (a) Impedance, and (b) Accumulated outlet concentration.

6. Discussion

Planning and design of numerous technologies in environmental, chemical and petroleum engineering, where suspension-colloidal flows in porous media occur, are based on mathematical modelling. Simultaneous application of numerical and analytical models yields better understanding of the physical phenomena and allows for multi-variant comparison of different technological

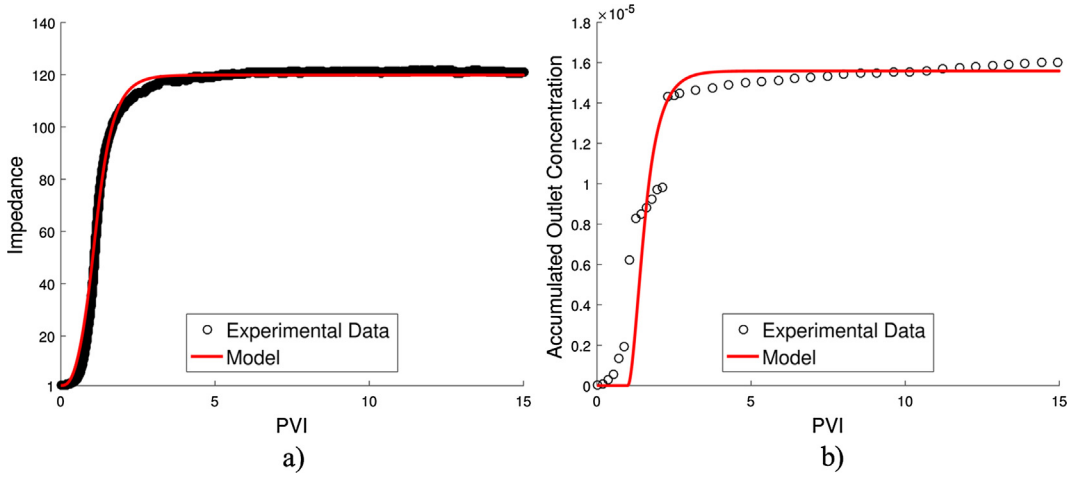

Fig. 11. Experimental data and tuned theoretical model for core 4 (a) Impedance, and (b) Accumulated outlet concentration.

decisions. The above applications have motivated numerous studies on exact solutions for one-dimensional (1D) suspension-colloidal flows in porous media.

In this work, the exact solution has been used to tune laboratory data to obtain model coefficients. This process requires computing the direct (forward) model many times and consequently any incremental computation time introduced by numerical techniques can be prohibitive to convergence of the fitting procedure. In addition, the exact solution presented here can be used as a benchmark for numerical models. The analytical model developed can also be used in three-dimensional (3D) reservoir simulation using stream-line techniques (Datta-Gupta and King, 2007).

The analytical solution is presented in an explicit form, allowing for direct implementation into widely available software like Matlab or Microsoft Excel. This allows interpreting laboratory data or making field-scale predictions without having to use computationally expensive numerical methods.

The laboratory results presented in Figs. 8–11 impedance values up to 450. Despite this substantial damage to the rock permeability, inlet pressures did not exceed the pressure limits of the injection pump (4000 psi) and the differential pressure transducers (1,10,100,1000 psi) of our experimental set-up. Similar papers (Sarkar and Sharma, 1990) have shown Impedance values growing up to ~1000.

The laboratory test conducted in this work shows significant variation in the stabilised value of impedance between the four cores. While a portion of this variation could be a result of heterogeneity, the observed trends can be explained in the context of the proposed model.

Firstly, for the same injection conditions, a longer core length results in a larger stabilised impedance. This follows directly from the strained concentration profiles presented in Fig. 3. While S_s reaches a constant value far from the core inlet, even after stabilization ($T \to \infty$) the strained particle concentration is small close to the inlet. The size of this low-damage zone does not change with the core length, and so for longer cores, its effect on the overall impedance will be small. Thus, when the only difference between two cores is the core length (e.g. Cores 3 and 4), we expect the longer core to have a greater stabilised impedance. Mathematically, the dependence of the stabilised impedance on the core length follows from the fact that the solution presented in Table 1 is not self-similar.

The other important condition which varies across the laboratory tests is the injected salinity. As outlined in the introduction, a lower injected salinity will result in more particle detachment and consequently a higher impedance. This is reflected in the laboratory results.

The variation in the model parameters obtained from tuning the laboratory data is attributed to heterogeneity in the clay content and pore structure of different rocks used in this study. This heterogeneity is also noted to have an effect on the initial permeability, which varies from 74 to 100 mD.

The laboratory test for full characterisation of the particulate flow system with delayed particle detachment includes measurements of breakthrough concentration and pressure drop across the core. Pressure measurements require simple and robust equipment providing high accuracy, while particle counters are cumbersome and expensive with low accuracy of concentration measurements. An alternative option is the use of pressure drop across the core section together with the overall pressure drop. This so-called 3-point-pressure method has been successfully developed for suspension-colloidal flow without detachment (Bedrikovetsky et al., 2001). Application of 3-point-pressure test for fines migration could simplify the equipment an increase the accuracy of measurements, yielding more reliable laboratory-based field-scale predictions.

Retention profiles during suspension-colloidal flows can be measured using X-ray computed micro-tomography (Al-Yaseri et al., 2016; Mikolajczyk et al., 2018). Tuning of the profiles $S_s(x, t)$ using the explicit formula, presented in Table 1, would improve the accuracy of determining the model constants.

The presented single-phase model with delayed fines detachment can be generalised for two-phase suspension-colloidal flows. Besides electrostatic and drag forces, the attached particles are subject to capillary forces, exerting from the menisci between two phases (Zhang and Hassanizadeh, 2017). The particles attached to menisci are transported by the phase-separating surface, which is not determined by the Darcy velocity. The full system of equations includes Maxwell constitutive equations (Shapiro, 2015; Shapiro, 2016).

7. Conclusions

Mathematical and laboratory modelling of suspension-colloidal transport in porous media accounting for the kinetics of particle detachment allows drawing the following conclusions:

1. The one-dimensional problem for low-salinity water induced fines migration with delay allows for an exact solution.

2. The solution provides explicit formulae for the suspended, attached, and strained particle concentrations as well as the impedance.
3. Introduction of the delay in detachment removes the discontinuities in the suspended concentration present in the solution with instantaneous detachment.
4. For the case where the particles and fluid propagate with the same velocity, the introduction of the delay factor regularises the problem.
5. The exact solution exhibits close agreement with laboratory coreflooding data.

Acknowledgements

The authors are grateful to Hayden Jarvis, Rangga Kusuma, Huynh Minh Tuan Tran, and Dao Hanh Ly Tu for their assistance with the laboratory study. In addition, the authors would like to thank Dr Tony Hall for performing the XRD study.

References

Akhmetgareev, V., Khisamov, R., 2015. 40 Years of low-salinity waterflooding in pervomaiskoye field, Russia: incremental oil, SPE European formation damage conference and exhibition. Soc. Petrol. Eng.
Aleksandrov, A.A., Dzhuraeva, E.V., Utenkov, V.F., 2012. Viscosity of aqueous solutions of sodium chloride. High Temp. 50 (3), 354–358.
Al-Yaseri, A., Al Mukainah, H., Lebedev, M., Barifcani, A., Iglauer, S., 2016. Impact of fines and rock wettability on reservoir formation damage. Geophys. Prospecting 64 (4), 860–874.
Barkman, J., Abrams, A., Darley, H., Hill, H., 1975. An oil-coating process to stabilize clays in fresh waterflooding operations (includes associated paper 6405). J. Petrol. Technol. 27 (09), 1053–1059.
Bedrikovetsky, P., 1993. Mathematical Theory of Oil & Gas Recovery. Kluwer Academic Publishers, London-Boston-Dordrecth.
Bedrikovetsky, P. et al., 2001. Characterisation of deep bed filtration system from laboratory pressure drop measurements. J. Petrol. Sci. Eng. 32 (2–4), 167–177.
Bedrikovetsky, P., Siqueira, F.D., Furtado, C.A., Souza, A.L.S., 2011. Modified particle detachment model for colloidal transport in porous media. Transport. Porous Med. 86 (2), 383–413.
Bedrikovetsky, P., Zeinijahromi, A., Siqueira, F.D., Furtado, C.A., de Souza, A.L.S., 2012. Particle detachment under velocity alternation during suspension transport in porous media. Transport. Porous Med. 91 (1), 173–197.
Bergendahl, J., Grasso, D., 2000. Prediction of colloid detachment in a model porous media: hydrodynamics. Chem. Eng. Sci. 55 (9), 1523–1532.
Bernasconi, C.F., 1976. Relaxation Kinetics. Academic Press, New York, New York.
Bhattacharya, S.S. et al., 2016. Fines mobilisation by low-salinity water injection: 3-point-pressure tests. In: SPE International Conference & Exhibition on Formation Damage Control, Lafayette, Louisiana, USA.
Chequer, L., Vaz, A., Bedrikovetsky, P., 2018. Injectivity decline during low-salinity waterflooding due to fines migration. J. Petrol. Sci. Eng.
Civan, F., 2014. Reservoir Formation Damage. Gulf Professional Publishing, Burlington, MA, USA.
Datta-Gupta, A., King, M.J., 2007. Streamline Simulation: Theory and Practice. Society of Petroleum Engineers.
Derjaguin, B., Landau, L., 1941. Theory of the stability of strongly charged lyophobic sols and of the adhesion of strongly charged particles in solutions of electrolytes. Acta Physicochim. URSS 14 (6), 633–662.
Ding, B.B., Li, C.L., Wang, Y.W., Xu, J.H., 2018. Effects of pore size distribution and coordination number on filtration coefficients for straining-dominant deep bed filtration from percolation theory with 3D networks. Chem. Eng. Sci. 175, 1–11.
Goldenberg, L.C., Magaritz, M., Mandel, S., 1983. Experimental investigation on irreversible changes of hydraulic conductivity on the seawater-freshwater interface in coastal aquifers. Water Resour. Res. 19 (1), 77–85.
Goldman, A.J., Cox, R.G., Brenner, H., 1967. Slow viscous motion of a sphere parallel to a plane wall - II Couette flow. Chem. Eng. Sci. 22, 653–660.
Joekar-Niasar, V., Mahani, H., 2016. Nonmonotonic pressure field induced by ionic diffusion in charged thin films. Indus. Eng. Chem. Res. 55 (21), 6227–6235.
Kalantariasl, A., Bedrikovetsky, P., 2013. Stabilization of external filter cake by colloidal forces in a "well–reservoir" system. Indus. Eng. Chem. Res. 53 (2), 930–944.
Kestin, J., Khalifa, H.E., Correia, R.J., 1981. Tables of the dynamic and kinematic viscosity of aqueous nacl solutions in the temperature-range 20–150-degrees-C and the pressure range 0.1–35 MPa. J. Phys. Chem. Ref. Data 10 (1), 71–87.
Khilar, K.C., Fogler, H.S., 1998. Migrations of fines in porous media. Kluwer Academic Publishers, Dordrecht.
Kia, S., Fogler, H.S., Reed, M., 1986. Effect of pH on colloidally induced fines migration. J. Colloid Interface Sci. 118 (1), 158–168.
Kia, S., Fogler, H.S., Reed, M., 1987. Effect of salt composition on clay release in Berea sandstones, SPE International Symposium on Oilfield Chemistry. Soc. Petrol. Eng.
Kretzschmar, R., Borkovec, M., Grolimund, D., Elimelech, M., 1999. Mobile subsurface colloids and their role in contaminant transport. Adv. Agron. 66, 121–193.
Kuo, R.J., Matijevic, E., 1979. Particle adhesion and removal in model systems: Part 2. – monodispersed chromium hydroxide on steel. J. Chem. Soc., Farad. Trans. 1: Phys. Chem. Condens. Phases 75, 2014–2026.
Lake, L.W., 2010. Enhanced oil recovery. Society of Petroleum Engineers, Richardson, TX.
Mahani, H., Berg, S., Ilic, D., Bartels, W.B., Joekar-Niasar, V., 2015. Kinetics of low-salinity-flooding effect. Spe J. 20 (1).
Mikolajczyk, G., Huang, L., Wilhelm, M., Dreher, W., Odenbach, S., 2018. Colloid deposition in monolithic porous media - Experimental investigations using X-ray computed microtomography and magnetic resonance velocimetry. Chem. Eng. Sci. 175, 257–266.
Oliveira, M.A. et al., 2014. Slow migration of mobilised fines during flow in reservoir rocks: Laboratory study. J. Petrol. Sci. Eng. 122, 534–541.
Pellicer, S.M., Aguilella, V.M., 1986. Ionic transport and space charge density in electrolytic solutions as described by Nernst-Planck and poisson equations. J. Phys. Chem. 90 (6045–6050).
Polyanin, A.D., Manzhirov, A.V., 2007. Handbook of mathematics for engineers and scientists. CRC Press.
Polyanin, A., Zaitsev, V., 2011. Handbook of Nonlinear Partial Differential Equations. CRC Press.
Prommer, H. et al., 2013. Final Report - Aquifer storage and recovery of potable water in the Leederville Aquifer, CSIRO: Water for a Healthy Country National Research Flagship, Australia.
Salimi, S., Ghalambor, A., 2011. Experimental study of formation damage during underbalanced-drilling in naturally fractured formations. Energies 4 (10), 1728–1747.
Sarkar, A.K., Sharma, M.M., 1990. Fines migration in two-phase flow. J. Petrol. Technol. 42 (05), 646–652.
Shapiro, A.A., 2015. Two-phase immiscible flows in porous media: The Mesocopic Maxwell-Stefan approach. Transport. Porous Med. 107 (2), 335–363.
Shapiro, A.A., 2016. Mechanics of the separating surface for a two-phase co-current flow in a porous medium. Transport. Porous Med. 112 (2), 489–517.
Tada, R., Maliva, R., Siever, R., 1987. A new mechanism for pressure solution in porous quartzose sandstone. Geochim. Cosmochim. Ac 51 (9), 2295–2301.
Verwey, E.J.W., Overbeek, J.T.G., 1999. Theory of the stability of lyophobic colloids. Courier Corporation.
Xie, Q., Saeedi, A., Delle Piane, C., Esteban, L., Brady, P.V., 2017. Fines migration during CO_2 injection: Experimental results interpreted using surface forces. Int. J. Greenhouse Gas Control 65, 32–39.
You, Z., Bedrikovetsky, P., Badalyan, A., Hand, M., 2015. Particle mobilization in porous media: Temperature effects on competing electrostatic and drag forces. Geophys Res Lett 42 (8), 2852–2860.
Yu, C., Gao, B., Muñoz-Carpena, R., 2012. Effect of dense vegetation on colloid transport and removal in surface runoff. J. Hydrol. 434, 1–6.
Yuan, B. et al., 2017. Permeability reduction of berea cores owing to nanoparticle adsorption onto the pore surface: mechanistic modeling and experimental work. Energy Fuel 31 (1), 795–804.
Zeinijahromi, A., Al-Jassasi, H., Begg, S., Bedrikovetski, P., 2015. Improving sweep efficiency of edge-water drive reservoirs using induced formation damage. J. Petrol. Sci. Eng. 130, 123–129.
Zhang, Q.L., Hassanizadeh, S.M., 2017. The role of interfacial tension in colloid retention and remobilization during two-phase flow in a polydimethylsiloxane micro-model. Chem. Eng. Sci. 168, 437–443.
Zhou, K. et al., 2017. An efficient LBM-DEM simulation method for suspensions of deformable preformed particle gels. Chem. Eng. Sci. 167, 288–296.

4.2 Effects of delayed particle detachment on injectivity decline due to fines migration

Russell, T., Wong, K., Zeinijahromi, A., Bedrikovetsky, P.

Journal of Hydrology, Volume 564, 2018, Pages 1099-1109

Statement of Authorship

Title of Paper	Effects of delayed particle detachment on injectivity decline due to fines migration
Publication Status	☑ Published ☐ Accepted for Publication ☐ Submitted for Publication ☐ Unpublished and Unsubmitted w ork w ritten in manuscript style
Publication Details	Thomas Russell, Kiet Wong, Abbas Zeinijahromi, Pavel Bedrikovetsky, Effects of delayed particle detachment on injectivity decline due to fines migration, Journal of Hydrology, Volume 564, 2018, Pages 1099-1109

Principal Author

Name of Principal Author (Candidate)	Thomas Russell		
Contribution to the Paper	Performed calculations and derivations, Performed laboratory tests, contributed to writing		
Overall percentage (%)	60%		
Certification:	This paper reports on original research I conducted during the period of my Higher Degree by Research candidature and is not subject to any obligations or contractual agreements with a third party that would constrain its inclusion in this thesis. I am the primary author of this paper.		
Signature		Date	16/02/2021

Co-Author Contributions

By signing the Statement of Authorship, each author certifies that:

i. the candidate's stated contribution to the publication is accurate (as detailed above);

ii. permission is granted for the candidate in include the publication in the thesis; and

iii. the sum of all co-author contributions is equal to 100% less the candidate's stated contribution.

Name of Co-Author	Kiet Wong		
Contribution to the Paper	Performed laboratory tests		
Signature		Date	16/02/2021

Name of Co-Author	Abbas Zeinijahromi		
Contribution to the Paper	Design of laboratory tests		
Signature		Date	

Please cut and paste additional co-author panels here as required.

Name of Co-Author	Pavel Bedrikovetsky		
Contribution to the Paper	Contributed to writing, contributed to derivations		
Signature		Date	17/02/2021

Journal of Hydrology 564 (2018) 1099–1109

Contents lists available at ScienceDirect

Journal of Hydrology

journal homepage: www.elsevier.com/locate/jhydrol

Research papers

Effects of delayed particle detachment on injectivity decline due to fines migration

Thomas Russell*, Kiet Wong, Abbas Zeinijahromi, Pavel Bedrikovetsky

Australian School of Petroleum, University of Adelaide, Australia

ARTICLE INFO

This manuscript was handled by C. Corradini, Editor-in-Chief, with the assistance of Brian D. Smerdon, Associate Editor

Keywords:
Fines migration
Formation damage
Injectivity decline
Low-salinity waterflooding
Analytical modelling
Axi-symmetric flow

ABSTRACT

Colloidal-suspension flows in porous media occur in numerous areas of environmental, chemical and petroleum engineering. The main processes are capture and detachment of particles, yielding permeability decline. We developed a governing system of transport equations with particle detachment kinetics, where the detachment by high velocities is instant, due to flow incompressibility, and the detachment by decreasing the fluid salinity is delayed, due to micro-scale diffusion. The system allows for a semi-analytical solution for axi-symmetric low-salinity water injection with fines migration. The model exhibits instant fines mobilization at the beginning of injection by drag force, fines release with delay behind the salinity front by electrostatic force, and the interaction of two concentration waves. The model can be used for laboratory-based injectivity decline prediction during injection of water in aquifers and oilfields, where the injected and formation water compositions are different, and also for fines-migration during drilling fluid invasion.

1. Introduction

During injection operations into a reservoir, natural reservoir particles can detach and become suspended in the injected fluid. The suspended particles strain in pore throats as they are carried through the pore space in the case where the particles have sizes comparable to the pore throats.

Straining results in a significant decline in the permeability of the porous media. This process is referred to as fines migration and poses a serious risk to the capability of injection wells to supply fluid to the reservoir.

Fines migration has been shown to have a significant impact on the injectivity of oil wells (Barkman et al., 1975) and of freshwater storage wells (Prommer et al., 2013). Any operations involving porous media that contains fine particles that are susceptible to both detachment and straining are potentially prone to fines migration. Example applications include groundwater flows (Kaplan and Muñoz-Carpena, 2014) and contaminant transport (Zhang et al., 2016).

Decision-making during the injection of foreign water into aquifers and oil-fields for displacement, storage, or disposal purposes is based on numerical and analytical modelling at the reservoir scale (Hayek, 2014; Hayek, 2015). The rheological relationships used for this modelling are determined by matching laboratory and micro-scale modelling (Mirabolghasemi et al., 2015).

Modelling fines migration required descriptions of the processes of detachment, migration, and straining, which are shown schematically in Fig. 1.

Particle detachment in response to changes to the flow conditions is described by the total concentration of detached particles and the rate of particle detachment.

It is helpful to imagine particles that remain attached under any flow conditions to be in a state of equilibrium. Certain changes to the flow conditions result in a shift in the equilibrium and a consequent detachment of particles. In describing the nature of this equilibrium, some authors have adopted empirical equations (Kuo and Matijevic, 1979), while others have neglected the equilibrium altogether (Vardoulakis et al., 1996), resulting in the detachment of all in-situ particles. More recent approaches have focused on the forces acting on particles (Yuan and Shapiro, 2011; Zeinijahromi and Bedrikovetsky, 2016). The balance of these forces, often assumed to be in the form of a torque balance, relates the prediction of particle detachment to state variables such as the fluid velocity or salinity through established relations for the acting forces.

The two primary forces acting on attached particles are the hydrodynamic drag force F_d, and the electrostatic force, F_e. Additional forces such as the lifting, gravitational, or Brownian forces are neglected from this discussion as they have been shown to be negligible for the conditions of fines detachment in natural reservoirs (Kalantariasl and

* Corresponding author.
E-mail address: thomas.l.russell@adelaide.edu.au (T. Russell).

https://doi.org/10.1016/j.jhydrol.2018.07.067
Received 21 May 2018; Received in revised form 18 July 2018; Accepted 26 July 2018
Available online 27 July 2018

Nomenclature

c	suspended particle concentration [–]
C_{acc}	accumulated suspended particle concentration [–]
D	slope of characteristic line [–]
F_d	drag force $[M][L]^{-1}[T]^{-2}$
F_e	electrostatic force $[M][L]^{-1}[T]^{-2}$
J	impedance [–]
k_0	initial core permeability $[L]^2$
l_d	drag lever arm [L]
l_n	normal lever arm [L]
P	dimensionless fluid pressure [–]
p	fluid pressure $[M][T]^{-2}[L]$
q	volumetric injection rate per unit formation thickness $[L]^2[T]^{-1}$
q_0	initial injection rate $[L]^3[T]^{-1}$
r	radial distance [L]
r_d	damaged zone radius [L]
r_e	drainage radius [L]
r_w	wellbore radius [L]
S_a	dimensionless attached particle concentration [–]
S_{aI}	dimensionless initial attached particle concentration [–]
S_s	dimensionless strained particle concentration [–]
t	elapsed time [T]
T	pore Volumes Injected [–]
T_0	[–]
U	fluid velocity $[L][T]^{-1}$
U_m	maximum velocity $[L][T]^{-1}$
U_p	particle velocity $[L][T]^{-1}$
X	dimensionless radial distance [–]
X_0	[–]

Greek Letters

α	drift delay factor [–]
β	formation damage coefficient [–]
Γ	dimensionless fluid salinity [–]
γ	fluid salinity $[N][L]^{-3}$
Γ'	dimensionless pseudo-salinity
γ'	pseudo-salinity $[N][L]^{-3}$
γ_i	initial fluid salinity $[N][L]^{-3}$
γ_{inj}	injected fluid salinity $[N][L]^{-3}$
ΔP	dimensionless pressure drop [–]
Δp_0	initial pressure drop $[M][T]^{-2}[L]$
$\Delta\sigma_{cr}$	total detached particle concentration [–]
ε	dimensionless delay factor [–]
Θ	temperature [Θ]
λ	filtration coefficient $[L]^{-1}$
μ	fluid viscosity $[M][L]^{-1}[T]^{-1}$
σ_0	maximum attached concentration [–]
σ_a	attached particle concentration [–]
σ_{aI}	initial attached particle concentration [–]
σ_{cr}	critical retention function [–]
σ_s	strained particle concentration [–]
τ	delay factor [T]
ϕ	porosity [–]

Bedrikovetsky, 2013).

The remaining two forces are shown acting on an attached particle alongside their respective lever arms l_d and l_n in Fig. 1. The mechanical equilibrium of the attached particle is determined by the balance of the torques generated by these forces (Bedrikovetsky et al., 2011; Sasidharan et al., 2017)

$$F_d(U)l_d = F_e(\gamma, pH, \Theta)l_n \quad (1)$$

where U is the fluid velocity, γ is the fluid salinity, and Θ is the temperature.

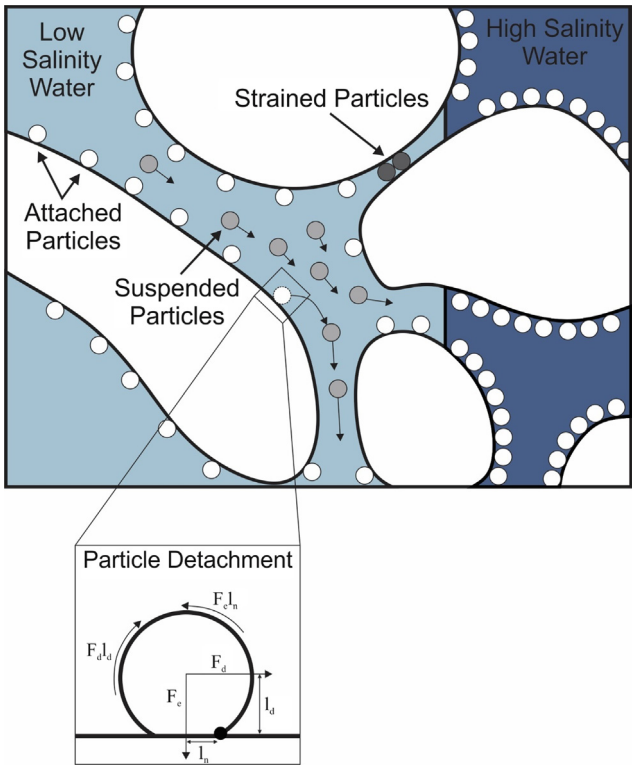

Fig. 1. Schematic of the process of fines migration.

Fines detachment occurs when the detaching torque generated by the drag force exceeds the attaching torque generated by the attractive electrostatic force. Higher fluid velocities result in a higher drag force (Goldman et al., 1967), and hence increase the extent of particle detachment (Zheng et al., 2014). Similarly, the electrostatic force decreases with decreasing fluid salinity (Khilar et al., 1983; Shen et al., 2018), or increasing pH (Kia et al., 1986; Patil et al., 2011), resulting in more particle detachment. This explains why low-salinity waterflooding operations are particularly prone to formation damage resulting from fines migration. Higher temperatures have also been shown to decrease the electrostatic force (You et al., 2015), which is important when injecting into deep reservoirs, or during geothermal operations (You et al., 2016).

Applying the torque balance condition to all particles within the porous medium allows the derivation of a macro-scale equation relating the flow conditions to the attached particle concentration. This function is referred to as the critical retention function

$$\sigma_{cr}(U, \gamma, pH, \Theta) \quad (2)$$

In natural reservoir rocks, properties such as pore size, particle size and geometry among others will be non-uniform. Thus, the properties which determine the condition of mechanical equilibrium (1) will be stochastically distributed. The torque balance can determine whether each particle is attached based on their own properties. The population of all particles whose mechanical equilibrium favours detachment gives the attached concentration, given here as the critical retention function. Therefore, despite the non-uniformity of micro-scale parameters, the function (2) is still valid.

In most experimental studies of fines migration, the flow conditions are controlled to study the effect of changing one variable on the

attached concentration. However, during uni-axial flows, such as during injection operations, the fluid velocity is a decreasing function of the distance from the wellbore. As such, a continuous relation between the attached concentration and the fluid velocity is required. The critical retention function satisfies this requirement.

Previous studies have demonstrated a significant delay in the response of attached oleic particles to changes in the fluid salinity (Mahani et al., 2015). The authors argue that diffusive processes slow the effect of decreasing salinity on altering the salinity between oil particles and the pore surface, thus delaying the detachment of these droplets. A similar argument will apply to the detachment of fines from the pore surface, and therefore a delay in particle detachment should be expected. Such a delay has been noted in several experimental works (Gravelle et al., 2011; Pazmino et al., 2014). As a result, many authors have adopted a first-order kinetics relation to describe particle detachment due to the injection of low-salinity water (Gravelle et al., 2011; Grolimund and Borkovec, 2006; Russell and Bedrikovetski, 2018). On the contrary, some authors assert that particle detachment by velocity is instantaneous, based on the notion that changes to the fluid velocity will instantly affect the drag force acting on particles (Yang et al., 2016). Thus, the kinetics of particle detachment should be evaluated in conjunction with the cause of the detachment. It follows that in scenarios where particle detachment can occur by either salinity or velocity, such as during the injection of low-salinity water, a single expression for detachment kinetics will be inadequate. Nonetheless, existing models for fines migration due to low-salinity water injection make use of a single particle detachment kinetics regime. The purpose of this work is to present a mathematical model for fines migration in uni-axial coordinates that separately describes the kinetics of particle detachment due to changes in both velocity and salinity.

The structure of the paper is as follows. The assumptions and governing equations for the mathematical model are presented in Sections 2.1 and 2.2 respectively. A semi-analytical solution for this system is derived in Section 2.3. Section 2.4 presents the equations for calculating injectivity and a specific form of the critical retention is provided in Section 2.5. Section 3 presents a laboratory study of fines migration, the results of which are treated in Section 4. Section 5 presents predictions of injectivity decline based on the results of the treatment of the laboratory data. A discussion of the model is presented in Section 6, and Section 7 concludes the paper.

2. Mathematical model

In the current section, a mathematical model is presented to describe fines migration during single-phase uni-axial flow.

2.1. Assumptions of the model

Both the fluid and particles are assumed to be incompressible. In addition, particle and fluid volumes are assumed to be additive during detachment and straining.

Suspended particles are assumed to move through the porous space with a velocity smaller than the fluid velocity (Oliveira et al., 2014)

$$U_p = \alpha U \tag{3}$$

where U_p is the particle velocity, U is the fluid velocity, and α is drift delay factor, which is significantly less than one. The discrepancy between the particle and fluid velocities follows from rolling and sliding of the suspended particles along the pore walls.

Particle straining is assumed to be an irreversible process. The strained concentration is also assumed to be negligibly small compared to the number of straining vacancies within the rock.

Particle attachment due to electrostatic attraction is ignored. As outlined above, particle detachment can occur due to an increase in fluid velocity or a decrease in the fluid salinity. Changes to the fluid salinity are assumed to have a delayed effect on the detachment of particles. This assumption follows from the diffusion-limited ion transport between the bulk solution and the solution between the particle and the grain (Mahani et al., 2015). The latter governs the electrostatic force and hence the critical retention function. Changes to the fluid velocity are however assumed to have an instantaneous effect on particle detachment.

Finally, both particle and salt diffusion/dispersion are ignored as these processes are assumed to be negligible compared to their respective advective fluxes (Polyanin and Dilman, 1994).

2.2. Governing equations

Following the assumptions outlined in the previous section, we now present the system of equation describing fines migration in uni-axial flow with delayed particle detachment.

The uni-axial incompressible flow results in a fluid velocity varying with radial distance:

$$U = \frac{q}{2\pi r} \tag{4}$$

where q is the volumetric injection flow rate per unit formation thickness, and r is the radial coordinate.

The mass balance of suspended, strained and attached particles transported by incompressible fluid with velocity given by Eq. (4) with drift delay factor (3) and neglecting particle dispersion is

$$\frac{\partial}{\partial t}(\phi c + \sigma_s + \sigma_a) + \frac{\alpha q}{2\pi r}\frac{\partial c}{\partial r} = 0 \tag{5}$$

where t is time, ϕ is the porosity, c is the suspended particle concentration, σ_s is the strained particle concentration, and σ_a is the attached particle concentration.

The straining rate is assumed to be proportional to the incoming suspended particle concentration

$$\frac{\partial \sigma_s}{\partial t} = \frac{\alpha \lambda c q}{2\pi r} \tag{6}$$

where λ is the filtration coefficient. The assumption of a small strained concentration compared to the number of straining sites leads to a constant λ (Altoe et al., 2006).

The transport of salt in the reservoir is governed by the mass balance equation for the electrolyte

$$\phi\frac{\partial \gamma}{\partial t} + \frac{q}{2\pi r}\frac{\partial \gamma}{\partial r} = 0 \tag{7}$$

Following the assumptions in Section 2.1, any description of the kinetics of particle detachment should satisfy the following statements. Firstly, the attached concentration should be governed by the critical retention function, which itself is a function of the fluid salinity and velocity. Secondly, the particle detachment rate should be infinite with respect to changes to velocity, and finite with respect to changes to salinity.

To satisfy these requirements, we introduce the pseudo-salinity, γ' such that:

$$\sigma_a(r, t) = \sigma_{cr}(U, \gamma') \tag{8}$$

Thus, the attached concentration is governed by the velocity and pseudo-salinity.

The pseudo-salinity is equal to the fluid salinity after some delay time, τ:

$$\gamma'(x, t + \tau) = \gamma(x, t) \tag{9}$$

By assuming a constant delay time, we can use a first order Taylor's series approximation to obtain the rate equation (Bernasconi, 1976)

$$\tau\frac{\partial \gamma'}{\partial t} = \gamma - \gamma' \tag{10}$$

This equation, which holds for small delay times ($\tau \ll t$), describes

the rate at which changes to the fluid salinity translate into changes to the pseudo-salinity.

Under this formulation, abrupt changes to the velocity translate to abrupt changes in the attached concentration. However, abrupt changes to the salinity have a gradual effect on particle detachment, as required.

Finally, the relationship between the strained concentration and the rock permeability is given by a first order Taylor series approximation

$$\frac{k_o}{k(\sigma_s)} \approx 1 + \beta\sigma_s \tag{11}$$

where k_0 is the initial permeability, and β is the formation damage coefficient.

Substituting this equation into Darcy's law yields

$$\frac{q}{2\pi r} = -\frac{k_0}{\mu(1+\beta\sigma_s)}\frac{\partial p}{\partial r} \tag{12}$$

where μ is the fluid viscosity, and p is the fluid pressure

The system of Eqs. (5–8), (10) and (12) describes the 6 unknowns (c, σ_s, σ_a, γ, γ', p).

Prior to solving the system of equations, we introduce the following dimensionless variables

$$r_n = r_e - r_w,\ X = \frac{r^2}{r_n^2},\ T = \frac{\int q dt}{\pi\phi r_n^2},\ S_s = \frac{\sigma_s}{\phi},$$
$$S_a = \frac{\sigma_a}{\phi},\ \Lambda = \lambda r_n,\ \varepsilon = \frac{q\tau}{\pi\phi r_n^2},\ \Gamma = \frac{\gamma-\gamma_{inj}}{\gamma_i-\gamma_{inj}},\ P = \frac{2\pi p k_0}{q\mu} \tag{13}$$

where r_e is the drainage radius of the reservoir, r_w is the wellbore radius, and γ_{inj} is the injected fluid salinity, which is lower than the initial fluid salinity γ_i. Dimensionless time T is expressed in pore volumes injected $\pi\phi r_n^2$ (PVI).

Using these variables, the Eqs. (5–8), (10) and (12) now take the dimensionless form

$$\frac{\partial}{\partial T}(c + S_s + S_a) + \alpha\frac{\partial c}{\partial X} = 0 \tag{14}$$

$$\frac{\partial S_s}{\partial T} = \frac{\alpha\Lambda c}{2\sqrt{X}} \tag{15}$$

$$S_a(X, T) = S_{cr}(U, \gamma') \tag{16}$$

$$\frac{\partial\Gamma}{\partial T} + \frac{\partial\Gamma}{\partial X} = 0 \tag{17}$$

$$\varepsilon\frac{\partial\Gamma'}{\partial T} = \Gamma - \Gamma' \tag{18}$$

$$\frac{1}{X} = -\frac{2}{1+\beta\phi S_s}\frac{\partial P}{\partial X} \tag{19}$$

The initial conditions for the system correspond to a reservoir initially saturated with high-salinity water with an absence of suspended and strained particles

$$T = 0{:}\ \Gamma = 1,\ c = 0,\ S_s = 0 \tag{20}$$

The attached concentration begins at some initial value

$$S_a = S_{aI} \tag{21}$$

The boundary condition for this problem is applied at the wellbore radius. The injected fluid has salinity γ_{inj} and contains no suspended particles

$$r = r_w{:}\ X = X_w{:}\ \Gamma = 0,\ c = 0 \tag{22}$$

The boundary condition for the strained particle concentration follows from substituting boundary condition (22) into Eq. (15) and integrating. This yields

$$S_s(X_w, T) = 0 \tag{23}$$

2.3. Solution

The equation for salt transport de-couples from the system (14–16,18,19) and so can be solved separately. Using the method of characteristics, the solution separates for the two regions behind and ahead of the injected salinity front, $X\text{-}X_w = T$. The final solution is

$$\Gamma(X, T) = \begin{cases} 1, & X - X_w > T \\ 0, & X - X_w < T \end{cases} \tag{24}$$

The discontinuity along the salinity front is a consequence of neglecting diffusion.

The pseudo-salinity can then be solved by substituting the solution for the salinity into Eq. (18) and integrating by separation of variables. The initial condition used for the pseudo-salinity is the same as that for the salinity. Ahead of the salinity front, the solution is

$$\Gamma' = 1 \tag{25}$$

Eq. (18) implies that the pseudo-salinity is continuous across the solution space. As such, Eq. (25) can be used as the initial condition ahead of the salinity front:

$$T = X{:}\ \Gamma' = 1 \tag{26}$$

Using this condition to solve Eq. (18) yields the solution behind the salinity front

$$\Gamma' = e^{\frac{X-T}{\varepsilon}} \tag{27}$$

Hence an immediate decrease in the salinity along the salinity front, $X\text{-}X_w = T$, results in an exponential decline in the pseudo-salinity from $\Gamma' = 1$ to $\Gamma' = 0$.

Next the particle mass balance Eq. (14) and the straining rate Eq. (15) are used to solve for the suspended particle concentration. The resulting partial differential equation (PDE) is

$$\frac{\partial c}{\partial T} + \alpha\frac{\partial c}{\partial X} = -\frac{\alpha\Lambda c}{2\sqrt{X}} - \frac{\partial S_a}{\partial T} \tag{28}$$

The solution space is naturally divided into three regions (shown in Fig. 2): ahead of the salinity front ($X\text{-}X_w > T$, region *0*), the intermediate region between the salinity front and the suspended particle front ($T > X\text{-}X_w > \alpha T$, region *I*), and the region behind the suspended particle front ($\alpha T > X\text{-}X_w$, region *II*). The method of characteristics can be used to derive the solution for each of these regions (Polyanin and Zaitsev, 2011; Polyanin and Manzhirov, 2007; Tikhonov and Smarskii, 2011).

In Region *0*, evaluating the PDE (28) along parametric curves given by

$$\frac{dT}{dX} = \frac{1}{\alpha} \tag{29}$$

reduces the PDE to an ordinary differential equation (ODE)

$$\frac{dc}{dX} = -\frac{\Lambda c}{\sqrt{2X}} - \frac{1}{\alpha}\frac{\partial S_a}{\partial T} \tag{30}$$

The initial condition for this region is given along the X-axis. Due to the assumptions that the fluid is incompressible and that particle detachment due to velocity occurs instantaneously, particle detachment by velocity at the initial salinity must be incorporated into the initial conditions. As such, on the X-axis, the attached concentration is

$$S_a(X, T=0) = \begin{cases} 0 & S_{cr}(\Gamma' = 1, U(X, 0)) > 0 \\ S_{cr}(\Gamma' = 1, U(X, 0)) & 0 > S_{cr}(\Gamma' = 1, U(X, 0)) > S_{aI} \\ S_{aI} & S_{aI} > S_{cr}(\Gamma' = 1, U(X, 0)) \end{cases} \tag{31}$$

The excess attached particles, below S_{aI}, become suspended in the carrier fluid. For brevity, we present the initial condition as

$$T = 0{:}\ c = S_{aI} - S_a(X, T = 0) \tag{32}$$

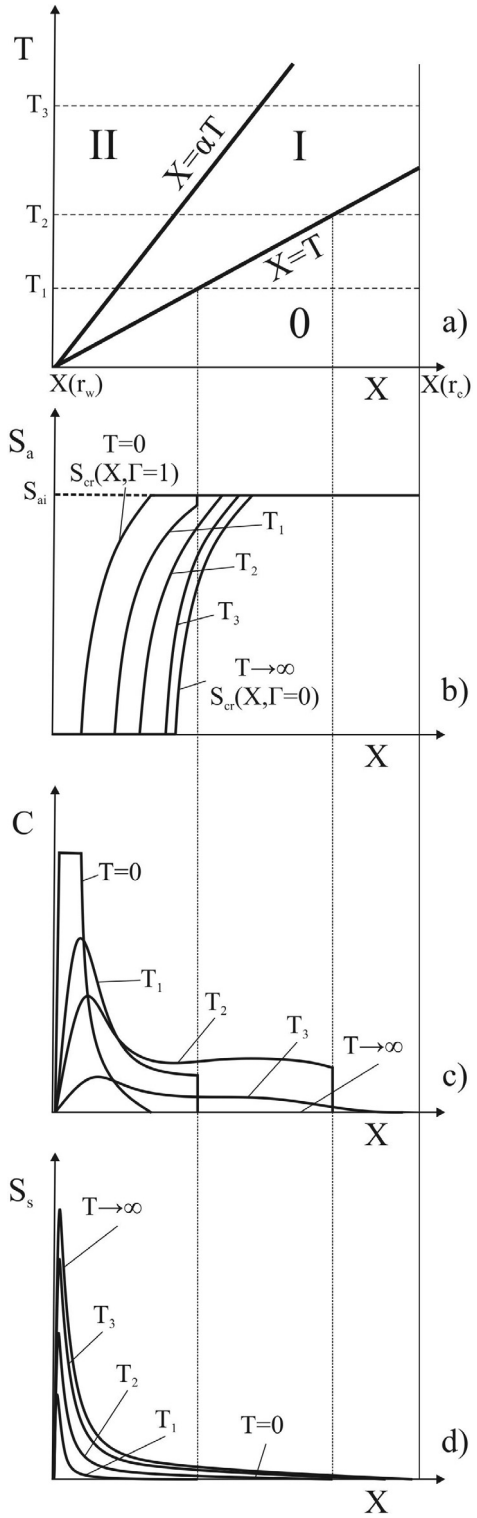

Fig. 2. Profiles for the behaviour of the semi-analytical solution: a) X-T plane, b) Attached particle concentration, c) Suspended particle concentration, and d) Strained particle concentration.

The pseudo-salinity and fluid velocity are independent of time within region *0*, and so the detachment rate in Eq. (30) is zero. Integrating Eq. (30) subject to initial condition (20) yields the solution for the suspended concentration ahead of the salinity front

$$c = e^{-\Lambda(\sqrt{X}-\sqrt{X-\alpha T})}(S_{aI}-S_a(X,\ T=0)) \tag{33}$$

The solution for region *0* along the salinity front serves as an initial condition for region *I*. It is first necessary to demonstrate that the suspended concentration is continuous along this front. To do so, we make use of a mass balance condition derived from Eq. (14) (Bedrikovetsky, 1993)

$$[c + S_a + S_s]D = \alpha[c] \tag{34}$$

where the square brackets indicate the change in a variable across the curve with slope *D*.

Eqs. (15) and (25,27) respectively demonstrate that for all positive (*X,T*), the strained and attached concentrations are continuous. Therefore, along the salinity front we have

$$[c] = \alpha[c] \tag{35}$$

For $\alpha < 1$, the solution follows

$$[c] = 0 \tag{36}$$

Thus, the suspended concentration is continuous along the salinity front.

In region *I*, the characteristic curves are given by

$$\frac{dX}{dT} = \alpha \tag{37}$$

Along these curves the PDE (28) reduces to

$$\frac{dc}{dT} + \frac{\alpha\Lambda c}{2\sqrt{X}} = -\frac{\partial S_a}{\partial T} \tag{38}$$

Eq. (37) can be solved to give the equation for the characteristics

$$X - X_0 = \alpha(T - T_0) \tag{39}$$

where the set of points ($X_w + X_o,\ T_o$) define the location where the initial condition is given. For this region, the initial condition is provided along the salinity front. As such, we have

$$X_w + X_0 = T_0 \tag{40}$$

So

$$X = \alpha T + T_0(1-\alpha) + X_w \tag{41}$$

Substituting Eq. (41) into Eq. (38) allows eliminating the variable *X* so that the ODE may be solved directly.

Performing the integration produces the implicit solution for the suspended particle concentration in this region

$$c = e^{[-\Lambda(\sqrt{X}-\sqrt{X-\alpha T})]}(S_{aI}-S_a(X,\ T=0)) - e^{-\Lambda(\sqrt{X})}\int_{T_0}^{T} e^{\Lambda\sqrt{X(T)}}\frac{\partial S_a(X(T),\ T)}{\partial T}dT \tag{42}$$

The dependence of the variable *X* on *T* in the integral persists as the integration is performed along the characteristics.

The solution is presented implicitly here due to the necessity of the form of the critical retention function to be known. The equations are presented generally for any form of this function, and a specific example is presented in Section 2.5.

In region *II*, Eq. (28) is evaluated along curves given by

$$\frac{dT}{dX} = \frac{1}{\alpha} \tag{43}$$

to reduce the PDE to the form

$$\frac{dc}{dX} = -\frac{\Lambda c}{\sqrt{2X}} - \frac{1}{\alpha}\frac{\partial S_a}{\partial T} \tag{44}$$

Performing the integration and making use of the boundary condition (22) results in

$$c = -\frac{e^{-\Lambda\sqrt{X}}}{\alpha}\int_{X_w}^{X} e^{\Lambda\sqrt{X}}\frac{\partial S_a(X,\ T(X))}{\partial T}dX \tag{45}$$

Equations for the attached and suspended concentrations can be found in Table 1.

Table 1
Semi-analytical solution for fines migration with delayed detachment during uni-axial, incompressible flow.

Variable	Region	Exact Solution
Salinity, Γ	$X < X_w + T$	0
	$X > X_w + T$	1
Pseudo-Salinity, Γ'	$X < X_w + T$	$e^{\frac{X-T}{\varepsilon}}$
	$X > X_w + T$	1
Attached Concentration, S_a	$\{(X, T) \mid S_{cr}(U(X), \Gamma'(X, T)) \geqslant S_{aI}\}$	S_{aI}
	$\{(X, T) \mid 0 < S_{cr}(U(X), \Gamma'(X, T)) < S_{aI}\}$	$S_{cr}(U, \Gamma')$
	$\{(X, T) \mid S_{cr}(U(X), \Gamma'(X, T)) \leqslant 0\}$	0
Suspended Concentration, c	$X < X_w + \alpha T$	$-\frac{e^{-\Lambda\sqrt{X}}}{\alpha}\int_{X_w}^{X} e^{\Lambda\sqrt{\bar{X}}}\frac{\partial S_a(X, T(\bar{X}))}{\partial T}d\bar{X}$
	$X_w + \alpha T < X < X_w + T$	$e^{-\Lambda(\sqrt{X}-\sqrt{X-\alpha T})}(S_{aI}-S_a(X, T=0))$ $-e^{-\Lambda\sqrt{X}}\int_0^T e^{\Lambda\sqrt{X(\bar{T})}}\frac{\partial S_a(X(\bar{T}), \bar{T})}{\partial T}d\bar{T}$
	$X > X_w + T$	$e^{-\Lambda(\sqrt{X}-\sqrt{X-\alpha T})}(S_{aI}-S_a(X, T=0))$

Once the suspended concentration is known, the strained concentration can be obtained by integrating Eq. (15).

2.4. Injectivity

Given any strained concentration profile, the dimensionless pressure drop can be calculated by integrating Eq. (19). The impedance is then calculated by normalising the dimensionless pressure drop by its initial value

$$J = \frac{q_0}{q}\frac{\Delta p}{\Delta p_0} = \frac{\Delta P}{\Delta P_0} \tag{46}$$

where the subscript *0* indicates the initial value, prior to any damage.

In order to calculate a dimensional output of the model, it is necessary to impose a boundary condition at the wellbore. The simplest case is the condition of constant injection rate. Under this condition, the pressure drop between the wellbore and the reservoir boundary is calculated as

$$\int_{r_w}^{r_e} dp = -\frac{q\mu}{2\pi k_0}\int_{r_w}^{r_e}\frac{1+\beta\phi S_s}{2X}dX \tag{47}$$

which reduces to

$$p(r_w)-p(r_e) = \Delta p(t) = \frac{q\mu}{2\pi k_0}\left(\ln\left(\frac{r_e}{r_w}\right) + \beta\phi\int_{X(r_w)}^{X(r_e)}\frac{S_s}{2X}dX\right) \tag{48}$$

Another common constraint on injection conditions is to maintain a constant bottom-hole pressure. To maximise injection rate, it is often maintained at a value just below the formation fracture pressure (Rose et al., 1989). Fines migration will then result in a decrease of the injection rate over time. The inclusion of a variable rate function *q(t)* highlights a key assumption used in the solution procedure in Section 2.3. In order to de-couple the modified Darcy's law Eq. (19) from the rest of the system, it is necessary to assume that particle detachment is governed by a single injection rate. For the case of constant injection rate this poses no problem, but for constant bottom-hole pressure, the decrease in injection rate violates this assumption.

In order to make use of the model to predict a decrease in injection rate, we make an additional assumption that particle detachment is determined only by the initial injection rate. Under this assumption, the equations governing the fine particle concentrations, and Darcy's law can still be separated, and the analysis presented in Section 2.3 still holds. After calculating the strained concentration, Eq. (12) can be integrated and re-arranged to obtain the expression for the injection rate

$$q(t) = \frac{2\pi k_0(p(r_w)-p(r_e))}{\mu\left(\ln\left(\frac{r_e}{r_w}\right) + \beta\phi\int_{X(r_w)}^{X(r_e)}\frac{S_s}{2X}dX\right)} \tag{49}$$

For the case of constant pressure drop, the relationship between the time and the dimensionless time, given in Eq. (13), is not known until the injection rate has been determined. As such, it is easier to perform calculations in dimensionless coordinates to calculate *q(T)*, and subsequently calculate the relationship *T(t)* from Eq. (13). Taking the derivative of this expression with respect to time yields

$$\frac{dT}{dt} = \frac{q(t)}{\phi\pi {r_n}^2} \tag{50}$$

Evaluating the derivative using a first order Taylor series approximation yields a simple iterative formula

$$t^n = t^{n-1} + (T^n - T^{n-1})\left(\frac{\phi\pi {r_n}^2}{q(t^n)}\right) \tag{51}$$

2.5. Example form of the critical retention function

All equations thus far have been presented for any form of the critical retention function, $\sigma_{cr}(U,\gamma)$. For the purposes of discussing the model, we now present a simple form for this function. The dependency of the critical retention function on the fluid velocity has been discussed previously (Bedrikovetsky et al., 2011). The resulting critical retention function takes the form of a parabola

$$\sigma_{cr}(U) = \sigma_0\left(1-\left(\frac{U}{U_m}\right)^2\right) \tag{52}$$

where σ_0 is the limit of the critical retention function with zero fluid velocity, and U_m is the maximum velocity, above which no more fine particles are detached. The quadratic form of the critical retention function follows from the velocity dependence of the drag force acting on attached particles (Goldman et al., 1967).

The dependency of the critical retention function on the fluid salinity follows from the dependency of the electrostatic force on the salinity. A simple and general form for this dependency has not been well developed for the purposes of fines migration. As such, we propose a simplification in which the maximum velocity U_m varies linearly with the fluid salinity

$$\begin{aligned} U_m &= U_m(\gamma') = U_m(\gamma' = \gamma_{inj}) + \gamma'[U_m(\gamma' = \gamma_i) - U_m(\gamma' = \gamma_{inj})] \\ &= U_{m0} + \gamma'(U_{m1} - U_{m0}) \end{aligned} \tag{53}$$

In dimensionless coordinates, the critical retention function then

takes the form

$$S_{cr}(U, \Gamma') = \frac{\sigma_0}{\phi}\left(1-\frac{\left(\frac{q}{2\pi r_n}\right)^2}{X(U_{m0} + (U_{m1}-U_{m0})\Gamma')^2}\right) \quad (54)$$

The critical retention function is then characterised by the three variables σ_0, U_{m0}, and U_{m1}. A more complex description of the critical retention function may be required for describing particle detachment in some conditions. Regardless, Eq. (54) is used in the remainder of this work to illustrate the behaviour of the model.

Based on this formulation, the parameter set required to characterise fines migration is then (α, λ, β, τ, σ_0, σ_{al}, U_{m1}, U_{m0}).

3. Laboratory study

In this section, a laboratory study is presented that has been designed to characterise the response of a sample porous media to low-salinity water. A successful characterisation will result in reliable estimates of the parameters outlined in Section 2.5.

3.1. Materials – Rock and fluids

The rocks used in this study were artificially created sand-kaolinite sandpacks. The use of artificial cores provides significant confidence in the reproducibility of the cores and hence allows multiple tests to be interpreted as if they were performed on the same core.

The sand used in the study consisted of more than 99% silica and was sieved prior to use to constrain the particle size distribution. A washing procedure outlined in Russell et al. (2017) was performed to remove impurities on the sand surface and enhance the reproducibility of the sandpacks. The kaolinite used in this study was analytical grade kaolinite powder which was dried at 60 °C prior to weighing to remove excess water.

A fixed mass of 85 g was used for the sandpacks, and for both cores, the kaolinite mass fraction was 10%. The sand-kaolinite mixture was wet slightly with high salinity water (0.6 mol/L NaCl) before being compacted in the core holder.

The homogeneous distribution of clay across the core, and the reproducibility of the procedure were outlined in Russell et al. (2017).

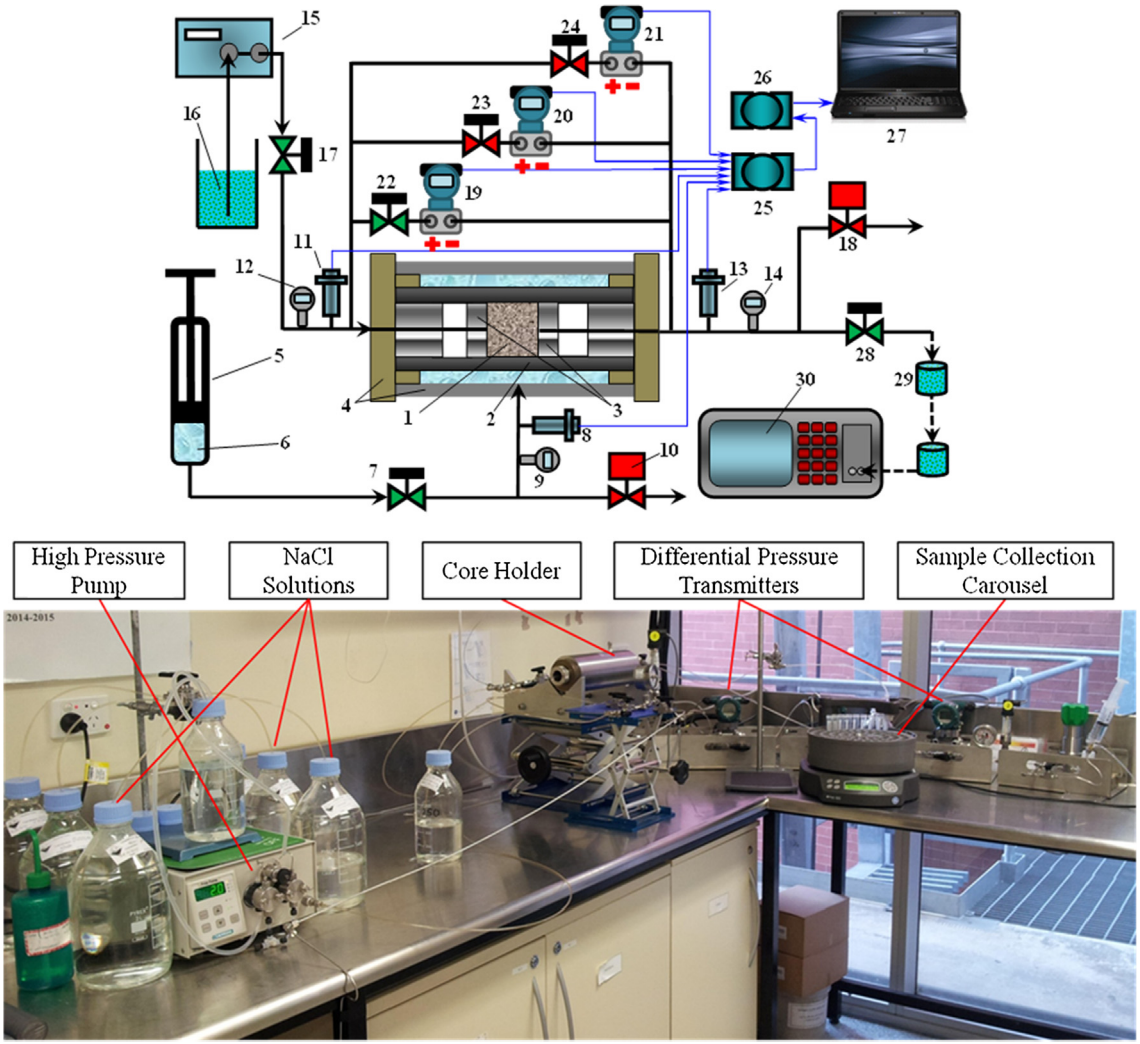

Fig. 3. Apparatus used for laboratory coreflooding tests: a) Schematic of all components, b) Photograph showing primary components. 1-Coreholder, 2-Viton Sleeve, 3-Stainless steel distributors, 4-Hassler-type coreholder, 5-Manual HiP piston pressure generator, 6-Deionised water (overburden fluid), 7-Overburden pressure valve, 8-Absolute pressure transmitter, 9,12,14-Bourdon-type pressure indicator, 10-Pressure relief value, 11, ,13-pressure transmitters, 15-High pressure pump, 16-Injection solutions, 17-Injection valve, 18- Back-pressure regulator, 19-21-Differential pressure transmitters, 22-24-Manual three-way valves, 25-ADAMView inlet acquisition module, 26-Signal conditioner, 27-PC for data acquisition, 28-Effluent valve, 29-Plastic sampling tubes, 30-POLA-2000 particle counter. Reproduced with permission from Russell et al., 2017

3.2. Apparatus

The experimental study on fines migration was carried out using a constant-rate coreflooding apparatus with real-time pressure measurements. A schematic and photograph of the set-up used in the study is provided in Fig. 3. A complete description of each component of the set-up is provided in the caption of this figure. In brief, the injection solutions were provided to the core with constant injection rate by the injection pump while the differential pressure transmitters measured the pressure difference between the core inlet and outlet. The pressure difference measurements were recorded in real-time using data acquisition software. Samples were collected at the effluent and then analysed using a particle counter to determine the suspended particle concentration.

3.3. Laboratory procedure

The laboratory procedure began by injecting each core with 0.6 mol/L NaCl at a low flow rate 0.2 mL/min, which corresponds to linear velocity $U = 2.93 \times 10^{-6}$ m/s), to fully saturate the core. The high salinity fluid and low flow rate were chosen to promote attachment of the kaolinite to the sand grains and to minimise particle detachment during saturation. After 24 h, the injected solution was changed to the test salinity, which was then maintained for the remainder of each test. The two cores were injected with 0.01 mol/L and 0.001 mol/L NaCl. These salinities cover the range of slightly brackish water to fresh water that is typical for fresh water aquifers (Prommer et al., 2013). After an additional 24 h, the test began by increasing the injection velocity. During each stage, the velocity was held constant and the pressure drop across the core and effluent suspended particle concentration were measured. After 24 h, which was sufficient in all cases for complete stabilisation of the pressure drop, the velocity was increased, and the process repeated. The injection rates used in each test were: 1, 5, 10, 15, 20, 30, 40, and 50 mL/min which have respective superficial velocities: 1.47×10^{-5}, 7.34×10^{-5}, 1.47×10^{-4}, 2.2×10^{-4}, 2.93×10^{-4}, 4.40×10^{-4}, 5.87×10^{-4}, and 7.34×10^{-4} m/s. The fluid velocity range was designed to encompass velocities that might be encountered in the near-wellbore and far-field regions during injection operations.

4. Treatment of laboratory data

The data sets obtained from the tests were the pressure drop and outlet concentration curves for each injection stage. These were fit with a 1-D model for fines migration with delayed detachment in linear coordinates. This model is analogous to the system (5–8,10,12) with a constant fluid velocity along the core. The output of this fitting procedure was the model parameters: α, τ, β, λ, and $\Delta\sigma_{cr}$. The latter describes the difference in the critical retention function at the velocity of the current stage and that of the previous stage. The set of these values for each injection stage facilitates the construction of the critical retention function against the injection velocity. These curves for both cores have been constructed and fit with the theoretical form given by Eq. (52). Experimental and theoretical curves are presented in Fig. 4. The experimental points show good agreement with the theoretical form of the critical retention function. The parameter values obtained from fitting were: $\sigma_0(0.01\,\mathrm{M}) = 0.01205$, $\sigma_0(0.001\,\mathrm{M}) = 0.01178$, $U_m(0.01\,\mathrm{M}) = 0.001622$ m/s, and $U_m(0.001\,\mathrm{M}) = 0.0008782$ m/s. The effect of salinity is captured in the different values of U_m, where a higher velocity is required to detach all particles in the presence of a higher salinity.

For the calculation of injectivity decline, the value of σ_0 was taken as the average of the two obtained from experiments. The other model parameters obtained from fitting the experimental data varied between injection cycles, so average values were taken from these ranges. The parameters which are present in traditional models for fines migration (α, λ, β, $\Delta\sigma_{cr}$) lie within ranges of parameters reported in the literature (Al-Abduwani et al., 2005; Bradford et al., 2003; Bradford et al., 2013; Chrysikopoulos and Katzourakis, 2015; Oliveira et al., 2014; Sotirelis and Chrysikopoulos, 2015) The complete set of parameters used in the calculations is presented in Table 2.

5. Predictions of wellbore injectivity

In this section predictions of wellbore injectivity both for the conditions of constant injection rate and constant bottom-hole pressure are presented.

The calculations for injectivity decline have been performed for three different initial bottom-hole pressures, P_{wf}. This value determines the initial injection rate, which for all calculations determines the detachment of particles. The three values of P_{wf} (4000, 5000, 6000 psi) correspond to initial injection rates of 2.504×10^{-4}, 5.007×10^{-4}, and 7.511×10^{-4} m^2/s (equivalent to 136, 272, and 408 bbl/d/m). The resulting critical retention profiles as a function of the radial distance, r, are presented in Fig. 5. As the velocity is a decreasing function of the radial distance, all critical retention curves are increasing functions of this distance. For larger values of P_{wf}, the pressure gradient ($P_{wf} - P_{res}$) is larger and hence the flow rate is larger. This results in lower values of the critical retention function.

5.1. Impedance

The impedance has been calculated as per the solution derived in Section 2.3. The resulting curves are presented in Fig. 6. Higher injection pressures result in strictly higher values of impedance. This follows straightforwardly from the higher concentrations of detached particles as explained above. The atypically large slope during the initial stages of injection is indicative of the instant detachment caused by the velocity, while the more gradual impedance growth which follows is a result of the detachment induced by the injected salinity. The stabilisation of the impedance corresponds to the injection of an insignificant fraction of the reservoir pore volume. It follows that a majority of the damage occurs in the near-wellbore region.

5.2. Injectivity for constant injection rate

Fig. 7 shows the increase in pressure drop that corresponds to the model parameters derived from the laboratory study. As expected from Eq. (46), these curves follow a similar trend to the impedance curves. The curves show that for low salinity water injection at high injection

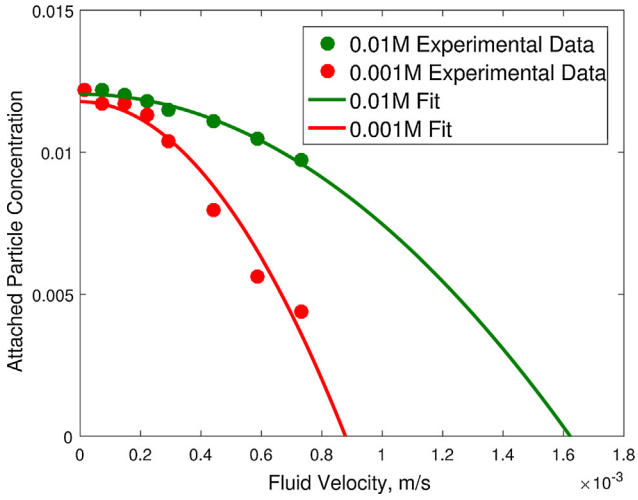

Fig. 4. Critical retention curves as a function of velocity at two different salinities derived from experiments and theoretical curves fit using Eq. (52).

Table 2
Parameters used for the prediction of injectivity decline.

Fines Migration Parameters	
Drift delay factor, α	0.02
Filtration coefficient, λ (1/m)	850
Formation damage coefficient, β	1100
Delay factor, τ (s)	1000
Maximum attached concentration, σ_0	1.191E−02
Initial attached concentration, σ_{al}	1.191E−02
U_{m1} (Initial reservoir salinity) (m/s)	1.622E−03
U_{m0} (Injected salinity) (m/s)	8.782E−04
Reservoir Properties	
Porosity, ϕ	0.3854
Drainage radius, r_e (m)	500
Initial permeability, k_0 (mD)	48
Fluid viscosity, μ (Pa.s)	8.9E−04
Reservoir pressure, P_{res} (psi)	3000
Well Parameters	
Wellbore radius, r_w (m)	0.1

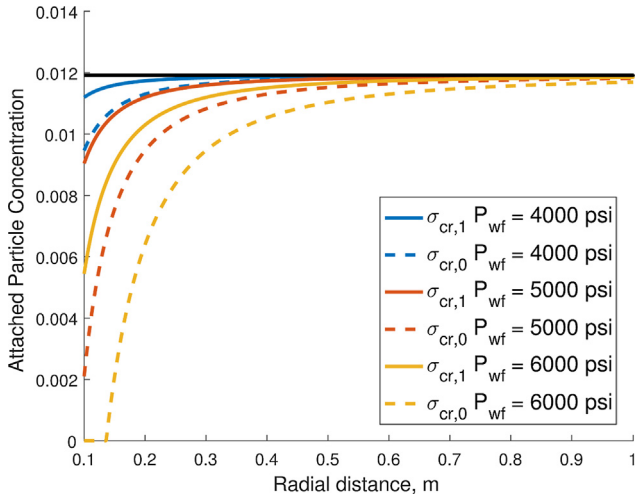

Fig. 5. Critical retention curves used in the injectivity decline predictions for different initial bottom-hole flowing pressures, P_{wf}. $\sigma_{cr,1}$ and $\sigma_{cr,0}$ are the critical retention functions at the initial and injected salinities respectively.

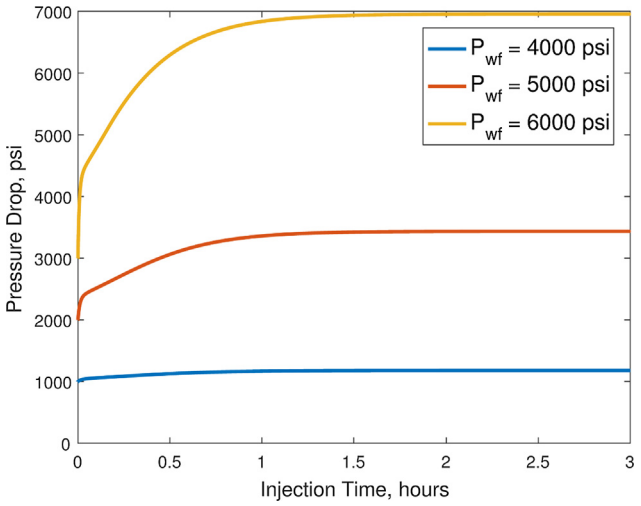

Fig. 7. Calculated bottom-hole pressures for three different values of the initial bottom-hole flowing pressure, P_{wf} under the condition of constant injection rate.

rates, more than 3000 psi of additional pressure drawdown would be required to maintain the initial injection rate. Such an increase is likely to test the capabilities of surface equipment or result in a bottom-hole pressure exceeding the formation fracture pressure.

5.3. Injectivity for constant bottom-hole pressure

The calculated decrease in injection rate due to fines migration is presented in Fig. 8. Similar to the increase in pressure drop, the calculations show that the injection rate can more than halve within only several hours of injection time.

Stabilisation of the injection rate takes longer than for the pressure drop discussed in the previous section. As outlined in Section 2.4, both variables share the same impedance curve and therefore stabilise after the same number of injected pore volumes. However, due to the decreasing injection rate, when the condition on the wellbore is of constant bottom-hole pressure, the rate at which pore volumes are injected decreases as per Eq. (50). The result is that while stabilisation occurs after a fixed number of injected pore volumes, a constant bottom-hole pressure results in a longer dimensional stabilisation time.

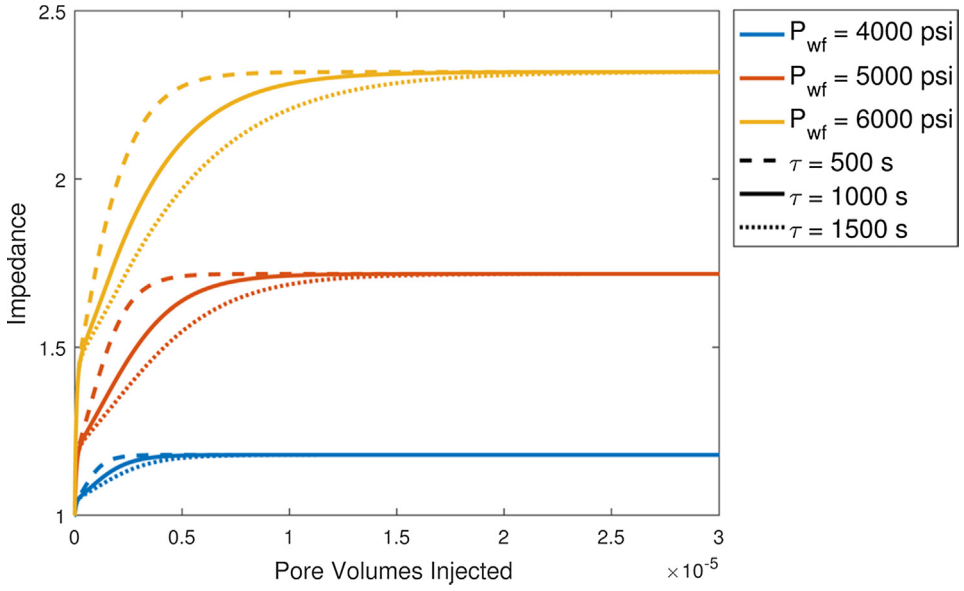

Fig. 6. Calculated well impedance for three different values of the initial bottom-hole flowing pressure, P_{wf} and three different values of the delay factor, τ.

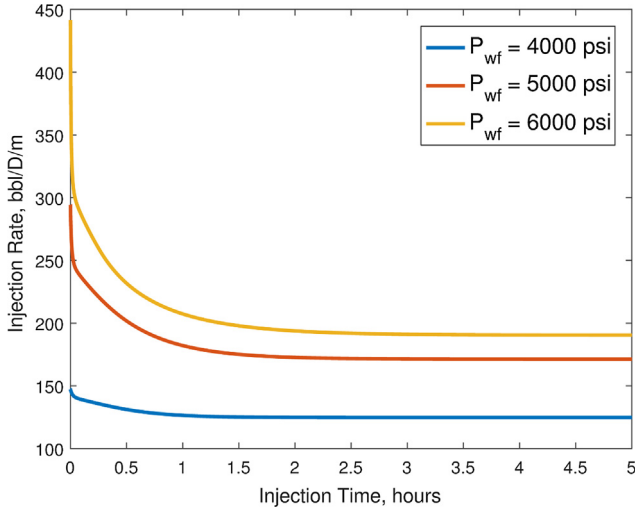

Fig. 8. Calculated injection rate for three different values of the initial bottom-hole flowing pressure, P_{wf} under the condition of constant bottom-hole pressure.

5.4. Damaged zone

Another result of the model is how far the formation damage extends from the wellbore. Fines detachment (Eq. (52)), straining (Eq. (6)), and the impact of permeability on pressure drawdown (Eq. (12)) are all increasing functions of velocity. Given the velocity distribution in Eq. (4), it follows that the damage due to fines migration is limited to within a certain distance from the wellbore. To that end we calculate the damaged zone radius, r_d, defined by (Nunes et al., 2010):

$$\frac{\int_{X(r_w)}^{X(r_e)} \frac{S_s(X,T)}{X} - \int_{X(r_w)}^{X(r_d)} \frac{S_s(X,T)}{X}}{\int_{X(r_w)}^{X(r_e)} \frac{S_s(X,T)}{X}} \leqslant \delta \tag{55}$$

which simplifies to

$$\frac{\int_{X(r_d)}^{X(r_e)} \frac{S_s(X,T)}{X}}{\int_{X(r_w)}^{X(r_e)} \frac{S_s(X,T)}{X}} \leqslant \delta \tag{56}$$

where δ is a small number indicating the extent to which removal of strained particles within the zone $[r_w, r_d]$ will remove the effect of fines migration on the well injectivity.

The damaged zone radius calculated from the laboratory data is presented in Fig. 9 with $\delta = 0.01$. The damaged zone is the same for the two lower values of P_{wf} but increases slightly when P_{wf} is increased to 6000 psi. All curves show a non-monotonic growth of the damaged zone radius with time. This effect is induced by the introduction of the delay factor. The initial growth is a result of detachment by the velocity. While these particles continue to strain, the effect of delay means that particles continue to detach very close to the wellbore, where damage is most significant. This results in a temporary decrease in r_d, which is quickly corrected by detachment by salinity further from the wellbore. The stabilised value is determined by the form of the critical retention function shown in Fig. 5, and the filtration coefficient, λ. The low values of r_d relative to the drainage radius, r_e support the notion outlined in Section 5.1 that the majority of damage occurs in the near-wellbore region.

Information of the damaged zone radius serves to guide re-perforation, acidizing, or backflow operations designed to mitigate injectivity issues caused by fines migration (Oyeneyin et al., 1996; Zhu et al., 2001). The values calculated for typical fines migration parameters indicates a damaged zone radius of less than 1 metre which suggests that damage due to fines migration is relatively shallow.

6. Discussion

Qualitative analysis of the solution Analysis of the solution for the suspended concentration shows that the solution can be separated into two solutions accounting for the detachment that occurs initially due to high velocities near the wellbore, and the detachment that is further induced by the low salinity water injection. The sum of the two solutions provides the complete solution given in Table 1. The separation of the two solutions is largely the consequence of the use of a constant filtration coefficient. As a result, detached particles will be transported and captured independently of each other.

Fig. 2 presents profiles for the particle concentrations at different moments.

Profiles of the attached concentration are given in Fig. 2b at $T = 0$, at three intermediate times, $T_1 < T_2 < T_3$, and after an infinite duration ($T \to \infty$). Immediately after injection has begun, particle detachment occurs at any point in the reservoir where the particle concentration lies above the critical retention function of the reservoir fluid ($S_{cr}(X,\Gamma = 1)$). Subsequently, for all points behind the salinity front ($X - X_w = T$), the attached concentration decreases exponentially towards the critical retention function of the injected salinity ($S_{cr}(X,\Gamma = 1)$). This profile is reached only after an infinite injection period.

Fig. 2c shows the suspended particle concentration profiles. The initial profile corresponds to the immediate detachment at the formation fluid salinity. This profile will tend to decrease due to particle straining and migration, but additional detachment induced by the injected fluid salinity can result in an increase in this profile at certain points in the reservoir. The suspended concentration remains at zero at the wellbore and tends to zero after an infinite injection period.

The strained concentration profiles are shown in Fig. 2d. The strained concentration begins at zero and tends to a finite profile after a sufficient injection period. As straining is modelled as an irreversible process, these profiles increase monotonically with time. The velocity dependence of the straining process results in profiles skewed towards the wellbore, where fluid velocities are higher.

Effect of the delay factor The impedance curves presented in Fig. 6 are shown for 3 different values of the delay factor, τ. As expected, smaller values of the delay factor result in faster stabilisation of the impedance. Despite the difference in stabilisation time, τ has no effect on the final value of the impedance, as it only changes the rate at which particles detach, not the total detached particle concentration. The sharp slope during the early times is independent of the delay factor, which supports the notion outlined in Section 5.1 that this atypically sharp increase in the impedance results from the straining of particles

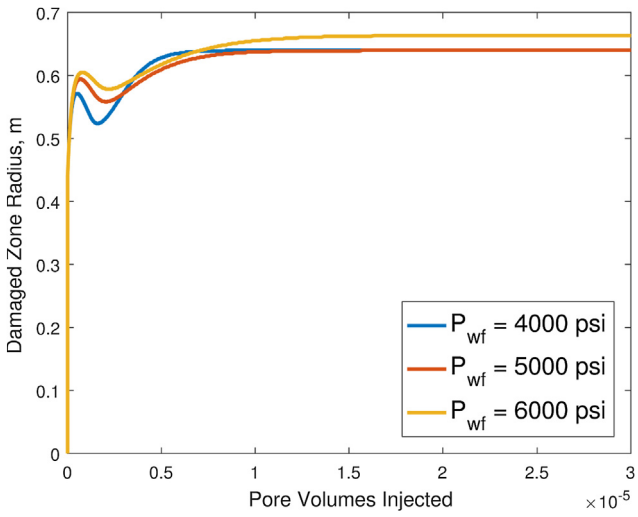

Fig. 9. Calculated damaged zone radius for three different values of the initial bottom-hole flowing pressure, P_{wf}.

detached due to velocity at the beginning of injection. These particles detach instantaneously, independent of τ.

Applications The developed model can be used for well injectivity prediction during water injection with an ionic composition which is different from that of formation water. The system of partial differential Eqs. (14)–(19) has been reduced to a set of implicit integral expressions using analytical techniques. The semi-analytical solution is much easier to implement into commercial software and provides more accurate and less computationally expensive results compared to a numerical solution of the original system.

7. Conclusions

In this paper, we have developed an analytical model of well injectivity decline due to fines migration with delayed detachment. Based on the mathematical modelling and laboratory-based injectivity predictions, the following conclusions can be drawn:

1. Introduction of the pseudo-salinity into the critical retention function while maintaining the direct dependency of velocity allows capturing physical effects of delayed detachment due to salinity variation and instant detachment due to high velocity.
2. The resulting mathematical model allows for a semi-analytical solution.
3. The solution allows predicting an increase in pressure drawdown or a decrease in the injection rate caused by fines migration.
4. Particle populations, instantly mobilised at the beginning of injection at high velocities, and gradually mobilised with delay behind the low-salinity front, perform deep bed filtration independently. The suspended concentration is the total of the suspended concentrations in both waves.
5. The delay factor results in an increased time until the well injectivity stabilises but has no effect on the final well injectivity.
6. Predictions of wellbore injectivity derived from a laboratory study show that high injection rates can result in injectivity index being reduced to less than half of its initial value.
7. The size of the formation damage zone due to fines migration, as calculated from laboratory data, does not exceed 1 metre.

References

Al-Abduwani, F.A., Shirzadi, A., van den Brock, W., Currie, P.K., 2005. Formation damage vs. solid particles deposition profile during. Lab. Simul. PWRI. Spe. J. 10 (02), 138–151.

Altoe, J.E., Bedrikovetsky, P., Siqueira, A.G., de Souza, A.L.S., Shecaira, F.S., 2006. Correction of basic equations for deep bed filtration with dispersion. J. Petrol Sci. Eng. 51 (1–2), 68–84.

Barkman, J., Abrams, A., Darley, H., Hill, H., 1975. An oil-coating process to stabilize clays in fresh waterflooding operations (includes associated paper 6405). J. Petrol. Technol. 27 (09), 1053–1059.

Bedrikovetsky, P., 1993. Mathematical Theory of Oil & Gas Recovery. Kluwer Academic Publishers, London-Boston-Dordrecth.

Bedrikovetsky, P., Siqueira, F.D., Furtado, C.A., Souza, A.L.S., 2011. Modified particle detachment model for colloidal transport in porous media. Transport Porous Med. 86 (2), 383–413.

Bernasconi, C.F., 1976. Relaxation Kinetics. Academic Press New York, New York.

Bradford, S.A., Simunek, J., Bettahar, M., Van Genuchten, M.T., Yates, S.R., 2003. Modeling colloid attachment, straining, and exclusion in saturated porous media. Environ. Sci. Technol. 37 (10), 2242–2250.

Bradford, S.A., Torkzaban, S., Shapiro, A., 2013. A theoretical analysis of colloid attachment and straining in chemically heterogeneous porous media. Langmuir: ACS J. Surfaces Colloids 29 (23), 6944–6952.

Chrysikopoulos, C.V., Katzourakis, V.E., 2015. Colloid particle size-dependent dispersivity. Water Resour. Res. 51 (6), 4668–4683.

Goldman, A.J., Cox, R.G., Brenner, H., 1967. Slow viscous motion of a sphere parallel to a plane wall - II Couette flow. Chem. Eng. Sci. 22, 653–660.

Gravelle, A., Peysson, Y., Tabary, R., Egermann, P., 2011. Experimental investigation and modelling of colloidal release in porous media. Transport Porous Med. 88 (3), 441–459.

Grolimund, D., Borkovec, M., 2006. Release of colloidal particles in natural porous media by monovalent and divalent cations. J. Contam. Hydrol. 87 (3–4), 155–175.

Hayek, M., 2014. Water pulse migration through semi-infinite vertical unsaturated porous column with special relative-permeability functions: exact solutions. J. Hydrol. 517, 668–676.

Hayek, M., 2015. An analytical model for steady vertical flux through unsaturated soils with special hydraulic properties. J. Hydrol. 527, 1153–1160.

Kalantariasl, A., Bedrikovetsky, P., 2013. Stabilization of external filter cake by colloidal forces in a "well–reservoir" system. Ind. Eng. Chem. Res. 53 (2), 930–944.

Kaplan, D.A., Muñoz-Carpena, R., 2014. Groundwater salinity in a floodplain forest impacted by saltwater intrusion. J. Contaminant Hydrol. 169, 19–36.

Khilar, K.C., Fogler, H.S., Ahluwalia, J., 1983. Sandstone water sensitivity: existence of a critical rate of salinity decrease for particle capture. Chem. Eng. Sci. 38 (5), 789–800.

Kia, S., Fogler, H.S., Reed, M., 1986. Effect of pH on colloidally induced fines migration. J. Colloid Interface Sci. 118 (1), 158–168.

Kuo, R.J., Matijevic, E., 1979. Particle adhesion and removal in model systems: Part 2 – Monodispersed chromium hydroxide on steel. J. Chem. Soc., Faraday Trans. 1 F 75, 2014–2026.

Mahani, H., Berg, S., Ilic, D., Bartels, W.B., Joekar-Niasar, V., 2015. Kinetics of low-salinity-flooding effect. Spec. J. 20 (1).

Mirabolghasemi, M., Prodanovic, M., DiCarlo, D., Ji, H.Y., 2015. Prediction of empirical properties using direct pore-scale simulation of straining through 3D micro-tomography images of porous media. J. Hydrol. 529, 768–778.

Nunes, M., Bedrikovetsky, P., Newbery, B., Paiva, R., Furtado, C., De Souza, A., 2010. Theoretical definition of formation damage zone with applications to well stimulation. J. Energy Res. Technol. 132 (3), 033101.

Oliveira, M.A., Vaz, A.S., Siqueira, F.D., Yang, Y., You, Z., Bedrikovetsky, P., 2014. Slow migration of mobilised fines during flow in reservoir rocks: laboratory study. J. Petrol. Sci. Eng. 122, 534–541.

Oyeneyin, M.B., Peden, J.M., Hosseini, A., Ren, G., 1996. Factors to Consider in the Effective Management and Control of Fines Migration in High Permeability Sands, European Formation Damage Conference. Society of Petroleum Engineers, The Hauge, The Netherlands.

Patil, S., Tawfiq, K., Chen, G., 2011. Colloid release and transport in agricultural soil as impacted by solution chemistry. J. Urban Environ. Eng. 5 (2), 84–90.

Pazmino, E., Trauscht, J., Johnson, W.P., 2014. Release of colloids from primary minimum contact under unfavorable conditions by perturbations in ionic strength and flow rate. Environ. Sci. Technol. 48 (16), 9227–9235.

Polyanin, A., Dilman, V.V., 1994. Methods of Modeling Equations and Analogies in Chemical Engineering. CRC Press, Boca Raton.

Polyanin, A., Zaitsev, V., 2011. Handbook of Nonlinear Partial Differential Equations. CRC Press.

Polyanin, A.D., Manzhirov, A.V., 2007. Handbook of Mathematics for Engineers and Scientists. CRC Press.

Prommer, H., et al., 2013. Final Report - Aquifer Storage and Recovery of Potable Water in the Leederville Aquifer. CSIRO Water for a Healthy Country National Research Flagship, Australia.

Rose, S.C., Buckwalter, J.F., Woodhall, R.J., 1989. The Design of Engineering Aspects of Waterflooding. Society of Petroleum Engineers, Richardson, TX, SPE Monograph Series.

Russell, T., Bedrikovetski, P., 2018. Colloidal-suspension flows with delayed fines detachment: analytical model & laboratory study. Chem. Eng. Sci. 190, 98–109.

Russell, T., Pham, D., Neishaboor, M.T., Badalyan, A., Behr, A., Genolet, L., Kowollik, P., Zeinijahromi, A., Bedrikovetsky, P., 2017. Effects of kaolinite in rocks on fines migration. J. Nat. Gas Sci. Eng. 45, 243–255.

Sasidharan, S., Bradford, S.A., Torkzaban, S., Ye, X., Vanderzalm, J., Du, X., Page, D., 2017. Unraveling the complexities of the velocity dependency of E. coli retention and release parameters in saturated porous media. Sci. Total Environ. 603–604, 406–415.

Shen, C., Bradford, S.A., Li, T., Li, B., Huang, Y., 2018. Can nanoscale surface charge heterogeneity really explain colloid detachment from primary minima upon reduction of solution ionic strength? J. Nanopart Res. 20 (6).

Sotirelis, N.P., Chrysikopoulos, C.V., 2015. Interaction between graphene oxide nanoparticles and quartz sand. Environ. Sci. Technol. 49 (22), 13413–13421.

Tikhonov, A.N., Smarskii, A.A., 2011. Equations of Mathematical Physics. Dover Publications Inc., United States.

Vardoulakis, I., Stavropoulou, M., Papanastasiou, P., 1996. Hydro-mechanical aspects of the sand production problem. Transport Porous Med 22 (2), 225–244.

Yang, Y., Siqueira, F.D., Vaz, A.S., You, Z., Bedrikovetsky, P., 2016. Slow migration of detached fine particles over rock surface in porous media. J. Nat. Gas Sci. Eng. 34, 1159–1173.

You, Z., Bedrikovetsky, P., Badalyan, A., Hand, M., 2015. Particle mobilization in porous media: temperature effects on competing electrostatic and drag forces. Geophys. Res. Lett. 42 (8), 2852–2860.

You, Z., Yang, Y., Badalyan, A., Bedrikovetsky, P., Hand, M., 2016. Mathematical modelling of fines migration in geothermal reservoirs. Geothermics 59, 123–133.

Yuan, H., Shapiro, A.A., 2011. Induced migration of fines during waterflooding in communicating layer-cake reservoirs. J. Petrol Sci. Eng. 78 (3), 618–626.

Zeinijahromi, A., Bedrikovetsky, P., 2016. Water Production Control Using Low-Salinity Water Injection, SPE Asia Pacific Oil & Gas Conference and Exhibition. Society of Petroleum Engineers.

Zhang, W., Tang, X.-Y., Xian, Q.-S., Weisbrod, N., Yang, J.E., Wang, H.-L., 2016. A field study of colloid transport in surface and subsurface flows. J. Hydrol. 542, 101–114.

Zheng, X.L., Shan, B.B., Chen, L., Sun, Y.W., Zhang, S.H., 2014. Attachment-detachment dynamics of suspended particle in porous media: experiment and modeling. J. Hydrol. 511, 199–204.

Zhu, D., Radjadhyax, N., Hill, A.D., 2001. Using Integrated Information to Optimizing Matrix Acidizing, SPE European Formation Damage Conference. Society of Petroleum Engineers, The Hague, The Netherlands.

5 Stochastic modelling of colloidal transport using Boltzmann's equation

5.1 Averaged Boltzmann's kinetics for colloidal transport in porous media

Russell, T., Dinariev, O. Yu., Pessoa Rego, L. A., Bedrikovetsky, P.

Water Resources Research, e2020WR029557

Statement of Authorship

Title of Paper	Upscaling Boltzmann's kinetics for colloidal transport in porous media
Publication Status	☐ Published ☑ Accepted for Publication ☐ Submitted for Publication ☐ Unpublished and Unsubmitted w ork w ritten in manuscript style
Publication Details	Russell, T., Dinariev, O. Yu., Pessoa Rego, L. A., Bedrikovetsky, P., Upscaling Boltzmann's kinetics for colloidal transport in porous media, Water Resources Research, Accepted for publication

Principal Author

Name of Principal Author (Candidate)	Thomas Russell		
Contribution to the Paper	Performed calculations, performed derivations, contributed to writing		
Overall percentage (%)	60%		
Certification:	This paper reports on original research I conducted during the period of my Higher Degree by Research candidature and is not subject to any obligations or contractual agreements with a third party that would constrain its inclusion in this thesis. I am the primary author of this paper.		
Signature		Date	16/02/2021

Co-Author Contributions

By signing the Statement of Authorship, each author certifies that:

i. the candidate's stated contribution to the publication is accurate (as detailed above);

ii. permission is granted for the candidate in include the publication in the thesis; and

iii. the sum of all co-author contributions is equal to 100% less the candidate's stated contribution.

Name of Co-Author	Osipov Dinariev		
Contribution to the Paper	Performed derivations		
Signature		Date	23/02/2021

Name of Co-Author	Rego Pesssoa		
Contribution to the Paper	Performed derivations		
Signature		Date	23/02/2021

Please cut and paste additional co-author panels here as required.

Name of Co-Author	Pavel Bedrikovetsky		
Contribution to the Paper	Performed derivations, contributed to writing		
Signature		Date	17/02/2021

Averaged Boltzmann's kinetics for colloidal transport in porous media

Russell, T. [2], Dinariev, O.Yu.[1], Pessoa Rego, L. A.[2], Bedrikovetsky, P.[2]
[1]Institute of the Earth Physics, Russian Academy of Sciences; [2]University of Adelaide, Australia

Key words: porous media; Boltzmann's equation; stochastic modelling; colloid; upscaling; averaging

Abstract Due to the stochastic nature of pore space geometry, particle velocities in a colloidal-suspension flux are also stochastically distributed. This phenomenon is captured by Boltzmann's kinetic equation. We formulate a BGK-form of Boltzmann's equation for particulate flow with a particle capture rate proportional to the particle speed and derive an exact method for the model's averaging. The averaged equation is of the form of a reaction-advection-diffusion equation with the average particle speed lower than the carrier fluid velocity. This delay, reported in numerous laboratory studies, is explained by preferential capture of fast particles. The large-scale model coefficients of delay, dispersion, and filtration are explicitly expressed via the micro-scale mixing length, equilibrium velocity distribution, and filtration coefficient. The properties of the averaged coefficients are discussed, and emerging dependencies between them are presented. The derived large-scale equation resolves two paradoxes of the traditional model for suspension-colloidal transport in porous media. The large-scale equation closely matches the laboratory breakthrough curves.

Nomenclature

v	Particle velocity, [L][T]$^{-1}$	L	Core length, [L]
c	Suspended particle concentration, [-]	Pe	Dimensionless Peclet number, [-]
t	Time, [T]	$\overline{v}$	Mean fluid velocity, [L][T]$^{-1}$
y	Normalised particle velocity, [-]	x	Distance, [L]
D	Diffusion coefficient, [L]^2[T]$^{-1}$	C_v	Coefficient of variation, [-]
q	Particle flux per unit area, [L][T]$^{-1}$	M_{-1}	Negative first moment
A	Cross sectional area, [L]^2	W	Lambert W function
Δz	Incremental distance along flow direction, [L]	w	Laplace variable
Δt	Incremental unit of time, [T]	R^2	Coefficient of determination, [-]
p	Probability of particle capture, [-]	H	Hilbert space of solutions to Boltzmann's equation
H_c	Hilbert subspace of averaged concentration	f	Suspended particle concentration, [-]
H_a	Hilbert subspace of deviation from average	$\lvert v\rvert$	Absolute velocity, [L][T]$^{-1}$
P_c	Projection operation from H to H_c	P_a	Projection operation from H to H_a
l	Mixing length, [L]	J_c	Embedding operator from H_c to H
s	Initial and boundary conditions, [-]	J_a	Embedding operator from H_a to H
a	Deviation of concentration from mean	k	Fourier variable corresponding to x
R_{ij}		q_F	Fourier transform of particle flux
$\overline{\lvert v\rvert}$	Mean of the absolute particle velocity, [L][T]$^{-1}$	ε_F	Fourier transform of particle capture rate
T	Dimensionless time, [-]	K_{ij}	Inverse Fourier transform of R_{ij}
X	Dimensionless distance, [-]		

Greek characters

$\psi_0(v)$	Equilibrium velocity distribution, [L]$^{-1}$[T]	θ	Delay factor, [-]
Ω	Dimensionless Filtration Coefficient, [-]	$\psi_1(v)$	Normalised equilibrium velocity distribution, [-]
ϕ	Porosity, [-]	σ	Standard deviation of the equilibrium velocity distribution, [L][T]$^{-1}$

α	Positive fraction of the equilibrium velocity distribution	ε	Particle capture rate, $[T]^{-1}$
σ_s	Captured particle concentration, [-]	$\delta(t)$	Delta function
λ	Filtration coefficient, $[L]^{-1}$	τ	Relaxation time, [T]
φ	Transformed suspended particle concentration, [-]	ω	Fourier variable corresponding to t

1. Introduction

During suspension flows through porous media, interaction of particles with the rock matrix leads to particle immobilisation. The capture of suspended particles leads to both a decrease in the suspended concentration, and a change in the rock properties by an alteration of the effective rock matrix. Both of these effects have granted particulate flows in porous media significant academic and industrial interest.

Particle flow and capture is prevalent in a number of industries. For example, some researchers in contaminant hydrology have noticed the impact that migrating clays can have on the retention and thus stabilisation of contaminants in soils (Bianco et al. 2016, Chrysikopoulos et al. 2017, Chrysikopoulos et al. 2012, Goldberg et al. 2014) Joint transport of clays, viruses, bacteria, and nanoparticles occurs in industrial applications of nanotechnology to prevent aquifer contamination (Sethi et al. 2014, Tosco et al. 2014, Tosco and Sethi 2010). In addition, a reduction in the rock permeability as a result of particle capture is significant for freshwater storage in aquifers (Prommer et al. 2013), catalytic chemical reactors (Boccardo et al. 2019), drilling operations (Salimi and Ghalambor 2011), as well as injection and production wells (Akhmetgareev and Khisamov 2015, Barkman et al. 1975) used in the petroleum industry and water resources management. Accurate modelling of the underlying processes is fundamental to improving industry practices. While often broadly referred to as particle capture, retention of particles can occur by several different mechanisms. Figure 1a shows some of the most common of these, being straining (size-exclusion) of particles by thin pore throats, attachment to the rock via attractive electrostatic forces, bridging via the construction of mechanically stable structures at wider pore throats, and trapping in dead-end pore throats, typically facilitated by diffusion (Elimelech et al. 2013, Hilpert and Johnson 2018, Johnson et al. 2018). The discussion in this work is limited to particle capture by straining.

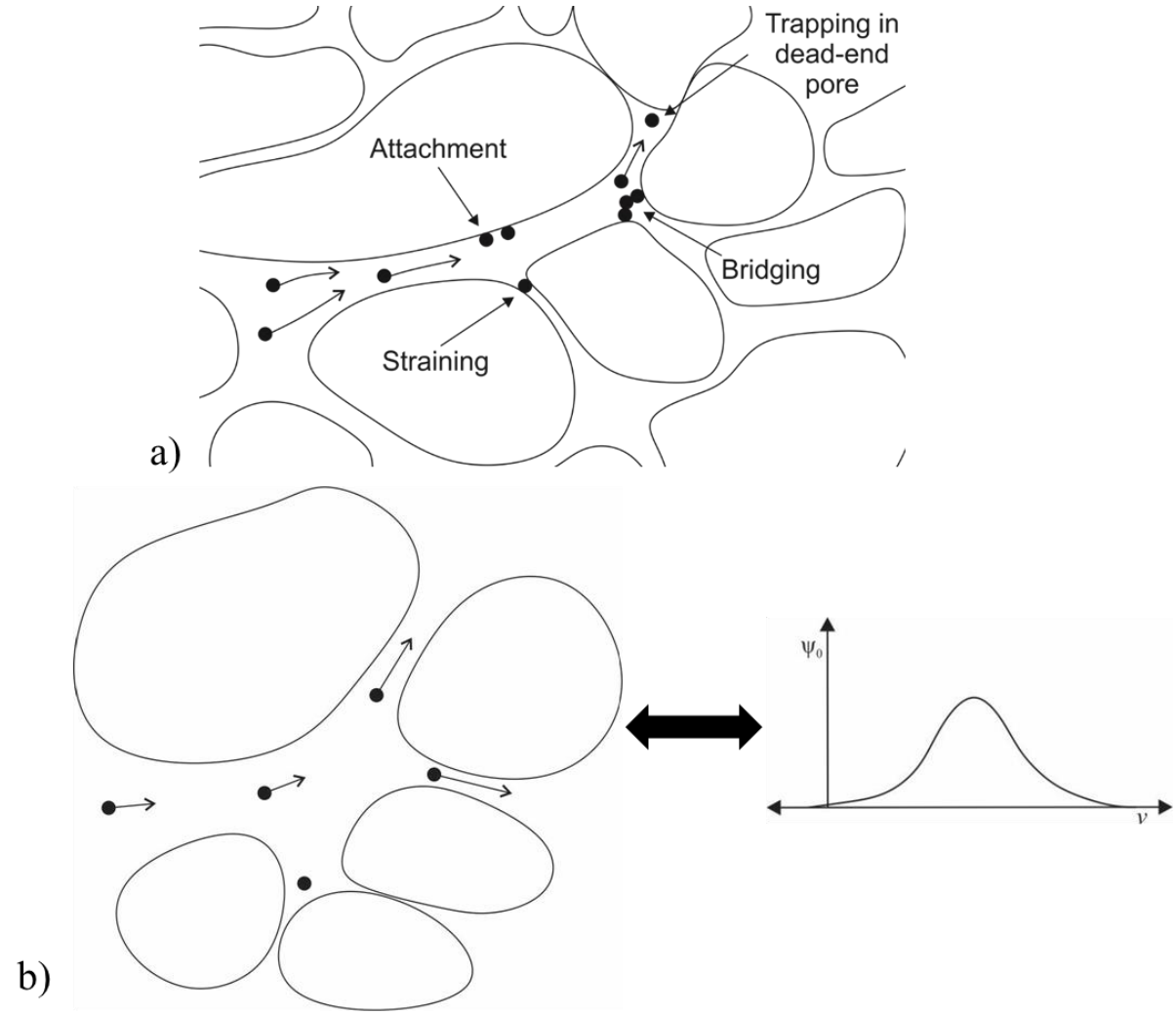

Figure 1: Pore scale processes occurring during particle transport in porous media: a) Various particle capture mechanisms, b) Distribution of particle velocities at the pore scale

At the core of the present study is to investigate the interaction between the particle transport and capture and the resulting impacts on large-scale behaviour. Particle transport, like many processes, possesses more detail and complexity than is typically of interest to practitioners. This is most evident in the distribution of individual particle velocities at the pore-scale (Arns 2004, Arns et al. 2005). This is illustrated in Figure 1b, where the collection of particle velocities is represented by a probability distribution, $\psi_0(v)$. In most studies or applications of particle transport in porous media, a detailed description of this distribution is unnecessary and overly cumbersome. However, it is at this level of detail that physical models of particle transport are most accurate. As a result, a means of deriving averaged or macro-scale equations from detailed or micro-scale equations is required.
An excellent example of this style of modelling employed to study particle flow without capture was provided by (Einstein 1905). He envisaged particle flow as a series of random jumps following a given jump distribution. Using this simple micro-scale model, he derived the advection-diffusion equation (ADE)

$$\frac{\partial c}{\partial t} + \bar{v}\frac{\partial c}{\partial x} = D\frac{\partial^2 c}{\partial x^2} \tag{1}$$

where c is the suspended particle concentration, t and x are the time and space coordinates respectively, $\bar{v}$ is the mean particle velocity, and D is the diffusion coefficient. We note here that in Einstein's original derivation, he added the additional condition that the probability of jumps forward any distance was equal to that of jumps of equal distance backwards, resulting in zero mean velocity. This derivation shows how detailed micro-scale models can be used to describe the large-scale

behaviour of a system. An alternative approach is to modify existing macro-scale equations to account for additional processes. Such has largely been the case for particle capture in porous media. While still adhering to the physical principles of the underlying processes, this second approach can create unreasonable large-scale behaviour, as will be shown below.

The basis for most models of particle flow with capture is a mass balance equation

$$\phi \frac{\partial c}{\partial t} + \frac{\partial q}{\partial x} = -\varepsilon \tag{2}$$

where ϕ is the rock porosity, q is the total particle flux, and ε is the particle capture rate.

In large-scale approximations, diffusion and dispersion are ignored, resulting in a purely advective particle flux; the corresponding scaling derivations are available from (Bedrikovetsky 1993, Tartakovsky and Dentz 2019)

$$q = \bar{v}c\,. \tag{3}$$

Otherwise, the flux is as it is for the regular advective-diffusive equations (ADE) (Boso and Tartakovsky 2016, Polyanin and Dilman 1994):

$$q = \bar{v}c - D\frac{\partial c}{\partial x} \tag{4}$$

For the particle capture rate, consider a cross section of the porous media of thickness, Δz, and area A. During a time Δt, the volume of retained particles will change from $A\Delta z\sigma_s$ (where σ_s is the retained particle concentration per unit volume) to $A\Delta z\left(\sigma_s + \frac{\partial \sigma_s}{\partial t}\Delta t\right)$. During this time, a volume $A\bar{v}c\Delta t$ of particles enters the volume of interest. Defining the capture probability as the change in retained volume per unit volume of particle entering the control volume, we obtain:

$$p = \frac{A\Delta z \frac{\partial \sigma_s}{\partial t}\Delta t}{A\bar{v}c\Delta t} = \frac{\Delta z}{\bar{v}c}\frac{\partial \sigma_s}{\partial t}\,. \tag{5}$$

Defining the filtration coefficient, λ, as this probability per unit length of the particle path Δz, we arrive at the following expression for the capture rate (Bradford et al. 2011, Messina et al. 2015, Yuan et al. 2012)

$$\varepsilon = \frac{\partial \sigma_s}{\partial t} = \lambda c\left|\bar{v}\right| \tag{6}$$

Here $\bar{v}$ is the mean particle speed. The absolute value sign around the mean velocity is used to signify that capture will occur regardless of the flow direction. This derivation was presented by (Herzig et al. 1970) and has largely formed the basis of models for particle capture in porous media since (Elimelech et al. 2013, Goldberg et al. 2014).

(Altoé F et al. 2006) and (Zhang et al. 2018) argued that in cases where diffusion/dispersion are significant, that the flux of particles entering the cross section should include this term. Thus, the equation for the capture rate becomes

$$\varepsilon = \frac{\partial \sigma_s}{\partial t} = \lambda\left|q\right| = \lambda\left|\bar{v}c - D\frac{\partial c}{\partial x}\right|. \tag{7}$$

While the arguments above seem logically consistent with the physics of particle capture, the resulting model has several inconsistencies. Consider for example, the case of particle flow with zero mean velocity and a constant initial suspended concentration in x. Intuition would provide that particles jump randomly in space, slowly becoming captured. Thus the initial, uniform profile of suspended particles should remain uniform, but decrease slowly with time. However, both equations (6) and (7) predicts a capture rate of zero, thus predicting a constant suspended concentration.

Another shortcoming of the model given by equations (2,4,7) is associated with the split of advection and diffusion/dispersion into additive terms in the mass balance equation, as described by (Zhang et al. 2018). Consider the motion of a single particle during a period Δt. As seen in Figure 2, the picture outlined by equation (4) is that of advection and diffusion occurring separately (dotted line), while in reality (solid line), the particle makes a single motion during this time period. This picture demonstrates that the model correctly models the final position of the particle. However, as was

shown earlier, particle capture via straining occurs with a fixed probability per unit travel distance. So, given that the total travel distance is over-estimated, so too will be the probability of capture.

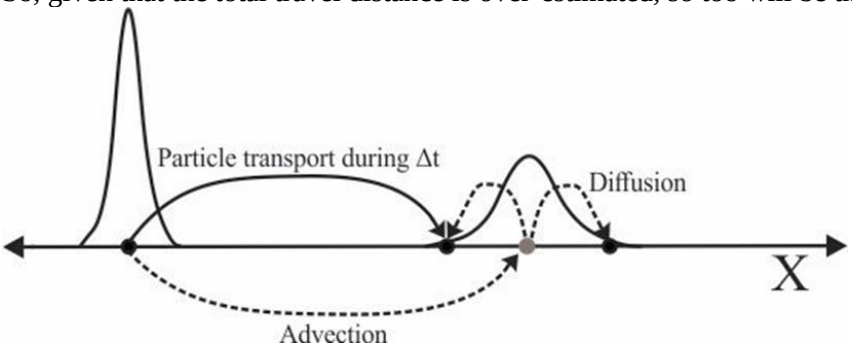

Figure 2: Diagrammatic depiction of the separation of particle transport into additive advective and diffusive components

The capture rate given by equation (7) also presents another paradox. When the particle capture or diffusion are particularly high, the second term in the capture rate exceeds the mean velocity. Thus the effective advective velocity, meaning the coefficient of the first order derivative of c, is negative. This leads to the rather confusing result that a concentration pulse will move on average in the direction opposite to the mean fluid velocity. We are aware of no physical reasoning that could make this plausible. Therefore, the equation seems to be invalid for this case. A more rigorously derived model ought to remedy this paradox, or at the very least provide some insight into the origin thereof.
Deriving a model for particle flow and capture by modifying the ADE clearly presents several paradoxes in the resulting large-scale behaviour. This suggests the need for the construction of an accurate micro-scale model for particle transport and capture and a consistent averaging procedure.
This approach to modelling processes in porous media has had significant attention for several decades. Various micro-scale models have been presented to solve problems related to particle capture, including continuous random walk models (Shapiro 2007, Yuan et al. 2012, Yuan and Shapiro 2010), trajectory analysis models (Payatakes et al. 1974), as well as models with distributions of filtration coefficients to model pore-scale heterogeneity (Yuan and Shapiro 2010). The population balance models to explicitly account for the changes in the particle and pore size distributions have been derived by (Bedrikovetsky 2008, Bedrikovetsky et al. 2019, Bedrikovetsky et al. 2017, Shapiro and Yuan 2012, Sharma and Yortsos 1987a, Sharma and Yortsos 1987b). A similar philosophy is also present in modelling of reactive flows (Kechagia et al. 2002) and biological processes (Knutson et al. 2007) in porous media. Another approach to upscaling is to introduce scale-dependent properties and perform stochastic averaging; the incomplete list of the related papers include (Arns and Adler 2018a, Arns and Adler 2018b, Arns et al. 2005, Dagan et al. 2013, Hou 2005, Messina et al. 2016, Pan and Tartakovsky 2013, Rabinovich 2017, Rabinovich et al. 2013, Tartakovsky et al. 2017, Winter and Tartakovsky 2002).
While numerous methods have been developed for modelling transport (Hunt and Sahimi 2017), reaction (Dentz et al. 2011), and colloid capture (Molnar et al. 2015) in porous media, no model has explicitly coupled the distribution of particle velocities with a velocity dependent capture rate. In this paper, we formulate the problem of particle transport with capture using Boltzmann's kinetic equation. Through the addition of particle velocity as an additional internal variable, we can explicitly couple the particle velocity distribution with the velocity dependent capture rate. The Boltzmann equation can be averaged to provide an equation similar to the previous model (equations (2,4,7)) which resolves the paradoxes discussed above. Further, we discuss the properties of the model, make a comparison with laboratory data on colloidal flow, and in this context discuss the limitations of the model.
This approach varies from the works described above in that it does not explicitly involve upscaling from a micro-scale model to a macro-scale one. Instead, we model particle transport with additional detail by modelling particle velocity in order to rigorously describe the interaction between particle diffusion and capture. This additional level of detail is then 'averaged' to arrive at an equation describing the evolution of the particle concentration.

The structure of the paper is as follows. Section 2 outlines the use of Boltzmann's equation to derive an accurate micro-scale model for colloidal flow and capture in porous media. Section 3 provides a detailed discussion of the averaged model and the derived coefficients. Section 4 presents a comparison of the model with several laboratory coreflooding tests. Section 5 provides a discussion of the extent to which the model presented in this work resolves the paradoxes outlined in the paragraphs above, as well as limitations of the model in the context of modelling water resources. Finally, Section 6 concludes the paper.

2. Kinetics equation for colloidal transport in porous media

Boltzmann originally formulated his famous equation to describe the kinetics of gases (Boltzmann 2012). Different formulations for Boltzmann's approach to transport in porous media have been undertaken by (Shapiro and Wesselingh 2008, Shapiro and Yuan 2012). In these works, the particle velocity distribution is a result of Brownian collisions. On the contrary, in the present work we discuss a distribution of particle velocities that results from the complex porous space. In 1996, (Dinariev 1996) formulated a novel averaging methodology for linear forms of Boltzmann's equation to describe the averaged properties of the gas. He applied this methodology to describe the properties of relativistic and nonrelativistic plasma (Dinariev 1996, 1999, 2005). Recently, the same approach has been used to describe particle transport and capture in porous media (Dinariev et al. 2020). Below we provide a brief description of this equation, and the motivation behind its use.

Boltzmann's equation for colloidal transport in porous media accounting for particle capture is

$$\phi\frac{\partial f}{\partial t}+v\frac{\partial f}{\partial x}=-\lambda|v|\,f+\frac{1}{\tau}\left[\int_{-\infty}^{\infty} f dv\,\psi_0-f\right] \tag{8}$$

where $f(x,t,v)$ is the particle concentration, t and x are the coordinates for time and space respectively, v, is the fluid velocity, λ is the filtration coefficient, and τ is the mixing time.
Here we have adopted a linear BGK relaxation term (Bhatnagar et al. 1954) to account for the tendency of the particle velocity distribution to 'relax' towards the equilibrium distribution, ψ_0.
In this context, the mixing time can be thought of as the average time for a population of particles, unimpeded by other factors, to achieve velocities distribution according to the equilibrium distribution.
The relaxation term as well as any degree of width in the particle velocity distribution leads to spreading of the particle concentration. Diffusion is typically negligible for particles large enough to experience straining, so we consider that this spreading occurs only via dispersion. Under most conditions, dispersion is proportional to the mean fluid velocity, so we take

$$\tau=\frac{l}{\bar{v}} \tag{9}$$

where l is the mixing length and the mean velocity is given by

$$\bar{v}=\int_{-\infty}^{\infty} v\psi_0(v)\,dv\,. \tag{10}$$

The scale at which equation (8) is postulated encompasses several pore sizes, where the porosity is well established. This scale significantly exceeds the mixing length, l.
In contrast with modelling approaches based on a mass balance equation, given by equation (2), this model describes the particle concentration as a function of fluid velocity. Thus particles are in essence divided not only in space and time, but also by their velocity. The advantage of this is that particles are captured according to their velocity, not in relation to the mean fluid velocity. This equation forms the description of particle flow and transport on the micro-scale.
Integration of equation (8) with respect to v across all possible values of the velocity yields equation (2), with

$$c(x,t)=\int_{-\infty}^{\infty} f(x,t,v)dv \tag{11}$$

$$q(x,t)=\int_{-\infty}^{\infty} v f(x,t,v)\,dv \tag{12}$$

$$\varepsilon(x,t)=\lambda\int_{-\infty}^{\infty} |v|\, f(x,t,v)\,dv \tag{13}$$

In order to derive a useful macro-scale equation, we wish to average equation (8) to express the flux, q, and capture rate, ε, in terms of the averaged particle concentration, c.

3. Averaged system

In this section we provide some details on the method used to average equation (8), provide the final form of the macro-scale equation, and then investigate various properties and consequences of this equation.
A complete description of the mathematics of the averaging method has been provided in a previous paper by (Dinariev et al. 2020). Thorough details of the derivation are presented in the Appendices.

3.1. Final form of the averaged model

Following the derivation outlined in the Appendices, the flux and capture rate can be written as

$$q=\bar{v}c-R_{11}\frac{\partial c}{\partial x}-\lambda R_{12}c \tag{14}$$

$$\varepsilon=\lambda\overline{|v|}c-\lambda R_{21}\frac{\partial c}{\partial x}-\lambda^2 R_{22}c \tag{15}$$

where R_{11}, R_{12}, and R_{22} are constants that depend on the micro-scale filtration coefficient, λ, the mixing length, l, and the equilibrium particle velocity distribution, $\psi_0(v)$:

$$R_{ij}=\int_{-\infty}^{\infty}\frac{v_i v_j}{\lambda|v|+\frac{\bar{v}}{l}}\psi_0 dv-\frac{\int_{-\infty}^{\infty}\frac{v_i}{\lambda|v|+\frac{\bar{v}}{l}}\psi_0 dv\int_{-\infty}^{\infty}\frac{v_j}{\lambda|v|+\frac{\bar{v}}{l}}\psi_0 dv}{\int_{-\infty}^{\infty}\frac{1}{\lambda|v|+\frac{\bar{v}}{l}}\psi_0 dv} \tag{16}$$

where $v_1=v$ and $v_2=|v|$.
Substituting the final expressions for the flux and capture rate into equation (2) yields

$$\phi\frac{\partial c}{\partial t}+\left(\bar{v}-2\lambda R_{12}\right)\frac{\partial c}{\partial x}=R_{11}\frac{\partial^2 c}{\partial x^2}-\left(\lambda\overline{|v|}-\lambda^2 R_{22}\right)c\ . \tag{17}$$

Introducing the dimensionless variables

$$T=\frac{\bar{v}t}{\phi L},\ X=\frac{x}{L} \tag{18}$$

allows equation (17) to be written in dimensionless form

$$\frac{\partial c}{\partial T}+\left(1-\frac{2\lambda R_{12}}{\bar{v}}\right)\frac{\partial c}{\partial X}=\frac{R_{11}}{\bar{v}L}\frac{\partial^2 c}{\partial x^2}-\frac{L}{\bar{v}}\left(\lambda\overline{|v|}-\lambda^2 R_{22}\right)c \tag{19}$$

This equation contains three dimensionless parameters

$$\theta=\frac{2\lambda R_{12}}{\bar{v}},\ \frac{1}{Pe}=\frac{R_{11}}{\bar{v}L},\ \Omega=\frac{L}{\bar{v}}\left(\lambda\overline{|v|}-\lambda^2 R_{22}\right) \tag{20}$$

We refer to θ as the delay number, Pe^{-1} is the inverse Peclet number, and Ω is the macroscopic filtration coefficient. Thus the final macro-scale equation is

$$\frac{\partial c}{\partial T}+(1-\theta)\frac{\partial c}{\partial X}=\frac{1}{Pe}\frac{\partial^2 c}{\partial x^2}-\Omega c\ . \tag{21}$$

A detailed derivation for each of these parameters has been provided in a previous work by (Dinariev et al. 2020). Here we provide only the final forms.
The delay number can be written as:

$$\theta = \frac{2}{\bar{v}}\left[\int_{-\infty}^{\infty}\frac{v|v|}{|v|+\frac{\bar{v}}{\lambda l}}\psi_0(v)\,dv - \frac{\left(\int_{-\infty}^{\infty}\frac{v}{|v|+\frac{\bar{v}}{\lambda l}}\psi_0(v)\,dv\right)\left(\int_{-\infty}^{\infty}\frac{|v|}{|v|+\frac{\bar{v}}{\lambda l}}\psi_0(v)\,dv\right)}{\int_{-\infty}^{\infty}\left(|v|+\frac{\bar{v}}{\lambda l}\right)^{-1}\psi_0(v)\,dv}\right] \tag{22}$$

The final expression depends only on the dimensionless product λl, and the equilibrium velocity distribution, $\psi_0(v)$. The term λl is referred to as the filtration-mixing number and quantifies the competition between the effects of capture and mixing on the velocity distribution.
The inverse Peclet number can be written as:

$$\frac{1}{Pe} = \frac{l}{L}\frac{1}{\bar{v}\lambda l}\left[\int_{-\infty}^{\infty}\frac{v^2}{|v|+\frac{\bar{v}}{\lambda l}}\psi_0(v)\,dv - \frac{\left(\int_{-\infty}^{\infty}\frac{v}{|v|+\frac{\bar{v}}{\lambda l}}\psi_0(v)\,dv\right)^2}{\int_{-\infty}^{\infty}\left(|v|+\frac{\bar{v}}{\lambda l}\right)^{-1}\psi_0(v)\,dv}\right] \tag{23}$$

The right-hand side only depends on the filtration-mixing number, and the term l/L, or the dimensionless mixing number. This ratio can be interpreted as the micro-scale dimensionless diffusion coefficient, while Pe^{-1} serves as the macro-scale equivalent.
Finally, the macro-scale filtration coefficient can be written as:

$$\Omega = \frac{\lambda L}{\bar{v}}\left[\int_{-\infty}^{\infty}|v|\psi_0(v)\,dv - \int_{-\infty}^{\infty}\frac{|v|^2}{|v|+\frac{\bar{v}}{\lambda l}}\psi_0(v)\,dv - \frac{\left(\int_{-\infty}^{\infty}\frac{|v|}{|v|+\frac{\bar{v}}{\lambda l}}\psi_0(v)\,dv\right)^2}{\int_{-\infty}^{\infty}\left(|v|+\frac{\bar{v}}{\lambda l}\right)^{-1}\psi_0(v)\,dv}\right] \tag{24}$$

Again, this expression depends on the filtration-mixing number, as well as the term, λL, which, as with the inverse Peclet number, can be viewed as the dimensionless micro-scale equivalent of Ω.
By making the substitution

$$\psi_0(v) = \frac{1}{\bar{v}}\psi_1(y), y = \frac{v}{\bar{v}} \tag{25}$$

It can be shown that the terms in the square brackets in equations (22-24) are directly proportional to the mean fluid velocity (Dinariev et al. 2020). As such, the macro-scale coefficients are all independent of the mean fluid velocity.
Table 1 presents asymptotic limits of the three macro-scale model coefficients. The results include the coefficient of variation, C_v, a standardised measure of the dispersion of the distribution.

$$C_v = \frac{\sigma}{\bar{v}} \tag{26}$$

where σ is the standard deviation, or the second central moment of the equilibrium velocity distribution.

Table 1: Asymptotic limits of the macroscale model coefficients

	$\lambda l \to 0$	$\lambda l << 1$	$\lambda l \to \infty$
Pe^{-1}	$\frac{l}{L} C_v^{\,2}$	$\frac{l}{L}\left[C_v^{\,2} - \lambda l \left[\int y^3 \psi_1(y)\, dy + 1 - 2C_v^{\,2} \right] \right]$	0
θ	0	$2\lambda l C_v^{\,2}$	$2\left[1 - \left(\int y^{-1} \psi_1(y)\, dy \right)^{-1} \right]$
Ω	0	$\lambda L \left[1 - \lambda l C_v^{\,2} \right]$	∞
$\Omega/\lambda L$	1	$1 - \lambda l C_v^{\,2}$	$\left(\int y^{-1} \psi_1(y)\, dy \right)^{-1}$

While explicit forms for the integrals in equations (22-24) may be difficult to find for arbitrary equilibrium velocity distributions, they are relatively easy to calculate using any numerical software package.

3.2. Properties of the transport coefficients

In this section we perform sensitivity analysis on the coefficients in order to further understand the physical meaning of the model coefficients in the final averaged equation.

First, let us be clear on the physical interpretation of each of the macro-scale coefficients. Each coefficient is a quantification of properties of the particle velocity distribution 'after' capture. In reality, the particle velocity distribution will vary substantially in time and space as capture and transport occur. However, as a result of the assumption (), the system loses its 'memory' (in order to be expressed as a finite partial differential equation), and the system models the post capture velocity distribution as per equations (22-24). The terms within each integral show the competing effects of the particle capture ($\lambda|v|$), which acts to unevenly reduce the number of particles, and dispersion ($\bar{v}/l$), which counters the effects of capture by normalising the distribution to its original form.

As can be seen from equations (22-24), the coefficients Pe^{-1}, θ, and Ω depend on λ, l, L, and $\psi_0(v)$. Dependency on the first three can be reformulated as dependency on the product λl, the ratio l/L (for Pe^{-1} only), and the product λL (for Ω only). Dependency on the latter two is a simple proportionality, demonstrating that for Pe^{-1} and Ω, the macro-scale coefficients derived using averaging are directly proportional to the micro-scale equivalents. Thus, for the following sensitivity analysis, we consider the ratio of the macro-scale to micro-scale coefficients where applicable.

Dependency on the equilibrium velocity distribution is slightly more complex. Here we consider the effect of the first two moments on the coefficients. This is appropriate because the two forms of the distributions we investigate (lognormal and normal), can be uniquely determined by their first two moments. In general, a distribution cannot be uniquely determined even by an infinite set of its moments. We leave the study in the context of such distributions to the interested reader.

As the coefficients do not depend on the first moment ($\bar{v}$), we consider dependency on the second moment through the coefficient of variation.

Applying the Cauchy-Schwarz inequality to the explicit formulae for the three large-scale model coefficients (equations (22-24)), yields positiveness of the Peclet number, coefficient R_{22}, and filtration coefficient Ω (Dinariev et al. 2020). While no definite proof has been derived proving the positiveness of θ, all numerical calculations support this statement.

First, we study the case where all particles move in the direction of the mean fluid velocity, or rather, where all particle velocities are positive. To this end, we use a lognormal distribution to describe $\psi_0(v)$. Figure 3 shows the results of the sensitivity study for this case.

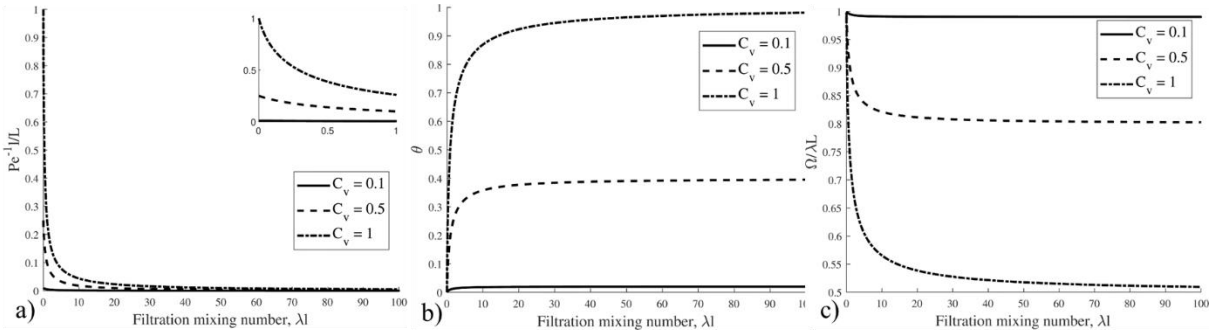

Figure 3: Sensitivity study for the case where all particle velocities are positive ($\psi_0(v)$ is lognormal): a) Macro-scale/micro-scale diffusion coefficient, $Pe^{-1}l/L$, b) Delay number, θ, c) Macro-scale/micro-scale filtration coefficient, $\Omega/\lambda L$

Figure 3a shows that the filtration coefficient decreases with the filtration-mixing number. Consider a fixed mixing number, l, with a varying filtration coefficient, λ. Given that particle capture is more significant for particles with higher velocities, naturally particle capture will disproportionally reduce the right tail of the velocity distribution. With higher capture, more of the larger velocities will be reduced, shifting the velocity distribution towards zero velocities. As the filtration coefficient tends to infinity, only particles with infinitely small velocities will avoid capture, resulting in a velocity distribution tending towards a delta function at $v = 0$. Particles sharing the same velocity will show no dispersion on the macro-scale, and thus the dispersion coefficient tends to zero.
The same tendency is true at a fixed filtration coefficient and an infinite mixing length, l. If we consider mixing not as a continuous, ongoing process, but rather a discrete process, occurring chambers at a fixed distance, l, apart. In these chambers, the velocity distribution is 'reset' to the equilibrium velocity distribution. If the distance between chambers is small, then the effect of particle capture on the velocity distribution will be limited, as the particles will quickly relax back to the equilibrium velocity distribution. As this distance increases, particle capture will have a larger and larger effect on the particles' distribution of velocity. As the distance between chambers tends to infinity, mixing will no longer have any effect on the velocity distribution, and even with a finite λ, the velocity distribution will tend to a delta function at $v = 0$, resulting in no macro-scale diffusion.
In the limit of the filtration-mixing number tending to zero, we have the important result that the inverse Peclet number tends to

$$\lim_{\lambda l \to 0} Pe^{-1} = \frac{l}{L}\left(\int_{-\infty}^{\infty} v^2 \psi_0(v)\, dv - \left(\int_{-\infty}^{\infty} v \psi_0(v)\, dv \right)^2 \right) = \frac{l}{L} C_v^2 \tag{27}$$

This is shown more clearly in the inset figure.
As expected, for any λl, the inverse Peclet number is higher for a higher value of C_v, as the equilibrium velocity distribution is wider, creating a larger spread of particles on the macro-scale.
Figure 3b shows the sensitivity study for the delay number, θ. The delay number represents the decrease in the effective mean velocity on the macro-scale as a result of the preferential capture of faster particles. When capture on the micro-scale is larger, the delay becomes more significant, with diminishing returns. When the mixing length is larger, the effect of capture on the particle velocity distribution will last for longer, so the effective mean velocity will be lower (larger θ).
When the equilibrium velocity distribution is narrow, particle capture occurs relatively uniformly for all particles, and thus the mean velocity will be mostly unchanged. For wider distributions, or larger coefficient of variation, the preferential capture of larger particles will be more effective at shifting the velocity distribution to the left, thus resulting in a lower mean particle velocity.
Lastly, Figure 3c shows the variation of the macro-scale filtration coefficient divided by the micro-scale filtration coefficient. As expected, when the filtration coefficient, λ increases, then so too will Ω, as more capture on the micro-scale translates to more capture on the macro-scale. However, this figure shows that this relationship is not straightforward.

When the filtration-mixing number is zero, then the macro- and micro-scale filtration coefficients are equal. As the filtration-mixing number increases, the ratio decreases monotonically, to a finite asymptote for infinite λl. As discussed above, capture will shift the velocity distribution towards smaller velocities. Macro-scale capture depends on the mean of the absolute velocity (exactly the mean particle velocity for the case where $\psi_0(v)=0$ for $v<0$). Thus given that capture decreases the mean velocity, a negative feedback loop appears, where capture partially reduces capture. However, at the point where further capture (larger λl) no longer reduces the mean fluid velocity, micro-scale capture will translate linearly into macro-scale capture. This can be observed in Figures 3b and 3c, as for the same value of C_v, the asymptotic behaviour of $\theta(\lambda l)$ matches that of $\Omega/\lambda L(\lambda l)$. Similar to the logic made in discussing the delay number, a higher coefficient of variation will result in a larger impact of capture on the mean particle velocity, and thus a larger deviation between the macro- and micro- particle capture.

We reiterate here for emphasis that the discussions here are true only for the case where all particle velocities are positive. As we will see below, many of these observations break down when negative velocities are present.

A convenient means to quantify the degree of deviation from the case of all positive velocities is to define a new variable, α, as the area under the equilibrium velocity PDF to the right of the y-axis (for $v>0$). Thus the above discussions correspond to the case of $\alpha=1$. Figure 4 shows α graphically for two typical velocity PDFs.

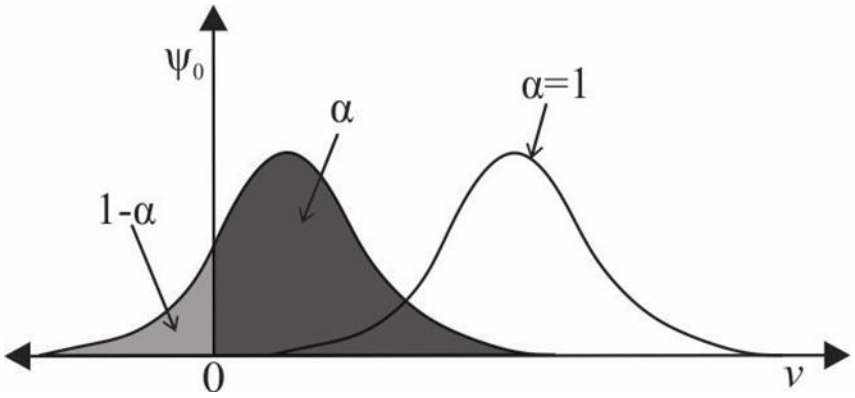

Figure 4: Two velocity probability density functions demonstrating the variable α: the PDF on the right (α=1) describes the case where all particle move in one direction, while the other PDF (α<1) describes the case where a 1- α fraction of particles move in the opposite direction to the mean fluid velocity

We now consider a normal distribution for the equilibrium particle velocity distribution as it can characterise systems with $\alpha<1$. For any normal distribution with finite positive mean, as the coefficient of variation is increased from 0, α will decrease from 1 and asymptotically tend towards 0.5.

Figure 5 shows the sensitivity study of the macroscopic parameters against the filtration-mixing number. The inverse Peclet number, presented in Figure 5a, presents similar behaviour here as in the case of only positive velocities; it decreases monotonically towards zero as the filtration-mixing number increases, equation (27) for the lower limit still holds, and it is strictly higher for higher coefficients of variation.

Figure 5b shows the results for the velocity delay number. Similar results are shown as with the above discussion for $\alpha = 1$; a higher C_v or a higher λl, lead to a higher delay number.

Figure 5c shows the macro- to micro-scale filtration coefficient ratio. While the monotonic dependency on λl is maintained from the α=1 case, the dependency on the coefficient of variation is not. At any given value of λl, C_v can result in either a monotonic increase, or a decrease then increase.

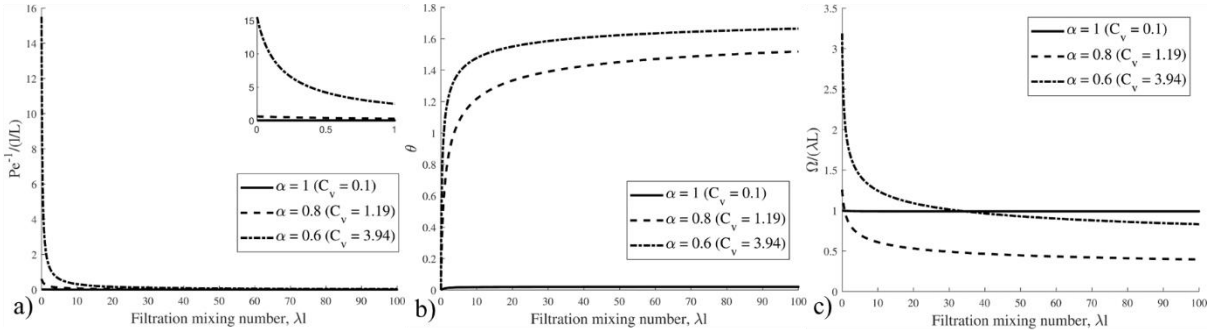

Figure 5: Sensitivity study for the case where particle velocities are both positive and negative ($\psi_0(v)$ is lognormal): a) Macro-scale/micro-scale diffusion coefficient, $Pe^{-1}l/L$, b) Delay number, θ, c) Macro-scale/micro-scale filtration coefficient, $\Omega/\lambda L$

3.3. Emergence of dependency of the coefficients

In the case of only positive particle velocities ($\alpha = 1$), the three macro-scale parameters exhibit an inter-dependency. That is to say that any of the three parameters can be expressed explicitly as a function of the other two. Consider equation (16). In the case of $\alpha = 1$:

$$R_{11} = R_{12} = R_{21} = R_{22} = R\,. \tag{28}$$

Using this result, the expressions in equation (20) can be collapsed to a single expression:

$$1 = \frac{2}{\theta}\left(1 - \frac{2\Omega D}{\theta}\right) \tag{29}$$

In order to verify this relationship, and to understand the form of this dependency, we performed Monte Carlo simulation, generating pairs of the micro-scale parameters (λ, l, C_v) and calculating the corresponding macro-scale parameters (θ, Pe^{-1}, Ω). The results are presented in Figure 6.

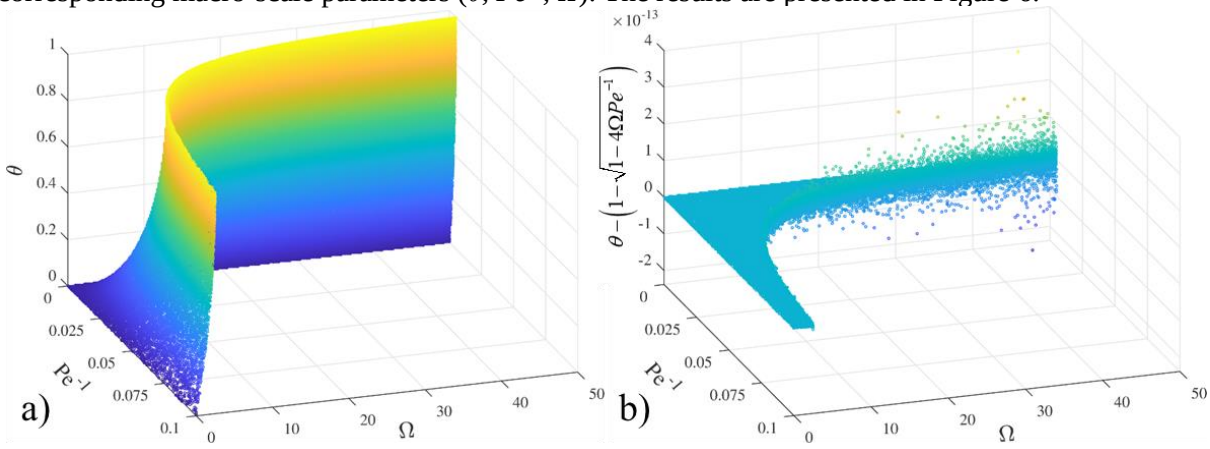

Figure 6: Results of Monte Carlo simulation of macro-scale parameters (D,θ,Ω) from micro-scale parameters (λ,l,C_v) when all particle velocities are positive: a) Macro-scale points, b) Deviation of numerical points from the analytical equation (equation (29)) derived for the surface

Figure 6a shows the subspace of possible macro-scale parameters. Equation (29) reduces the dimension of this space from three (θ, Pe^{-1}, Ω) to two ($\theta(\lambda,R)$, $Pe^{-1}(\lambda,R)$, $\Omega(\lambda,R)$). Thus what we see when we plot the simulation points is a 2-dimensional surface. The form of this surface affirms the physical intuitions established in the previous section. The discussion of parameter sensitivities was simpler for $\alpha = 1$ because the dependencies are resolved by discussing the total magnitude of capture (λ) as well as some measure of the spread of the distribution (R).

This result is particularly significant in the context of practical use of the model (equation (21)). Initially, it appeared that the derivation resulted in a more general advection-diffusion equation, where the mean velocity is an independent parameter, varying with capture. However the underlying

physical connection between the parameters results in a model which permits only certain sets of macro-scale parameters. This will be discussed further in Section 4 where we consider the matching of the model with laboratory data.
Monte Carlo simulation was also performed using a normal distribution, to allow for negative velocities. The analytical derivation of the surface is not valid for this case, and a similar inspection of The expressions in equation (20) suggests that the 'permissible' subspace of macro-scale parameters does not reduce to two dimensions. Figure 7 shows the results for $\alpha = 1$ (a) and $\alpha \leq 1$ (b). The set of points is shown transparently, with 2-dimensional slices taken at fixed values of θ. This visualisation shows that allowing negative velocities expands the subspace of permissible parameters, but this subspace remains smaller than the set of all positive triples. This suggests that there is a set of macro-scale parameters that is not supported in any case by the model presented in Section 3.2.

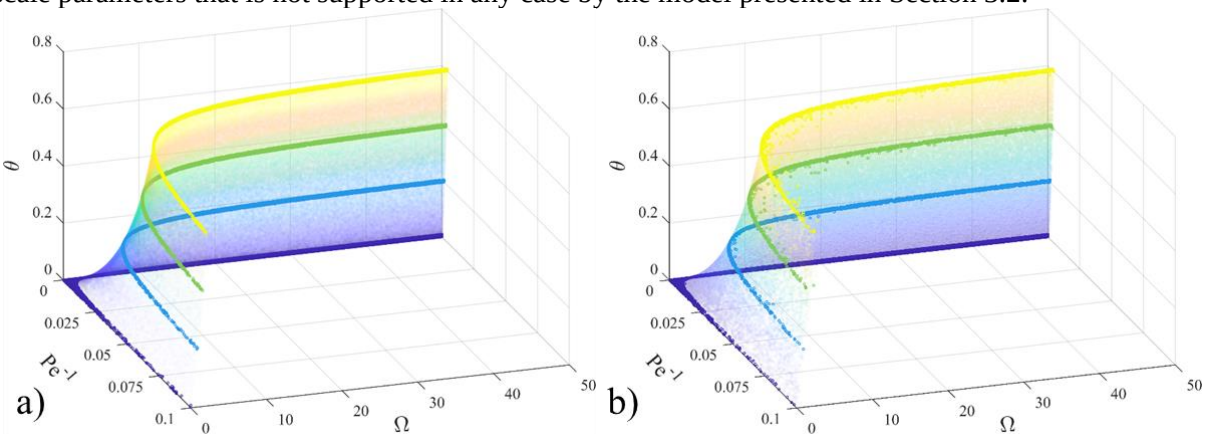

Figure 7: Results of Monte Carlo simulation of macro-scale parameters (D,θ,Ω) from micro-scale parameters (λ,l,C_v): a) Only positive particle velocities, b) Negative and positive particle velocities

3.4. Estimating the delay factor: A useful rule of thumb for practitioners

Superficially, the model presented here differs from the traditional ADE only by the introduction of the velocity delay factor, θ. In large scale systems, a slight variation of the mean particle velocity can have significant impacts on the evolution of the particle concentration. Thus it is useful to provide a means of estimating this parameter from existing system parameters more commonly encountered, such as the filtration coefficient and the inverse Peclet number. The ratio of θ to the product of these two parameters is presented in Figure 8a and 8b for the cases of $\alpha = 1$, and $\alpha \leq 1$ respectively.
For the case where all velocities are positive, the ratio is 2 at $\lambda l = 0$, and increases monotonically, to an asymptote at large λl. This asymptote can be expressed as

$$\lim_{\lambda l \to \infty} \frac{\theta}{\Omega Pe^{-1}} = \int_{-\infty}^{\infty} \frac{\psi_0(v)}{v} dv = 2M_{-1} \tag{30}$$

where M_{-1} is the first negative moment of the equilibrium velocity distribution.
For a lognormal distribution, the first negative moment can be approximated as:

$$M_{-1} \approx \int_0^{\infty} \frac{e^{\left(-\frac{W^2\left(-we^{\mu}\sigma^2\right)+2W\left(-we^{\mu}\sigma^2\right)}{2\sigma^2}\right)}}{\sqrt{1+W\left(-we^{\mu}\sigma^2\right)}} dw \tag{31}$$

where W is the Lambert W function. This approximation is derived in Appendix B.
We can see in Figure 8a that the ratio $\theta/(\Omega Pe^{-1})$ is strictly higher for higher values of C_v.
The case for $\alpha \leq 1$ is more complex, and the rather simple conclusion that $\theta \approx 2\Omega Pe^{-1}$ is no longer valid.

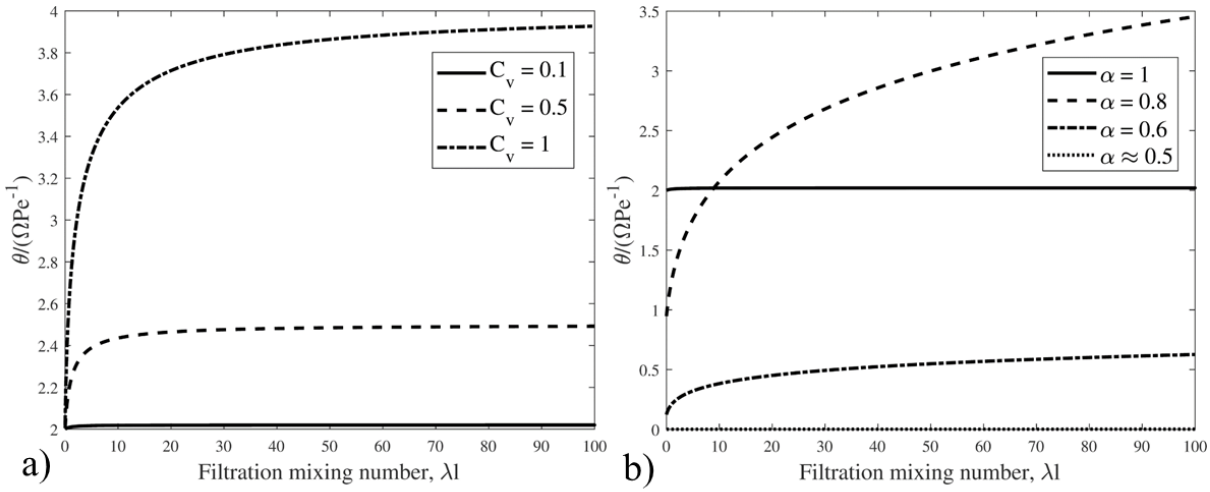

Figure 8: Sensitivity of the ratio $\theta(\Omega Pe^{-1})^{-1}$ for different values of the filtration mixing number, λl: a) Dependence on the coefficient of variation of the velocity distribution, C_v where all velocities are positive, b) Dependence on α (through changing C_v) where particle velocities can be both negative and positive.

3.5. Obtaining the micro-scale parameters

While the averaged equation contains only a single additional unknown parameter in comparison with the traditional ADE, the micro-scale description involves more complexity. As discussed in the previous sections, by assuming a particular form of the equilibrium velocity distribution, the micro-scale system can be parameterised with relative ease (See Section 4). These parameters can then be derived indirectly from laboratory or field-scale data through tuning. Alternatively, practitioners can use relations between the velocity distribution and the pore size distribution (de Anna et al. 2017, Siena et al. 2014), which can be measured using a variety of techniques (Basan et al. 1997). Some authors have even used confocal microscopy to measure the velocity distribution directly (Datta et al. 2013), although this technique is naturally limited to particular, artificial porous media.
Prediction of the filtration coefficient has received substantial attention across various fields (Molnar et al. 2015). Careful attention must be placed as to ensure that the estimates of the filtration coefficient correspond to the appropriate capture mechanism. As outlined earlier, the capture rate equation used in this study is most suitable for straining.

3.6. Comparison with existing approaches

While developments in upscaling and averaging techniques has led to a plethora of macroscale models for flow in porous media (Battiato et al. 2019), the central focus of this study has been the explicit coupling of a distribution of particle velocities and a velocity dependent particle capture rate. The resulting delay in advective velocity has been presented in a previous work by (Altoé F et al. 2006), resulting in the model represented by equations (2,4,7). This leads to a dimensionless ADE of the form:

$$\frac{\partial c}{\partial T} + \left(1 - \frac{\lambda D}{\bar{v}}\right)\frac{\partial c}{\partial X} = \frac{D}{L\bar{v}}\frac{\partial^2 c}{\partial x^2} - \lambda L c \tag{32}$$

This differs from what can be considered the standard model only by the velocity delay factor.
This model was developed using intuitive arguments regarding particle diffusion and capture. In this work, by use of the Boltzmann equation and averaging, we were able to derive an equation of the same form but with more accurate formulae for the coefficients. For practical applications it is of interest to understand the quantitative differences between these approaches. To compare the models, we consider a continuous injection into a porous media using a 3rd type inlet boundary condition of the form
The outlet boundary condition used corresponds to a semi-infinite domain:

$$\frac{\partial c(\infty,T)}{\partial X}=0 \tag{33}$$

which corresponds to the inability of perturbations at the inlet to disturb the initial profile at infinite distances from the inlet.

The initial condition corresponds to an absence of suspended particles in the core

$$c(X,0)=0 \tag{34}$$

Under these conditions, (Van Genuchten and Alves 1982) provide an analytical solution:

$$\frac{c(X,T)}{c_0}=\frac{v}{v+u}e^{\frac{(v-u)X}{2Pe^{-1}}}erfc\left[\frac{X-uT}{2\left(Pe^{-1}T\right)^{1/2}}\right]+\frac{v}{v-u}e^{\frac{(v+u)X}{2Pe^{-1}}}erfc\left[\frac{X+uT}{2\left(Pe^{-1}T\right)^{1/2}}\right]$$

$$+\frac{v^2}{2\Omega Pe^{-1}}e^{\frac{vX}{Pe^{-1}}-\Omega T}erfc\left[\frac{X+vT}{2\left(Pe^{-1}T\right)^{1/2}}\right]$$

where v is the coefficient of the ADE in dimensionless form, and u is defined as follows:

$$u=v\left(1+\frac{4\Omega Pe^{-1}}{v^2}\right)^{1/2} \tag{35}$$

Using this equation, we present outlet concentration (X=1) curves in Figure 9, for the model presented in this study (Boltzmann), equation (21), and the standard model, given by equations (2,4, 6) where the first order spatial derivative of c has coefficient 1.

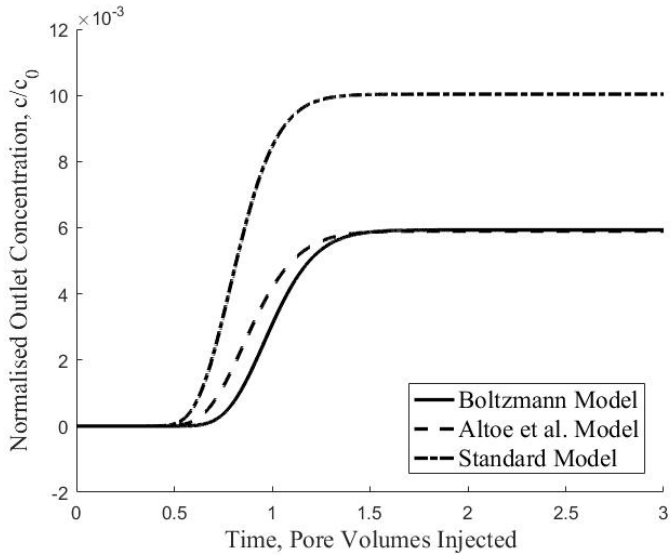

Figure 9: Comparison of existing approaches coupling particle diffusion and capture

The results show that the standard model predicts an earlier arrival of the injected particles and lower total capture when compared with the other two models. The model presented by Altoe et al. still shows earlier arrival when compared to the model presented in this study, but for this example calculation, the total diffusion and capture are approximately equal.

Figure 10 presents a comparison of the velocity delay factor for both of these models across a range of filtration coefficients. The non-linear dependence of θ on λ results in an overprediction of the velocity delay factor by the model of Altoe et al. when capture is low, and an overprediction when capture is more significant. This non-linearity discussed in detail in Section 3.2 results from accounting explicitly for the change in particle velocity distribution due to capture. Higher capture rates for faster particles results in their depletion, narrowing the distribution, reducing the effects of capture on the mean velocity. This leads to diminishing effects of capture on the mean velocity of the particle

population, and consequently, an ever-increasing overprediction of the delay by the model of Altoe et al. where these effects are not described.

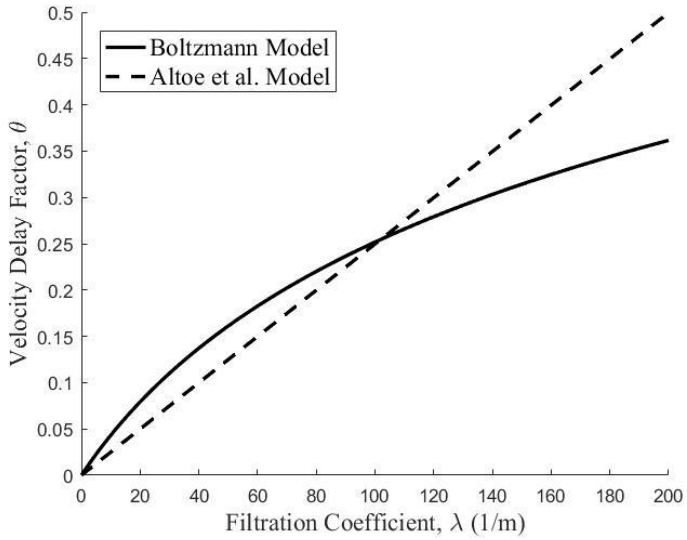

Figure 10: Comparison of Velocity Delay Factor from this study and from the model of Altoe et al.

4. Treatment of laboratory data

In this section we match the laboratory data using the derived mathematical model (equation (21)). The laboratory data involves particle injection via an instantaneous pulse; wherein a fixed mass of particles is injected instantly (relative to the injection period) and travels through the core, and the suspended concentration is measured at the core outlet. Figure 11 shows a general schematic of the laboratory test, as well as typical breakthrough curves of the outlet suspended concentration.

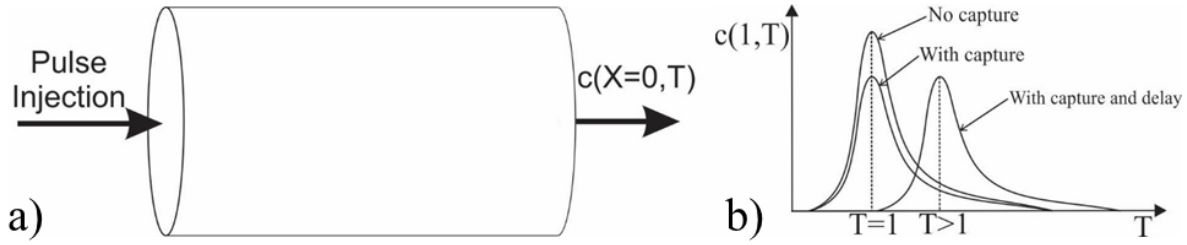

Figure 11: Outline of experimental validation: a) Experimental scheme, and b) Typical breakthrough curves accounting for various effects

The general features of these breakthrough curves are reflected by the macro-scale parameters in the equation (21); a wider plume at the outlet corresponds to a higher inverse Peclet number Pe^{-1}, a lower total volume under the curve corresponds to more particle capture, i.e. a higher value of the macro-scale filtration coefficient Ω, and a late pulse arrival after T=1 corresponds to large delay number θ,. As a result of the non-dimensionalisation of the system, a plume injected at $T = 0$ should arrive at the outlet at T = 1 as at this point a total injected volume equal to the porous volume of the rock has been injected. The model shows that the mean particle velocity can be less than that of the carrier fluid, and thus the plume would arrive with some delay, characterised by the delay number.

As discussed earlier, while the averaged model contains 3 macro-scale parameters (θ, Ω, Pe^{-1}), the model permits only certain sets of these parameters, which honour the simultaneous influence of capture, mixing, and transport on each parameter. In order to account for this, we instead tune the micro-scale parameters (λ, l, C_v), and calculate the corresponding macro-scale parameters using equations (22-24). This will be referred to as *micro-scale fitting.* We also fit with the macro-scale

parameters, ignoring the reduction of possible parameter sets induced by the model. This will be referred to as *macro-scale fitting*.
The laboratory data is tuned using a 3rd type inlet boundary condition of the form:

$$-\frac{1}{Pe}\frac{\partial c(0,T)}{\partial X}+(1-\theta)c(0,T)=c_0\delta(t) \tag{36}$$

where $\delta(t)$ is the generalized Dirac delta function. In the following discussion, the concentration is normalised by the injected concentration.
With these boundary conditions, equation (21) has an exact solution (Van Genuchten and Alves 1982):

$$\frac{c(X,T)}{c_0}=\frac{(1-\theta)\exp\left[-\frac{\left((1-\theta)T-X\right)^2}{4Pe^{-1}T}-\Omega T\right]}{\sqrt{\pi Pe^{-1}T}}-\frac{(1-\theta)^2\exp\left[\frac{(1-\theta)X}{Pe^{-1}}-\Omega T\right]}{2Pe^{-1}}erfc\left[\frac{(1-\theta)T+X}{2\sqrt{Pe^{-1}T}}\right] \tag{37}$$

This equation is tuned to the laboratory data using a gradient-based curve fitting algorithm implemented in Matlab (Mathworks, 2019).
The experimental breakthrough curves considered below are taken from the work by (Bai et al. 2017). They considered the injection of red mud filtrate (series 1,2, presented in Figures 12,13) and silicon powders (series 3, presented in Figure 14) into cores comprised of quartz sand. They injected the particles during a period of 2 seconds, which is significantly less than the total injected period in all cases. Thus they considered this a pulse-type injection.
The fitting results for three different experimental series are presented in Figures 12-14. The optimal parameters found through tuning, as well as the coefficient of determination (R^2) are presented in Tables 2-4.

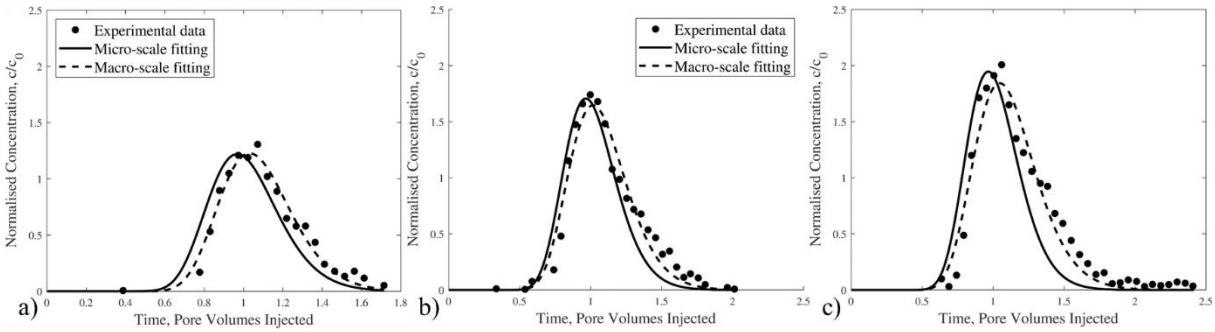

Figure 12: Tuning of three experimental breakthrough curves from Bai et al., 2017 (series 1) using both Micro-scale fitting (tuning (λ, l, C_v)), and Macro-scale fitting (tuning (Pe^{-1}, θ, Ω))

Table 2: Tuning parameters for fitting of experimental series 1

	v = 0.076 cm.s^{-1}		v = 0.148 cm.s^{-1}		v = 0.23 cm.s^{-1}	
	Micro-scale fitting	Macro-scale fitting	Micro-scale fitting	Macro-scale fitting	Micro-scale fitting	Macro-scale fitting
Pe^{-1}	0.0166	0.0147	0.0175	0.0185	0.0174	0.0192
θ	0.0199	0.0757	0.0086	0.0599	0.0041	0.0831
Ω	0.5931	0.5249	0.2434	0.1641	0.1178	0.0000
R^2	0.8106	0.9666	0.8763	0.9528	0.7983	0.9519

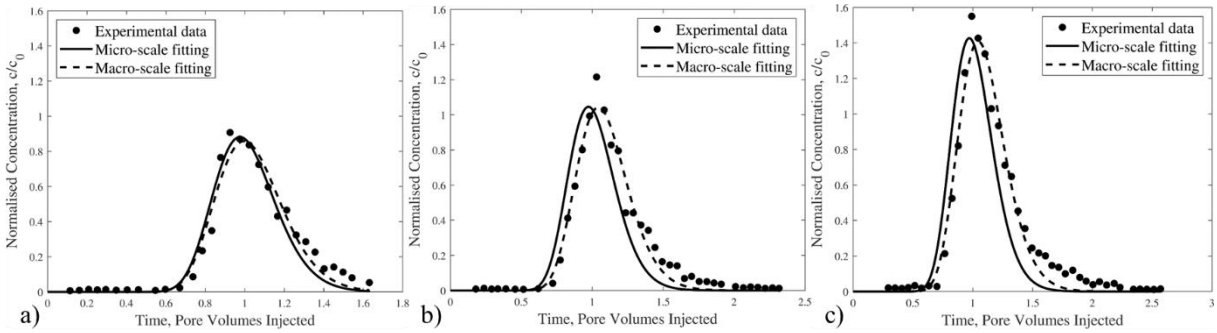

Figure 13: Tuning of three experimental breakthrough curves from Bai et al., 2017 (series 2) using both Micro-scale fitting (tuning (λ, l, C_v)), and Macro-scale fitting (tuning (Pe^{-1}, θ, Ω))

Table 3: Tuning parameters for fitting of experimental series 2

	v = 0.076 cm.s^{-1}		v = 0.148 cm.s^{-1}		v = 0.23 cm.s^{-1}	
	Micro-scale fitting	Macro-scale fitting	Micro-scale fitting	Macro-scale fitting	Micro-scale fitting	Macro-scale fitting
Pe^{-1}	0.0127	0.0135	0.0139	0.0136	0.0150	0.0151
θ	0.0266	0.0499	0.0232	0.0879	0.0148	0.0853
Ω	1.0351	0.9751	0.8267	0.6892	0.4898	0.3604
R^2	0.9420	0.9571	0.8463	0.9692	0.8431	0.9739

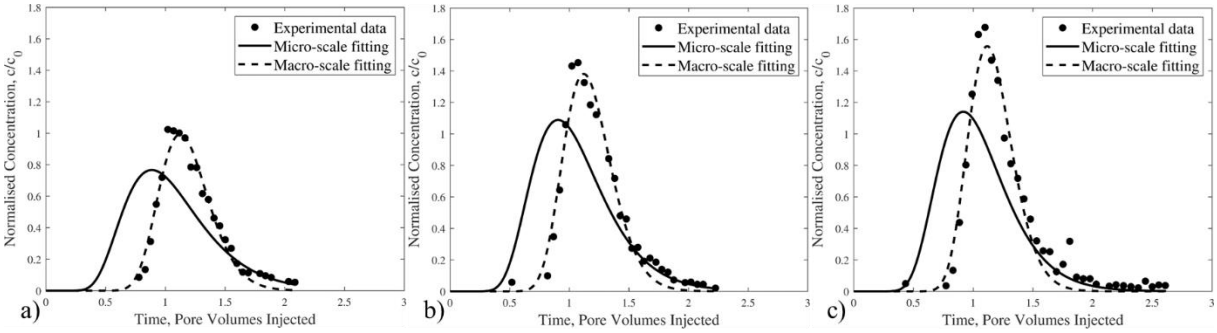

Figure 14: Tuning of three experimental breakthrough curves from Bai et al., 2017 (series 3) using both Micro-scale fitting (tuning (λ, l, C_v)), and Macro-scale fitting (tuning (Pe^{-1}, θ, Ω))

Table 4: Tuning parameters for fitting of experimental series 3

	v = 0.076 cm.s^{-1}		v = 0.148 cm.s^{-1}		v = 0.23 cm.s^{-1}	
	Micro-scale fitting	Macro-scale fitting	Micro-scale fitting	Macro-scale fitting	Micro-scale fitting	Macro-scale fitting
Pe^{-1}	0.0652	0.0144	0.0526	0.0135	0.0457	0.0116
θ	0.0553	0.1578	0.0194	0.1441	0.0183	0.1359
Ω	0.4121	0.5529	0.1828	0.3141	0.1978	0.2855
R^2	0.3493	0.964	0.5334	0.9613	0.501	0.9552

The micro-scale fitting was performed using a normal distribution to allow for optimal parameter sets with $\alpha < 1$. Fitting was repeated using a lognormal distribution, and all parameter and R^2 values were equal to those obtained using a normal distribution.

The three data sets show significant variance in both optimal parameter sets as well as the agreement of the model with the experimental data. Consistent through all tests is that the macro-scale fitting procedure produced a better agreement with the data. This is expected, given that the space of

permissible parameters that will be searched by the micro-scale algorithm is a subspace of that searched by the macro-scale algorithm, such that

$$R^2_{micro} \leq R^2_{macro}$$

with equality occurring when the optimal parameter set is permitted by the derived model.
Regardless, for the first two experimental series, the agreement between the model and data is acceptable. We note that for these two data sets, the values of θ are relatively low, in agreement with the arrival time of the peak being roughly centred around $T = 1$. This is not the case for the third series, in which, for each velocity, the peak of the concentration plume arrives with a significant delay at the outlet. However, this significant delay is only captured by the macro-scale fitting; the micro-scale model is unable to capture the relatively large value of θ . This can be understood in the context of the parameter dependency illustrated in Figure 6. In order to achieve a high value of θ, both the filtration coefficient, and the inverse Peclet number must be high. Despite the long core and high injection velocities, the spreading of the injected plume is quite significant. This is reflected in the high magnitude of Pe^{-1}. The total concentration of particles collected at the outlet is only slightly less than the total injected concentration, which is reflected in the low values of Ω. Thus the permissible parameter sets involve only small values of θ, preventing the tuning procedure from attaining a good match with the data.
The limited applicability of the model is likely related to the assumptions made in its derivation. Most importantly, particle capture has assumed to take place via straining, where arguments made in Section 1 arrive at the conclusion that capture should be directly proportional to the magnitude of the particle velocity. This will not be true in general for any other particle capture mechanism. In context of this, we note that while experimental series 1 and 2 were performed at pH 12, series 3 was performed at pH 7.2. The high pH used for the first two tests is highly prohibitive to particle attachment, meaning that where present, straining will dominate. In the third test, a lower pH will allow particle attachment to occur, for which the model presented in Section 1 may not be valid.

5. Discussion

This section considers how the averaged model resolves the paradoxes, formulated in Introduction for the traditional models, and the limitations of the averaged model.

5.1. Resolution of paradoxes in previous models

In Section 1, we outlined three paradoxes which are present in the existing models for particle transport and capture. In this section, we will outline the extent to which the model presented in this paper resolves these paradoxes.
The first paradox relates to the inability of the existing models to correctly describe the situation in which the mean particle velocity is zero, and the initial concentration profile is constant. As noted earlier, both capture rates given in equations (6,7) predict no capture. This is because both the mean particle velocity, and the mean diffusive flux, are zero. However intuitively, we know that particles are still in motion, moving back and forth within the porous matrix such that their average position is constant. Thus if there is motion, there ought to be particle capture. This is correctly predicted by the capture rate derived in this work, equation (19). This is because the first term in equation (19) is proportional not to the mean particle velocity, but to the mean of the absolute velocity. For a symmetrical equilibrium velocity distribution centred on zero, the former is equal to zero, while the latter is positive. Thus the paradox is resolved.
The second paradox relates to the apparent overestimation of particle travel distance inherent in the advection diffusion equation. This fault will lead to an overestimation of particle capture for particles that travel with a velocity less than the mean particle velocity (see Figure 2). In the introduction we attributed this to the decomposition of particle transport in the traditional ADE into advective and dispersive components. No such decomposition is made in the current paper. While these two components are still additive in the derived macro-scale equation (equation (21)), capture was included in the micro-scale model, where dispersion arises naturally as a result of the width of the equilibrium particle velocity distribution.

The third and final paradox is the particular case of large capture or dispersion which can lead to negative advective velocities. The parameter which encapsulates this paradox, the delay number θ, has been studied extensively throughout this paper. It is shown clearly in Figure 5, that it can exceed one, resulting in the same problem present with the capture rate given by equation (7). So this paradox is not resolved by the present model, but perhaps we can provide more insight as to its origins. Equation (21) is derived using the long waves, large times approximation, which equates to a limitation placed on the variance of the concentration in both space and time. Thus, while not explicitly expressed by equations (22-24), the averaged equation is only valid for parameter values which provide a suspended concentration that varies smoothly in both space and time. This will be violated by large values of the filtration coefficient, as large capture rates will lead to rapid decline in the concentration with time. Thus the model is only valid for small values of the filtration coefficient. As discussed in Section 4, in the limit of small capture, the delay number is limited. Therefore, the model is only valid for small θ, wherein the paradox is not present.

5.2. Limitations of the model and future developments

Despite the arguments that have led to equation (21), a poor match to certain laboratory tests presented in Section 4 suggests that the model has limited applicability. A possible explanation for this limitation is the micro-scale picture of capture utilized in this paper. Figure 1 shows multiple capture mechanisms, yet the argument leading to the direct proportionality of capture to the absolute value of particle velocity is only relevant for particle straining. For other particle capture mechanisms, different equations may prove to be more accurate. The averaging methodology employed relies on the linearity of Boltzmann's equation in the particle concentration, $f(x,t,v)$. Thus the employed methodology should permit various dependencies of the capture term on the particle velocity. A detailed investigation will be presented in a future work.

Another possible source of the model's limitation is the large waves, long times approximation made in Appendix A (equation (A-29)). This assumption translates to assuming that changes in the particle concentration are small both in space and time. Prior to this assumption, the large-scale equation is nonlocal, meaning that concentration changes at any point in time and space require knowledge of the concentration history for all X and at all times prior. The assumption of large waves and long times reduces the equation to a local one, where the impacts of capture and mixing to the particle velocity distribution are limited to a small region around each point (x, t). Relaxing this assumption will result in result in a final equation containing higher order partial derivatives. The impact of these higher order derivatives, reflecting the non-locality of the exact equation, is not clear.

In order to investigate the model more rigorously, and to investigate potential limitations of the model, more specific laboratory tests would be required. According to the model, high dispersion and high capture rock-particle systems ought to yield high values of θ. Performance of such tests over a wide range of mean velocity, as well as particle capture rate (by variation of particle size, salinity, etc) would provide the opportunity for more rigorous validation of the model.

The derivation presented here attempts to accurately model a largely unstudied phenomena related to particle flow and capture, namely the interplay between diffusion and capture. However other phenomena, such as non-zero initial suspended concentration and the decrease in capture rate with captured particle concentration (Yang and Bedrikovetsky 2017), or the impact of particle population heterogeneity (Malgaresi et al. 2019), are not captured within the current study. This is owed largely to mathematical complexity, but fusion of these various modelling efforts will likely result in a model that can accurately model particle transport and capture in ever more scenarios.

The derived large-scale model can be used in water-resources area for tuning the model coefficients from laboratory data with delayed particle breakthrough. The tuned model coefficients can be used for laboratory-based prediction of the colloidal-suspension-nano transport at the reservoir scale.

6. Conclusions

Exact homogenisation of Boltzmann's equation that accounts for particle capture, physical interpretation of the large-scale equation, analysis of the model coefficients and validation by laboratory data allows drawing the following conclusions.

The averaging produces the advection-diffusion equation with a linear capture term and a delayed advective velocity

The averaged equation differs from the traditional advection-diffusion equation with capture by the delay in the particle advection, the diffusion-dependent filtration coefficient, and the capture-rate dependency for dispersion.

The averaged model contains three dimensionless groups of delay, dispersion, and capture.

The delay in the particle motion if compared with the carrier water speed is explained by preferential capture of fast particles.

The averaged equation overcomes the shortcoming of the traditional and modified models under no fluid advection, which predict no particle capture from the diffusive flux, while the averaged equation predicts capture that is proportional to concentration.

The averaged equation overcomes another shortcoming of the traditional models that accounts twice for capture of the particles that perform diffusive jumps against the advective flux

The averaged model is valid for small filtration coefficients, where the delay is lower than one, and the particles are transported in the direction of the carrier fluid flow.

If all particle velocities are positive, the three coefficients of the averaged equation become functionally dependent, reducing the subspace of possible sets of predicted values from three to two.

For the particulate transport with positive velocities, the capture rate is proportional to the overall advective-diffusive flux.

The averaged equation successfully reproduces the breakthrough curves with delay, exhibited in numerous laboratory tests.

When fitting of the macro-scale model coefficients, the model highly agrees with the laboratory data, correctly capturing the delay in mean velocity.

When fitting micro-scale model parameters, only experiments where straining is expected show good agreement with the model, which is consistent with the assumption of proportionality between the capture rate and particle speed.

Appendix A. Relating the flux and capture rate to the averaged concentration

Using the sink-source method, we include the initial and boundary conditions into the governing equation. We assume that particles introduced in the IBC are introduced with the equilibrium velocity distribution, ψ_0.

$$\phi\frac{\partial f}{\partial t}+v\frac{\partial f}{\partial x}=-\lambda|v|\,f+\frac{\overline{v}}{l}\left[\left(\int_{-\infty}^{\infty}f dv\right)\psi_0-f\right]+s(x,t)\psi_0 \qquad \text{(A-1)}$$

Make the substitution

$$f\left(x,t,v\right)=\varphi\left(x,t,v\right)\psi_0 \tag{A-2}$$

resulting in

$$\phi\frac{\partial\varphi}{\partial t}+v\frac{\partial\varphi}{\partial x}=-\lambda\left|v\right|\varphi+\frac{\overline{v}}{l}\left[\left(\int_{-\infty}^{\infty}\varphi\psi_0 dv\right)-\varphi\right]+s\left(x,t\right) \tag{A-3}$$

Assume that the function $\varphi=\varphi\,(x,t,v)$ belongs to the Hilbert space H with scalar product

$$\left(\varphi_1,\varphi_2\right)=\int_{-\infty}^{\infty}\psi_0\varphi_1^{*}\varphi_2 dv \tag{A-4}$$

Consider the Hilbert space H as an orthogonal sum:

$$H=H_c\oplus H_a \tag{A-5}$$

where H_c is a subspace of constants (with respect to velocity). Introduce the orthogonal projections into these two subspaces:

$$P_c:H\to H_c\ ,P_a:H\to H_a \tag{A-6}$$

and the corresponding embeddings back into the original Hilbert space:

$$J_c:H_c\to H\ \ ,J_a:H_a\to H \tag{A-7}$$

Based on the decomposition of the Hilbert space, we can write any function φ as

$$\varphi=c+a\ ,\ c=\left(1,\varphi\right)=\int_{-\infty}^{\infty}\varphi\psi_0 dv\ \ ,\ a=\varphi-c \tag{A-8}$$

where c represents the average of the function φ in regards to the scalar product defined earlier, and a represents the deviation of the function φ from its average in the velocity space.

The projections to each subspace are

$$c=P_c\varphi\ \ ,a=P_a\varphi \tag{A-9}$$

From equation (A-8) we can see that

$$P_c\left(\varphi\right)=\left(1,\varphi\right)\ ,\ P_a\left(\varphi\right)=\varphi-\left(1,\varphi\right) \tag{A-10}$$

Applying the 2-dimensional Fourier transform to equation (A-3) we obtain

$$i\omega\phi\varphi_F+ikv\varphi_F+\lambda\left|v\right|\varphi_F-\frac{\overline{v}}{l}\left[\left(\int_{-\infty}^{\infty}\varphi_F\psi_0 dv\right)-\varphi_F\right]=s_F\left(x,t\right) \tag{A-11}$$

Which is in the form:

$$L\varphi_F=s_F \tag{A-12}$$

Projecting equation (A-12) into H_a yields

$$P_aL\varphi_F=P_as_F \tag{A-13}$$

Given that s_F is independent of velocity, it belongs to the H_c subspace and therefore its projection into H_a is zero

$$P_aL\varphi_F=0 \tag{A-14}$$

Based on the decomposition of the Hilbert space (equation (A-8)), we can decompose the operator L into its components projecting to and from each of the two subspaces:

$$L=\begin{bmatrix}L_{cc} & L_{ca}\\ L_{ac} & L_{aa}\end{bmatrix} \tag{A-15}$$

where the matrix elements are

$$L_{ik}=P_iLJ_k \tag{A-16}$$

The operator P_aL can therefore be written as:

$$P_aL=\begin{bmatrix}L_{ac} & L_{aa}\end{bmatrix}:H\to H_a \tag{A-17}$$

In addition to the operator, the function φ_F can be decomposed into the sum of its component in each subspace, which allows us to write equation (A-14) as follows:

$$L_{ac}c_F + L_{aa}a_F = 0 \tag{A-18}$$

Thus

$$a_F = -L_{aa}^{-1}L_{ac}c_F \tag{A-19}$$

Consider the Fourier transform of equation (12) for the flux:

$$q_F = \int_{-\infty}^{\infty} v\varphi_F\psi_0 dv \tag{A-20}$$

Decomposing φ_F using equation (A-8), then using equation (A-19) results in

$$q_F = c_F\bar{v} - ikc_F\left(P_a v, L_{aa}^{-1}\left[v-(1,v)\right]\right) - \lambda c_F\left(P_a v, L_{aa}^{-1}\left[|v|-(1,|v|)\right]\right) \tag{A-21}$$

Introducing the R_{ij} terms:

$$R_{ij}(\omega,k) = \int_{-\infty}^{\infty}\frac{v_i v_j}{\lambda|v|+\frac{\bar{v}}{l}+i\omega+ikv}\psi_0 dv - \frac{\int_{-\infty}^{\infty}\frac{v_i}{\lambda|v|+\frac{\bar{v}}{l}+i\omega+ikv}\psi_0 dv \int_{-\infty}^{\infty}\frac{v_j}{\lambda|v|+\frac{\bar{v}}{l}+i\omega+ikv}\psi_0 dv}{\int_{-\infty}^{\infty}\frac{1}{\lambda|v|+\frac{\bar{v}}{l}+i\omega+ikv}\psi_0 dv} \tag{A-22}$$

results in

$$q_F = c_F\bar{v} - ikR_{11}c_F - \lambda R_{12}c_F \tag{A-23}$$

The derivation of the R_{ij} terms from the L_{aa}^{-1} operator is presented in detail in (Dinariev et al. 2020).

Similarly, for the capture rate, we take the Fourier transform of equation (13):

$$\varepsilon_F = \int_{-\infty}^{\infty}\lambda\varphi_F\psi_0 dv \tag{A-24}$$

Substituting equation (A-19):

$$\varepsilon_F = \lambda|v|c_F - ik\lambda c_F\left(|v|, L_{aa}^{-1}\left[v-(1,v)\right]\right) - \lambda^2 c_F\left(|v|, L_{aa}^{-1}\left[|v|-(1,|v|)\right]\right) \tag{A-25}$$

Lastly, simplifying, we get:

$$\varepsilon_F = \lambda|v|c_F - ik\lambda R_{21}c_F - \lambda^2 R_{22}c_F \tag{A-26}$$

Taking the inverse Fourier transform of equations (A-23,A-26), we obtain:

$$q = \bar{v}c - K_{11} * \frac{\partial c}{\partial x} - \lambda K_{12} * c \tag{A-27}$$

$$\varepsilon = \lambda\overline{|v|}c - \lambda K_{21} * \frac{\partial c}{\partial x} - \lambda^2 K_{22} * c \tag{A-28}$$

where the K_{ij} terms are the inverse Fourier transformations of the R_{ij} terms and * refers to convolution in space and time.

We simplify this by taking the long waves and large times approximation

$$\omega, k \to 0 \tag{A-29}$$

This results in the K_{ij} terms becoming equal to the R_{ij} terms given by equation (16), and the convolution devolving into multiplication. This results in equations (A-27,A-28) becoming equal to the expressions given in equations (14,15).

Appendix B. Upper limit of the coefficient ratio for a lognormal distribution

Consider the case of α=1. Here, we have

$$\theta = \frac{2\lambda R}{\bar{v}},\ D = \frac{R}{\bar{v}L} \tag{B-1}$$

Combining, we get

$$\theta = 2\lambda LD \tag{B-2}$$

We also have

$$\Omega = \lambda L\left(1-\frac{\lambda R}{\overline{v}}\right) \tag{B-3}$$

Consider the *R* term:

$$R = \int_0^\infty \frac{v^2}{\lambda v + \frac{\overline{v}}{l}}\psi_0 dv - \frac{\int_0^\infty \frac{v}{\lambda v + \frac{\overline{v}}{l}}\psi_0 dv \int_0^\infty \frac{v}{\lambda v + \frac{\overline{v}}{l}}\psi_0 dv}{\int_0^\infty \frac{1}{\lambda v + \frac{\overline{v}}{l}}\psi_0 dv} \tag{B-4}$$

Note the change in the integration limits and the dropping of the absolute sign on the velocity to reflect that $\psi_0(v<0) = 0$.

In the limit of $\lambda \to \infty$, we can simplify the denominator in each integral

$$R = \int_0^\infty \frac{v^2}{\lambda v}\psi_0 dv - \frac{\int_0^\infty \frac{v}{\lambda v}\psi_0 dv \int_0^\infty \frac{v}{\lambda v}\psi_0 dv}{\int_0^\infty \frac{1}{\lambda v}\psi_0 dv} \tag{B-5}$$

Simplifying, we get

$$R = \frac{1}{\lambda}\left[\int_0^\infty v\psi_0 dv - \frac{1}{\int_0^\infty \frac{1}{v}\psi_0 dv}\right] \tag{B-6}$$

As per equation (25), we substitute the equilibrium velocity distribution, $\psi_0(v)$ in the second term for the unit-mean equivalent, $\psi_1(v)$:

$$R = \frac{1}{\lambda}\left[\int_0^\infty v\psi_0 dv - \frac{1}{\frac{1}{v}\int_0^\infty \psi_1(y)\,dy}\right] \tag{B-7}$$

$$R = \frac{\overline{v}}{\lambda}\left[1 - M_{-1}^{-1}(\psi_1)\right] \tag{B-8}$$

where M_{-1} is the first negative moment of the normalised equilibrium velocity distribution.
Thus

$$\Omega = \lambda L M_{-1}^{-1}(\psi_1) \tag{B-9}$$

Substituting this into equation (B-2) we get:

$$\theta = 2\Omega D M_{-1} \tag{B-10}$$

$$\frac{\theta}{\Omega D} = 2M_{-1} \tag{B-11}$$

According to (Cressie et al. 1981), the first negative moment can be calculated from the Laplace transform, $L(w)$, of the PDF of a distribution as

$$E\left(y^{-1}\right) = M_{-1}(\psi_1) = \int_0^\infty L(w)dw \tag{B-12}$$

where *w* is the Laplace variable.
(Asmussen et al. 2016) provided an approximation of the Laplace transformation for a lognormal distribution, which when combined with equation (B-12), results in equation (31).

Acknowledgments This research did not receive any specific grant from funding agencies in the public, commercial, or not-for-profit sectors. The authors are thankful to Prof. Anthony Roberts and Dr. J. Bunder for fruitful discussions. The data used in this paper are available in the cited references, or are included in the tables and figures. The data on which the laboratory tuning is based are available in Bai et al. (2017).

References

Akhmetgareev, V. and Khisamov, R. (2015) 40 Years of Low-Salinity Waterflooding in Pervomaiskoye Field, Russia: Incremental Oil, Society of Petroleum Engineers.
Altoé F, J.E., Bedrikovetsky, P., Siqueira, A.G., de Souza, A.L.S. and Shecaira, F.S. (2006) Correction of basic equations for deep bed filtration with dispersion. Journal of Petroleum Science and Engineering 51(1), 68-84.
Arns, C. and Adler, P. (2018a) Fast Laplace solver approach to pore-scale permeability. Physical Review E 97(2), 023303.
Arns, C.H. (2004) A comparison of pore size distributions derived by NMR and X-ray-CT techniques. Physica A: Statistical Mechanics and its Applications 339(1), 159-165.
Arns, C.H. and Adler, P.M. (2018b) Fast Laplace solver approach to pore-scale permeability. Physical Review E 97(2), 023303.
Arns, C.H., Knackstedt, M.A. and Martys, N.S. (2005) Cross-property correlations and permeability estimation in sandstone. Physical Review E 72(4), 046304.
Asmussen, S., Jensen, J.L. and Rojas-Nandayapa, L. (2016) On the Laplace Transform of the Lognormal Distribution. Methodology and Computing in Applied Probability 18(2), 441-458.
Bai, B., Wang, J., Zhai, Z. and Xu, T. (2017) The Penetration Processes of Red Mud Filtrate in a Porous Medium by Seepage. Transport in Porous Media 117(2), 207-227.
Barkman, J., Abrams, A., Darley, H. and Hill, H. (1975) An Oil-Coating Process To Stabilize Clays in Fresh Waterflooding Operations (includes associated paper 6405). Journal of Petroleum Technology 27(09), 1,053-051,059.
Basan, P.B., Lowden, B.D., Whattler, P.R. and Attard, J.J. (1997) Pore-size data in petrophysics: a perspective on the measurement of pore geometry. 122(1), 47-67.
Battiato, I., Ferrero V, P.T., O' Malley, D., Miller, C.T., Takhar, P.S., Valdés-Parada, F.J. and Wood, B.D. (2019) Theory and Applications of Macroscale Models in Porous Media. Transport in Porous Media 130(1), 5-76.
Bedrikovetsky, P. (1993) Mathematical Theory of Oil and gas Recovery, Kluwer Academic Publishers, Dordrecht, The Netherlands.
Bedrikovetsky, P. (2008) Upscaling of stochastic micro model for suspension transport in porous media. Transport in Porous Media 75(3), 335-369.
Bedrikovetsky, P., Osipov, Y., Kuzmina, L. and Malgaresi, G. (2019) Exact upscaling for transport of size-distributed colloids. Water Resources Research 55(2), 1011-1039.
Bedrikovetsky, P., You, Z., Badalyan, A., Osipov, Y. and Kuzmina, L. (2017) Analytical model for straining-dominant large-retention depth filtration. Chemical Engineering Journal 330, 1148-1159.
Bhatnagar, P.L., Gross, E.P. and Krook, M. (1954) A Model for Collision Processes in Gases. I. Small Amplitude Processes in Charged and Neutral One-Component Systems. Physical Review 94(3), 511-525.
Bianco, C., Tosco, T. and Sethi, R. (2016) A 3-dimensional micro- and nanoparticle transport and filtration model (MNM3D) applied to the migration of carbon-based nanomaterials in porous media. Journal of contaminant hydrology 193, 10-20.
Boccardo, G., Sethi, R. and Marchisio, D.L. (2019) Fine and ultrafine particle deposition in packed-bed catalytic reactors. Chemical Engineering Science 198, 290-304.
Boltzmann, L. (2012) Wissenschaftliche Abhandlungen, Cambridge University Press, Cambridge.

Boso, F. and Tartakovsky, D.M. (2016) The method of distributions for dispersive transport in porous media with uncertain hydraulic properties. Water Resources Research 52(6), 4700-4712.
Bradford, S.A., Torkzaban, S. and Simunek, J. (2011) Modeling colloid transport and retention in saturated porous media under unfavorable attachment conditions. Water Resources Research 47(10).
Chrysikopoulos, C.V., Sotirelis, N.P. and Kallithrakas-Kontos, N.G. (2017) Cotransport of graphene oxide nanoparticles and kaolinite colloids in porous media. Transport in Porous Media 119(1), 181-204.
Chrysikopoulos, C.V., Syngouna, V.I., Vasiliadou, I.A. and Katzourakis, V.E. (2012) Transport of Pseudomonas putida in a 3-D bench scale experimental aquifer. Transport in porous media 94(3), 617-642.
Cressie, N., Davis, A.S., Folks, J.L. and Policello, G.E. (1981) The Moment-Generating Function and Negative Integer Moments. The American Statistician 35(3), 148-150.
Dagan, G., Fiori, A. and Jankovic, I. (2013) Upscaling of flow in heterogeneous porous formations: Critical examination and issues of principle. Advances in Water Resources 51, 67-85.
Datta, S.S., Chiang, H., Ramakrishnan, T.S. and Weitz, D.A. (2013) Spatial Fluctuations of Fluid Velocities in Flow through a Three-Dimensional Porous Medium. Physical Review Letters 111(6), 064501.
de Anna, P., Quaife, B., Biros, G. and Juanes, R. (2017) Prediction of the low-velocity distribution from the pore structure in simple porous media. Physical Review Fluids 2(12), 124103.
Dentz, M., Le Borgne, T., Englert, A. and Bijeljic, B. (2011) Mixing, spreading and reaction in heterogeneous media: A brief review. Journal of contaminant hydrology 120-121, 1-17.
Dinariev, O., Rego, A. and Bedrikovetsky, P. (2020) Boltzmann Physical Kinetic for Deep Bed Filtration: Homogenization by solving operator equation in Hilbert space. arXiv preprint arXiv:2001.08069.
Dinariev, O.Y. (1996) Nonlocality effects in the hydrodynamics of a nonrelativistic plasma. Russian Physics Journal 39(1), 56-61.
Dinariev, O.Y. (1999) Transition from kinetic theory to nonlocal hydrodynamics and the law of increasing entropy. Russian Physics Journal 42(2), 197-202.
Dinariev, O.Y. (2005) Nonlocal Hydrodynamics of a Relativistic Classical Collisionless Plasma. Russian Physics Journal 48(8), 824-832.
Einstein, A. (1905) On the movement of small particles suspended in stationary liquids required by the molecular-kinetic theory of heat. Annalen der Physik 17, 549-560.
Elimelech, M., Gregory, J. and Jia, X. (2013) Particle deposition and aggregation: measurement, modelling and simulation, Butterworth-Heinemann.
Goldberg, E., Scheringer, M., Bucheli, T.D. and Hungerbühler, K. (2014) Critical assessment of models for transport of engineered nanoparticles in saturated porous media. Environ Sci Technol 48(21), 12732-12741.
Herzig, J., Leclerc, D. and Goff, P.L. (1970) Flow of suspensions through porous media—application to deep filtration. Industrial & Engineering Chemistry 62(5), 8-35.
Hilpert, M. and Johnson, W.P. (2018) A binomial modeling approach for upscaling colloid transport under unfavorable attachment conditions: emergent prediction of nonmonotonic retention profiles. Water Resources Research 54(1), 46-60.
Hou, T.Y. (2005) Handbook of Materials Modeling, pp. 1507-1528, Springer.
Hunt, A.G. and Sahimi, M. (2017) Flow, Transport, and Reaction in Porous Media: Percolation Scaling, Critical-Path Analysis, and Effective Medium Approximation. 55(4), 993-1078.
Johnson, W., Rasmuson, A., Pazmiño, E. and Hilpert, M. (2018) Why variant colloid transport behaviors emerge among identical individuals in porous media when colloid–surface repulsion exists. Environ Sci Technol 52(13), 7230-7239.
Kechagia, P.E., Tsimpanogiannis, I.N., Yortsos, Y.C. and Lichtner, P.C. (2002) On the upscaling of reaction-transport processes in porous media with fast or finite kinetics. Chemical Engineering Science 57(13), 2565-2577.
Knutson, C., Valocchi, A. and Werth, C. (2007) Comparison of continuum and pore-scale models of nutrient biodegradation under transverse mixing conditions. Advances in Water Resources 30(6-7), 1421-1431.

Malgaresi, G., Collins, B., Alvaro, P. and Bedrikovetsky, P. (2019) Explaining non-monotonic retention profiles during flow of size-distributed colloids. Chemical Engineering Journal 375, 121984.
Messina, F., Marchisio, D.L. and Sethi, R. (2015) An extended and total flux normalized correlation equation for predicting single-collector efficiency. Journal of Colloid and Interface Science 446, 185-193.
Messina, F., Tosco, T. and Sethi, R. (2016) On the failure of upscaling the single-collector efficiency to the transport of colloids in an array of collectors. Water Resources Research 52(7), 5492-5505.
Molnar, I.L., Johnson, W.P., Gerhard, J.I., Willson, C.S. and O'Carroll, D.M. (2015) Predicting colloid transport through saturated porous media: A critical review. 51(9), 6804-6845.
Pan, W. and Tartakovsky, A. (2013) Dissipative particle dynamics model for colloid transport in porous media. Advances in water resources 58, 41-48.
Payatakes, A., Rajagopalan, R. and Tien, C. (1974) Application of porous media models to the study of deep bed filtration. The canadian journal of chemical engineering 52(6), 722-731.
Polyanin, A. and Dilman, V.V. (1994) Methods of modeling equations and analogies in chemical engineering, CRC Press, Boca Raton, FI.
Prommer, H., Descourvieres, C., Handyside, M., Johnston, K., Harris, B., Li, Q., Fang, H., Costello, P., Seibert, S. and Martin, M. (2013) Final Report—Aquifer Storage and Recovery of Potable Water in the Leederville Aquifer.
Rabinovich, A. (2017) Estimation of sub-core permeability statistical properties from coreflooding data. Advances in Water Resources 108, 113-124.
Rabinovich, A., Dagan, G. and Miloh, T. (2013) Dynamic effective properties of heterogeneous geological formations with spherical inclusions under periodic time variations. Geophysical research letters 40(7), 1345-1350.
Salimi, S. and Ghalambor, A. (2011) Experimental study of formation damage during underbalanced-drilling in naturally fractured formations. Energies 4(10), 1728-1747.
Sethi, R., Tosco, T., Luna, M., Gastone, F., Velimirovic, M., Gemoets, J., Muyshond, R., Sapion, H., Klaas, N. and Bastiaens, L. (2014) Field injection of microscale zerovalent iron for groundwater remediation.
Shapiro, A. and Wesselingh, J. (2008) Gas transport in tight porous media: Gas kinetic approach. Chemical Engineering Journal 142(1), 14-22.
Shapiro, A. and Yuan, H. (2012) Statistical mechanics and random walks: Principles, processes and applications, pp. 1-36, Nova Science Publishers.
Shapiro, A.A. (2007) Elliptic equation for random walks. Application to transport in microporous media. Physica A: Statistical Mechanics and its Applications 375(1), 81-96.
Sharma, M. and Yortsos, Y. (1987a) Fines migration in porous media. AIChE Journal 33(10), 1654-1662.
Sharma, M.M. and Yortsos, Y. (1987b) Transport of particulate suspensions in porous media: model formulation. AIChE Journal 33(10), 1636-1643.
Siena, M., Riva, M., Hyman, J.D., Winter, C.L. and Guadagnini, A. (2014) Relationship between pore size and velocity probability distributions in stochastically generated porous media. Physical Review E 89(1), 013018.
Tartakovsky, A., Panzeri, M., Tartakovsky, G. and Guadagnini, A. (2017) Uncertainty quantification in scale-dependent models of flow in porous media. Water Resources Research 53(11), 9392-9401.
Tartakovsky, D.M. and Dentz, M. (2019) Diffusion in porous media: phenomena and mechanisms. Transport in Porous Media 130(1), 105-127.
Tosco, T., Gastone, F. and Sethi, R. (2014) Guar gum solutions for improved delivery of iron particles in porous media (Part 2): Iron transport tests and modeling in radial geometry. Journal of contaminant hydrology 166, 34-51.
Tosco, T. and Sethi, R. (2010) Transport of Non-Newtonian Suspensions of Highly Concentrated Micro- And Nanoscale Iron Particles in Porous Media: A Modeling Approach. Environ Sci Technol 44(23), 9062-9068.
Van Genuchten, M. and Alves, W.J. (1982) Analytical Solutions of One Dimensional Convective Dispersive Solute Transport Equations.
Winter, C.L. and Tartakovsky, D.M. (2002) Groundwater flow in heterogeneous composite aquifers. Water Resources Research 38(8), 23-21-23-11.

Yang, Y. and Bedrikovetsky, P. (2017) Exact Solutions for Nonlinear High Retention-Concentration Fines Migration. Transport in Porous Media 119(2), 351-372.
Yuan, H., Shapiro, A., You, Z. and Badalyan, A. (2012) Estimating filtration coefficients for straining from percolation and random walk theories. Chemical Engineering Journal 210, 63-73.
Yuan, H. and Shapiro, A.A. (2010) Modeling non-Fickian transport and hyperexponential deposition for deep bed filtration. Chemical Engineering Journal 162(3), 974-988.
Zhang, H., Malgaresi, G. and Bedrikovetsky, P. (2018) Exact solutions for suspension-colloidal transport with multiple capture mechanisms. International Journal of Non-Linear Mechanics 105, 27-42.

5.2 Boltzmann's colloidal transport in porous media with velocity-dependent capture probability

Russell, T., Bedrikovetsky, P.

Physics of Fluids, Accepted for publication

Statement of Authorship

Title of Paper	Boltzmann's colloidal transport in porous media with velocity-dependent capture probability
Publication Status	☐ Published ☑ Accepted for Publication ☐ Submitted for Publication ☐ Unpublished and Unsubmitted w ork w ritten in manuscript style
Publication Details	Russell, T., Bedrikovetsky, P., Boltzmann's colloidal transport in porous media with velocity-dependent capture probability, Physics of Fluids, Submitted

Principal Author

Name of Principal Author (Candidate)	Thomas Russell		
Contribution to the Paper	Performed calculations, performed derivations, contributed to writing		
Overall percentage (%)	90%		
Certification:	This paper reports on original research I conducted during the period of my Higher Degree by Research candidature and is not subject to any obligations or contractual agreements with a third party that would constrain its inclusion in this thesis. I am the primary author of this paper.		
Signature		Date	25/02/2021

Co-Author Contributions

By signing the Statement of Authorship, each author certifies that:

i. the candidate's stated contribution to the publication is accurate (as detailed above);

ii. permission is granted for the candidate in include the publication in the thesis; and

iii. the sum of all co-author contributions is equal to 100% less the candidate's stated contribution.

Name of Co-Author	Pavel Bedrikovetsky		
Contribution to the Paper	Performed derivations, contributed to writing		
Signature		Date	25/02/2021

Please cut and paste additional co-author panels here as required.

Boltzmann's colloidal transport in porous media with velocity-dependent capture probability

Thomas Russell, Pavel Bedrikovetsky[a)]

Australian School of Petroleum and Energy Resources, The University of Adelaide, Adelaide, SA, 5005, Australia

a) Author to whom correspondence should be addressed: pavel.bedrikovetski@adelaide.edu.au

ABSTRACT Mathematical modelling of suspension-colloidal-nano transport in porous media at different scales has long been a fascinating topic of fluid mechanics. In this study, we discuss the multi-pore scale, where Boltzmann's approach of distributed velocities is valid, and average (homogenise) the micro-scale equation up to the core scale. The focus is on the filtration function (particle capture probability per unity trajectory length) that highly depends on the carrier fluid velocity. We develop a modified form of the Boltzmann equation for micro-scale particle capture and diffusion. An equivalent sink term is introduced into the kinetic equation instead of non-zero initial data, resulting in the solution of an operator equation in the Fourier space and an exact homogenization. The upper scale transport equation is obtained in closed form. The upscaled model contains the dimensionless delay number and large-scale dispersion and filtration coefficients. The explicit formulae for the large-scale model coefficients are derived in terms of the micro-scale parameters for any arbitrary velocity-dependent filtration function. We focus on three micro-scale models for the velocity-dependent particle capture rate corresponding to various retention mechanisms, i.e. straining, attachment, and inertial capture. The explicit formulae for large-scale transport coefficients reveal their typical dependencies of velocity and the micro-scale parameters. Treatment of several laboratory tests reveal close match with the modelling-based predictions.

Nomenclature

ϕ	Porosity, [-]	η_0	Single-collector contact efficiency, [-]
f	Particle concentration, [-]	d_p	Particle diameter, [L]
t	Time, [T]	D_∞	Bulk diffusion coefficient, [$L^2.T^{-1}$]
v	Velocity, [LT^{-1}]	A	Hamaker constant, [ML^2T^{-2}]
x	Position, [L]	k	Boltzmann's constant, [$ML^2T^{-2}K^{-1}$]
$\lambda(v)$	Filtration coefficient, [L^{-1}]	T	Absolute temperature, [K]
τ	Mixing time, [T]	r_p	Particle radius, [L]
ψ_0	Equilibrium velocity distribution, [$L^{-1}T$]	ρ_p	Particle density, [ML^{-3}]
l	Mixing length, [L]	ρ_f	Fluid density, [ML^{-3}]
$\bar{v}$	Average velocity, [LT^{-1}]	μ	Fluid viscosity, [$ML^{-1}T^{-1}$]
c	Averaged particle concentration, [-]	g	Gravitational acceleration, [MT^{-2}]
q	Total particle flux, [$L.T^{-1}$]	β	Characteristic capture constant, [-]
ε	Total particle capture rate, [T^{-1}]	ψ^*	Modified particle velocity distribution, [L]
s	Initial and boundary conditions, [-]	σ	Standard deviation, [$L.T^{-1}$]
φ	Modified particle concentration, [-]	C_v	Coefficient of variation, [-]
a	Particle concentration deviation from average, [-]	H	Hilbert space
T	Dimensionless time, [-]	H_c	Hilbert subspace of averaged concentration
X	Dimensionless position, [-]	H_a	Hilbert subspace of deviations from average

L	Core length, [L]	P_c	Projection operator from H to H_c
R_{ij}	[L^{-1}.T]	P_a	Projection operator from H to H_a
θ	Velocity delay factor, [-]	J_c	Embedding operator from H_c to H
Pe	Peclet number, [-]	J_a	Embedding operator from H_a to H
Ω	Macro-scale filtration coefficient, [-]	ω	Fourier variable corresponding to t
d_c	Collector diameter¸ [L]	k	Fourier variable corresponding to x
α	Attachment efficiency, [-]	K_{ij}	Inverse Fourier transform of R_{ij}

I. INTRODUCTION

Multiscale physics of transport in porous media is an area that has garnered much attention from researchers. The upscaled (homogenized) equations which describe transport processes in porous media and the estimates of transport coefficients from micro-scale models provide theoretical fundamentals and modelling tools for numerous natural and engineering processes. The focus of the current paper is on upscaling of suspension-colloidal-nano flows in porous media, which highly contributes to chemical, environmental, and civil engineering along with geology and water resources[1-3].

The traditional model for suspension-colloidal-nano flows in porous media consists of mass balance of suspended and retained particles and the rate equation for particle capture[1, 4, 5]

$$\phi\frac{\partial c}{\partial t}+\overline{v}\frac{\partial c}{\partial x}=-\lambda\overline{v}c \tag{1}$$

where ϕ is the porosity, c is the suspended concentration, t is time, x is the single spatial dimension, $\overline{v}$ is the carrier fluid velocity, and λ is the filtration coefficient. The capture rate in Eq. (1) is proportional to the mean flow velocity. It follows then that the filtration coefficient represents the capture probability per until length of the particles' trajectory and has dimension 1/L [6], while an equivalent chemical reaction coefficient would have dimension 1/T [7].

Numerous works upscale (average) solute and particle transport over areal rock micro-heterogeneity, in both linear and nonlinear formulations; the incomplete list of the works is represented by [8-13]. An important particular case is stochastic non-correlated properties of fluids and porous media, where the properties in different points are independent random processes[5, 7, 11]. Homogenization of micro-scale population balance model with distributed rock properties yields the tradition model (Eq. (1))[4, 5, 14]. Upscaling of the population balance model with distributed particle sizes substitutes suspension concentration c in right hand side of Eq. (2) by a function of c referred to as the filtration function[5, 15]. When accounting for the reduction in capture rate due to occupation of capture sites by a heterogeneous particle population, upscaling results in supplementing Eq. (1) with an occupation kinetics equation[15, 16]. Homogenisation of random walk model with the length- and time- jumps distribution yields the elliptic advective-diffusion-capture equation[17].

For suspension-colloidal transport in porous media, the suspended particles are distributed over velocity as a result of their transport through a complex, highly heterogeneous porous space. Particles are distributed over velocity in each elementary volume. Figure 1 shows a simplified cross-section of a porous media which is roughly equivalent to a system of capillaries of varying size, leading to the aforementioned distribution of particle velocity. Significant velocity variation across the porous media justify the relevance of the Boltzmann's approach of physical kinetics[18-24].

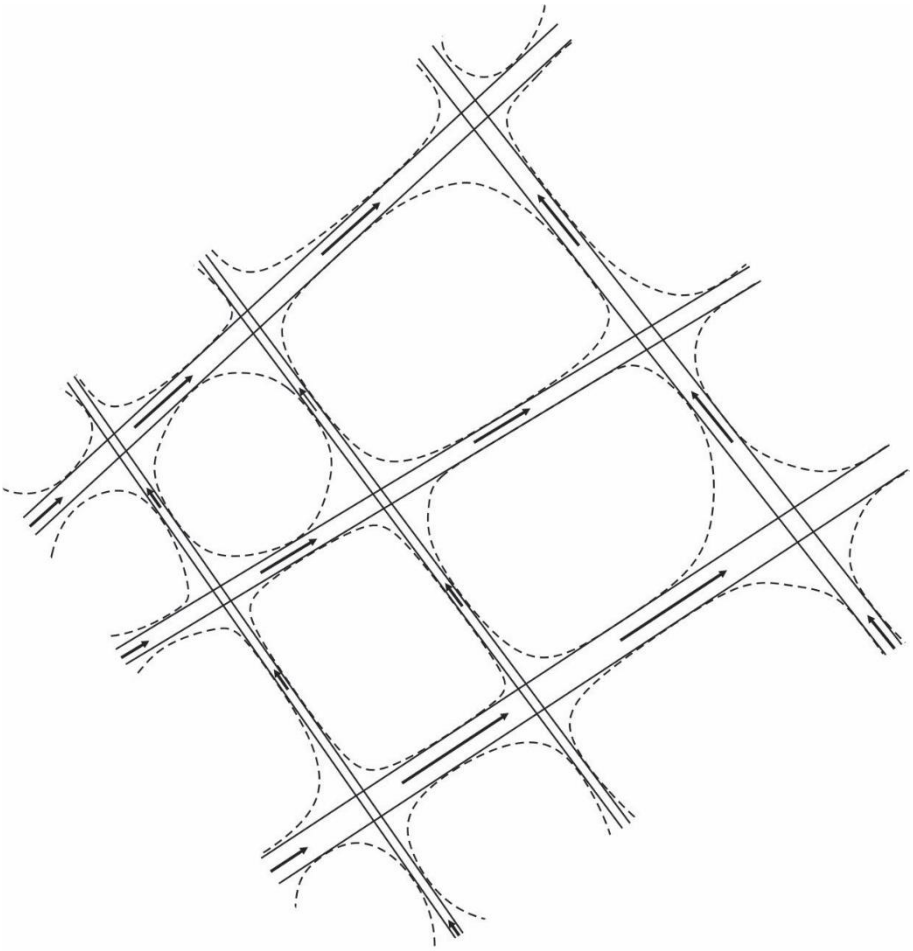

FIG 1. Network-model geometric description of porous media demonstrating a distribution of particle velocities *v*

The Boltzmann kinetics equation describes the dynamics of the continuous particle ensemble during fluid flow in porous media[25, 26]:

$$\phi\frac{\partial f}{\partial t}+v\frac{\partial f}{\partial x}=-\lambda(v)|v|\,f+\frac{1}{\tau}\left[\left(\int_{-\infty}^{\infty}f dv\right)\psi_0-f\right] \tag{2}$$

where ϕ is the porosity, $f(x,t,v)$ is the particle concentration as a function of position, x, time, t, and particle velocity, v, $|\,|$ refers to the magnitude of the variable, $\lambda(v)$ is the filtration function, and τ is the mixing time. Compared with the linearized BGK version of the Boltzmann equation, Eq. (2) differs only in the addition of the particle capture term[27]. We make the distinction here between this formulation, and the popular Lattice Boltzmann formulation that is also used to study flow of particles in porous media[28-30], albeit in an entirely different manner.

The first term on the right-hand side describes a decrease in the particle concentration due to particle capture. The proportionality to the magnitude of velocity follows the general convention for particle capture in porous media wherein particle capture is conceptualized to occur at fixed locations along the particles' trajectory. Travelling at greater speeds and higher concentrations, particles reach these locations at greater rates, thus increasing the particle capture rate. In general, the filtration function, $\lambda(v)$ depends only on the magnitude of the velocity, but to preserve generality we write the dependence on the velocity itself.

The second term on the right-hand side of Eq. (2) represents the relaxation of the particle distribution towards the equilibrium velocity distribution, ψ_0. In traditional applications of the Boltzmann equation in gas kinetics, this term describes the impact of molecular collisions[26]. In particulate flows in porous media, this term encapsulates both inter-particle collisions and particle collisions with the internal surface of the porous media[31]. The homogenization of the relaxation yields an effective diffusion/dispersion term. In most applications in porous media, dispersion is significantly more prominent than diffusion. Given that dispersion is proportional to the mean fluid velocity, we can substitute

$$\tau = \frac{l}{\overline{v}} \tag{3}$$

where l is the mixing length and $\overline{v}$ is the mean particle velocity. While τ represents the time required for a population of particles to relax to the equilibrium velocity, l represents the average length the particles will need to travel in order to relax to the equilibrium velocity distribution. Here the mean particle velocity is given by:

$$\overline{v} = \int_{-\infty}^{\infty} v\psi_0 dv \tag{4}$$

We consider micro-scale with the reference size of tenths of pores (10^{-5}-10^{-4} m) where the porosity is established as a volumetric average of the pore space, but the velocities are stochastically distributed.

Integrating Eq. (2) with respect to velocity 'averages' the equation to produce a differential equation in terms of what will be referred to as the macroscopic variables

$$\phi \frac{\partial c}{\partial t} + \frac{\partial q}{\partial x} = -\varepsilon \tag{5}$$

This includes the average particle concentration, the total particle flux, and the total capture rate, respectively

$$c = \int_{-\infty}^{\infty} f dv, \qquad q = \int_{-\infty}^{\infty} v f dv, \quad \varepsilon = \int_{-\infty}^{\infty} \lambda(v)|v|\, f dv \tag{6}$$

For the standard model presented in Eq. (1), the capture rate can be presented as[32, 33]

$$\varepsilon = \lambda c \overline{v} \tag{7}$$

Equation (1) is obtained from Eqs. (5,7) assuming that $q = c\overline{v}$. It is well known that the inclusion of a distribution of particle velocities as described above can result in a diffusion/dispersion term being supplemented to Eq. (1). An important motivation for upscaling of micro-scale Boltzmann's equation is how to reconcile the dependency of capture on particle velocity and the distribution of these velocities on the pore scale. To this end, some authors proposed an alternative particle rate equation, where the capture rate is proportional to the overall particle flux that consists of the advective and diffusive components[6, 34]:

$$\varepsilon = \lambda \left| cv - D\frac{\partial c}{\partial x} \right| \tag{8}$$

Substitution of Eq. (8) into the mass balance, Eq. (5), yields a delay in the particle velocity with respect to carrier fluid velocity v by a factor $(1-\lambda D)$. Equation (8) is derived by averaging the micro-

scale continuous Markov chains (Fokker-Plank equations)[35, 36]. Moreover, papers[2, 37, 38] validated this model by comparison with laboratory corefloods.

The model comprised of Eqs. (1,8) appended with a second order derivative of c with respect to x presents a seemingly logical model to account for the combined effects of particle diffusion/dispersion and particle capture. This model however has several inconsistencies. Firstly, consider the case of a population of particles with zero mean velocity and a constant initial concentration over some domain. While the particles on average experience no motion, we can imagine the particles moving back and forth as described by diffusion/dispersion. As the particles move, they will almost surely experience particle capture, resulting in a concentration profile that is uniform in space, and decreasing in time. However, the model described by Eqs. (1,8) predicts that the concentration profile will remain constant, with seemingly no capture.

Another inconsistency is the strange result that when the product of the filtration coefficient and diffusion coefficient is high, then particle capture can result in a negative velocity delay factor, $(1-\lambda D)$. This would imply that due to the large extent of particle capture and diffusion, the mean particle motion is in the opposite direction to the carrier fluid. These inconsistencies suggest that a more rigorous approach is required to describe the coexistence of particle capture and diffusion/dispersion.

The benefit of the use of the Boltzmann equation over this approach is that at the scale of Eq. (2), the velocity dependence of particle capture is modelled explicitly. Thus, upon averaging this equation, we can investigate the impact that this velocity dependence has on the evolution of the averaged concentration.

Numerous works have developed numerical Boltzmann models for transport in porous media[22, 24, 39-41] . In particular, BCs for Boltzmann's equation have been formulated on solid rough walls[21, 23, 42, 43] including slip effects during gas flow[19, 25, 44, 45].Similar numerical kinetics models are formulated for micro channels[46, 47] including slip phenomena in rarefied gases[48-50] and micro-channels . Micro-scale numerical modelling yields the estimates of transport coefficients at the upper scale[8-10, 41].

Under the assumption of constant filtration coefficient, Dinariev et al. upscaled the micro-scale model[27], i.e. they derived explicit expressions for the flux q and capture rate ε as functions of the average concentration c and its derivatives, yielding closure of Eq. (5) and providing the macro-scale equation.

However, the filtration coefficient can be strongly dependent on the fluid velocity. Different theoretical and empirical models for velocity-dependent filtration coefficient have been obtained by various authors in attempts to model different particle capture mechanisms. While these authors rarely focus on the velocity dependence of their expressions, as we will show, such dependencies can result in widely varying macro-scale behavior. Figure 2 shows a schematic of several of these capture mechanisms.

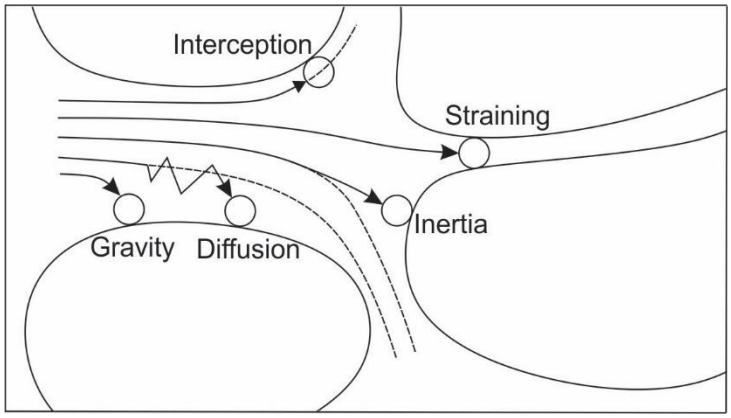

FIG 2. Schematic for the primary mechanisms of particle capture in porous media

In addition to variation of individual particle velocities within a reference volume, the macroscopic flow velocity can significantly vary in natural and engineering processes that involve suspension-colloidal-nano transport in porous media. For flow in a system of injection and production wells, the flow velocity can decrease by up to three orders of magnitude from the well to the natural reservoir. For flow of an incompressible fluid in a 3D domain, an increase in the average viscosity yields a proportional velocity increase in each point of the domain. Thus, any potential dependency of the macroscopic variables on the fluid velocity that arises from a general $\lambda(v)$ could have significant impacts on field predictions and design. However, the upscaled model for velocity-dependent particle capture is not available.

The present paper fills the gap. We derive the large-scale equation for suspension-colloidal-nano transport in porous media, which accounts for velocity dependent particle capture probability. The upscaled model includes explicit expressions for transport coefficients as functions of the micro-scale transport properties. We investigate the behavior of the macro-scale transport coefficients for different models for the velocity dependency of the filtration coefficient, which correspond to various particle-capture mechanisms. The averaged equation matches the experimental data with high accuracy yet matching using the micro-scale coefficients can result in high deviation.

The structure of the text is as follows. Section II presents the exact averaging of the Boltzmann's equation and the upper-scale equation. Section III presents different micro-scale models for particle capture and investigates their effect on upscaled transport coefficients. Section IV presents the results of matching the laboratory data. Section V concludes the paper.

II. KINETIC FORMULATION OF COLLOIDAL TRANSPORT IN POROUS MEDIA

In this Section, we introduce the Boltzmann equation as we apply it to particulate flow and capture in porous media. We also present the averaged equation and the macro-scale coefficients present therein.

A. Exact averaging of the Boltzmann equation with velocity-dependent capture probability

In this Section we provide a brief outline of the averaging methodology. The methodology largely follows that presented by Dinariev et al., 2020. A detailed description is provided in Appendices A, B, and C.

The assumptions of the micro-scale formulation are as follows:

The flow domain is a multiply connected manifold, like an irregular pore network with distributed capillary sizes. Equations of viscous incompressible flow determine filling of the porous space by smooth streamlines. The particles move along the streamlines. The particle size is negligible if compared with the pore size, all streamlines are accessible for the particles movement, i.e. there is no inaccessible volume due to particle size. The particle concentration is small, so the particle flow does not change the position of streamlines. It also allows assuming no effect of particle concentration on suspension density. Besides, small concentration of captured particles does not change the capture probability, so the filtration coefficient is constant. As it follows from the mechanical equilibrium equations for attached particles, attachment and detachment do not occur simultaneously[51]. So, only capture is assumed in the model. The capture rate is proportional to

The streamlines determine the equilibrium particle distribution between the channels according to fluxes in the channels. This determines the equilibrium particle-velocity distribution $\psi_0(v)$. The current particle velocity distribution, which differs from $\psi_0(v)$ due to a flux perturbation

asymptotically tends to the equilibrium distribution; the stabilisation occurs after the particles move over the mixing length l, such that the relaxation time $\tau=l/\langle v\rangle$ is the reference time of stabilisation. So, the particle velocity distribution is caused by mixing in a multiply connected domain due to dispersion; the mean "drift" velocity has the same order of magnitude as the local flow velocities. This determines the difference between Boltzmann's equation for colliding particles in gases and that for the colloidal transport in porous media.

The domain size is large enough to introduce stable porosity value, which comprises several pore lengths. So, porosity is already present in the micro-scale formulation as a volumetric fraction of the pore space in reference volume.

The goal of the averaging is to express the total flux, $\underline{q(x,t)}$ and total capture rate, $\varepsilon(x,t)$ in terms of the averaged concentration, $c(x,t)$ and its derivatives.

Firstly, we make use of the sink-source method, to include initial and boundary conditions (IBC) into the equation. It is assumed that all particles introduced through the IBC are distributed over velocity according to the equilibrium velocity distribution, $\psi_0(v)$, such that Eq. (2) is appended by adding

$$s(x,t)\psi_0(v) \tag{9}$$

where $s(x,t)$ describes the manner in which particles are introduced via the IBC. By including the initial and boundary conditions into the Boltzmann equation prior to upscaling, we can investigate whether or not posing them has any effect on the final upscaled equation.

A distinguishing feature of the modified Boltzmann equation, Eq. (2), is that even if the IBCs are posed such that the particles are introduced with the equilibrium velocity distribution, then this distribution will still not be a solution of the equation. This is in contrast with the same equation without particle capture, wherein posing the IBCs in this way would indeed lead to $\psi_0(v)$ being a solution of the equation. This distinction is due to the velocity dependence of the capture rate as given in Eq. (2), resulting in preferential capture of either slow or fast particles, consequently changing the velocity distribution of particles remaining in suspension.

For simplicity, we make the substitution:

$$f(x,t,v)=\varphi(x,t,v)\psi_0(v) \tag{10}$$

The next step in the averaging methodology is to consider the solution of Eq. (2) as a general function belonging to a Hilbert space. Doing so allows us to decompose the solution into two orthogonal subspaces. In this case, we choose solutions with no dependence on velocity, $c(x,t)$, and those with zero velocity average. In this sense we can decompose the solution into the average and fluctuations around the average:

$$\varphi(x,t,v)=c(x,t)+a(x,t,v) \tag{11}$$

By making use of the projection and embedding operators into and out of the H_c and H_a subspaces, as well as Fourier transforms we can arrive at an expression relating $a(x,t,v)$ in terms of $c(x,t)$. Substitution into Eq. (6) for the flux and total capture rate and then taking the inverse Fourier transform results in the desired expressions (Eqs. (B-30,31)).The brief derivations follow Dinariev et al. 2020 and are presented in Appendixes A, B, and C. Appendix A presents the Hilbert space decomposition of the solutions φ into the two orthogonal subspaces H_c and H_a, according to Eq. (11). Appendix B transforms Eq. (2) into an operator equation in Fourier images, and presents the solution. Appendix C presents detailed derivations of the R_{ij} terms which form the basis for the macroscale

coefficient. The final form of the upscaled transport equation for colloids in porous media is presented in the next Section.

B. Large-scale colloidal transport equation

Following the averaging procedure outlined in Appendices A and B, the final form of the equation can be presented as follows

$$\phi\frac{\partial c}{\partial t}+\left(\bar{v}-2R_{12}\right)\frac{\partial c}{\partial x}=R_{11}\frac{\partial^2 c}{\partial x^2}-\left(\overline{\lambda|v|}-R_{22}\right)c \tag{12}$$

Introducing dimensionless variables

$$T=\frac{\bar{v}t}{\phi L},\ X=\frac{x}{L} \tag{13}$$

reduces Eq. (12) to a dimensionless form

$$\frac{\partial c}{\partial T}+\left(1-\frac{2R_{12}}{\bar{v}}\right)\frac{\partial c}{\partial X}=\frac{R_{11}}{\bar{v}L}\frac{\partial^2 c}{\partial X^2}-\left(\frac{L\overline{\lambda|v|}}{\bar{v}}-\frac{LR_{22}}{\bar{v}}\right)c \tag{14}$$

The equation can be simplified by introducing symbols for the three dimensionless groups present

$$\frac{\partial c}{\partial T}+\left(1-\theta\right)\frac{\partial c}{\partial X}=\frac{1}{Pe}\frac{\partial^2 c}{\partial X^2}-\Omega c \tag{15}$$

where the dimensionless coefficients are

$$\theta=\frac{2R_{12}}{\bar{v}},\frac{1}{Pe}=\frac{R_{11}}{\bar{v}L},\Omega=\frac{L}{\bar{v}}\left(\overline{\lambda|v|}-R_{22}\right) \tag{16}$$

We refer to θ as the dimensionless velocity delay factor, *Pe* here is the Peclet number, and Ω is the macroscale filtration coefficient.

The R_{ij} terms can be calculated using the following equation (see Appendix C for a derivation)

$$R_{ij}=\int_{-\infty}^{\infty}\frac{u_i u_j}{\Lambda}\psi_0 dv-\frac{\int_{-\infty}^{\infty}\frac{u_i}{\Lambda}\psi_0 dv\int_{-\infty}^{\infty}\frac{u_j}{\Lambda}\psi_0 dv}{\int_{-\infty}^{\infty}\frac{1}{\Lambda}\psi_0 dv} \tag{17}$$

where

$$u_1=v,\ u_2=\lambda(v)|v|\quad \Lambda=\lambda(v)|v|+\frac{\bar{v}}{l}\ . \tag{18}$$

Using Eq. (17), we can write each of the macro-scale coefficients explicitly:

$$\theta = \frac{2}{\bar{v}}\left[\int_{-\infty}^{\infty}\frac{v\lambda(v)|v|}{\lambda(v)|v|+\frac{\bar{v}}{l}}\psi_0 dv - \frac{\int_{-\infty}^{\infty}\frac{v}{\lambda(v)|v|+\frac{\bar{v}}{l}}\psi_0 \times dv \int_{-\infty}^{\infty}\frac{\lambda(v)|v|}{\lambda(v)|v|+\frac{\bar{v}}{l}}\psi_0 dv}{\int_{-\infty}^{\infty}\frac{1}{\lambda(v)|v|+\frac{\bar{v}}{l}}\psi_0 dv}\right] \tag{19}$$

$$\frac{1}{Pe} = \frac{1}{\bar{v}L}\left[\int_{-\infty}^{\infty}\frac{v^2}{\lambda(v)|v|+\frac{\bar{v}}{l}}\psi_0 dv - \frac{\left(\int_{-\infty}^{\infty}\frac{v}{\lambda(v)|v|+\frac{\bar{v}}{l}}\psi_0 dv\right)^2}{\int_{-\infty}^{\infty}\frac{1}{\lambda(v)|v|+\frac{\bar{v}}{l}}\psi_0 dv}\right] \tag{20}$$

$$\Omega = \frac{L}{\bar{v}}\left(\overline{\lambda(v)|v|} - \left[\int_{-\infty}^{\infty}\frac{(\lambda(v)|v|)^2}{\lambda(v)|v|+\frac{\bar{v}}{l}}\psi_0 dv - \frac{\left(\int_{-\infty}^{\infty}\frac{\lambda(v)|v|}{\lambda(v)|v|+\frac{\bar{v}}{l}}\psi_0 dv\right)^2}{\int_{-\infty}^{\infty}\frac{1}{\lambda(v)|v|+\frac{\bar{v}}{l}}\psi_0 dv}\right]\right) \tag{21}$$

We note here that as discussed by Dinariev et al., Eqs. (15,16) immediately resolve one of the inconsistencies with previous models outlined in the introduction[27]. That is, that for a population of particles with zero mean velocity and a uniform initial concentration profile, Eqs. (15,16) correctly predict that the concentration profile will decrease with time.

III. PROPERTIES OF TRANSPORT COEFFICIENTS

In this Section, we discuss the dimensionless coefficients present in the averaged equation. We present three models for the velocity-dependence of particle capture (Section A). Section B explores the ramifications of each model on the behavior of the macro-scale coefficients. Further, we discuss a simple model that accounts simultaneously for two major primary mechanisms of particle capture – size exclusion and attachment (Section C).

A. Three models for particle-speed dependency of filtration coefficient

The generality of Eq. (2) with respect to the filtration function *λ(v)*, allows us to explore a variety of filtration mechanisms. Equipped with Eqs. (19-21), we can utilize the velocity-dependence of the filtration mechanisms as described by other authors to explore the emerging macro-scale behavior.

The straining model that we consider is the simplest and is used to describe straining and size exclusion. We use the term straining to refer to mechanical capture of particles that encounter pores larger than their largest radius in the cross-section to flow; this term also describes particle capture between two asperities. Previous authors have made the argument that capture by straining will be

directly proportional to the magnitude of the particles velocity[52, 53]. This follows from two arguments: firstly, that during laminar flow in porous media, particles travel along fixed streamlines, regardless of the average fluid velocity, and secondly, that the higher the fluid velocity, the faster particles encounter pore throats. Thus for straining, the filtration function is simply a constant:

$$\lambda(v) = \lambda \tag{22}$$

which is equal to particle capture probability per unit length of the particle trajectory.

The attachment model[54] is given by the correlation equation to describe the capture rate of particles undergoing physico-chemical filtration in porous media. The authors expressed the filtration coefficient as

$$\lambda = \frac{3}{4}\frac{(1-\phi)}{r_g}\alpha\eta_0 \tag{23}$$

where d_c is the grain radius, α is the attachment efficiency, and η_0 is the single-collector contact efficiency. The attachment efficiency α describes the fraction of particles which become attached following collision with grains, and the single-collector contact efficiency describes the fraction of particles which come into contact with a grain while flowing past it. Following Tufenkji and Elimelech, we consider the case where $\alpha = 1$.

They investigated the dependence of the single-collector contact efficiency due to diffusion, interception resulting from finite particle size, and gravity, with the single-collector contact efficiency given empirically as:

$$\eta_0 = 2.4A_S^{1/3}N_R^{-0.081}N_{Pe}^{-0.715}N_{vdW}^{0.052} + 0.55A_S N_R^{1.675}N_A^{0.125} + 0.22N_R^{-0.24}N_G^{1.11}N_{vdW}^{0.053}. \tag{24}$$

Here the dimensionless numbers are defined as follows:

$$A_s = \frac{2(1-\gamma^5)}{2-3\gamma+3\gamma^5-2\gamma^6},\ N_R = \frac{r_p}{r_c},\ N_{Pe} = \frac{2|v|r_c}{D_\infty},\ N_{vdW} = \frac{A}{kT},\ N_A = \frac{A}{12\pi\mu r_p^2|v|},$$
$$N_G = \frac{2}{9}\frac{r_p^2(\rho_p-\rho_f)g}{\mu|v|} \tag{25}$$

where $\gamma=(1-\phi)^{1/3}$, r_p is the particle radius, D_∞ is the bulk diffusion coefficient (described by the Stokes-Einstein equation), A is the Hamaker constant, k is Boltzmann's constant, T is the absolute fluid temperature, ρ_p and ρ_f are the particle and fluid densities respectively, μ is the fluid viscosity, and g is gravitational acceleration. We have replaced the velocity with its magnitude.

The inertial capture model by presented by Andrade Jr et al.[55]reflects particle capture for non-Brownian, inertial particles. Inertial particles are likely to deviate from fluid streamlines that curve through the porous space of porous media. Larger particles, travelling at higher velocities, are more likely to deviate from their streamlines and collide with grains. These authors developed the following equation for the filtration coefficient:

$$\lambda = \frac{10}{9}\frac{(1-\phi)r_p^2\rho_f}{\beta r_g^2\mu}|v| \tag{26}$$

where β is a characteristic constant of the capture process, identified by the authors to be approximately 0.058.

As before, we exchange the velocity for its absolute value to account for capture resulting from particles moving in the direction opposite to the mean velocity.

These three models by no means present a comprehensive review of particle capture mechanisms, nor the modelling thereof. They do however provide explicit formulae for the filtration functions of three distinct capture mechanisms (straining, attachment, and inertial capture). The shape of the filtration coefficients for each of the capture mechanisms is shown below in Fig. 3.

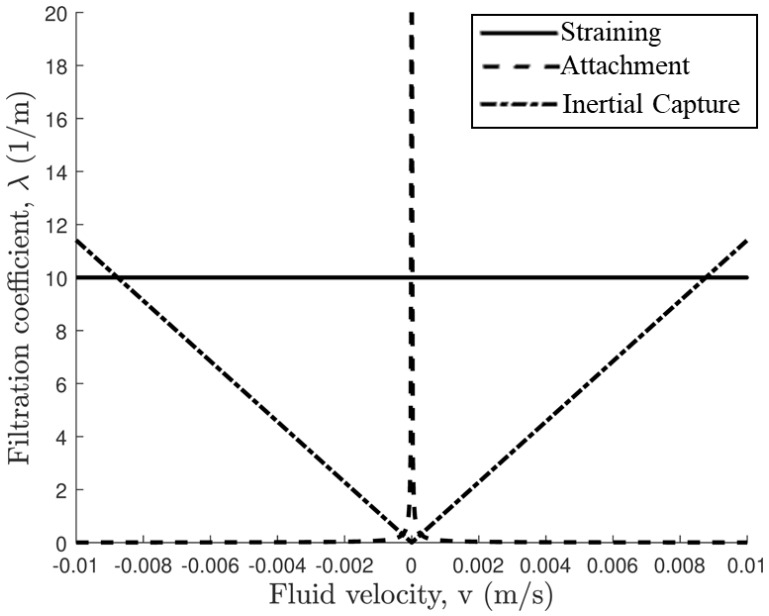

FIG 3. Three examples of microscale filtration coefficient functions: Straining (direct proportionality of modulus of velocity) following Dinariev et al., 2020 (mechanical size exclusion of particles), Attachment (accounting for capture by diffusion, interception with grains, and gravity)as described by Tufenkji and Elimelech, 2004, and Inertial Capture (accounting for capture of non-Brownian particles by deviation from fluid streamlines by inertia) as described by Andrade et al., 2008

B. Effects of mean velocity, mixing length and coefficient of variation on macroscale transport parameters

In this section we perform sensitivity analysis of the macro-scale parameters, (θ, Pe^{-1},Ω) for the different capture models presented in the previous section. All results use a normal distribution for the equilibrium velocity distribution, $\psi_0(v)$.

Dinariev et al., 2020 demonstrated that for the straining model, each of the macro-scale parameters is independent of the mean fluid velocity[27]. The mean fluid velocity is a known parameter in laboratory coreflooding studies (with the exception of constant drawdown tests) and is easy to vary. In addition, fluid velocities in laboratory studies are often orders of magnitude lower than fluid velocities in the near-wellbore environment of industrial production or injection wells. Thus the fluid-velocity dependence of macro-scale behavior of suspensions is of critical importance both to laboratory studies of particle capture, and to industrial applications. The dependence for the three mechanisms considered in this study is presented below in Fig. 4.

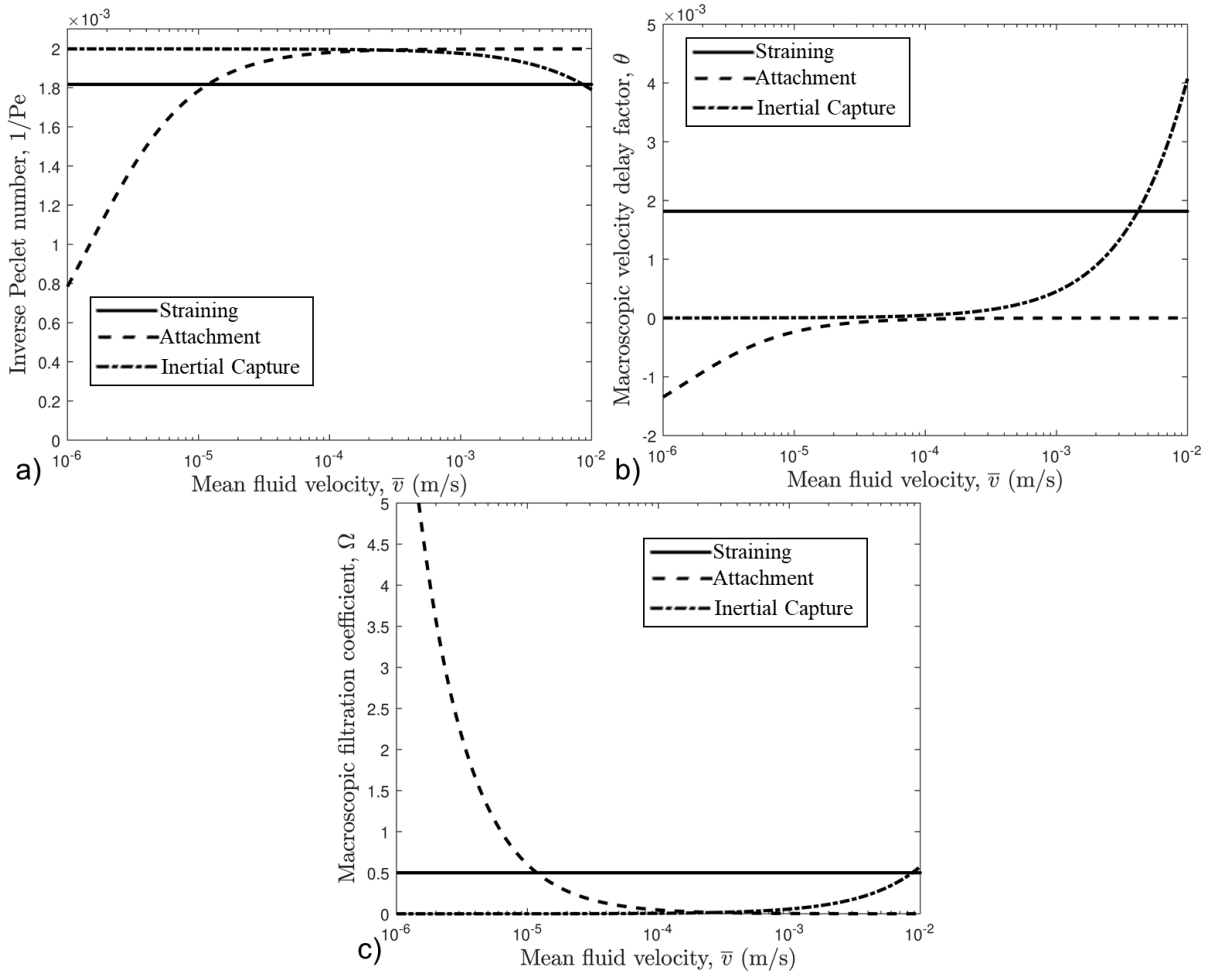

FIG 4. Variation of macro-scale parameters with mean fluid velocity for a normal equilibrium velocity distribution for three different capture models, a) Inverse Peclet number, b) Macroscopic velocity delay factor, c) Macroscopic filtration coefficient

For the straining model, the particle capture probability per unit length is independent of the fluid velocity. For the attachment model, to a good approximation, particles are captured with a fixed probability per unit time. Given that, for higher fluid velocities, particles spend a smaller time period travelling along a fixed trajectory, the probability of capture per unit length will be lower for attachment. Lastly, for inertial capture as described by Andrade et al., the probability for capture per unit length increases with fluid velocity. This is a consequence of a deviation of particle trajectories from the streamlines, resulting in their collision with the rock surface, resulting in particle capture. These statements provide the basis for the behaviour in Fig. 4.

In Fig. 4(a), we can see that higher mean fluid velocities lead to constant, increasing, and decreasing diffusion for the straining, attachment, and inertial capture models respectively. This follows from the idea that selective particle capture, either of faster (straining, inertial capture) or slower particles (attachment) results in a reduction in the width of the particle velocity distribution, and consequently, less spreading of particles. The linear dependency of straining to particle velocity leads to a direct proportionality of the diffusion coefficient to the mean fluid velocity. Division by the mean velocity during the non-dimensionalisation (see Eq. (13)) results in the independence of velocity presented in Fig. 4a. In fact, this is true for each of the macro-scale variables.

Figure 4(b) presents the dependency of the velocity delay factor with the mean fluid velocity. While unproven, Dinariev et al. argued that θ was non-negative as a result of straining selectively capturing

faster particles. This is consistent with our results. In addition, inertial capture also results in a positive θ, and thus a reduction in the mean particle velocity due to capture. Higher velocities further accentuate the effect of inertial capture, resulting in additional deceleration of the particle front. Attachment, however, shows an acceleration of the particle front, provided by a negative value of the velocity delay factor. As the mean fluid velocity increases, more and more particles move too quickly to have any significant risk to be captured by attachment, and thus θ tends to zero.

Figure 4(c) presents the sensitivity analysis for the macro-scale filtration coefficient. Consistent with the above comments, the observed particle capture rate increases with mean fluid velocity for inertial capture, decreases for attachment, and is constant for straining (once non-dimensionalised).

In addition to investigating the dependence on the mean fluid velocity, we also investigate the impact of various flow properties. First, let us consider the mixing length, l, which describes the travel distance required for the particle velocity distribution to relax to the equilibrium velocity distribution, ψ_0. Many of the impacts of particle capture observed in the macro-scale behaviour are due to the effect of capture on the fluid velocity distribution. Thus, we expect that for larger mixing lengths, these effects will persist for longer, and the resulting impact on transport will be more pronounced. The result of the sensitivity study is presented below in Fig. 5.

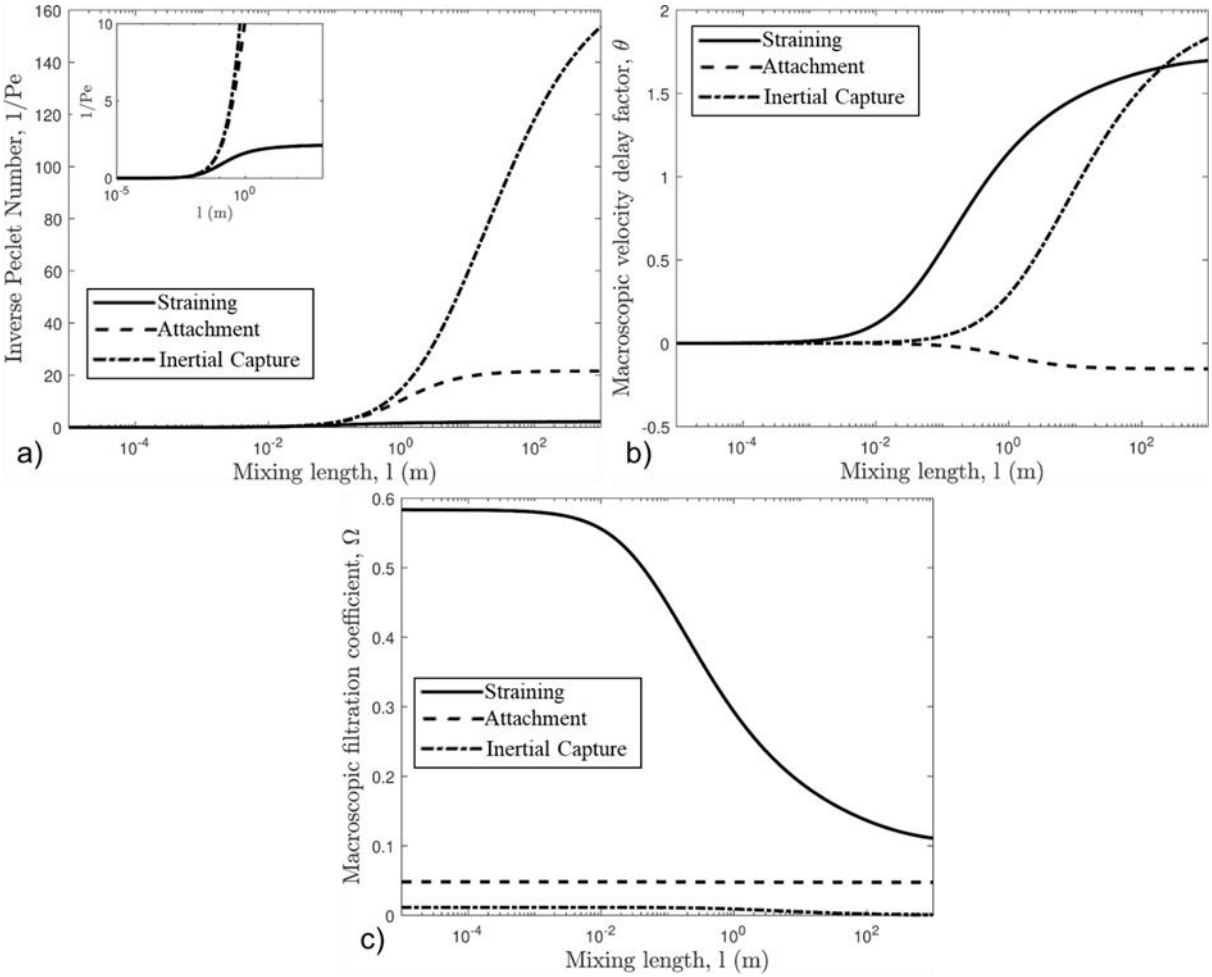

FIG 5. Variation of macro-scale parameters with mixing length for a normal equilibrium velocity distribution for three different capture models, a) Inverse Peclet number, b) Macroscopic velocity delay factor, c) Macroscopic filtration coefficient

Equation (18) for the Λ term located in the denominator of all integrals Eqs. (19-21) highlights the competition between capture (first term) and relaxation (second term) on the effective particle

velocity distribution. When relaxation is large (small l), then the effective distribution is essentially a constant multiple of the original. In this case, dispersion negates the impact of capture on the velocity distribution.

Figure 5(a) presents the results for the impact of mixing length on the inverse Peclet number. For all capture models, increasing the mixing length increases the effective diffusion. Imagine a small pulse of particles injected into a porous media. When the mixing length is small, fast particles that move ahead of the pulse will quickly 'relax', reducing their velocity towards the mean particle velocity due to the last term in Eq. (2). Similarly, slow particles that fall behind the pulse will accelerate. Thus, the relaxation process reduces the spread of the pulse by shifting the particle velocity distribution everywhere in the porous media towards $\psi_0(v)$. This explains why the inverse Peclet number increases monotonically with the mixing length. When capture is non-existent, this process will result in Pe^{-1} diverging. However, with finite capture, the diffusion will tend asymptotically to some value depending on the magnitude of the capture, $\lambda(v)|v|$ over the range where $\psi_0(v)$ is non-zero.

Figure 5(b) presents the results for the velocity delay factor. This factor arises due to the alteration of the velocity distribution due to capture. It follows from Fig. 5(b) that this alteration is more significant as the mixing length increases. This effect has diminishing returns, and at very large values of the mixing length, θ stabilizes for all three models.

Figure 5(c) presents the results for the macro-scale filtration coefficient. Equation (16) shows that Ω is comprised of two additive terms. The first term represents capture due to the velocity average of the $\lambda|v|$ term. The second term is more complex. Changes to the velocity distribution due to capture occur when capture is selective with respect to velocity. When these changes occur, the proportion of particles moving at fluid velocities more prone to capture decreases (i.e. when fast particles are captured preferentially, there will be fewer fast particles). This results in less capture. This is the effect described by the second term in Eq. (16). It is only the second of the two terms that depends on the mixing length. Figure 5(c) shows the at large values of the mixing length, this second term becomes significant (except for the attachment model) and Ω decreases.

Lastly, we consider the effect of the coefficient of variation of the equilibrium particle velocity distribution, C_v:

$$C_v = \frac{\sigma}{\bar{v}} \tag{27}$$

Where σ is the standard deviation of $\psi_0(v)$. This is a normalized measure of the width of the distribution. The sensitivity analysis for C_v is presented below in Fig. 6.

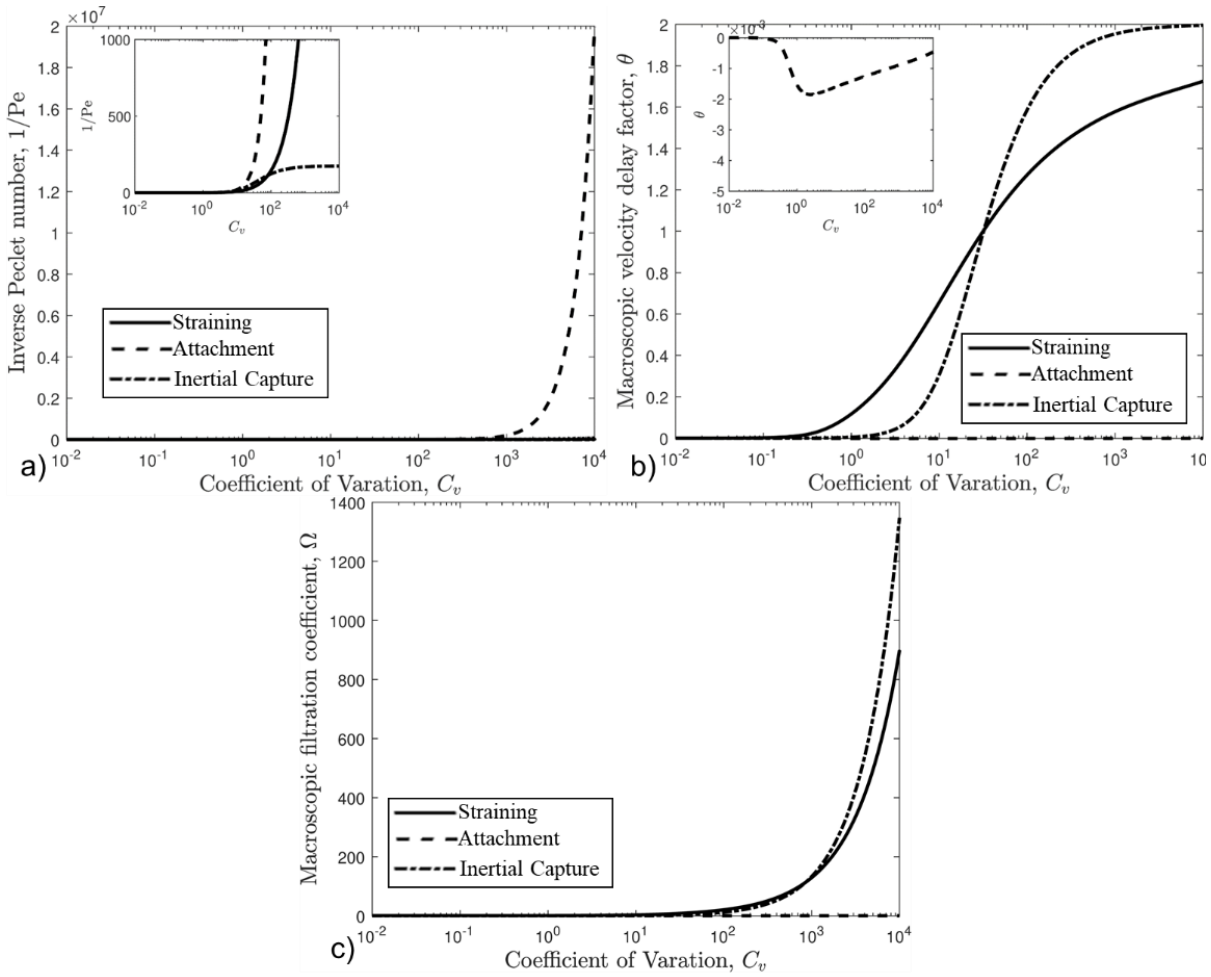

FIG 6. Variation of macro-scale parameters with the coefficient of variation of the velocity distribution for a normal equilibrium velocity distribution for three different capture models, a) Inverse Peclet number, b) Macroscopic velocity delay factor, c) Macroscopic filtration coefficient

As C_v increases, the proportion of particles with high velocity magnitude will increase. This will increase the extent of capture for straining and inertial capture but decrease it for attachment. In the absence of capture, increasing the coefficient of variation will increase the inverse Peclet number. This is evident in Fig. 6(a) for both attachment and straining. The sharp increase for straining occurs at higher values of C_v due to the increasing capture, which acts to decrease diffusion. For inertial capture, as capture increases more significantly with the magnitude of particle velocity, Pe^{-1} increases, then stabilises at higher C_v.

Similarly, in Fig. 6(b), as C_v increases, the velocity delay factor increases for both straining and inertial capture, due to an increasing extent of capture. For attachment, θ reaches a minimum at a fixed value of C_v. At lower values, the distribution is not wide enough for particle capture to significantly alter the mean particle velocity. At higher values, most particles are moving at speeds too large to experience attachment to any consequential degree.

The results for Ω presented in Fig. 6(c) follow directly from the above statements. The macroscopic filtration coefficient increases rapidly for both straining and inertial capture, and as expected, the increase is faster for inertial capture. The total capture for attachment is negligible in comparison.

C. A simple approach to account for simultaneous straining and attachment

While there are a plethora of possible particle capture mechanisms and modelling approaches towards them, many practical applications are focused on straining and attachment. These two mechanisms are by no means mutually exclusive. While we have already presented a model developed by Tufenkji and Elimelech to describe attachment, in this Section we will discuss a simpler method to illustrate the behavior when both straining and attachment are present.

It was argued in Section I that straining occurs with a fixed capture probability per unit particle travel distance. However, for attachment, particles are not captured along the fluid streamlines, but instead are captured when they deviate from them. Here we consider that deviation being a result of diffusion, which is independent of the particles' velocity. It follows that particle capture will occur at a fixed probability per unit time. Therefore, the filtration coefficient for attachment becomes:

$$\lambda(v) = \frac{\lambda_0}{|v|} \tag{28}$$

Substitution into Eq. (17) results in

$$R_{ij} = \frac{1}{\lambda_0 + \frac{\overline{v}}{l}} \mathrm{cov}\left(u_i, u_j\right) \tag{29}$$

where cov is the covariance between two variables weighted by $\psi_0(v)$. Given that $u_2=\lambda_0$ and thus is constant, R_{12} and R_{22} become zero. This simplifies greatly the analysis of the macro-scale variables and their dependence on other variables. We can express each of the macro-scale variables as:

$$\frac{1}{Pe} = \frac{1}{\overline{v}L\left(\lambda_0 + \frac{\overline{v}}{l}\right)}\sigma^2, \theta = 0, \Omega = \frac{L\lambda_0}{\overline{v}} \tag{30}$$

Combining Eq. (28) with the straining model presented in Eq. (22) results in:

$$\lambda(v) = \frac{\lambda_0}{|v|} + \lambda_1 \tag{31}$$

Note here that we have assumed that the filtration coefficient in the presence of two mechanisms is the sum of their individual filtration coefficients. Similar reasoning was used by Tufenkji and Elimelech to derive Eq. (24)[54]. While this approach may seem intuitive, strictly speaking it is rigorous only when each individual filtration coefficient is small, in which case Eq. (31) results from the truncation of the Taylor series expansion of the general $\lambda(v)$ centered around each individual λ equal to zero.

We will now present a sensitivity study on this combined model, the results of which are shown below in Fig. 7.

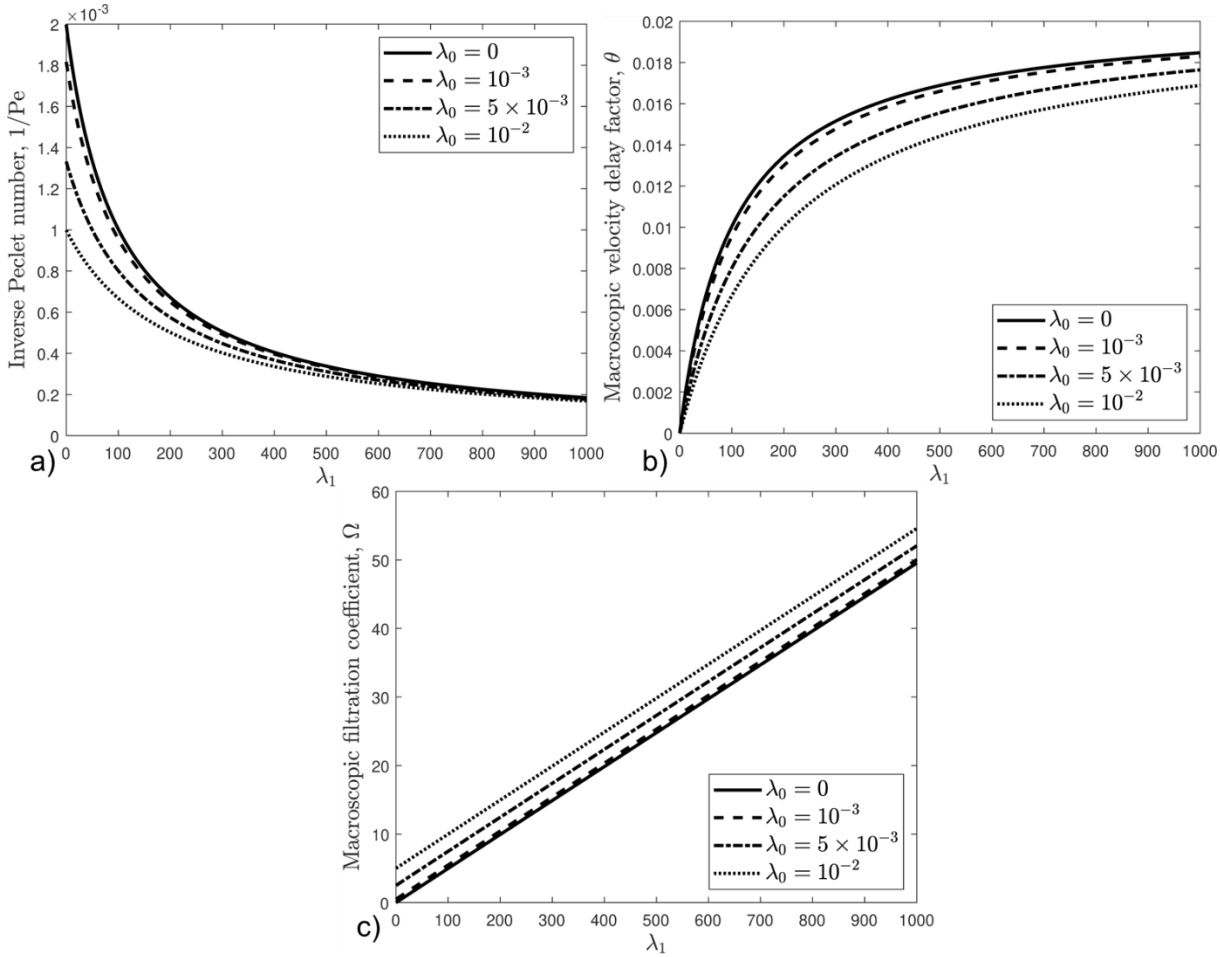

FIG 7. Sensitivity study of the impact of straining and attachment in hybrid model presented in Eq. (31), a) Inverse Peclet number, b) Macroscopic velocity delay factor, c) Macroscopic filtration coefficient

Interpretation of the hybrid model begins with an understanding of each of two components of particle capture.

The filtration coefficient for attachment is independent of particle velocity. This reflects the concept that straining occurs at fixed sites along fluid streamlines. Thus, the total particle capture rate increases with particle velocity, as these particles will encounter straining sites more frequently. Attachment on the other hand scales inversely with fluid velocity, as slower particles have more time to diffuse from fluid streamlines and collide with the porous matrix. This results in a total particle capture rate that is independent of particle velocity.

In context of these statements, we now consider Fig. 7(a) which shows the effect of both λ_1 and λ_0 on the inverse Peclet number. The effect of λ_0 on Pe^{-1}, as outlined in Eq. (30) can be seen to be roughly equivalent to the term $\overline{v}/l$. The latter describes the relaxation of the particle velocity distribution towards $\psi_0(v)$. Thus faster particles that move ahead of the front are shifted, by this term, towards slower velocities and vice versa. The effect of λ_0 is similar, but rather than shifting the velocity of these particles, they are simply removed due to capture. The result is a direct equivalence of these two terms in the case of λ_1=0. The effect of λ_1 is two-fold: firstly, it acts similarly to λ_0 in that straining captures particles which move faster or slower than the average particle front, secondly, straining preferentially captures faster particles, so that it acts to reduce the proportion of faster particles. This will narrow the particle velocity distribution, reducing particle spread, and hence diffusion. The decrease in diffusion resulting from both straining and attachment on diffusion is diminishing.

Figure 7(b) presents the results for the macroscopic velocity delay factor, θ. This factor arises due to the selectivity of particle capture based on particle velocity. It follows that the greater the impact of straining, the greater the impact of preferential capture, and thus the greater the value of θ. When there is only attachment, Eq. (30) shows that θ=0, as particles are captured independently of their velocity. Thus, regardless of the extent of particle capture, the resulting population of particles will have an unchanged mean velocity. However, Fig. 7(b) shows that when straining is present, the magnitude of λ_0 can impact the value of θ. This results from the competition between straining and attachment. When straining is present, increasing the magnitude of attachment reduces the total concentration of particles affected by straining, thus reducing the extent of preferential capture, resulting in a lower value of θ.

Lastly, Fig. 7(c) shows the results for the macroscopic filtration coefficient, Ω. It should first be noted, that Ω does not in general scale linearly with λ_1, but the degree of nonlinearity arising from the R_{22} term in Eq. (16) is minimal for these example calculations. The curves show an expected result, that increasing the extent of attachment or straining results in an increase in the total capture rate.

IV. Treatment of laboratory data by the upscaled colloidal transport model

In this Section we will perform tuning of laboratory results using the models presented in Section IIIA.

The laboratory tests considered here were performed in a work by Bai et al.[56].An instantaneous pulse (or approximation thereof) of particles was injected into a porous medium (L = 30 cm) followed by particle-free water. The porous media was comprised of qurartz grains, with a porosity of 0.421 with particle sizes ranging from 1 to 3.5 mm. The quartz was pretreated with a H_2SO_4 solution for 24 hours and rinsed several times to remove impurities. The particles used here were red-mud filtrate with a median diameter of 5 μm. The tests were performed at velocities varying from 0.076 to 0.230 cm/s, injected concentrations of 0.2 to 3 mg/L, and solution pH from 9 to 12. A significant number of tests show significant delay in the arrival of the particle front indicating a decrease in the mean particle velocity.

Coreflooding tests are tuned by varying the macro-scale parameters until maximum agreement is achieved between the measured effluent breakthrough concentration curve (BTC) and that predicted by the model. While only the macro-scale variables are present in this process, it is important to recognize that by using a particular model for $\lambda(v)$ we are inadvertently establishing an interdependence between the macro-scale parameters. This dependence will in general depend on the form of the filtration coefficient. The dependence results in a reduction of the possible vectors (Pe^{-1},θ,Ω) that the model permits. This is expressed formally as:

$$\left(\frac{1}{Pe},\theta,\Omega\right)\Big|_{\lambda(v)} \subseteq \left(\frac{1}{Pe},\theta,\Omega\right) = \mathbb{R}^3_+ \tag{32}$$

We can conceptualize this by considering the origin of θ. The velocity delay factor becomes non-zero only when two things are present: first, particles must move at different velocities at equilibrium ($\psi_0(v) \neq \delta(v)$), and second, particles must be captured preferentially based on their velocity. Consider then a theoretical case resulting in large Pe^{-1} and small Ω, here it follows that we satisfy the first condition, but not the second, as there is clearly very little particle capture. While inexact, it is clear that this region of the (Pe^{-1},θ,Ω) space is unlikely to be feasible for most functions $\lambda(v)$.

Thus when tuning laboratory data, it is most correct to choose a filtration coefficient and tune the micro-scale coefficients present in Eqs. (19-21). While two of the three models presented in Section IIIA contain no tuning parameters, for the sake of comparison, we reduce them only to their dependence on the particle velocity. Thus the tuning equations for straining, attachment, and inertial capture are, respectively:

$$\lambda(v) = \lambda_1 \tag{33}$$

$$\lambda(v) = A|v|^{-0.715} + B|v|^{-0.125} + C|v|^{-1.11} \tag{34}$$

$$\lambda(v) = D|v| \tag{35}$$

Where depending on the model used, λ_1, A, B, C, and D are treated as tuning parameters. In addition, we tune the mixing length, l, and the coefficient of variation of the equilibrium particle velocity distribution, C_v.

For the purposes of comparison, we also include fitting purely by the macro-scale variables. This serves as a theoretical 'best-fit', regardless of $\lambda(v)$. As per Eq. (32), using any particular function λ(v) will restrict the search space for the optimization algorithm. Such a restriction will impose an upper limit to the quality of fit.

Fitting was performed using a gradient-based optimization algorithm within Matlab (Mathworks Inc, 2019). Following the fitting, we calculate the coefficient of determination, R^2 for each test, to determine the quality of the fit:

$$R^2 = 1 - \frac{\sum\left(\left(\frac{c}{c_0}\right)_{data} - \left(\frac{c}{c_0}\right)_{model}\right)^2}{\sum\left(\left(\frac{c}{c_0}\right)_{data} - \overline{\left(\frac{c}{c_0}\right)_{data}}\right)^2} \tag{36}$$

where c here is the outlet, or breakthrough, concentration of particles, and c_0 is the injected concentration of particles.

The results are shown below in Fig. 8.

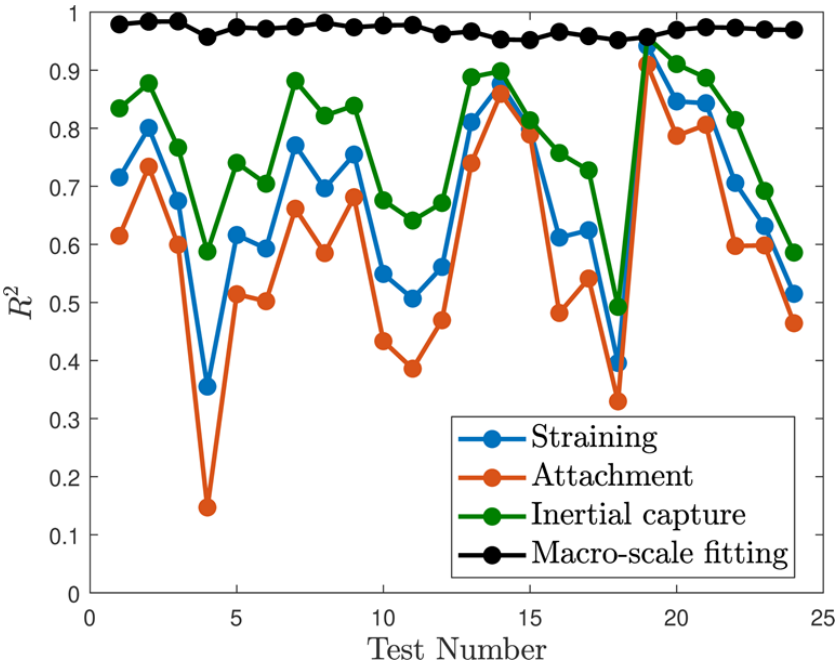

FIG 8. Coefficient of determination, R^2, for the tuning of laboratory coreflooding tests from Bai et al., using the models presented in Section IIIA as well as freely fitting with the macro-scale coefficients (Pe^{-1},θ,Ω)

For every test, inertial capture results in the best fit, disregarding macro-scale fitting. These tests were performed at flow velocities of 0.076, 0.148, and 0.23 cm/s. These velocities are relatively large for colloidal flows in porous media. The superiority of inertial capture in combination with this would suggest that this mechanism is both present and dominant.

The high quality of fit using macro-scale fitting suggests that the form of Eq. (15) is well-suited for the experimental data. The significant deviations between the black and colored curves indicates a discrepancy between the choice of ($\lambda(v)$,$\psi_0(v)$) used to fit and those that correctly model the underlying behavior present in the laboratory tests.

To better visualize the appropriateness of each model, Fig. 9 presents three example breakthrough curves with the optimal curves for each model.

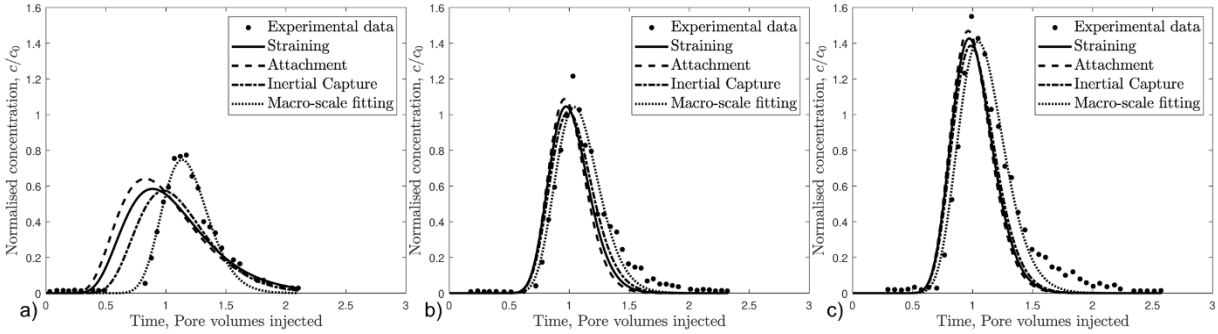

FIG 9. Three sample breakthrough curves taken from [56]fitted by the three models considered in Section IIIA as well as freely fitting with the macro-scale coefficients (Pe^{-1},θ,Ω) , a) $\bar{v}$ = 0.076 cm/s, c_0 = 3 mg/L, pH = 10, b) $\bar{v}$ = 0.248 cm/s, c_0 = 2 mg/L, pH = 12, c) $\bar{v}$ = 0.230 cm/s, c_0 = 2 mg/L, pH = 10

The three breakthrough curves demonstrate qualitatively the behavior of each model when tuning this data. Firstly, it can be seen immediately that the macro-scale fitting better suits the data. The difference between this method and the three micro-scale models is less evident in Figs. 9(b,c), where all models fit reasonably well. In both of these cases, the value of θ, while positive, is relatively low. For Fig. 9(a) however, θ is significant, and the delay in the arrival of the peak of the concentration plume is easily verified visually. In this case, while the macro-scale fitting reproduced the behavior well, each of the micro-scale models failed to do so. This is explained by the limitations placed on the variables (Pe^{-1},θ,Ω) imposed by the particular function λ(v) used in each case. It is clear that while the match is still poor, the model for inertial capture is more appropriate, and the model for attachment is least appropriate for this data set.

The physical origin of the difference between the first two tests potentially lies in the solution chemistry. The first test was performed using a fluid with a lower pH (pH = 10) compared with the following two tests (pH = 12). The literature on particle attachment in porous media has consistently shown that lower pH increases the extent of particle attachment as a result of changes to the electrostatic force between the particles and the porous matrix[57, 58]. An increase in the total capture rate with lower pH is consistent with the tests presented in Fig. 9.

While not presented here, comparison of different capture mechanisms or models in the context of laboratory results could in theory be used to identify the underlying capture mechanism by identifying the most appropriate model.

V. CONCLUDING REMARKS

Exact averaging of the Boltzmann physical kinetics equation for colloidal-suspension-nano transport in porous media with particle-speed-dependent particle capture probability allows concluding as follows.

- Introduction of sink-source term in the Boltzmann equation with stochastic particle speeds and any arbitrary speed-dependency of the filtration coefficient $\lambda(v)$ instead of solving the initial-value problem yields linear operator equation in Hilbert space, which is solved by decomposition of the operator. This yields the exact averaging over the distributed velocity and leads to closed macroscale equation for average particle concentration
- The large-scale equation is of the form of a linear advection-diffusion equation with a reaction term; the upscaled model coefficients of drift velocity, dispersion and capture probability are explicitly expressed via the micro-scale model parameters
- The distinguishing feature of the upscaled equation is that the average particle velocity differs from the carrier fluid velocity. The particles can move faster or slower than the mean fluid velocity depending on whether faster or slower particles are capture preferentially
- The coefficients have been calculated for existing models for attachment, straining, and inertial capture and the coefficients show very distinct trends for different mean flow velocities, mixing lengths, and equilibrium velocity coefficient of variation
- For straining and inertial capture, where faster particles are capture preferentially, increasing capture results in a deceleration of the particle velocity front
- For particle capture by attachment to the surface, the upscaled equation allows for acceleration of the particles, by preferential capture of the slowest particles
- Utilizing micro-scale models for different capture mechanisms allows for more accurate tuning of a wide-set of laboratory data

ACKNOWLEDGEMENTS

The authors are deeply grateful to Prof Anthony Roberts (University of Adelaide) for numerous discussions and friendly support. Numerous detailed considerations and co-authorship with Prof O. Dinariev (Russian Academy of Sciences), Prof A. Shapiro (Denmark Technical University), and A. Rego (State University of Rio de Janeiro) are gratefully acknowledged.

DATA AVAILABILITY

The data that support the findings of this study are available from the corresponding author upon reasonable request.

Appendix A. Splitting / decomposition of operator equation in Hilbert space

We begin by making the substitution

$$f\left(x,t,v\right)=\varphi\left(x,t,v\right)\psi_0 \tag{A-1}$$

resulting in

$$\phi\frac{\partial\varphi}{\partial t}+v\frac{\partial\varphi}{\partial x}=-\lambda(v)|v|\varphi+\frac{\bar{v}}{l}\left[\left(\int_{-\infty}^{\infty}\varphi\psi_0 dv\right)-\varphi\right]+s(x,t) \tag{A-2}$$

The distinguishing feature of this model compared to that presented in Dinariev et al.[27] is the general dependency of the filtration coefficient, λ on the fluid velocity. As we will see below, this generalization poses no additional difficulties in following the averaging procedure presented in this previous work; the inability to remove the filtration coefficient from velocity integrals simply changes the constants present in the final equation.

Assume that the function $\varphi=\varphi(x,t,v)$ belongs to the Hilbert space H with scalar product

$$(\varphi_1,\varphi_2)=\int_{-\infty}^{\infty}\psi_0\varphi_1^*\varphi_2 dv \tag{A-3}$$

Under this definition, we can express the macroscopic variables defined earlier in terms of the scalar product:

$$c=(1,\varphi)=\int_{-\infty}^{\infty}\varphi\psi_0 dv \tag{A-4}$$

$$q=(v,\varphi)=\int_{-\infty}^{\infty}v\varphi\psi_0 dv \tag{A-5}$$

$$\varepsilon=(\lambda(v)|v|,\varphi)=\int_{-\infty}^{\infty}\lambda(v)|v|\varphi f\psi_0 dv \tag{A-6}$$

Consider the Hilbert space H as an orthogonal sum:

$$H=H_c\oplus H_a \tag{A-7}$$

where H_c is a subspace of constants (with respect to velocity). Introduce the orthogonal projections into these two subspaces:

$$P_c: H\to H_c,\ P_a: H\to H_a \tag{A-8}$$

and the corresponding embeddings back into the original Hilbert space:

$$J_c: H_c\to H,\ J_a: H_a\to H \tag{A-9}$$

Based on the decomposition of the Hilbert space, we can write any function φ as

$$\varphi=c+a,\ c=(1,\varphi)=\int_{-\infty}^{\infty}\varphi\psi_0 dv,\ a=\varphi-c \tag{A-10}$$

where c represents the average of the function φ in regards to the scalar product defined earlier, and a represents the deviation of the function φ from its average in the velocity space.

The projections to each subspace are

$$c=P_c\varphi,\ a=P_a\varphi \tag{A-11}$$

From Eqs. (A-10,11) we can see that

$$P_c(\varphi) = (1, \varphi) \ , \ P_a(\varphi) = \varphi - (1, \varphi) \tag{A-12}$$

Appendix B. Solution of operator equation in Fourier images

Applying the 2-dimensional Fourier transform to Eq. (A-2) we obtain

$$i\omega\phi\varphi_F + ikv\varphi_F + \lambda(v)|v|\varphi_F - \frac{\overline{v}}{l}\left[\left(\int_{-\infty}^{\infty} \varphi_F \psi_0 dv\right) - \varphi_F\right] = s_F(x,t) \tag{B-1}$$

where the subscript *F* refers to variables in Fourier space.

Equation (B-1) is in the form:

$$L\varphi_F = s_F \tag{B-2}$$

Where the operator *L(y)* is

$$L(y) = i\omega\phi y + ikvy + \lambda(v)|v|y - \frac{\overline{v}}{l}\left[\int_{-\infty}^{\infty} y\psi_0 dv - y\right] \tag{B-3}$$

Projecting Eq. (B-2) into H_a yields

$$P_a L\varphi_F = P_a s_F \tag{B-4}$$

Given that s_F is independent of velocity, it belongs to the H_c subspace and therefore its projection into H_a is zero

$$P_a s_F = 0 \tag{B-5}$$

Therefore the solution φ_F belongs to the kernel of the operator P_aL

$$P_a L\varphi_F = 0 \tag{B-6}$$

Based on the decomposition of the Hilbert space (Eq. (A-7)), we can write the decompose the operator *L* into its components projecting to and from each of the two subspaces:

$$L = \begin{bmatrix} L_{cc} & L_{ca} \\ L_{ac} & L_{aa} \end{bmatrix} \tag{B-7}$$

where the matrix elements are

$$L_{ik} = P_i L J_k \tag{B-8}$$

The operator P_aL can therefore be written as:

$$P_a L = \begin{bmatrix} L_{ac} & L_{aa} \end{bmatrix} : H \to H_a \tag{B-9}$$

In addition to the operator, the function φ_F can be decomposed into the sum of its component in each subspace, which allows us to write Eq. (B-6) as follows:

$$L_{ac} c_F + L_{aa} a_F = 0 \tag{B-10}$$

Thus

$$a_F = -L_{aa}^{-1} L_{ac} c_F \tag{B-11}$$

With Eq. (B-11), we can now return to Eqs. (A-5) and (A-6) with the goal of describing the total flux and capture rates in terms of the averaged concentration.

Beginning with the total flux

$$q_F = \int_{-\infty}^{\infty} v \varphi_F \psi_0 dv \tag{B-12}$$

We begin by making use of the decomposition in Eq. (A-10):

$$q_F = \int_{-\infty}^{\infty} v\left(c_F + a_F\right) \psi_0 dv \tag{B-13}$$

Separating the two integral terms

$$q_F = c_F \int_{-\infty}^{\infty} v \psi_0 dv + \int_{-\infty}^{\infty} v a_F \psi_0 dv \tag{B-14}$$

The first integral term is simply the average particle velocity

$$q_F = c_F \overline{v} + \int_{-\infty}^{\infty} v a_F \psi_0 dv \tag{B-15}$$

We then consider the second term as an inner product

$$q_F = c_F \overline{v} + \left(v, a_F\right) \tag{B-16}$$

Substituting Eq. (B-11)

$$q_F = c_F \overline{v} - \left(v, L_{aa}^{-1} L_{ac} c_F\right) \tag{B-17}$$

The L operators were derived in Dinariev et al., 2020. They are as follows

$$L_{ac}\left(y\right) = iky\left[v - \left(1, v\right)\right] + y\left[\lambda\left(v\right)|v| - \left(1, \lambda\left(v\right)|v|\right)\right] \tag{B-18}$$

$$L_{aa}^{-1}\left(y\right) = y\Lambda^{-1} - \Lambda^{-1}\frac{\left(y, \Lambda^{-1}\right)}{\left(1, \Lambda^{-1}\right)} \tag{B-19}$$

Substituting and rearranging, results in

$$q_F = c_F \overline{v} - ikc_F\left(v, L_{aa}^{-1}\left[v - \left(1, v\right)\right]\right) - c_F\left(v, L_{aa}^{-1}\left[\lambda\left(v\right) - \left(1, \lambda\left(v\right)\right)\right]\right) \tag{B-20}$$

Here we introduce the R_{ij} terms

$$R_{ij} = \left(u_i, \frac{u_j}{\Lambda + i\omega + ikv}\right) - \frac{\left(u_j, \frac{1}{\Lambda + i\omega + ikv}\right)\left(u_i, \frac{1}{\Lambda + i\omega + ikv}\right)}{\left(1, \frac{1}{\Lambda + i\omega + ikv}\right)} \tag{B-21}$$

where

$$u_1 = v,\ u_2 = \lambda(v)|v| \quad \Lambda = \lambda(v)|v| + \frac{\overline{v}}{l} \tag{B-22}$$

$$q_F = c_F \overline{v} - ikR_{11}c_F - R_{12}c_F \tag{B-23}$$

We return now to Eq. (A-6) for the total particle capture rate

$$\varepsilon_F = \int_{-\infty}^{\infty} \lambda(v)|v|\varphi_F \psi_0 dv \tag{B-24}$$

As the derivation is almost identical as to that for the flux, we will present only the final result

$$\varepsilon_F = c_F \overline{\lambda|v|} - ikc_F\left(\lambda(v), L_{aa}^{-1}\left[v - (1, v)\right]\right) - c_F\left(\lambda(v), L_{aa}^{-1}\left[\lambda(v) - (1, \lambda(v))\right]\right) \tag{B-25}$$

$$\varepsilon_F = c_F \overline{\lambda|v|} - ikR_{21}c_F - R_{22}c_F \tag{B-26}$$

What remains is to transform the two Eqs. (B-23) and (B-26) from the Fourier space (ω,k) to the original coordinates (x,t). Doing so results in

$$q = \overline{v}c - K_{11} * \frac{\partial c}{\partial x} - K_{12} * c \tag{B-27}$$

$$\varepsilon = \overline{\lambda|v|}c - K_{21} * \frac{\partial c}{\partial x} - K_{22} * c \tag{B-28}$$

where * refers to convolution in both space and time.

As per the derivation presented in Dinariev et al., 2020, we approximate Equations (B-27,28) by considering the solution only under the conditions of large waves and long times. This is equivalent to

$$\omega, k \to 0 \tag{B-29}$$

Under these conditions, Eq. (B-21) for the $\underline{R_{ij}}$ terms reduces to a constant. Thus the convolution in Eqs. (B-27,28) reduces to multiplication and the flux and total particle capture rate can be expressed as follows

$$q = \overline{v}c - R_{11}\frac{\partial c}{\partial x} - R_{12}c \tag{B-30}$$

$$\varepsilon = \overline{\lambda|v|}c - R_{21}\frac{\partial c}{\partial x} - R_{22}c \tag{B-31}$$

Substitution of Eqs. (B-30,31) into Eq. (5) results in the modified advection-diffusion equation, Eq. (12).

Appendix C. Calculation of transport coefficients Rij

First, we derive the L_{ac} and L_{aa}^{-1} operators presented in Appendix B.

$$L_{ac} = P_a L J_c \tag{C-1}$$

Substituting Equation (B-3) for the L operator:

$$L_{ac} = P_a L J_c = P_a \left[\phi iwc + ikvc + \lambda(v)|v|c - \frac{\overline{v}}{l}\left[\int_{-\infty}^{\infty} c\psi_0 dv - c \right] \right] \tag{C-2}$$

We now perform the projection into H_a. This projection is given explicitly by Eq. (A-12). The process is made simpler by the fact that projecting terms with no velocity dependence results in zero.

$$L_{ac}(y) = iky\left[v - (1, v)\right] + y\left[\lambda(v)|v| - \left(1, \lambda(v)|v|\right)\right] \tag{C-3}$$

Returning to the definition of L_{aa}:

$$L_{aa} = P_a \Lambda J_a \tag{C-4}$$

In this case, we wish to solve the inverse of this relation, such that we wish to solve for p in the following equation

$$P_a \Lambda J_a p = q \tag{C-5}$$

where

$$\Lambda = i\omega + ikv + \lambda(v)|v| + \frac{\overline{v}}{l} \tag{C-6}$$

Given that p already belongs to H_a, and that $J_a(p) = p$, we have

$$P_a \Lambda p = q \tag{C-7}$$

Performing the projection into the H_a space

$$\Lambda p - (\Lambda, p) = q \tag{C-8}$$

Thus

$$p = \frac{(\Lambda, p) + q}{\Lambda} \tag{C-9}$$

Taking the inner product with unity:

$$(1, p) = (\Lambda, p)\left(1, \frac{1}{\Lambda}\right) + \left(q, \frac{1}{\Lambda}\right) \tag{C-10}$$

Given that p belongs in H_a, its inner product with unity is zero

$$0 = (\Lambda, p)\left(1, \frac{1}{\Lambda}\right) + \left(q, \frac{1}{\Lambda}\right) \tag{C-11}$$

Which allows us to write

$$(\Lambda, p) = -\frac{\left(q, \Lambda^{-1}\right)}{\left(1, \Lambda^{-1}\right)} \tag{C-12}$$

Substituting this into Eq. (C-9) results in

$$p = \frac{q}{\Lambda} - \frac{1}{\Lambda}\frac{\left(q, \Lambda^{-1}\right)}{\left(1, \Lambda^{-1}\right)} \tag{C-13}$$

Thus

$$L_{aa}^{-1}\left(y\right) = \frac{y}{\Lambda} - \frac{1}{\Lambda}\frac{\left(y, \Lambda^{-1}\right)}{\left(1, \Lambda^{-1}\right)} \tag{C-14}$$

Finally, we may return to Eqs. (B-20,25) where we introduced the R_{ij} operators

$$R_{ij} = \left(u_i, L_{aa}^{-1}\left[u_j - \left(1, u_j\right)\right]\right) \tag{C-15}$$

Substituting the expression for L_{aa}^{-1}:

$$R_{ij} = \left(u_i, \frac{u_j - \left(1, u_j\right)}{\Lambda} - \frac{1}{\Lambda}\frac{\left(u_j - \left(1, u_j\right), \Lambda^{-1}\right)}{\left(1, \Lambda^{-1}\right)}\right) \tag{C-16}$$

Separating each term

$$R_{ij} = \left(u_i, \frac{u_j}{\Lambda}\right) - \left(1, u_j\right)\left(u_i, \Lambda^{-1}\right) - \frac{\left(u_j, \Lambda^{-1}\right)\left(u_i, \Lambda^{-1}\right)}{\left(1, \Lambda^{-1}\right)} + \left(1, u_j\right)\left(u_i, \Lambda^{-1}\right) \tag{C-17}$$

Finally, we arrive at

$$R_{ij} = \left(u_i, \frac{u_j}{\Lambda}\right) - \frac{\left(u_j, \Lambda^{-1}\right)\left(u_i, \Lambda^{-1}\right)}{\left(1, \Lambda^{-1}\right)} \tag{C-18}$$

References

1. S. A. Bradford, S. Torkzaban, andA. Shapiro, "A theoretical analysis of colloid attachment and straining in chemically heterogeneous porous media," Langmuir : the ACS journal of surfaces and colloids **29**, 6944 (2013).
2. C. V. Chrysikopoulos, N. P. Sotirelis, andN. G. Kallithrakas-Kontos, "Cotransport of graphene oxide nanoparticles and kaolinite colloids in porous media," Transport Porous Med **119**, 181 (2017).
3. W. Johnson, A. Rasmuson, E. Pazmino, andM. Hilpert, "Why variant colloid transport behaviors emerge among identical individuals in porous media when colloid–surface repulsion exists," J Environmental Science and Technology **52**, 7230 (2018).
4. P. Bedrikovetsky, "Upscaling of stochastic micro model for suspension transport in porous media," Transport Porous Med **75**, 335 (2008).
5. M. M. Sharma, andY. C. Yortsos, "Transport of particulate suspensions in porous media: Model formulation," AIChE Journal **33**, 1636 (1987).
6. P. Bedrikovetsky, A. Siqueira, A. de Souza, andF. Shecaira, "Correction of basic equations for deep bed filtration with dispersion," Journal of Petroleum Science Engineering **51**, 68 (2006).
7. P. Charrier, andB. Dubroca, "Asymptotic transport models for heat and mass transfer in reactive porous media," Multiscale Modeling and Simulation **2**, 124 (2003).
8. Y. Efendiev, andL. J. Durlofsky, "A generalized convection-diffusion model for subgrid transport in porous media," Multiscale Modeling and Simulation **1**, 504 (2003).

9. Y. Efendiev, andA. Pankov, "Numerical homogenization of monotone elliptic operators," Multiscale Modeling and Simulation **2**, 62 (2003).
10. Y. Efendiev, andA. Pankov, "Numerical homogenization of nonlinear random parabolic operators," Multiscale Modeling and Simulation **2**, 237 (2004).
11. W. Pan, andA. Tartakovsky, "Dissipative particle dynamics model for colloid transport in porous media," Advances in water resources **58**, 41 (2013).
12. A. M. Tartakovsky, M. Panzeri, G. Tartakovsky, andA. Guadagnini, "Uncertainty quantification in scale-dependent models of flow in porous media," Water Resour Res **53**, 9392 (2017).
13. A. G. Hunt, andM. Sahimi, "Flow, Transport, and Reaction in Porous Media: Percolation Scaling, Critical-Path Analysis, and Effective Medium Approximation," **55**, 993 (2017).
14. P. Bedrikovetsky, Z. You, A. Badalyan, Y. Osipov, andL. Kuzmina, "Analytical model for straining-dominant large-retention depth filtration," Chem Eng J **330**, 1148 (2017).
15. P. Bedrikovetsky, Y. Osipov, L. Kuzmina, andG. Malgaresi, "Exact upscaling for transport of size-distributed colloids," Water Resour Res **55**, 1011 (2019).
16. G. Malgaresi, B. Collins, P. Alvaro, andP. Bedrikovetsky, "Explaining non-monotonic retention profiles during flow of size-distributed colloids," Chem Eng J **375**, 121984 (2019).
17. A. A. Shapiro, andP. G. Bedrikovetsky, "A stochastic theory for deep bed filtration accounting for dispersion and size distributions," Physica A: Statistical Mechanics and its Applications **389**, 2473 (2010).
18. C. Cercignani, *Mathematical methods in kinetic theory* (Springer, 1969).
19. D. Lasseux, F. V. Parada, J. O. Tapia, andB. Goyeau, "A macroscopic model for slightly compressible gas slip-flow in homogeneous porous media," Physics of Fluids **26**, 053102 (2014).
20. D. Lasseux, andF. Valdés-Parada, "Symmetry properties of macroscopic transport coefficients in porous media," Physics of Fluids **29**, 043303 (2017).
21. D. Lasseux, A. A. Abbasian Arani, andA. Ahmadi, "On the stationary macroscopic inertial effects for one phase flow in ordered and disordered porous media," Physics of fluids **23**, 073103 (2011).
22. V. Aristov, A. Frolova, andS. Zabelok, "Nonequilibrium kinetic processes with chemical reactions and complex structures in open systems," EPL (Europhysics Letters) **106**, 20002 (2014).
23. S. Brull, andP. Charrier, "Boundary conditions for the Boltzmann equation for rough walls," **1628**, 368 (2014).
24. P. Barbante, A. Frezzotti, andL. Gibelli, "A kinetic theory description of liquid menisci at the microscale," Journal of Kinetic Related Models **8**, 235 (2015).
25. P. L. Bhatnagar, E. P. Gross, andM. Krook, "A Model for Collision Processes in Gases. I. Small Amplitude Processes in Charged and Neutral One-Component Systems," Physical Review **94**, 511 (1954).
26. C. Cercignani, *The Boltzmann Equation and Its Applications* (Springer-Verlag New York, 1988).
27. O. Dinariev, A. Rego, andP. Bedrikovetsky, "Boltzmann Physical Kinetic for Deep Bed Filtration: Homogenization by solving operator equation in Hilbert space," arXiv preprint arXiv:2001.08069 (2020).
28. S. Tsushima, I. Nakamura, S. Sakashita, S. Hirai, andD. Kitayama, *Lattice Boltzmann Simulation on Particle Transport and Captured Behaviors in a 3D-Reconstructed Micro Porous DPF* (SAE International, 2010).
29. M. Vasheghani Farahani, S. Foroughi, S. Norouzi, andS. Jamshidi, "Mechanistic Study of Fines Migration in Porous Media Using Lattice Boltzmann Method Coupled With Rigid Body Physics Engine," Journal of Energy Resources Technology **141**, (2019).
30. Q. Li, andV. Prigiobbe, "Numerical Simulations of the Migration of Fine Particles Through Porous Media," Transport Porous Med **122**, 745 (2018).
31. A. Shapiro, andJ. Wesselingh, "Gas transport in tight porous media: Gas kinetic approach," Chem Eng J **142**, 14 (2008).
32. J. Herzig, D. Leclerc, andP. L. Goff, "Flow of suspensions through porous media—application to deep filtration," Industrial & Engineering Chemistry **62**, 8 (1970).
33. M. Elimelech, J. Gregory, andX. Jia, *Particle deposition and aggregation: measurement, modelling and simulation* (Butterworth-Heinemann, 2013).

34. H. Zhang, G. V. C. Malgaresi, andP. Bedrikovetsky, "Exact solutions for suspension-colloidal transport with multiple capture mechanisms," International Journal of Non-Linear Mechanics **105**, 27 (2018).
35. X. Li, Y. Liu, H. Sheng, andR. Feng, "Model for the flow of emulsion in porous media with micro-heterogeneities," Lixue Xuebao/Chinese Journal of Theoretical and Applied Mechanics **41**, 313 (2009).
36. L. Quansheng, C. Xianze, andZ. Chengyuan, "Research advances in the characterization of transportation and deposition of suspended particles in porous media," Chinese Journal of Rock Mechanics and Engineering **34**, 2410 (2015).
37. J. Xu, "Propagation behavior of permeability reduction in heterogeneous porous media due to particulate transport," EPL (Europhysics Letters) **114**, 14001 (2016).
38. X. Chen, B. Bai, andQ. Cai, "Theoretical solution of particle release-transport in saturated porous media," SCIENTIA SINICA Technologica **44**, 610 (2014).
39. V. Aristov, I. Voronich, andS. Zabelok, "Direct methods for solving the Boltzmann equations: Comparisons with direct simulation Monte Carlo and possibilities," Physics of Fluids **31**, 097106 (2019).
40. A. Frezzotti, P. Barbante, andL. Gibelli, "Direct simulation Monte Carlo applications to liquid-vapor flows," Physics of Fluids **31**, 062103 (2019).
41. Y. Efendiev, T. Hou, L. Durlofsky, andH. Tchelepi, Multiscale analysis and computation for flows in heterogeneous media Document No. Number, 2016.
42. S. Brull, P. Charrier, andL. Mieussens, "Gas-surface interaction and boundary conditions for the Boltzmann equation," arXiv preprint (2013).
43. S. Brull, P. Charrier, andL. Mieussens, "Nanoscale roughness effect on Maxwell-like boundary conditions for the Boltzmann equation," Physics of Fluids **28**, 082004 (2016).
44. L. Gibelli, "Velocity slip coefficients based on the hard-sphere Boltzmann equation," Physics of Fluids **24**, 022001 (2012).
45. K. H. Jensen, A. X. C. N. Valente, andH. A. Stone, "Flow rate through microfilters: Influence of the pore size distribution, hydrodynamic interactions, wall slip, and inertia," Physics of Fluids **26**, 052004 (2014).
46. A. Sauret, E. C. Barney, A. Perro, E. Villermaux, H. A. Stone, andE. Dressaire, "Clogging by sieving in microchannels: Application to the detection of contaminants in colloidal suspensions," Applied Physics Letters **105**, 074101 (2014).
47. H. A. Stone, A. D. Stroock, andA. Ajdari, "Engineering Flows in Small Devices: Microfluidics Toward a Lab-on-a-Chip," Annu. Rev. Fluid Mech. **36**, 381 (2004).
48. V. Hemadri, V. V. Varade, A. Agrawal, andU. Bhandarkar, "Rarefied gas flow in converging microchannel in slip and early transition regimes," Physics of Fluids **29**, 032002 (2017).
49. V. Varade, A. Agrawal, andA. Pradeep, "Slip flow through a converging microchannel: experiments and 3D simulations," Journal of Micromechanics Microengineering **25**, 025015 (2015).
50. A. Agrawal, L. Djenidi, andR. Antonia, "Simulation of gas flow in microchannels with a sudden expansion or contraction," Journal of Fluid Mechanics **530**, 135 (2005).
51. P. Bedrikovetsky, F. D. Siqueira, C. A. Furtado, andA. L. S. Souza, "Modified Particle Detachment Model for Colloidal Transport in Porous Media," Transport Porous Med **86**, 383 (2011).
52. C. Tien, andA. C. Payatakes, "Advances in deep bed filtration," AIChE Journal **25**, 737 (1979).
53. C. Tien, andB. V. Ramarao, *Granular Filtration of Aerosols and Hydrosols, 2nd Edition* (Elsevier, 2007).
54. N. Tufenkji, andM. Elimelech, "Correlation equation for predicting single-collector efficiency in physicochemical filtration in saturated porous media," Environmental science & technology **38**, 529 (2004).
55. J. S. Andrade, A. D. Araújo, T. F. Vasconcelos, andH. J. Herrmann, "Inertial capture in flow through porous media," The European Physical Journal B **64**, 433 (2008).
56. B. Bai, J. Wang, Z. Zhai, andT. Xu, "The Penetration Processes of Red Mud Filtrate in a Porous Medium by Seepage," Transport in Porous Media **117**, 207 (2017).
57. S. Kia, H. S. Fogler, andM. Reed, "Effect of pH on colloidally induced fines migration," J. Colloid Interface Sci. **118**, 158 (1986).

58. N. Mungan, "Permeability reduction through changes in pH and salinity," Journal of Petroleum Technology **17**, 1 (1965).

5.3 Colloidal transport in anisotropic porous media: kinetic equation and its upscaling

Russell, T., Bedrikovetsky, P.

Physics of Fluid, Submitted for publication

Statement of Authorship

Title of Paper	Colloidal transport in anisotropic porous media: kinetic equation and its upscaling
Publication Status	☐ Published ☐ Accepted for Publication ☑ Submitted for Publication ☐ Unpublished and Unsubmitted w ork w ritten in manuscript style
Publication Details	Russell, T., Bedrikovetsky, P., Colloidal transport in anisotropic porous media: kinetic equation and its upscaling, Submitted

Principal Author

Name of Principal Author (Candidate)	Thomas Russell		
Contribution to the Paper	Performed calculations, performed derivations, contributed to writing		
Overall percentage (%)	90%		
Certification:	This paper reports on original research I conducted during the period of my Higher Degree by Research candidature and is not subject to any obligations or contractual agreements with a third party that would constrain its inclusion in this thesis. I am the primary author of this paper.		
Signature		Date	25/02/2021

Co-Author Contributions

By signing the Statement of Authorship, each author certifies that:

i. the candidate's stated contribution to the publication is accurate (as detailed above);

ii. permission is granted for the candidate in include the publication in the thesis; and

iii. the sum of all co-author contributions is equal to 100% less the candidate's stated contribution.

Name of Co-Author	Pavel Bedrikovetsky		
Contribution to the Paper	Technical discussions, contributed to writing		
Signature		Date	25/02/2021

Please cut and paste additional co-author panels here as required.

Colloidal transport in anisotropic porous media: kinetic equation and its upscaling

Thomas Russell, Pavel Bedrikovetsky[a)]

Australian School of Petroleum and Energy Resources, The University of Adelaide, Adelaide, SA, 5005, Australia

a) Author to whom correspondence should be addressed: pavel.bedrikovetski@adelaide.edu.au

Key words: anisotropic porous media; Boltzmann's equation; stochastic modelling; colloid; averaging; upscaling

Abstract We discuss three-dimensional suspension-colloidal-nano transport in anisotropic porous media. The Boltzmann kinetic equation captures stochastic particle velocity distribution on the micro-scale due to the stochastic nature of the pore-space geometry. The anisotropy is expressed by tensorial micro-scale transport coefficients and a direction-dependent velocity distribution. We formulate a BGK-form of Boltzmann's equation for particle transport with a particle capture rate which is proportional to the particle velocity. The exact probabilistic averaging is performed by solution of a functional equation in Fourier space. The homogenised macro-scale model has the form of a 3-D advective-diffusive-reactive equation, where the particle flow in all directions is slower than the carrier fluid speed. This delay is the collective result of particle flow and capture and is explained by preferential capture of faster particles. For the particular case of quasi-one-dimension flow, where the total of the transverse flux is zero, we derive the effective equation and investigate the continuous and pulse colloidal injection.

Nomenclature

ϕ	Porosity, [-]	L	Fourier Boltzmann operator
f	Particle concentration, [-]	a	Particle concentration deviation from average, [-]
t	Time, [T]	P_c	Projection operator from H to H_c
x	First spatial coordinate, [L]	P_a	Projection operator from H to H_a
y	Second spatial coordinate, [L]	J_c	Embedding operator from H_c to H
z	Third spatial coordinate, [L]	J_a	Embedding operator from H_a to H
v	Velocity, [LT^{-1}]	R_{ij}	
λ	Filtration coefficient, [L^{-1}]	$\overline{v}$	Average velocity, [LT^{-1}]
τ	Relaxation time, [T]	$\overline{\lvert v \rvert}$	Average of absolute velocity, [LT^{-1}]
ψ_0	Equilibrium velocity distribution, [$L^{-3}T^3$]	θ	Velocity delay factor, [-]
c	Averaged particle concentration, [-]	D	Diffusion matrix, [-]
q	Total particle flux, [$L.T^{-1}$]	Ω	Macroscale filtration coefficient, [-]
ε	Total particle capture rate, [T^{-1}]	T	Dimensionless time, [-]
s	Initial and boundary conditions, [-]	L_c	Core length, [L]
φ	Modified particle concentration, [-]	X	Dimensionless position, [-]
ω	Fourier variable corresponding to t	Pe	Peclet number, [-]
k	Fourier variable corresponding to x	C_v	Covariance matrix, [L^2T^{-2}]
p	Fourier variable corresponding to y	σ	Covariance, [LT^{-1}]
h	Fourier variable corresponding to z	ρ	Correlation. [-]
i	Imaginary unit		

Subscripts

x	Pertaining to first spatial coordinate
y	Pertaining to second spatial coordinate
z	Pertaining to third spatial coordinate
F	In Fourier space

I. Introduction

Suspension-colloidal-nano flows in porous media are commonplace during a number of natural and industrial processes. Interactions between the suspended particles and the porous matrix can result in significant changes to the rock properties. Knowledge of the dynamics for suspended concentration and permeability decline is critical for informed decision-making in several environmental, chemical, and energy-generation technologies. Performing predictive analysis and understanding the laboratory and field data requires an accurate mathematical model of fines transport and capture by the rock.

Pore and particle sizes and shapes, surface charges of particles and rocks, micro-heterogeneity of mineral rock composition, irregularity of pore space geometry, among other properties vary over several orders of magnitude and are randomly distributed at the micro scale[1]. These effects are captured by stochastic mathematical models with randomly distributed rock and fluid properties. The stochastic micro-scale models include population-balance models[2-5], transport equations with fast-oscillating coefficients[6-9], coupled flow and capture equations with random coefficients[8, 10-12], random-walk equations[13], and Boltzmann's kinetic equations[14-17]. Exact upscaling (homogenisation) of population balance models is performed for the cases of distributed pore sizes[2] and particle sizes[5, 18]. Probabilistic averaging of a random walk model with the length- and time- jump distribution yields the elliptic advective-diffusion-capture equation[13, 19].

Derivations of governing equations for colloidal flow in porous media revolve around modelling particle transport and capture[20-22]. Previous modelling efforts and experimental studies have indicated a velocity dependence, often linear, of the particle capture on velocity[23]. This intrinsic connection between capture and transport is reflected a kinetic formulation for particle transport and capture using Boltzmann's equation[15, 24] arising from the pore size distribution[25]. Justification for the appropriateness and relevance of Boltzmann's equation for flow in porous media follows from the wide variation in pore-scale velocities[26-29]. Averaging of this equation for one-dimensional (1-D) flows leads to an advective-diffusion equation with linear reaction and a delayed advective velocity. This modelling approach leads to explicit expressions for three key phenomena: the reduction of the mean particle velocity due to preferential capture of faster particles, a reduction in the diffusion coefficient due to capture, and a non-linear relationship between micro- and macro-scale filtration coefficients. These phenomena were discovered as a result of the explicit coupling of transport and capture. What remains unclear is the result of this coupling when both transport and capture occur in multiple directions.

Besides, rock anisotropy is a natural wide-spread feature of geological formations. Direction-dependent sedimentation, deformation, and micro-fracturing yield tensorial rock properties of permeability, diffusivity, and filtration coefficient. However, the governing equation for suspension-colloidal-nano transport in anisotropic porous media is unavailable.

The present paper fills the gap. We formulate Boltzmann's kinetic equation for three-dimensional (3-D) transport with an arbitrary 3-D equilibrium particle velocity distribution. Exact probabilistic averaging yields a 3-D advective-diffusive-reaction equation at the upper scale. The upscaled transport coefficients are functions of the micro-scale parameters and the equilibrium distribution of particle velocity distributions in different directions. The analytical models are developed by quasi 1-D flow where the total flux in the transverse directions is equal to zero. The dependencies of the macro-scale transport coefficients on the micro-scale parameters are investigated and explained.

The structure of the paper is as follows. Section II formulates the main assumptions of 3-D Boltzmann's equation with anisotropic flow and particle capture and performs probabilistic averaging by solving an operator equation in Fourier space. Section III formulates quasi 1-D flow problem with zero averaged transversal flux and investigates the dependency of the macro-scale transport coefficients on the micro-scale parameters. Conclusive remarks close the paper.

II. Kinetic formulation of anisotropic colloidal flow in porous media

We consider the flow of a colloidal suspension within a multiply connected manifold, namely an irregular pore network with a distribution of pore sizes and directions. The distribution of fluid flow within the pore network is determined by the equations of viscous incompressible flow. These equations determine a set of smooth, static streamlines along which the suspended particles move through the porous medium. The assumption of static streamlines ignores the potential impact of captured particles. We make this assumption based on the small fraction of captured particles relative to the total pore volume. Fig. 1 shows a schematic representation of the porous media, with particle flow and capture in multiple directions.

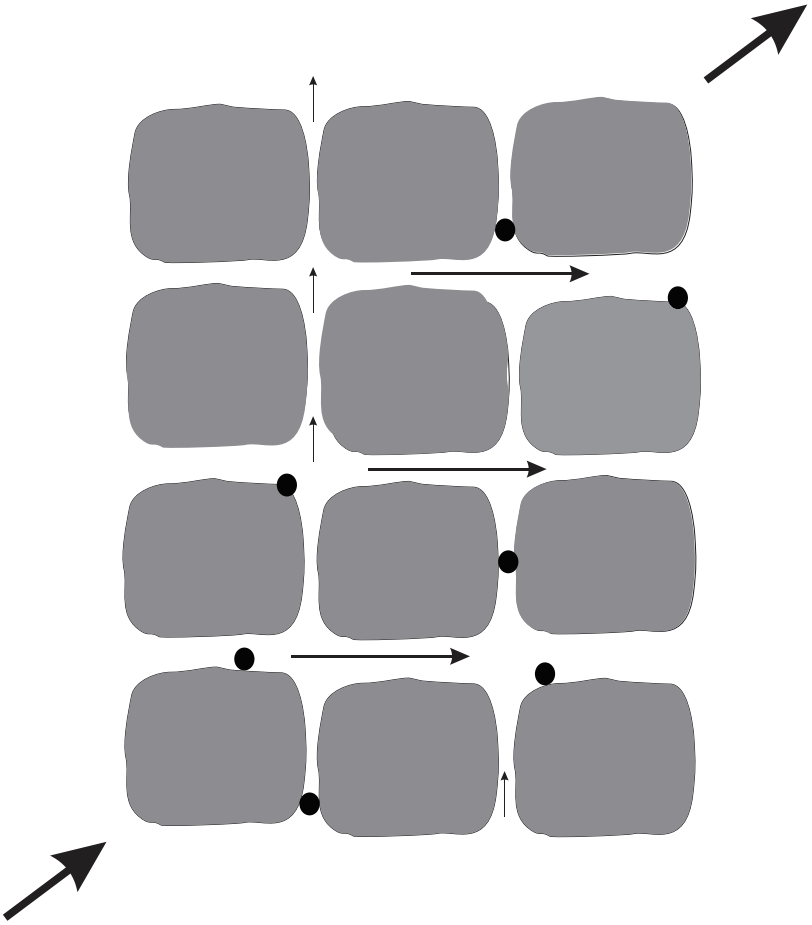

FIG 1. Schematic representation of porous media with particle transport and capture along fluid streamlines

Particle sizes are negligibly small compared to the pore size, such that particles and travel along each streamline and are not excluded from any portion of the porous space. The concentration of particles is sufficiently small that they do not influence the position of the fluid streamlines or the suspension density. The small particle concentration also means that the captured particle concentration is small enough for the filtration coefficient to be constant. Following the mechanical equilibrium of attached particles, under set conditions, attachment and detachment cannot co-occur. Thus we neglect particle detachment. The particle capture rate in each direction is proportional to the particle velocity in that direction[30, 31].

The distribution of flux within the pore network determines the equilibrium particle velocity distribution, ψ_0. When the instantaneous particle velocity distribution differs from the equilibrium it will tend asymptotically towards the equilibrium. This relaxation occurs with characteristic time τ and results from mixing within the multiply connected pore space due to dispersion.

The reference volume is sufficiently large that we can introduce the porosity, the ratio of pore volume to bulk volume, as an averaged rock property. This reference volume comprises multiple pores.

Boltzmann's kinetic equation formulated in three dimensions with a modified BGK relaxation term[32] can be written as follows[33, 34]

$$\phi\frac{\partial f}{\partial t}+v_x\frac{\partial f}{\partial x}+v_y\frac{\partial f}{\partial y}+v_z\frac{\partial f}{\partial z}=-\lambda_x|v_x|f-\lambda_y|v_y|f-\lambda_z|v_z|f+\frac{1}{\tau}\left(\int_{-\infty}^{\infty}\int_{-\infty}^{\infty}\int_{-\infty}^{\infty}f dv_x dv_y dv_z\psi_0-f\right) \quad (1)$$

where ϕ is the rock porosity, t is time, x, y, and z are the three spatial dimensions, $f(x,t,v)$ is the particle concentration, v is the particle velocity, and λ is the filtration coefficient. The relaxation time, τ represents the average time required for particles to relax towards the equilibrium velocity distribution, $\psi_0(v_x,v_y,v_z)$. This formulation, and the averaging procedure that follows allow for τ to be any arbitrary function of each velocity (v_x,v_y,v_z) given that it is positive and finite.

The equilibrium velocity distribution has the following property

$$\int_{-\infty}^{\infty}\int_{-\infty}^{\infty}\int_{-\infty}^{\infty}\psi_0 dv_x dv_y dv_z=1 \quad (2)$$

This quantity describes the distribution of particles by velocity in the 'equilibrium' state, achieved by collisions between the particles and the rock matrix.

Integrating Eq. (1) over velocity results in

$$\phi\frac{\partial c}{\partial t}+\frac{\partial q_x}{\partial x}+\frac{\partial q_y}{\partial y}+\frac{\partial q_z}{\partial z}=-\varepsilon_x-\varepsilon_y-\varepsilon_z \quad (3)$$

where

$$c=\int_{-\infty}^{\infty}\int_{-\infty}^{\infty}\int_{-\infty}^{\infty}f\,dv_x dv_y dv_z \quad (4)$$

is the averaged particle concentration, and

$$q_i=\int_{-\infty}^{\infty}\int_{-\infty}^{\infty}\int_{-\infty}^{\infty}v_i f\,dv_x dv_y dv_z \quad (5)$$

$$\varepsilon_i=\lambda_i\int_{-\infty}^{\infty}\int_{-\infty}^{\infty}\int_{-\infty}^{\infty}|v_i|f\,dv_x dv_y dv_z \quad (6)$$

are the flux and capture terms in each direction.

Equation (3) is the averaged equation, with 7 unknown variables. The goal of averaging is to derive relationships between the flux and capture terms and the suspended concentration, c and its derivatives.

Averaging

Central to the averaging procedure presented by Dinariev, Rego and Bedrikovetsky[15] is the sink-source method. Rather than posing initial and boundary conditions (IBC) alongside Eq. (1) as would be done normally[29, 35, 36], we pose these conditions by adding to Eq. (1) a term that encapsulates all particles that would be introduced to the system through the IBC. Using this method, any effects of the IBC on the averaging will be quantified explicitly. We do not make any assumptions about the form of the IBC, only that particles introduced through them have the equilibrium velocity distribution. Thus, Eq. (1) becomes

$$\phi\frac{\partial f}{\partial t}+v_x\frac{\partial f}{\partial x}+v_y\frac{\partial f}{\partial y}+v_z\frac{\partial f}{\partial z}=-\lambda_x|v_x|f-\lambda_y|v_y|f-\lambda_z|v_z|f+\frac{1}{\tau}\left(\int_{-\infty}^{\infty}\int_{-\infty}^{\infty}\int_{-\infty}^{\infty}f\,dv_x dv_y dv_z\psi_0-f\right)+s(x,y,z,t)\psi_0$$

(7)

Making the substitution

$$f\left(x,y,z,t,v_x,v_y,v_z\right)=\varphi\left(x,y,z,t,v_x,v_y,v_z\right)\psi_0\left(v_x,v_y,v_z\right) \tag{8}$$

and dividing by ψ_0 :

$$\phi\frac{\partial \varphi}{\partial t}+v_x\frac{\partial \varphi}{\partial x}+v_y\frac{\partial \varphi}{\partial y}+v_z\frac{\partial \varphi}{\partial z}=-\lambda_x|v_x|\varphi-\lambda_y|v_y|\varphi-\lambda_z|v_z|\varphi+\frac{1}{\tau}\left(\int_{-\infty}^{\infty}\int_{-\infty}^{\infty}\int_{-\infty}^{\infty}\varphi\psi_0 dv_x dv_y dv_z-\varphi\right)+s(x,y,z,t)$$

(9)

Next we perform the four-dimensional Fourier transform, $(x,y,z,t)\rightarrow(k,p,h,w)$ resulting in

$$\phi i\omega\varphi_F+v_x ik\varphi_F+v_y ip\varphi_F+v_z ih\varphi_F=-\lambda_x|v_x|\varphi_F-\lambda_y|v_y|\varphi_F-\lambda_z|v_z|\varphi_F+\frac{1}{\tau}\left(\int_{-\infty}^{\infty}\int_{-\infty}^{\infty}\int_{-\infty}^{\infty}\varphi_F\psi_0 dv_x dv_y dv_z-\varphi_F\right)+s_F$$

(10)

This equation can be written as

$$L\varphi_F=s_F \tag{11}$$

where the operator *L* is

$$L(\varphi)=\phi i\omega\varphi+v_x ik\varphi+v_y ip\varphi+v_z ih\varphi+\lambda_x|v_x|\varphi+\lambda_y|v_y|\varphi+\lambda_z|v_z|\varphi-\frac{1}{\tau}\left(\int_{-\infty}^{\infty}\int_{-\infty}^{\infty}\int_{-\infty}^{\infty}\varphi\psi_0 dv_x dv_y dv_z-\varphi\right)$$

(12)

Next we propose that the set of all solutions, φ, is a Hilbert space with an inner product defined as

$$(\varphi_1,\varphi_2)=\int_{-\infty}^{\infty}\int_{-\infty}^{\infty}\int_{-\infty}^{\infty}\varphi_1\varphi_2\psi_0\,dv_x dv_y dv_z \tag{13}$$

This allows us to decompose the set of solutions

$$\varphi_F=a_F+c_F \tag{14}$$

where a_F describes the deviation of the solution φ_F around its mean c_F defined by the inner product. This decomposition is central to the derivation and is illustrated in Fig. 2 below.

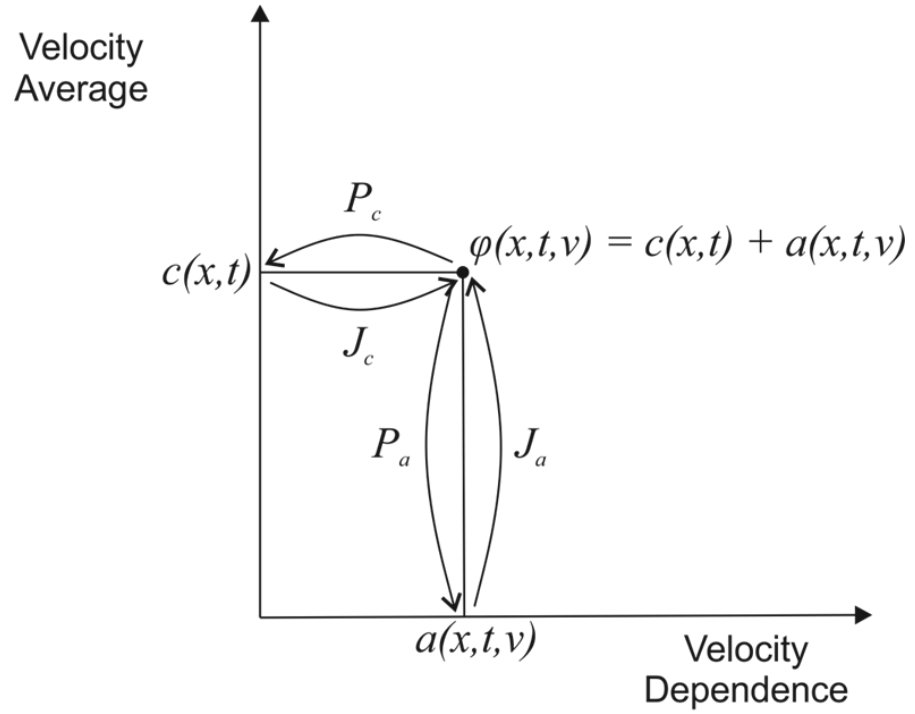

FIG 2. Schematic illustration of decomposition of solution $\varphi(x,t,v)$ of the Boltzmann equation into its velocity average, $c(x,t)$, and fluctuations around the average, $a(x,t,v)$. The P and J terms refer to projection and embedding operators into and out of the respective subspaces of the decomposition

Next we project Eq. (11) into the space of deviations (containing a_F)

$$P_a L\varphi_F = P_a s_F \tag{15}$$

The term s_F is independent of velocity, and thus lies within the kernel of this projection operator, so

$$P_a L\varphi_F = 0 \tag{16}$$

Following the decomposition in Eq. (14), we can decompose the L operator

$$L_{ac}c_F + L_{aa}a_F = 0 \tag{17}$$

rearranging

$$a_F = -L_{aa}^{-1}L_{ac}c_F \tag{18}$$

Expressions for L_{aa}^{-1} and L_{ac} are derived in Appendix A.

Thus for any solution, φ_F, we have derived an expression relating the velocity average, c_F, and the fluctuations around this average, a_F. Using this relationship, Eqs. (5,6) for the flux and capture rate terms can be written in terms of the suspended concentration, c. The derivation of these terms is presented in Appendix B.

The resulting expressions are

$$q_x = c\left(\overline{v_x} - \lambda_x R_{12}^{xx} - \lambda_y R_{12}^{xy} - \lambda_z R_{12}^{xz}\right) - R_{11}^{xx}\frac{\partial c}{\partial x} - R_{11}^{xy}\frac{\partial c}{\partial y} - R_{11}^{xz}\frac{\partial c}{\partial z} \tag{19}$$

$$q_y = c\left(\overline{v_y} - \lambda_x R_{12}^{yx} - \lambda_y R_{12}^{yy} - \lambda_z R_{12}^{yz}\right) - R_{11}^{yx}\frac{\partial c}{\partial x} - R_{11}^{yy}\frac{\partial c}{\partial y} - R_{11}^{yz}\frac{\partial c}{\partial z} \tag{20}$$

$$q_z = c\left(\overline{v_z} - \lambda_x R_{12}^{zx} - \lambda_y R_{12}^{zy} - \lambda_z R_{12}^{zz}\right) - R_{11}^{zx}\frac{\partial c}{\partial x} - R_{11}^{zy}\frac{\partial c}{\partial y} - R_{11}^{zz}\frac{\partial c}{\partial z} \tag{21}$$

$$\varepsilon_x = c\left(\lambda_x\overline{|v_x|} - \lambda_x^2 R_{22}^{xx} - \lambda_x\lambda_y R_{22}^{xy} - \lambda_x\lambda_z R_{22}^{xz}\right) - \lambda_x R_{21}^{xx}\frac{\partial c}{\partial x} - \lambda_x R_{21}^{xy}\frac{\partial c}{\partial y} - \lambda_x R_{21}^{xz}\frac{\partial c}{\partial z} \tag{22}$$

$$\varepsilon_y = c\left(\lambda_y\overline{|v_y|} - \lambda_y\lambda_x R_{22}^{yx} - \lambda_y^2 R_{22}^{yy} - \lambda_y\lambda_z R_{22}^{yz}\right) - \lambda_y R_{21}^{yx}\frac{\partial c}{\partial x} - \lambda_y R_{21}^{yy}\frac{\partial c}{\partial y} - \lambda_y R_{21}^{yz}\frac{\partial c}{\partial z} \tag{23}$$

$$\varepsilon_z = c\left(\lambda_z\overline{|v_z|} - \lambda_z\lambda_x R_{22}^{zx} - \lambda_z\lambda_y R_{22}^{zy} - \lambda_z^2 R_{22}^{zz}\right) - \lambda_z R_{21}^{zx}\frac{\partial c}{\partial x} - \lambda_z R_{21}^{zy}\frac{\partial c}{\partial y} - \lambda_z R_{21}^{zz}\frac{\partial c}{\partial z} \tag{24}$$

Substituting these expressions into Eq. (3) and making use of the fact that $R_{ij}^{qq} = R_{ji}^{qq}$

$$\begin{aligned}
&\phi\frac{\partial c}{\partial t} + \left(\overline{v_x} - 2\lambda_x R_{12}^{xx} - \lambda_y\left(R_{12}^{xy} + R_{21}^{yx}\right) - \lambda_z\left(R_{12}^{xz} + R_{21}^{zx}\right)\right)\frac{\partial c}{\partial x} \\
&+ \left(\overline{v_y} - \lambda_x\left(R_{12}^{yx} + R_{21}^{xy}\right) - 2\lambda_y R_{12}^{yy} - \lambda_z\left(R_{12}^{yz} + R_{21}^{zy}\right)\right)\frac{\partial c}{\partial y} \\
&+ \left(\overline{v_z} - \lambda_x\left(R_{12}^{zx} + R_{21}^{xz}\right) - \lambda_y\left(R_{12}^{zy} + R_{21}^{yz}\right) - 2\lambda_z R_{12}^{zz}\right)\frac{\partial c}{\partial z} \\
&- R_{11}^{xx}\frac{\partial^2 c}{\partial x^2} - R_{11}^{xy}\frac{\partial^2 c}{\partial x\partial y} - R_{11}^{xz}\frac{\partial^2 c}{\partial x\partial z} - R_{11}^{yx}\frac{\partial^2 c}{\partial y\partial x} - R_{11}^{yy}\frac{\partial^2 c}{\partial y^2} - R_{11}^{yz}\frac{\partial^2 c}{\partial y\partial z} - R_{11}^{zx}\frac{\partial^2 c}{\partial z\partial x} - R_{11}^{zy}\frac{\partial^2 c}{\partial z\partial y} - R_{11}^{zz}\frac{\partial^2 c}{\partial z^2} \\
&= -\left(\lambda_x\overline{|v_x|} + \lambda_y\overline{|v_y|} + \lambda_z\overline{|v_z|} - \lambda_x^2 R_{22}^{xx} - \lambda_y^2 R_{22}^{yy} - \lambda_z^2 R_{22}^{zz} - \lambda_x\lambda_y\left(R_{22}^{xy} + R_{22}^{yx}\right) - \lambda_x\lambda_z\left(R_{22}^{xz} + R_{22}^{zx}\right) - \lambda_y\lambda_z\left(R_{22}^{yz} + R_{22}^{zy}\right)\right)c
\end{aligned} \tag{25}$$

Assuming the continuity of all second derivatives of *c*, then by Schwarz's theorem, the second derivatives are symmetric, resulting in the final expression

$$\phi\frac{\partial c}{\partial t} + \overline{v_x}\left(1-\theta_x\right)\frac{\partial c}{\partial x} + \overline{v_y}\left(1-\theta_y\right)\frac{\partial c}{\partial y} + \overline{v_z}\left(1-\theta_z\right)\frac{\partial c}{\partial z} - \nabla\cdot\left(D\nabla c\right) = -\Omega c \tag{26}$$

where we have exact expressions for the velocity delay factors,

$$\theta_x = \frac{2\lambda_x R_{12}^{xx} - 2\lambda_y R_{12}^{xy} - 2\lambda_z R_{12}^{xz}}{\overline{v_x}} \tag{27}$$

$$\theta_y = \frac{2\lambda_x R_{12}^{yx} - 2\lambda_y R_{12}^{yy} - 2\lambda_z R_{12}^{yz}}{\overline{v_y}} \tag{28}$$

$$\theta_z = \frac{2\lambda_x R_{12}^{zx} - 2\lambda_y R_{12}^{zy} - 2\lambda_z R_{12}^{zz}}{\overline{v_z}} \tag{29}$$

the symmetric diffusion matrix,

$$D = \begin{bmatrix} R_{11}^{xx} & R_{11}^{yx} & R_{11}^{zx} \\ R_{11}^{xy} & R_{11}^{yy} & R_{11}^{zy} \\ R_{11}^{xz} & R_{11}^{yz} & R_{11}^{zz} \end{bmatrix} \tag{30}$$

and the macroscale filtration coefficient,

$$\Omega = \vec{\lambda} \cdot \overrightarrow{|v|} - \vec{\lambda} \cdot R_{22} \cdot \vec{\lambda} \tag{31}$$

where

$$\vec{\lambda} = \begin{bmatrix} \lambda_x & \lambda_y & \lambda_z \end{bmatrix} \tag{32}$$

$$\overrightarrow{|v|} = \begin{bmatrix} \overline{|v_x|} & \overline{|v_y|} & \overline{|v_z|} \end{bmatrix} \tag{33}$$

$$R_{22} = \begin{bmatrix} R_{22}^{xx} & R_{22}^{yx} & R_{22}^{zx} \\ R_{22}^{xy} & R_{22}^{yy} & R_{22}^{zy} \\ R_{22}^{xz} & R_{22}^{yz} & R_{22}^{zz} \end{bmatrix} \tag{34}$$

The constant coefficients are given by the following equation:

$$R_{ij}^{kl} = \left(v_i^k v_j^l, \Lambda^{-1}\right) - \frac{\left(v_i^k, \Lambda^{-1}\right)\left(v_j^l, \Lambda^{-1}\right)}{\left(1, \Lambda^{-1}\right)} \tag{35}$$

which in integral form is

$$R_{ij}^{kl} = \int_{-\infty}^{\infty}\int_{-\infty}^{\infty}\int_{-\infty}^{\infty} \frac{v_i^k v_k^l}{\lambda_x |v_x| + \lambda_y |v_y| + \lambda_z |v_z| + \frac{1}{\tau}} \psi_0 dv_x dv_y dv_z - \frac{\int_{-\infty}^{\infty}\int_{-\infty}^{\infty}\int_{-\infty}^{\infty} \frac{v_i^k}{\lambda_x |v_x| + \lambda_y |v_y| + \lambda_z |v_z| + \frac{1}{\tau}} \psi_0 dv_x dv_y dv_z \int_{-\infty}^{\infty}\int_{-\infty}^{\infty}\int_{-\infty}^{\infty} \frac{v_k^l}{\lambda_x |v_x| + \lambda_y |v_y| + \lambda_z |v_z| + \frac{1}{\tau}} \psi_0 dv_x dv_y dv_z}{\int_{-\infty}^{\infty}\int_{-\infty}^{\infty}\int_{-\infty}^{\infty} \frac{1}{\lambda_x |v_x| + \lambda_y |v_y| + \lambda_z |v_z| + \frac{1}{\tau}} \psi_0 dv_x dv_y dv_z} \tag{36}$$

where $v_1 = v$, and $v_2 = |v|$.

Note that both the diffusion matrix and the R_{22} matrix are symmetric.

We note here two important simplified cases. First, if all λ terms are small, then all terms of $O(\lambda^2)$ can be neglected. This results in the macroscopic filtration coefficient, Ω, being equal to the scalar product of the λ vector and the vector of absolute mean velocities. Secondly, if all particles move with approximately the same velocity, i.e. $\psi_0 = \delta(v_x - v_1, v_y - v_2, v_z - v_3)$ then the R_{ij} terms vanish, resulting again in a macroscopic filtration coefficient equal to the scalar product of the λ vector and the vector (v_1, v_2, v_3).

III. Impact of cross-flow in one-dimensional case

In this section we consider one-dimensional flow and compare the results of this study with the one-dimensional equations derived in the previous work[15], which doesn't account for flow in directions perpendicular to flow.

Suppose that the particle concentration is uniform in each cross-section perpendicular to the x-direction, such that

$$\frac{\partial c}{\partial y} = \frac{\partial c}{\partial z} = 0 \tag{37}$$

This highly simplifies Eq. (25), resulting in

$$\begin{aligned} &\phi \frac{\partial c}{\partial t} + \left(\overline{v_x} - 2\lambda_x R_{12}^{xx} - 2\lambda_y R_{12}^{xy} - 2\lambda_z R_{12}^{xz} \right) \frac{\partial c}{\partial x} - R_{11}^{xx} \frac{\partial^2 c}{\partial x^2} \\ &= -\left(\lambda_x \overline{|v_x|} + \lambda_y \overline{|v_y|} + \lambda_z \overline{|v_z|} - \lambda_x^2 R_{22}^{xx} - \lambda_y^2 R_{22}^{yy} - \lambda_z^2 R_{22}^{zz} - 2\lambda_x \lambda_y R_{22}^{xy} - 2\lambda_x \lambda_z R_{22}^{xz} - 2\lambda_y \lambda_z R_{22}^{yz} \right) c \end{aligned} \tag{38}$$

Note that we have simplifications following from the fact that $R_{12}^{kl} = R_{21}^{lk}$ and $R_{22}^{ij} = R_{22}^{ji}$.

Introduce dimensionless variables:

$$T = \frac{t\overline{v_x}}{\phi L_c}, X = \frac{x}{L_c} \tag{39}$$

$$\begin{aligned} &\frac{\partial c}{\partial T} + \left(1 - \frac{2\lambda_x R_{12}^{xx} - \lambda_y \left(R_{12}^{xy} + R_{21}^{yx} \right) - \lambda_z \left(R_{12}^{xz} + R_{21}^{zx} \right)}{\overline{v_x}} \right) \frac{\partial c}{\partial X} - \frac{R_{11}^{xx}}{\overline{v_x} L_c} \frac{\partial^2 c}{\partial X^2} \\ &= -\frac{L_c}{\overline{v_x}} \left(\lambda_x \overline{|v_x|} + \lambda_y \overline{|v_y|} + \lambda_z \overline{|v_z|} - \lambda_x^2 R_{22}^{xx} - \lambda_y^2 R_{22}^{yy} - \lambda_z^2 R_{22}^{zz} - \lambda_x \lambda_y \left(R_{22}^{xy} + R_{22}^{yx} \right) - \lambda_x \lambda_z \left(R_{22}^{xz} + R_{22}^{zx} \right) - \lambda_y \lambda_z \left(R_{22}^{yz} + R_{22}^{zy} \right) \right) c \end{aligned} \tag{40}$$

which is of the form

$$\frac{\partial c}{\partial T} + (1-\theta) \frac{\partial c}{\partial X} - \frac{1}{Pe} \frac{\partial^2 c}{\partial X^2} = -\Omega c \tag{41}$$

where *Pe* is the Peclet number.

Thus we obtain the same equation as in the 1-D case [15], except that the coefficients of the PDE now account for capture due to the zero-mean displacement particle movement in the *y* and *z* directions.

We can compare this with the dimensionless 1D equation derived from the 1D Boltzmann equations:

$$\frac{\partial c}{\partial T} + \left(1 - \frac{2\lambda R_{12}}{\overline{v}} \right) \frac{\partial c}{\partial X} = \frac{R_{11}}{\overline{v} L} \frac{\partial^2 c}{\partial X^2} - \frac{L_c}{\overline{v}} \left(\lambda \overline{|v|} - \lambda^2 R_{22} \right) c \tag{42}$$

where the R_{ij} terms are defined as:

$$R_{ij} = \int_{-\infty}^{\infty} \frac{v_i v_j}{\lambda |v_x| + \frac{1}{\tau}} \psi_0 (v_x) dv \tag{43}$$

Next we wish to illustrate the differences between the two formulations. The equations presented assume nothing about either the equilibrium velocity distribution, $\psi_0(v_x,v_y,v_z)$ or the relaxation time, $\tau(v_x,v_y,v_z)$. In order to perform calculations, we assume that the velocity distribution takes the form a of a multivariate normal distribution, and that the relaxation time is a constant. The multivariate normal distribution is parameterised by the three mean velocities, $\overline{v_x}$, $\overline{v_y}$, $\overline{v_z}$, and the covariance matrix:

$$C_v = \begin{bmatrix} \sigma_x^2 & \rho_{xy}\sigma_x\sigma_y & \rho_{xz}\sigma_x\sigma_z \\ \rho_{xy}\sigma_x\sigma_y & \sigma_y^2 & \rho_{xy}\sigma_y\sigma_z \\ \rho_{xz}\sigma_x\sigma_z & \rho_{xy}\sigma_y\sigma_z & \sigma_z^2 \end{bmatrix} \tag{44}$$

where σ is the covariance, and ρ is the correlation between velocities in two directions.

Unless otherwise stated, the variables used in each of the calculations are presented in Table 1.

Table 1: Default coefficients used in sensitivity study

Variable	Value	Units
x-filtration coefficient, λ_x	10	m^{-1}
y-filtration coefficient, λ_y	10	m^{-1}
z-filtration coefficient, λ_z	10	m^{-1}
x-mean velocity, $\overline{v_x}$	10^{-3}	$m.s^{-1}$
y-mean velocity, $\overline{v_y}$	0	$m.s^{-1}$
z-mean velocity, $\overline{v_z}$	0	$m.s^{-1}$
xx-covariance, σ_{xx}	5×10^{-4}	$m.s^{-1}$
yy-covariance, σ_{yy}	5×10^{-4}	$m.s^{-1}$
zz-covariance, σ_{zz}	5×10^{-4}	$m.s^{-1}$
xy-correlation, ρ_{xy}	0.5	-
xz-correlation, ρ_{xz}	0.5	-
yz-correlation, ρ_{yz}	0.2	-
Relaxation time, τ	10^4	s

In order to have as much equivalence between the two models, the equilibrium velocity distribution for the 1-D formulation is calculated as follows:

$$\psi_{0,1-D}\left(v_x\right) = \int_{-\infty}^{\infty}\int_{-\infty}^{\infty} \psi_{0,3-D}\left(v_x, v_y, v_z\right) dv_y dv_z \tag{45}$$

Fig. 3 shows approximate iso-density points of the equilibrium velocity distribution.

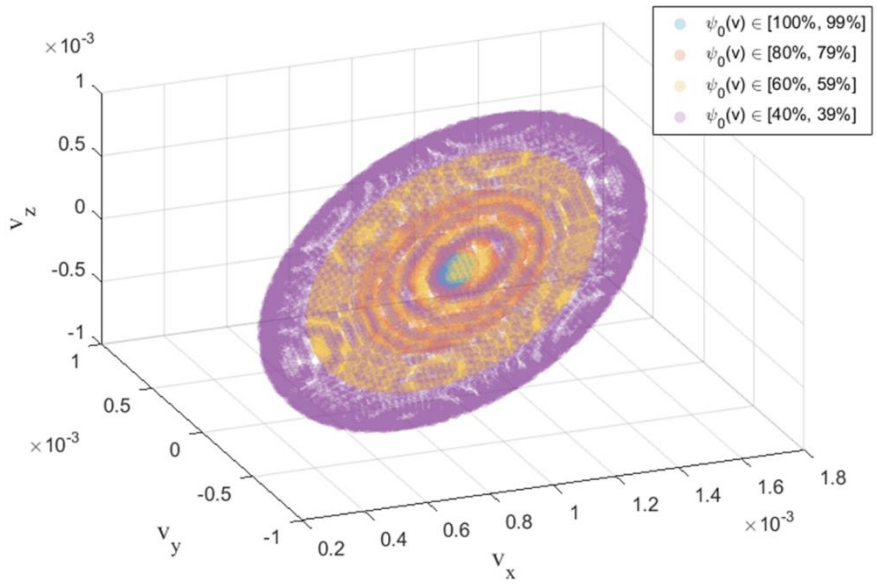

FIG 3. Three-dimensional equilibrium velocity distribution $\psi_0(v_x,v_y,v_z)$. Different colours present numerical values of the distribution at selected intervals of fractions of $\psi_0(v_x,v_y,v_z)$

First we compare the models by calculating effluent concentration that would be predicted during coreflooding tests. Coreflooding tests with particle injection are typically done one of two ways; either by injecting a fixed concentration uninterrupted (continuous injection), or by injecting a small concentration during a negligibly small time period followed by particle-free water (pulse injection). We present calculations for both cases. Regardless of the injection program, we consider the core to initially be free of particles:

$$c\left(x,t=0\right)=0 \tag{46}$$

The inlet boundary condition for the continuous injection is taken to be a third type boundary condition

$$-\frac{1}{Pe}\frac{\partial c\left(0,T\right)}{\partial X}+\left(1-\theta\right)c\left(0,T\right)=c_0 \tag{47}$$

where the initial condition for the pulse injection is

$$-\frac{1}{Pe}\frac{\partial c\left(0,T\right)}{\partial X}+\left(1-\theta\right)c\left(0,T\right)=c_0\delta\left(t\right) \tag{48}$$

For both cases we consider a semi-infinite domain and pose the boundary condition

$$\frac{\partial c\left(\infty,t\right)}{\partial X}=0 \tag{49}$$

For the continuous injection, Van Genuchten and Alves[37] provide an analytical solution:

$$\frac{c(X,T)}{c_0}=\frac{v}{v+u}e^{\frac{(v-u)X}{2Pe^{-1}}}erfc\left[\frac{X-uT}{2\left(Pe^{-1}T\right)^{1/2}}\right]+\frac{v}{v-u}e^{\frac{(v+u)X}{2Pe^{-1}}}erfc\left[\frac{X+uT}{2\left(Pe^{-1}T\right)^{1/2}}\right]$$
$$+\frac{v^2}{2\Omega Pe^{-1}}e^{\frac{vX}{Pe^{-1}}-\Omega T}erfc\left[\frac{X+vT}{2\left(Pe^{-1}T\right)^{1/2}}\right] \tag{50}$$

where

$$v=(1-\theta) \tag{51}$$

and

$$u=v\left(1+\frac{4\Omega Pe^{-1}}{v^2}\right)^{1/2} \tag{52}$$

For the pulse injection, we also have an analytical solution[37]

$$\frac{c(X,T)}{c_0}=\frac{(1-\theta)\exp\left[-\frac{\left((1-\theta)T-X\right)^2}{4Pe^{-1}T}-\Omega T\right]}{\sqrt{\pi Pe^{-1}T}}-\frac{(1-\theta)^2\exp\left[\frac{(1-\theta)X}{Pe^{-1}}-\Omega T\right]}{2Pe^{-1}}erfc\left[\frac{(1-\theta)T+X}{2\sqrt{Pe^{-1}T}}\right] \tag{53}$$

Using the parameters in Table 1, we get the results presented in Fig. 4.

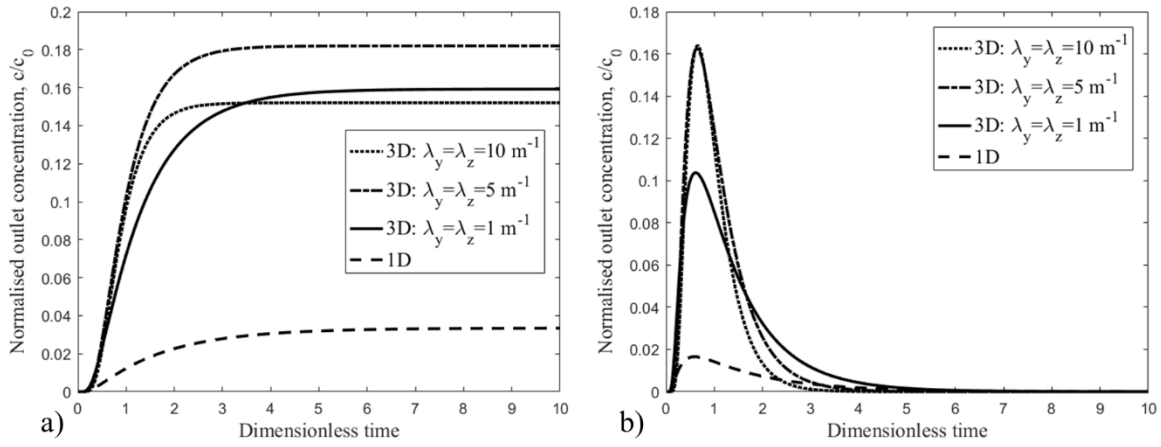

FIG 4. Effluent concentration curves for the 1-Dimensional advection-diffusion equation with capture derived from the 3-D and 1-D formulations of the Boltzmann equation, a) Continuous injection, b) Pulse injection. Sensitivity for the 3-D case is shown with the transverse filtration coefficients λ_y,λ_z. The case where they are zero is exactly the 1-D case.

The parameters in Table 1 provide (θ, Pe^{-1}, Ω) for the 3-D model: for $\lambda_y=\lambda_z=1$, (0.6727, 0.3620, 0.7548), for $\lambda_y=\lambda_z=5$, (0.4112, 0.5037, 1.1474), for $\lambda_y=\lambda_z=10$, (0.2923, 0.1694, 1.5231), and for the 1D model: (0.9502, 0.5037, 0.5467). The correlation variables for the equilibrium velocity distribution were set to zero here, so that the case of $\lambda_y=\lambda_z=1$ would align with the 1-D case. We note here the significance of the delay factor, θ. Despite a higher value of Ω, the 3-D formulation shows a larger effluent concentration, indicating less capture. This is a direct result of the significantly higher value of θ that is

calculated using the 1-D formulation. These calculations are entirely dependent on the parameters chosen, and such a significant difference is not always expected.

Below we compare the two models by performing sensitivity analysis with the primary variables. In the following, we make little distinction between the two directions perpendicular to the mean flow (*y,z*), as they play the same role in the following calculations. First, we consider the effect of the filtration coefficient in the x-direction. The results of the sensitivity study for the dimensionless delay factor, θ, macroscale filtration coefficient, Ω, and the inverse Peclet number, Pe^{-1} are presented in Fig. 5.

Before discussing the sensitivities on each particular variable, we briefly discuss the physical interpretation of each variable. The R_{ij} terms are in essence a measure of interdependence. If we define a second velocity distribution:

$$\psi^*(v_x, v_y, v_z) = \frac{\psi_0(v_x, v_y, v_z)}{\Lambda} = \frac{\psi_0(v_x, v_y, v_z)}{\lambda_x |v_x| + \lambda_y |v_y| + \lambda_z |v_z| + \tau^{-1}} \tag{54}$$

Then the R_{ij} terms become equivalent to covariances, calculated according to this modified velocity distribution. This modified distribution accounts for 'local' or 'first-order' effects of particle capture and velocity relaxation on the velocity distribution. In truth, particle capture, transport, and relaxation will result in an instantaneous velocity distribution at any point (*x,y,z,t*) that can vary greatly from ψ_0. This is captured in the original formulation, but is simplified to this 'local' quantification following the long waves, large times approximation made during the derivation (see Eq. (B-17)).

The dimensionless velocity delay factor, θ represents a delay in the effective advective velocity in the x-direction. This arises due to the preferential capture of faster particles, which shifts the instantaneous particle velocity distribution towards lower values. The first term in θ in Eq. (40) describes covariance between v_x and the x-directional capture term, $\lambda_x|v_x|$. The correlation between these terms quantifies precisely the effect of faster particles being captured, or the co-occurrence of fast particles and particle capture. The second and third terms in θ are unique to the three-dimensional formulation. They describe respectively, the covariance between the velocity v_x, and capture in the *y* and *z* directions. It is important to note here that this covariance is measured with respect to the modified velocity distribution, such that even with no correlations between the velocities, such that

$$\psi_0\left(v_x, v_y, v_z\right) = \psi_{0,x}\left(v_x\right)\psi_{0,y}\left(v_y\right)\psi_{0,z}\left(v_z\right) \tag{55}$$

then the R_{ij} terms can still be non-zero.

The inverse Peclet number is of a similar form for both the 3-D and 1-D formulations. The R_{11} term describes the covariance between v_x and itself, a common feature of a statistically derived diffusion coefficient. In this case, we measure this covariance relative to the modified velocity distribution, which accounts for particle capture and relaxation.

The macroscale filtration coefficient, Ω contains two types of terms. The first are the product between microscale filtration coefficients and the mean of the absolute velocity. These are the 'zero-order' capture terms, that are simply the averaged representation of particle capture. The second set of terms involve two filtration coefficients, and an R_{22} term. These second terms include every combination of each direction, with cross-direction terms being represented twice. These terms describe the extent to which capture in the two directions occurs simultaneously. This co-occurrence describes the 'first-order' capture effect, wherein particle capture changes the instantaneous particle velocity distribution thus changing the extent of capture. In this case, particle capture reduces the proportion of fast particles, and given that these particles are captured at higher rates, this reduces the overall capture rate.

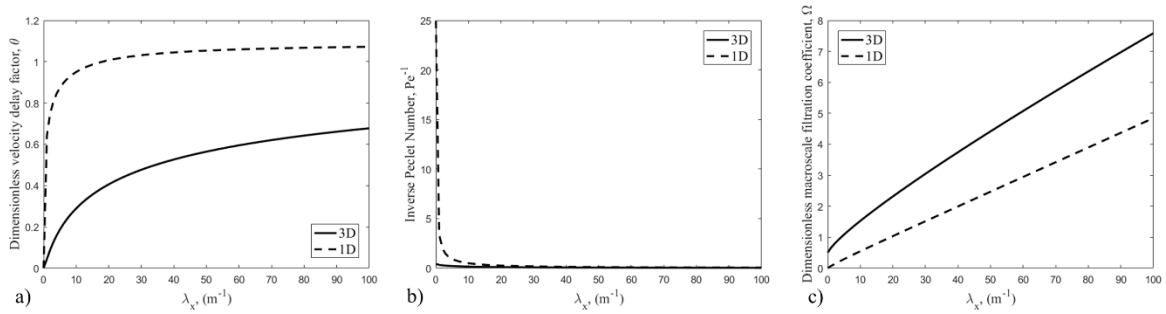

FIG 5. Sensitivity of the parameters of the 1-Dimensional advection-diffusion equation with capture derived from the 3-D and 1-D formulations of the Boltzmann equation with respect to the filtration coefficient in the direction parallel to flow (x)

Dependencies of the two approaches on λ_x are qualitatively the same; θ increases with increases capture. This follows directly from the physical interpretation outlined above; θ arises from preferential capture of faster particles, so increasing capture increases this effect. Both models predict a θ of zero with no capture in the x-direction. The asymptotic tendency at high values of λ_x indicates exhaustion of faster particles whose capture leads to θ.

The results for the inverse Peclet number are presented in Fig. 5(b). Both curves show a decreasing trend, consistent with the idea that capture narrows the particle velocity distribution, resulting in less dispersion.

Fig. 5(c) shows the sensitivity of the macro-scale filtration coefficient. Again, both methods show the same general positive tendency. A key difference is that while macroscale capture is zero when λ_x is zero for the 1-D formulation, it is finite for the 3-D formulation due to capture in the two cross-flow directions. Both curves are non-linear, with diminishing returns resulting from the 'first-order' terms. This balancing effect of capture is slightly stronger for the 3-D formulation, as capture in each of the three-directions can reduce the propensity of capture.

Next we consider the effect of the capture in the two cross-flow directions (y,z). Again, all variables for these two variables are the same for these calculations, so sensitivity is done similarly by varying both simultaneously. The results are presented in Fig. 6.

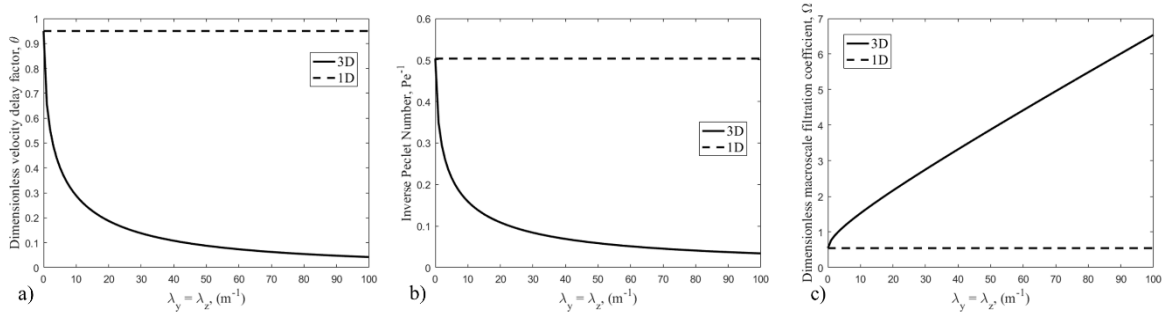

FIG 6. Sensitivity of the parameters of the 1-Dimensional advection-diffusion equation with capture derived from the 3-D and 1-D formulations of the Boltzmann equation with respect to the filtration coefficient in the directions perpendicular to flow (y,z)

The first observation is that variation of λ_y and λ_z has no effect on the 1-D formulation. For the 3-D formulation, the velocity delay factor shows a decreasing trend, contrary to the trend with λ_x. While capture in the two cross-directions are also proportional to velocity, it is independent on the x-directional velocity. The dimensionless velocity delay factor arises due to preferential capture of particles moving quickly in the x-direction. Thus while increasing λ_y and λ_z increases the total amount of particle capture, it decreases the selectivity of particle capture on large values of v_x, thus decreasing θ.

Suppose we introduce at a point a finite concentration of particles into a porous medium with velocity distribution ψ_0. The concentration pulse will have an average motion, however faster and slower particles will tend to drift from the centroid of the pulse. While they separate from the concentration pulse due to their x-direction velocity, their movement in the y,z-directions will result in their capture. This results in a reduction of the dispersion of particles, as seen in Fig. 6(b).

Lastly, Fig. 6(c) shows that under the 3-D formulation, capture in the cross-directions translates directly into the total capture rate, with some non-linearity noted at low values.

Next we present sensitivity on the width of the equilibrium velocity distribution. The three dimensional velocity distribution used in this study is parameterised by 9 variables $\left(\overline{v_x}, \overline{v_y}, \overline{v_z}, \sigma_x, \sigma_y, \sigma_z, \rho_{xy}, \rho_{xz}, \rho_{yz}\right)$, however, there is no observed dependency on $\overline{v_x}$, and $\overline{v_y}$ and $\overline{v_z}$ are zero, so we will restrict our investigation to the three covariances, σ_x, σ_y, and σ_z.

First we consider the results for the primary flow direction. Results are presented in Fig. 7.

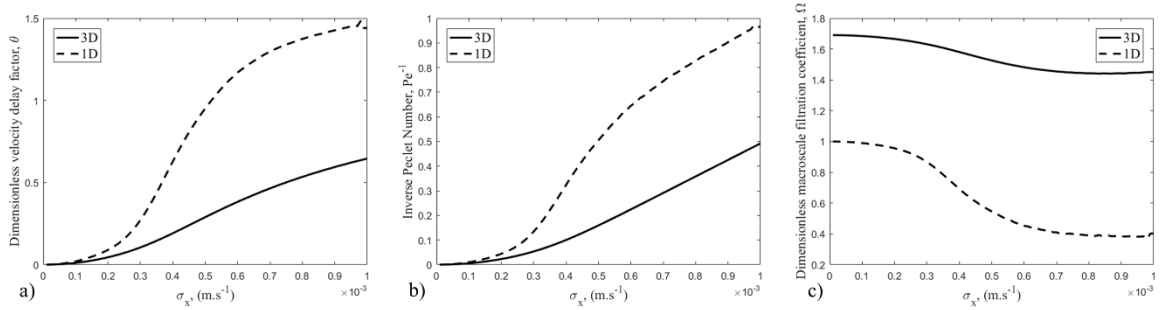

FIG 7. Sensitivity of the parameters of the 1-Dimensional advection-diffusion equation with capture derived from the 3-D and 1-D formulations of the Boltzmann equation with respect to the covariance of the equilibrium velocity distribution in the direction parallel to flow (x)

Both models exhibit an increasing tendency on advective velocity delay with the width of velocities in the x-direction. A greater variance in velocities implies that the velocity preference of capture can have a greater effect on the velocity distribution. On the contrary, when particles all move with approximately the same velocity, then their capture rate will be equal, and θ will be negligibly small.

The results for the inverse Peclet number in Fig. 7(c) illustrate a positive trend, which is expected even in the absence of particle capture. Both trends are lower than the no-capture trend $Pe^{-1} \propto \sigma_x^2$ directly as a result of the reduction of dispersion due to capture.

The macroscale filtration coefficient, presented in Fig. 7(b), is finite at zero σ_x under either formulation. Given that the distribution ψ_0 is centred around a positive value of v_x, increasing it will initially result in an increase in number of both fast and slow particles, but a disproportionate increase in slower particles, decreasing the overall effectiveness of capture. Once σ_x increases sufficiently, given that our choice of ψ_0 permits negative values of v_x, increasing the width of the distribution results in an ever-increasing proportion of velocities with large magnitudes, thus increasing particle capture. While normal distributions are common, it is important to note that this sensitivity study, while illustrative of some physical properties of the coefficients, is dependent on our choice of distribution.

Next we investigate the effect of σ_y and σ_z, which we vary simultaneously. The results are presented in Fig. 8.

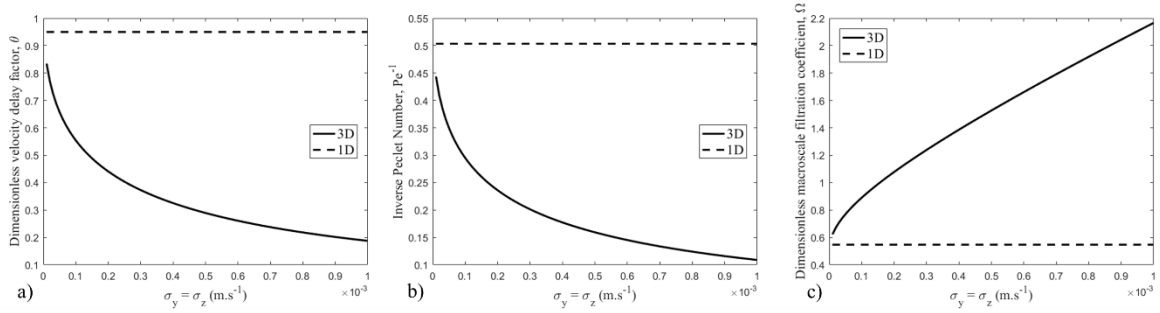

FIG 8. Sensitivity of the parameters of the 1-Dimensional advection-diffusion equation with capture derived from the 3-D and 1-D formulations of the Boltzmann equation with respect to the covariance of the equilibrium velocity distribution in the directions perpendicular to flow (y,z)

Again, we note that the 1-D formulation is independent on the covariance of ψ_0 in the two cross-flow directions, as expected. For all three coefficients, the trend is the opposite when compared with the sensitivity performed on σ_x. First, we consider the effect on Ω. With increasing σ_y and σ_z, a larger proportion of particles will exhibit cross-flow velocities with high magnitudes, thus increasing the total extent of capture. This is reflected in the results of the sensitivity study presented in Fig. 8(c).

The negative tendency observed in Fig. 8(a) for θ is a result of an increase in capture that is largely independent on the velocity of particles in the x-direction. When particles begin to move faster in the y- and z-directions, they begin to be captured regardless of their velocity in the x-direction. The velocity delay factor arises due to the selective capture of particles whose velocity magnitude in the x-direction is high, so reducing this selectivity naturally reduces θ. It is of interest that while increasing σ_y and σ_z increases the total capture, it decreases θ, a parameter that arises specifically due to capture.

Similar to the discussions surrounding σ_x, the increased capture from a wider particle velocity distribution leads to a narrower effective distribution, leading to less dispersion, as illustrated in Fig. 8(b).

Lastly we present a sensitivity study on the relaxation time, τ, presented in Fig. 9.

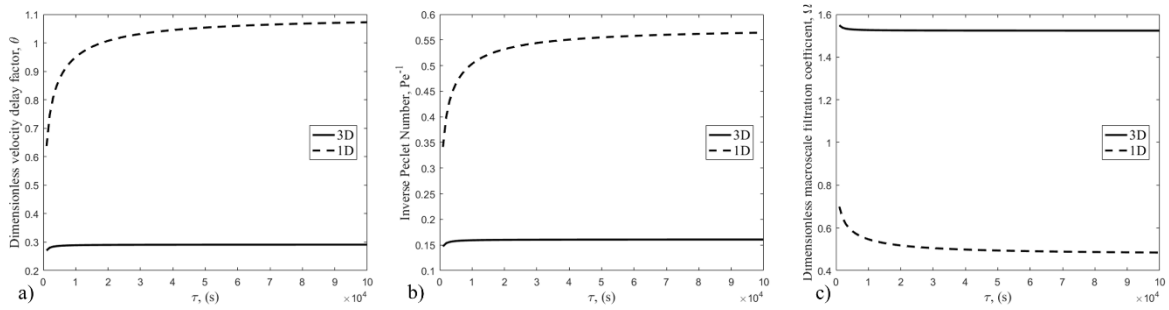

FIG 9. Sensitivity of the parameters of the 1-Dimensional advection-diffusion equation with capture derived from the 3-D and 1-D formulations of the Boltzmann equation with respect to the relaxation time

The impact of this relaxation time is to counteract the effect of particle capture on the effective particle velocity distribution, as highlighted in Eq. (54). When the relaxation time is small, the effect of capture on the particle velocity distribution becomes negligible, as induced perturbations are removed almost instantly. This is reflected in Fig. 9(a) which presents the sensitivity of θ with respect to τ. As θ arises exactly due to a change in the effective velocity distribution, being a shift to lower velocities, it follows that when such perturbations are dampened by the effects of relaxation, θ reduces. Increasing τ results in an asymptotic tendency towards a limit where relaxation plays no role, and the effect of capture on transport is fully realised.

The trend for the inverse Peclet number is similar to that of θ, although the physical interpretation differs. Consider a particle concentration front moving through the porous media. On the front, we consider a particle moving in the x-direction faster than average. After some time, this particle will move ahead of the front, alongside other fast particles. Relaxation will cause these particles to decelerate, moving the instantaneous velocity distribution back towards the equilibrium distribution. The same effect is true for slow particles which fall behind the progressing concentration front. Without the relaxation, these fast and slow particles would spread ever quicker from the centroid of the concentration front, in essence enhancing dispersion. This is why in Fig. 9(b), we see that decreasing τ decreases the dispersion coefficient. When capture is absent, this positive tendency continues, with Pe^{-1} diverging. With capture present, both the 3-D and 1-D formulations show an asymptotic tendency.

As discussed earlier, the derived equations for Ω account for the depletion of faster particles by capture, which consequently reduces the total capture rate. Relaxation of the particle velocity distribution counteracts this effect, increasing the concentration of faster particles, and thus increasing capture. This is evident in Fig. 9(c), which shows a negative tendency for Ω in both the 3-D and 1-D formulations.

For all three coefficients, the effect of τ is much greater in the 1-D formulation than in the 3-D. This is clear mathematically from Eq. (54) for the effective particle velocity distribution, where the analogue for the 1-D formulation is the same albeit without the cross-flow capture terms in the denominator. We expect from this equation, that the two cross-flow terms act in a similar way to τ, dampening the effect of capture in the x-direction on the particle velocity distribution. In effect this is true, but they do this in two different ways; τ directly relaxes the particle velocity distribution back to the equilibrium distribution, ψ_0 as a result of dispersion, while the $\lambda_y|v_y|$ and $\lambda_z|v_z|$ terms create a competition, wherein some of the particles are now being captured with little regard for their velocity in the x-direction, and so the resulting impact of x-directional capture is lessened.

IV. Concluding Remarks

Formulation of Boltzmann's kinetics equation in 3-dimensions with anisotropic capture and diffusion and exact upscaling allows us to conclude the following:

- Introduction of a sink-source term into the Boltzmann equation and solution of functional equation in Fourier images allows for exact upscaling;
- The upscaled equation takes the form of a 3-Dimensional advection-diffusion equation with a linear capture term and mixed-derivative diffusion terms;
- The upscaling procedure yields explicit formulae for upper-scale transport coefficients versus micro-scale coefficients and the equilibrium velocity distribution in all basic dirtections;
- As with the 1-Dimensional formulation, the resulting ADE equation has delayed advective velocity, resulting from the preferential capture of fast particles
- In the case where the suspended concentration of particles is uniform in the *y* and *z* directions, then the upscaled equation devolves into a 1-Dimensional ADE with three dimensionless coefficients describing diffusion, capture, and velocity delay
- The three coefficients in the 1-D case account for the impacts of capture and diffusion in the *y* and *z* directions, which can significantly change the magnitude of each parameter, even in the presence of zero mean velocity in these two directions
- Several sensitivity studies illustrate the relationships between the dimensionless coefficients and the microscale parameters, for both the 1-Dimensional ADE's derived from the 3-Dimensional and 1-Dimensional formulations of the Boltzmann equation

ACKNOWLEDGEMENTS

The authors are deeply grateful to Prof Anthony Roberts (University of Adelaide) for numerous discussions and friendly support. Numerous detailed considerations and co-authorship with Prof

Dinariev (Russian Academy of Sciences), Prof A. Shapiro (Denmark Technical University), and A. Rego (State University of Rio de Janeiro) are gratefully acknowledged.

DATA AVAILABILITY

The data that support the findings of this study are available from the corresponding author upon reasonable request.

Appendix A. Determination of L_{ac} and L_{aa}^{-1} operators

First we derive the L_{ac} term. From the derivation of the decomposition of the Hilbert space in Eq. (14), it follows that the projection P_a can be written as

$$P_a(x) = x - (1, x) \tag{A-1}$$

where the brackets denote the inner product defined in Eq. (13).

Due to the linearity of both terms, we perform this projection on each of the terms in L, where we make note that we are considering the embedding of the solution φ_F in the c-subspace:

$$P_a \phi i\omega c = 0 \tag{A-2}$$

$$P_a v_x ikc = ikc\left(v_x - (1, v_x)\right) \tag{A-3}$$

$$P_a v_y ipc = ipc\left(v_y - (1, v_y)\right) \tag{A-4}$$

$$P_a v_z ihc = ihc\left(v_z - (1, v_z)\right) \tag{A-5}$$

$$P_a \lambda_x |v_x| c = \lambda_x c\left(|v_x| - (1, |v_x|)\right) \tag{A-6}$$

$$P_a \lambda_y |v_y| c = \lambda_y c\left(|v_y| - (1, |v_y|)\right) \tag{A-7}$$

$$P_a \lambda_z |v_z| c = \lambda_z c\left(|v_z| - (1, |v_z|)\right) \tag{A-8}$$

$$P_a \frac{1}{\tau}\left(\int_{-\infty}^{\infty}\int_{-\infty}^{\infty}\int_{-\infty}^{\infty} c\psi_0 dv_x dv_y dv_z - c\right) = 0 \tag{A-9}$$

Thus we get

$$L_{ac} = c\begin{bmatrix} ik\left(v_x - (1, v_x)\right) + ip\left(v_y - (1, v_y)\right) + ih\left(v_z - (1, v_z)\right) \\ +\lambda_x\left(|v_x| - (1, |v_x|)\right) + \lambda_y\left(|v_y| - (1, |v_y|)\right) + \lambda_z\left(|v_z| - (1, |v_z|)\right) \end{bmatrix} \tag{A-10}$$

Now let us derive L_{aa}^{-1}. We seek to derive an explicit form for p in the equation:

$$L_{aa} p = q \tag{A-11}$$

L_{aa} can be written as

$$L_{aa} = P_a\left(\phi i\omega x + v_x ikx + v_y ipx + v_z ihx + \lambda_x |v_x| x + \lambda_y |v_y| x + \lambda_z |v_z| x - \frac{1}{\tau}\left((1,x) - x\right)\right) J_a$$
$$= P_a\left(\phi i\omega x + v_x ikx + v_y ipx + v_z ihx + \lambda_x |v_x| x + \lambda_y |v_y| x + \lambda_z |v_z| x + \frac{1}{\tau} x\right) J_a \quad \text{(A-12)}$$

We write

$$L_{aa} = P_a \Lambda J_a \quad \text{(A-13)}$$

which is equivalent to solving the following equation for p

$$P_a \Lambda J_a p = q \quad \text{(A-14)}$$

We consider the term p to be within the a-subspace

$$P_a \Lambda p = q \quad \text{(A-15)}$$

Performing the projection (see Eq. (A-1))

$$\Lambda p - (\Lambda, p) = q \quad \text{(A-16)}$$

Rearranging, we get

$$p = \frac{(\Lambda, p) + q}{\Lambda} \quad \text{(A-17)}$$

Next we take the inner product of both sides with unity

$$(1, p) = (\Lambda, p)\left(1, \frac{1}{\Lambda}\right) + \left(q, \frac{1}{\Lambda}\right) \quad \text{(A-18)}$$

Given that p lies within the a-subspace, its inner product with unity is zero

$$0 = (\Lambda, p)\left(1, \frac{1}{\Lambda}\right) + \left(q, \frac{1}{\Lambda}\right) \quad \text{(A-19)}$$

Rearranging

$$(\Lambda, p) = -\frac{\left(q, \Lambda^{-1}\right)}{\left(1, \Lambda^{-1}\right)} \quad \text{(A-20)}$$

Substituting this into Eq. (A-17) we obtain

$$p = \frac{q}{\Lambda} - \frac{1}{\Lambda}\frac{\left(q, \Lambda^{-1}\right)}{\left(1, \Lambda^{-1}\right)} \quad \text{(A-21)}$$

Which is equivalent to

$$L_{aa}^{-1}(\varphi) = \frac{\varphi}{\Lambda} - \frac{1}{\Lambda}\frac{\left(\varphi, \Lambda^{-1}\right)}{\left(1, \Lambda^{-1}\right)} \quad \text{(A-22)}$$

where

$$\Lambda = \phi i\omega + v_x ik + v_y ip + v_z ih + \lambda_x |v_x| + \lambda_y |v_y| + \lambda_z |v_z| + \frac{1}{\tau} \tag{A-23}$$

Appendix B. Determination of fluxes and capture terms in Fourier space

We begin with the Fourier transform of the x-directional flux

$$q_{x,F} = \int_{-\infty}^{\infty}\int_{-\infty}^{\infty}\int_{-\infty}^{\infty} v_x \varphi_F \psi_0 \, dv_x dv_y dv_z \tag{B-1}$$

We make the decomposition given in Eq. (14)

$$q_{x,F} = \int_{-\infty}^{\infty}\int_{-\infty}^{\infty}\int_{-\infty}^{\infty} v_x \left(a_F + c_F\right) \psi_0 \, dv_x dv_y dv_z \tag{B-2}$$

We can separate these two terms

$$q_{x,F} = \int_{-\infty}^{\infty}\int_{-\infty}^{\infty}\int_{-\infty}^{\infty} v_x c_F \psi_0 \, dv_x dv_y dv_z + \int_{-\infty}^{\infty}\int_{-\infty}^{\infty}\int_{-\infty}^{\infty} v_x a_F \psi_0 \, dv_x dv_y dv_z \tag{B-3}$$

The averaged concentration, c_F is independent of velocity, and so can be taken out of the integral, leaving the average velocity in the x-direction.

Next, we add and subtract $(1,v_x)$ in the second integral

$$q_{x,F} = c_F \overline{v_x} + \int_{-\infty}^{\infty}\int_{-\infty}^{\infty}\int_{-\infty}^{\infty} \left(v_x - \left(1, v_x\right) + \left(1, v_x\right)\right) a_F \psi_0 \, dv_x dv_y dv_z \tag{B-4}$$

Rearranging the integral terms

$$q_{x,F} = c_F \overline{v_x} + \int_{-\infty}^{\infty}\int_{-\infty}^{\infty}\int_{-\infty}^{\infty} \left(v_x - \left(1, v_x\right)\right) a_F \psi_0 \, dv_x dv_y dv_z + \int_{-\infty}^{\infty}\int_{-\infty}^{\infty}\int_{-\infty}^{\infty} \left(1, v_x\right) a_F \psi_0 \, dv_x dv_y dv_z \tag{B-5}$$

The third time is zero, and the second term can be simplified using the definition of the inner product (Eq. (13)) and the P_a projection operator (Eq. (A-1))

$$q_{x,F} = c_F \overline{v_x} + \left(P_a v_x, a_F\right) \tag{B-6}$$

Substituting Eq. (18)

$$q_{x,F} = c_F \overline{v_x} + \left(P_a v_x, -L_{aa}^{-1} L_{ac} c_F\right) \tag{B-7}$$

Substituting Eq. (A-10) for the L_{ac} operator

$$q_{x,F} = c_F \overline{v_x} + \left(P_a v_x, -L_{aa}^{-1} \left[c_F \begin{Bmatrix} ik\left(v_x - \left(1, v_x\right)\right) + ip\left(v_y - \left(1, v_y\right)\right) + ih\left(v_z - \left(1, v_z\right)\right) \\ +\lambda_x \left(|v_x| - \left(1, |v_x|\right)\right) + \lambda_y \left(|v_y| - \left(1, |v_y|\right)\right) + \lambda_z \left(|v_z| - \left(1, |v_z|\right)\right) \end{Bmatrix} \right] \right) \tag{B-8}$$

Lastly, we substitute the L_{aa}^{-1} operator

$$q_{x,F} = c_F \left\{ \begin{array}{l} \overline{v_x} - ik\left(P_a v_x, L_{aa}^{-1}\left[v_x - \left(1, v_x\right)\right]\right) - ip\left(P_a v_x, L_{aa}^{-1}\left[v_y - \left(1, v_y\right)\right]\right) - ih\left(P_a v_x, L_{aa}^{-1}\left[v_z - \left(1, v_z\right)\right]\right) \\ -\lambda_x\left(P_a v_x, L_{aa}^{-1}\left[|v_x| - \left(1, |v_x|\right)\right]\right) - \lambda_y\left(P_a v_x, L_{aa}^{-1}\left[|v_y| - \left(1, |v_y|\right)\right]\right) - \lambda_z\left(P_a v_x, L_{aa}^{-1}\left[|v_z| - \left(1, |v_z|\right)\right]\right) \end{array} \right\}$$

(B-9)

Here we introduce terms:

$$R_{ij}^{kl} = \left(P_a v_i^k, L_{aa}^{-1}\left[v_j^l - \left(1, v_j^l\right)\right]\right) \tag{B-10}$$

where $i, j \in (1,2)$ with $v_1 = v$, $v_2 = |v|$, and $k, l \in (x, y, z)$. This results in

$$q_{x,F} = c_F\left(\overline{v_x} - ikR_{11}^{xx} - ipR_{11}^{xy} - ihR_{11}^{xz} - \lambda_x R_{12}^{xx} - \lambda_y R_{12}^{xy} - \lambda_z R_{12}^{xz}\right) \tag{B-11}$$

Similarly:

$$q_{y,F} = c_F\left(\overline{v_y} - ikR_{11}^{yx} - ipR_{11}^{yy} - ihR_{11}^{yz} - \lambda_x R_{12}^{yx} - \lambda_y R_{12}^{yy} - \lambda_z R_{12}^{yz}\right) \tag{B-12}$$

$$q_{z,F} = c_F\left(\overline{v_z} - ikR_{11}^{zx} - ipR_{11}^{zy} - ihR_{11}^{zz} - \lambda_x R_{12}^{zx} - \lambda_y R_{12}^{zy} - \lambda_z R_{12}^{zz}\right) \tag{B-13}$$

The same procedure can be performed to derive expressions for the Fourier transforms of the capture terms

$$\varepsilon_{x,F} = \lambda_x c_F\left(\overline{|v_x|} - ikR_{21}^{xx} - ipR_{21}^{xy} - ihR_{21}^{xz} - \lambda_x R_{22}^{xx} - \lambda_y R_{22}^{xy} - \lambda_z R_{22}^{xz}\right) \tag{B-14}$$

$$\varepsilon_{y,F} = \lambda_y c_F\left(\overline{|v_y|} - ikR_{21}^{yx} - ipR_{21}^{yy} - ihR_{21}^{yz} - \lambda_x R_{22}^{yx} - \lambda_y R_{22}^{yy} - \lambda_z R_{22}^{yz}\right) \tag{B-15}$$

$$\varepsilon_{z,F} = \lambda_z c_F\left(\overline{|v_z|} - ikR_{21}^{zx} - ipR_{21}^{zy} - ihR_{21}^{zz} - \lambda_x R_{22}^{zx} - \lambda_y R_{22}^{zy} - \lambda_z R_{22}^{zz}\right) \tag{B-16}$$

We make the long waves, large times approximation, which is equivalent to

$$k, p, h, \omega \to 0 \tag{B-17}$$

Consequently, the R_{ij} terms become constants.

References

1. S. A. Bradford, S. Torkzaban, andA. Shapiro, "A theoretical analysis of colloid attachment and straining in chemically heterogeneous porous media," Langmuir : the ACS journal of surfaces and colloids **29**, 6944 (2013).
2. P. Bedrikovetsky, "Upscaling of stochastic micro model for suspension transport in porous media," Transport Porous Med **75**, 335 (2008).
3. M. M. Sharma, andY. C. Yortsos, "Transport of particulate suspensions in porous media: Model formulation," AIChE Journal **33**, 1636 (1987).
4. P. Bedrikovetsky, Z. You, A. Badalyan, Y. Osipov, andL. Kuzmina, "Analytical model for straining-dominant large-retention depth filtration," Chem Eng J **330**, 1148 (2017).
5. P. Bedrikovetsky, Y. Osipov, L. Kuzmina, andG. Malgaresi, "Exact upscaling for transport of size-distributed colloids," Water Resour Res **55**, 1011 (2019).
6. Y. Efendiev, andA. Pankov, "Numerical homogenization of monotone elliptic operators," Multiscale Modeling and Simulation **2**, 62 (2003).

7. Y. Efendiev, andA. Pankov, "Numerical homogenization of nonlinear random parabolic operators," Multiscale Modeling and Simulation **2**, 237 (2004).
8. W. Pan, andA. Tartakovsky, "Dissipative particle dynamics model for colloid transport in porous media," Advances in water resources **58**, 41 (2013).
9. X. Li, Y. Liu, H. Sheng, andR. Feng, "Model for the flow of emulsion in porous media with micro-heterogeneities," Lixue Xuebao/Chinese Journal of Theoretical and Applied Mechanics **41**, 313 (2009).
10. A. M. Tartakovsky, M. Panzeri, G. Tartakovsky, andA. Guadagnini, "Uncertainty quantification in scale-dependent models of flow in porous media," Water Resour Res **53**, 9392 (2017).
11. M. Elimelech, J. Gregory, andX. Jia, *Particle deposition and aggregation: measurement, modelling and simulation* (Butterworth-Heinemann, 2013).
12. Y. Efendiev, T. Hou, L. Durlofsky, andH. Tchelepi, Multiscale analysis and computation for flows in heterogeneous media Document No. Number, 2016.
13. H. Yuan, andA. A. Shapiro, "Modeling non-Fickian transport and hyperexponential deposition for deep bed filtration," Chem Eng J **162**, 974 (2010).
14. P. Barbante, A. Frezzotti, andL. Gibelli, "A kinetic theory description of liquid menisci at the microscale," Journal of Kinetic Related Models **8**, 235 (2015).
15. O. Dinariev, A. Rego, andP. Bedrikovetsky, "Boltzmann Physical Kinetic for Deep Bed Filtration: Homogenization by solving operator equation in Hilbert space," arXiv preprint arXiv:2001.08069 (2020).
16. A. Shapiro, andJ. Wesselingh, "Gas transport in tight porous media: Gas kinetic approach," Chem Eng J **142**, 14 (2008).
17. V. Aristov, I. Voronich, andS. Zabelok, "Direct methods for solving the Boltzmann equations: Comparisons with direct simulation Monte Carlo and possibilities," Physics of Fluids **31**, 097106 (2019).
18. G. Malgaresi, B. Collins, P. Alvaro, andP. Bedrikovetsky, "Explaining non-monotonic retention profiles during flow of size-distributed colloids," Chem Eng J **375**, 121984 (2019).
19. A. A. Shapiro, "Elliptic equation for random walks. Application to transport in microporous media," Physica A: Statistical Mechanics and its Applications **375**, 81 (2007).
20. H. Zhang, G. V. C. Malgaresi, andP. Bedrikovetsky, "Exact solutions for suspension-colloidal transport with multiple capture mechanisms," International Journal of Non-Linear Mechanics **105**, 27 (2018).
21. A. Sauret, E. C. Barney, A. Perro, E. Villermaux, H. A. Stone, andE. Dressaire, "Clogging by sieving in microchannels: Application to the detection of contaminants in colloidal suspensions," Applied Physics Letters **105**, 074101 (2014).
22. C. Tien, andA. C. Payatakes, "Advances in deep bed filtration," **25**, 737 (1979).
23. J. Herzig, D. Leclerc, andP. L. Goff, "Flow of suspensions through porous media—application to deep filtration," Industrial & Engineering Chemistry **62**, 8 (1970).
24. T. Russell, O. Y. Dinariev, L. A. Pessoa Rego, andP. Bedrikovetsky, "Averaged Boltzmann's kinetics for colloidal transport in porous media," **n/a**, e2020WR029557.
25. K. H. Jensen, A. X. C. N. Valente, andH. A. Stone, "Flow rate through microfilters: Influence of the pore size distribution, hydrodynamic interactions, wall slip, and inertia," Physics of Fluids **26**, 052004 (2014).
26. D. Lasseux, A. A. Abbasian Arani, andA. Ahmadi, "On the stationary macroscopic inertial effects for one phase flow in ordered and disordered porous media," Physics of fluids **23**, 073103 (2011).
27. D. Lasseux, andF. Valdés-Parada, "Symmetry properties of macroscopic transport coefficients in porous media," Physics of Fluids **29**, 043303 (2017).
28. V. Aristov, A. Frolova, andS. Zabelok, "Nonequilibrium kinetic processes with chemical reactions and complex structures in open systems," EPL (Europhysics Letters) **106**, 20002 (2014).
29. S. Brull, P. Charrier, andL. Mieussens, "Gas-surface interaction and boundary conditions for the Boltzmann equation," arXiv preprint (2013).
30. L. Quansheng, C. Xianze, andZ. Chengyuan, "Research advances in the characterization of transportation and deposition of suspended particles in porous media," Chinese Journal of Rock Mechanics and Engineering **34**, 2410 (2015).

31. J. Xu, "Propagation behavior of permeability reduction in heterogeneous porous media due to particulate transport," EPL (Europhysics Letters) **114**, 14001 (2016).
32. P. L. Bhatnagar, E. P. Gross, andM. Krook, "A Model for Collision Processes in Gases. I. Small Amplitude Processes in Charged and Neutral One-Component Systems," Physical Review **94**, 511 (1954).
33. C. Cercignani, *Mathematical methods in kinetic theory* (Springer, 1969).
34. C. Cercignani, *The Boltzmann Equation and Its Applications* (Springer-Verlag New York, 1988).
35. S. Brull, andP. Charrier, "Boundary conditions for the Boltzmann equation for rough walls," **1628**, 368 (2014).
36. S. Brull, P. Charrier, andL. Mieussens, "Nanoscale roughness effect on Maxwell-like boundary conditions for the Boltzmann equation," Physics of Fluids **28**, 082004 (2016).
37. M. Van Genuchten, andW. J. Alves, *Analytical Solutions of One Dimensional Convective Dispersive Solute Transport Equations* (1982).

6 Conclusions

The laboratory experiments and mathematical modelling of particle detachment, transport, and capture in porous media allows drawing the following conclusions:

1. In artificial sand-kaolinite cores, above kaolinite contents of 3%, cores show very similar permeability decline in response to the injection of low-salinity water, suggesting that clay content is not in itself a good indicator for the sensitivity of rocks to formation damage by fines migration. In addition, only a fraction of the present clay is detached during low-salinity water injection, suggesting that a majority of the clay within the rock does not contribute to fines migration directly.
2. The detachment of particles due to the reduction of injected fluid salinity is dependent on the type of ions within the injected fluid. Bivalent Ca^{2+} ions demonstrate a hysteretic adsorption behaviour, wherein cores saturated with calcium salts exhibit no sensitivity even to extremely low salinity fluids. This hysteresis is not present with Na^{+} ions to the extent that low-salinity sensitivity can be averted. Saturation of cores previously saturated with Ca^{2+} ions with Na^{+} ions can restore the rock's sensitivity to low-salinity water.
3. Including a finite particle detachment kinetics rate while retaining the critical retention function within the 1-Dimensional formulation of fines migration allows for an exact solution. The discontinuity present in the solution without delay is no longer present once the delay in detachment is introduced. The effect of the delay is to increase the stabilisation time, with no effect on the final strained particle profile or impedance. The model exhibits good agreement with laboratory coreflooding data.
4. Formulation of the axisymmetric fines migration problem with two delay factors also allows for an analytical solution, albeit with implicit expressions for all concentrations and impedance. The instantaneous detachment of particles once flow commences is formulated in the initial conditions, while the subsequent detachment due to the injected fluid salinity occurs with delay. This formulation requires the critical retention function to be defined over

the entire range of velocities and salinities encountered during the injection. Calculations using laboratory data show decreases of injectivity more than twice, with stabilisation occurring in less than three hours in all cases.

5. The formulation of colloidal transport using Boltzmann's kinetic equation allows for a direct coupling of particle capture and diffusion/dispersion. Using Hilbert space projections, the equation can be upscaled to produce an advection diffusion equation with capture and a delayed advective velocity. The coefficients of the upscaled equation can be expressed explicitly in the microscale parameters for capture and transport. The three macroscale parameters exhibit an inherent relationship, which reduces to a two-dimensional space when all particle velocities are positive. The model shows good agreement with laboratory data that exhibits a delayed advective velocity.
6. Generalising the Boltzmann model to allow for arbitrary dependence of capture on the particle velocity permits the same upscaling procedure, resulting in an upscaled equation of the same form, with different relationships for the coefficients. Several existing models for capture which exhibit velocity dependence are presented and are shown to exhibit different macroscale behaviour including an attachment model which results in an advective particle velocity greater than that of the carrier fluid. Use of the existing models is shown to improve agreement with laboratory data. Agreement between laboratory data and the model can be used to identify the underlying physical processes that occur during the coreflood.
7. Further generalisation of the model to three dimensions results in a 3-Dimensional advection diffusion equation with capture, cross diffusion terms, delayed advective velocity in each principal direction, and macroscale coefficients that now account for capture in all three directions. Under the assumption that particles move with the same velocity in each direction, the upscaled capture term is equal to the scalar product of the filtration coefficients and particle velocities in each direction. Reduction of the 3-Dimensional equation to 1-Dimension results in the familiar ADE with capture, with the addition that now the capture of particles due to diffusion in the two directions perpendicular to flow is now accounted for in all three coefficients.

Recommendations

- Investigation and experimental validation of more complex formulations for particle detachment delay
- Experimental tests that are designed specifically for high diffusion and high capture to validate the delayed advection derived using Boltzmann's equation
- Experimental regime designed to determine all coefficients in the 3-Dimensional formulation of the ADE derived using Boltzmann's equation
- Comparison of the modelling results from Boltzmann's equation (as in this thesis) and other statistical approaches such as random walks and population balance